FINAL REPORT

NASA GRANT NSG-2112

for

TRANSONIC FLOW STUDIES

from the

University of Arizona
Tucson, Arizona 85721

Principal Investigator: Dr. A. Richard Seebass

Co-principal Investigator: Dr. K.-Y. Fung

Technical Officer: Dr. William F. Ballhaus
NASA Ames Research Center

Period: 1 November 1975 - 31 October 1980

28 February 1981

FINAL REPORT

NSG-2112

INTRODUCTION

This final report delineates research activities on NASA Grant NSG-2112 from 1976 to 1980. These research activities were also supported in part by the AFOSR and the ONR. This research resulted in fifteen publications to October 31, 1980; four additional publications are planned as a consequence of this research. The publications are listed in chronological order in the Appendix. The list is annotated to indicate the cited source of funding for the research reported upon in the publication. The Appendix also lists the talks given by various investigators supported by this grant, as well as the eleven Transonic Fluid Dynamic Reports we have issued during the grant period.

SHOCK-FREE AIRFOIL AND WING DESIGN

For most of the grant period we had an active research program on the direct and indirect design of shock-free airfoils and wings. We report on this research here, noting that while some minor activities continue, the major thrust of this research has been completed. We limit the main part of our discussion to results that have not yet been published.

Transonic Airfoils with a Given Pressure Distribution

Our original collaboration with Dr. Helmut Sobieczky resulted from a plan to adopt his rheograph design method that used analog computations to a completely digital approach. As a result of this collaboration, we have developed a procedure that uses a map of the hodograph plane to find transonic airfoils with a given pressure distribution. This work complements related studies that provide airfoil modifications to achieve shock-free flow. The method is limited to a prescription of the subsonic portion of the pressure distribution and to shock-free supersonic flows. We have no plans to extend this capability further. The procedure we have developed is fairly efficient for subcritical flows; we feel that this will remain true for supercritical flows, but we have only preliminary results for this case.

The procedure we use is the following: We first note that if we use the Prandtl-Meyer function, ν , and the flow deflection angle, θ , as independent variables, then the equations for the stream function and velocity potential are not only linear, as they would be with the hodograph transformation, but they are also in canonical form. That is, the second-order derivatives either form the Laplacian or the wave operator depending on whether or not the flow is subsonic or supersonic. Thus the equations for the subsonic flow are invariant in form under a conformal transformation. We thus assume that a conformal map from the two-sheeted Riemann surface of the subsonic portion of the ν, θ-plane into the unit circle. Part of the boundary of the unit circle corresponds to the airfoil surface wetted by subsonic flow; the other part corresponds to the sonic line. These portions are then chosen and the pressure on the subsonic part of the unit circle is prescribed. On the sonic line segment the pressure takes its critical value. With the pressure given on the boundary of the unit circle, and with the subsonic portion of the flow inside the unit cicle, we take advantage of the fact that the mapping to this plane is conformal. Thus the Prandtl-Meyer function and the flow deflection angle are conjugate harmonics. Because the pressure is given on the unit circle we know the Prandtl-Meyer function there. We then solve Laplace's equation for the Prandtl-Meyer function inside the unit circle using Fourier series; this immediately determines the flow deflection angle to within a constant.

On the portion of the airfoil surface that corresponds to subsonic flow the stream function is zero. We prescribe a distribution for the stream function on the sonic line to complete the boundary value problem for the stream function. This boundary value problem is then solved using a fast Poisson solver, determining the stream function and thereby the velocity potential, as functions of ν and θ in the subsonic portion of the flow and on the sonic line. These results are then mapped back to the physical plane to see if the corresponding airfoil is a reasonable one. If it is not, then the input must be modified. When a suitable airfoil is found, the data on the sonic line is integrated in the ν, θ-plane to find the zero streamline. This, then, determines that portion of the airfoil wetted by supersonic flow. This calculation may fail due to a singularity in the mapping back to the physical plane. This indicates that the sonic line data is not consistent with shock-free flow and requires that the input be changed.

There are several minor points that cause great difficulty and have required some imagination to circumvent. These include the logarithmic singularity in ν at $q = 0$, a $-1/3$ power singularity in the normal derivative of the stream function at the sonic line in the ν, θ-plane, and the need to choose the circulation of the far-field singularity, which occurs at the origin in the ν, θ-plane, so that the stagnation streamlines are normal to the body. The latter two are especially difficult because they must be resolved very accurately in order to achieve satisfactory results.

Fictitous Gas Techniques

The concept of the fictitious gas has been described in earlier grant reports. Thus, we only give a brief synopsis of this research here. In two dimensions we have extended our studies to include viscous effects. Our results are reported in a recent AGARD paper. As we suggested in last year's brief proposal, shock-free designs can be found with little computational effort even when globally weak and locally strong viscous - inviscid interactions are included. This is simply a consequence of the fictitious pressure gradient in the supersonic domain being close enough to the actual pressure gradient for the design process to essentially duplicate the boundary layer displacement thickness of the real shock-free flow.

In a collaborative effort with Dr. Sobieczky of the DFVLR in Gottingen we have examined adaptive airfoils and wings in order to achieve shock-free flow over an extended range of Mach numbers and lift coefficients. These results are reported in a recent ICAS preprint.

During the past year we have implemented the fictitous gas procedure with the full potential code FLO 22. Parallel work at Lockheed by Drs. Miranda and Raj has also been successful.

CONTROL ALGORITHM FOR ADAPTIVE WALL TUNNELS

As part of our NASA supported research we have been investigating a control algorithm for three-dimensional adaptive wall transonic wind tunnels. This research was interrupted last year when the student carrying out the investigation, was forced to return to Poland because his visa expired. These political problems now seem to be resolved and he is back with us. We have developed a relatively fast ADI algorithm for the subsonic flow past lifting wing-body in a circular or rectangular wind tunnel. The boundary conditions on the wind tunnel wall corresponding to variable porosity and plenum pressure are modeled by

$$\phi_r(x,R,\theta) + \alpha(x,\theta)\ \phi_x\ (x,R,\theta) = \beta(x,\theta)$$

for a cylindrical wind tunnel of radius R. Here α and β are directly, but empirically, related to the porosity and plenum pressure.

A similar algorithm is used to compute the external flow. Thus, we may simulate adaptive wall strategies numerically. The algorithm is now being extended to the transonic range. When this is complete our studies can begin in earnest. The fundamental question we wish to address is this: Given a measurement of ψ_r and ψ_x on some surface near, but not at, the wind tunnel walls, what strategy is to be invoked to modify α and β so that the errors in, say lift and drag, due to the wind tunnel walls are minimized? There are, of course, also constraints on the values that α and β can assume since they model to some degree the effects of wall porosity and plenum pressure.

We are thus faced with an optimal control problem which involves a nonlinear partial differential equation. There is not much literature on optimal control with partial differential equation constraints and we may have to invent our theory for the case at hand. To do so we will begin with the linear subsonic equation. We can set up certain simple model situations and write down formulas for analytical solutions using Green's functions. We presume that we will be able to discern an appropriate strategy for determining the changes to be made in α and β in order to find their optimum values. With this body of theory in hand, the results will be verified by numerical experiments for the prototype linear problem. We will next extend these results to the general linear problem. When we are convinced that we have a workable strategy for subsonic flow we will then attempt to generalize it to transonic flow. No doubt changes will be required to account for the possibility that part of the tunnel supersonic flow will extend to the wind tunnel wall. It is, of course, not clear that the problem we have posed has a unique mathematical solution. Still, if adaptive wall wind tunnels are to be developed for truly three-dimensional flows, then some practical strategy for control is essential.

UNSTEADY TRANSONIC FLOW

In the course of refining our time-linearized algortihm for unsteady transonic flows it became clear that acoustic waves were being reflected from the boundary and contaminating the results computed for indicial motions. This would not necessarily be noticed in a harmonic analysis, nor is it especially easy to discern in the indicial motion. It is clear, however, that serious errors in phase lag occur if the boundary conditions for the far-field reflect acoustic waves as the common $\psi = 0$ boundary condition does. In order to remedy this situation Dr. K-Y. Fung derived the correct unsteady far-field and this is now implemented in our algorithm. The results of this research have been accepted for publication in the AIAA Journal.

Our study of two-dimensional time-linearized flows is essentially complete except for the studies of the unsteady behavior of shock-free airfoils to see how their buffet boundaries might differ from supercritical airfoils with well developed shock waves. A paper is being prepared by Dr. Fung that will report the conclusions of this study. We note several here: 1) For determining flutter boundaries a time-linearized algorithm that captures shock motions of arbitrarily small size is probably more efficient than a nonlinear algorithm; for more moderate amplitudes either a nonlinear or a time-linearized algorithm will do; for larger amplitudes a nonlinear treatment is essential. 2) One must be concerned about the accuracy of wind tunnel data for unsteady transonic flows as wall reflections may lead to serious errors in the phase lags. Numerical simulations give strong evidence of such phase lag errors due to boundary reflections. 3) Shock-free airfoils have markedly diffferent phase lags than their counterparts with well formed shock waves.

COMPUTATIONAL FACILITIES

This NASA grant was, at least in part, responsible for the development of an advanced remoted job entry capbility in the University of Arizona's Computational Mechanics Laboratory. We now have an Eclipse S/140 computer with 256 kilobytes of core memory, two CRT terminals with local intelligence, four standard CRT terminals, and a TI 745 portable terminal. Funds from the College of Engineering have been used for some of these facilities; they have also been used to provide work space for eight graduate students. These facilities provide us with remote access to the NASA Ames CDC 7600 via a UT 200 interface. The same interface is used to go directly to the University's Cyber 175. There is also a direct line to the Interactive Graphics Engineering Laboratory's Eclipse S/230, and thereby to its other facilities such as the Ramtek color display.

PAPERS AND TALKS 1980

We list here the papers and talks for our last grant year as they have not previously been reported. As noted earlier, the list for the complete grant period is to be found in Appendix A.

Tijdeman, H. and R. Seebass. "Transonic Flow Past Oscillating Airfoils,' Annual Review of Fluid Mechanics, Vol. 12, 1980.
Fung, K.-Y., Sobieczky, H., and R. Seebass. "Shock-Free Wing Design," AIAA J., Vol. 18, 1980.
Fung, K.-Y. "Far-Field Boundary Conditions for Unsteady Transonic Flows," (to appear AIAA J.).
Fung, K.-Y. "Shock Wave Formation at a Caustic," SIAM J. APPL. MATH., Vol. 39, 1980.
Nebeck, H. E., Seebass, A. R. and H. Sobieczky. "Inviscid - Viscous Interactions in the Nearly Direct Design of Shock-Free Supercritical Airfoils," (to appear AGARD Conference Proceedings)
Sobieczky, H. and A. R. Seebass. "Adaptive Airfoils and Wings for Efficient Transonic Flight," ICAS preprint, October 1980.
R. Seebass: Unsteady Transonic Flow, NASA Langley, February 1980.
R. Seebass: Shock-Free Airfoil and Wing Design, Caltech Colloquium April 1980.
R. Seebass: as above, University of Colorado, April 1980.
R. Seebass: as above, University of Minnesota, April 1980.
R. Seebass: DFVLR Seminars on Unsteady Transonic Flows, Shock-Free Design, and Nonlinear Waves, May 1980.
R. Seebass: as above at Haifa Universtiy, Tel Aviv University, Mathematics and Fluid Mechanics Departments, May 1980.
R. Seebass: General Aviation Appplications of Shock-Free Design, General Aviation Technolgyfest, Wichita, November 1980.

APPENDIX

PAPERS, REPORTS, TALKS 1977 - 1980

Papers

*** 1. Seebass, A. R. and Fung, K.-Y., "Unsteady Transonic Flows: Time-Linearized Calculations," Numerical and Physical Aspects of Aerodynamic Flows (to appear).

** 2. Fung, K.-Y., "Far Field Boundary Conditions for Unsteady Transonic Flows," (accepted AIAA J.).

* 3. Fung, K.-Y., "Shock Wave Formation at a Caustic," SIAM J. Appl. Math., Vol. 39, No. 2, pp. 355-371, October 1980.

** 4. Fung, K.-Y., Sobieczky, H. and Seebass, R., "Shock-Free Wing Design," AIAA J., Vol. 18, No. 10, pp. 1153-1158, October 1980.

5. Sobieczky, H. and Seebass, A. R., "Adaptive Airfoils and Wings for Efficient Transonic Flight," ICAS Preprint, Munich, October 1980.

** 6. Nebeck, H., Seebass, A. R. and Sobieczky, H., "Inviscid-Viscous Interactions in the Nearly Direct Design of Shock-Free Supercritical Airfoils," AGARD Fluid Dynamics Panel Symposium, Computation of Viscous-Inviscid Interactions, Colorado Springs, September 1980.

* 7. Moran, J., Cole, K. and Wahl, D., "Analysis of Two-Dimensional Incompressible Flows by a Subsurface Panel Method," AIAA J., Vol. 18, No. 5, pp. 526-533., May 1980.

** 8. Tijdeman, H. and Seebass, R., "Transonic Flow Past Oscillating Airfoils," Ann. Rev. Fluid Mech., 12, pp. 181-222, 1980.

**** 9. Cramer, M. S., "Lifting Three-Dimensional Wings in Transonic Flow," J. Fluid Mech., Vol. 95, Part 2, pp. 223-240, 1979.

*** 10. Sobieczky, H., Yu, N. J., Fung, K.-Y. and Seebass, A. R., "A New Method for Designing Shock-Free Transonic Configurations," AIAA J., Vol. 17, No. 7, pp. 722-729, July 1979.

** 11. Sobieczky, H., "Related Analytical Analog and Numerical Methods in Transonic Airfoil Design," AIAA 12th Fluid & Plasma Dynamics Conference, Paper 79-1556, Williamsburg, Virginia, 23-25 July 1979.

---

*ONR funded
**AFOSR and ONR joint funding
***AFOSR, NASA, and ONR joint funding
****AFOSR and NASA joint funding
*****NASA funded

*** 12. Seebass, A. R., Yu, N. J. and Fung, K.-Y., "Unsteady Transonic Flow Computations," AGARD Conference on Unsteady Aerodynamics, CP No. 227, pp. 11, 1-17, 1978.

** 13. Fung, K.-Y., Yu, N. J. and Seebass, R., "Small Unsteady Perturbations in Transonic Flows," AIAA J., Vol. 16, No. 8, pp. 815-822, August 1978.

** 14. Cramer, M. S. and Seebass, A. R., "Focusing of Weak Shock Waves at an Arête," J. Fluid Mech., Vol. 88, Part 2, pp. 209-222, 1978.

**** 15. Yu, N. J., Seebass, A. R. and Ballhaus, W. F., "Implicit Shock-Fitting Scheme for Unsteady Transonic Flow Computations," AIAA J., Vol. 16, No. 7, pp. 673-378, July 1978.

Talks

7th Annual General Aviation Technologyfest, Wichita, November 1980. (Seebass)

International Council of the Aeronautical Sciences Meeting, Munich, October 1980. (Sobieczky)

AGARD Fluid Dynamics Panel Symposium on Viscous-Inviscid Interactions, Colorado Springs, September 1980. (Seebass)

University of Haifa Colloquium, May 1980. (Seebass)

University of Tel Aviv Mathematics Seminar and Fluid Mechanics Colloquium, May 1980. (Seebass)

Israel Aviation Industry, Tel Aviv, May 1980. (Seebass)

DFVLR, Göttingen Colloquia (3), May 1980. (Seebass)

University of Minnesota Colloquium, Minneapolis, April 1980. (Seebass)

University of Colorado Colloquium, Boulder, April 1980. (Seebass)

California Institute of Technology Colloquium, Pasadena, April 1980. (Seebass)

Unsteady Transonic Flow, NASA Langley Workshop, February 1980. (Seebass)

Shock-Free Flows, NASA Lewis, November 1979. (Seebass)

AIAA 12th Fluid & Plasma Dynamic Conference, Williamsburg, July 1979. (Fung)

AIAA 12th Fluid & Plasma Dynamic Conference, Williamsburg, July 1979. (Sobieczky)

Lockheed-Georgia Company Seminar, July 1979. (Seebass)

AFFDL/AFOSR Review, Dayton, June 1979. (Seebass)

Lockheed-California Company Seminar, April 1979. (Seebass)

University of Washington Colloquium, Seattle, February 1979. (Seebass)

Ohio State Meeting on Unsteady Transonic Flow, Columbus, February 1979. (Seebass)

University of Southern California Colloquium, Los Angeles, October 1978. (Seebass)

AIAA 11th Fluid & Plasma Dynamics Conference, Seattle, July 1978. (Sobieczky)

AGARD Fluid Dynamics Panel Symposium on Unsteady Aerodynamics, Ottawa, September 1977. (Seebass)

AIAA 10th Fluid & Plasma Dynamic Conference, Albuquerque, June 1977. (Yu)

AIAA 10th Fluid & Plasma Dynamic Conference, Albuquerque, June 1977. (Fung)

University of Arizona Colloquium, Tucson, April 1977. (Fung)

University of Arizona Colloquium, Tucson, Arpil 1977. (Yu)

Dr. H. Sobieczky of the DFVLR in Göttingen was a Visiting Adjunct Professor at the University of Arizona in 1977 - 1978 with ONR and AFOSR support. Dr. Sobieczky gave a series of lectures on Transonic Fluid Dynamics at the University of Arizona. He also gave the seminars listed below.

California Institute of Technology, Pasadena, January 1978.

Stanford University, Stanford, February 1978.

University of California, Berkeley, February 1978.

Naval Postgraduate School, Monterey, February 1978.

University of Southern California, Los Angeles, February 1978.

NASA Research Center, Hampton, Panel Member, Airfoil Conference, March 1978.

Virginia Polytechnic Institute, Blacksburg, March 1978.

University of California, San Diego, March 1978.

University of California, Los Angeles, May 1978.

Transonic Fluid Dynamics Reports - Engineering Experiment Station

Report TFD 80-03, Seebass, A. R. and Fung, K.-Y., "Unsteady Transonic Flows: Time-Linearized Calculations," October 1980 (same as Paper 1).

Report TFD 80-02, Nebeck, H., Seebass, A. R., and Sobieczky, H., "Inviscid-Viscous Interactions in the Nearly Direct Design of Shock-Free Supercritical Airfoils," October 1980 (same as Paper 6).

Report TFD 80-01, Sobieczky, H., "Computational Algorithms for Wing Geometry Generation, Transonic Analysis and Design," July 1980.

Report TFD 79-02, Sobieczky, H. and Seebass, A. R., "Shock-Free Supercritical Aerodynamic Structure and Method for Designing Same," August 1979.

Report TFD 79-01, Fung, K.-Y., Sobieczky, H. and Seebass, A. R., "Numerical Aspects of the Design of Shock-Free Wings," July 1979 (same as Paper 4).

Report TFD 78-05, Ballhaus, W. F., Cramer, M. S., Yu, N. J., Fung, K.-Y., and Seebass, A. R., "Unsteady Transonic Flow Studies," [Focusing of Weak Shock Wave at an Arête (same as Paper 14); Unsteady Transonic Flow Computations (same as Paper 12); Small Unsteady Perturbations in Transonic Flow (same as Paper 13); Implicit Shock-Fitting Scheme for Unsteady Transonic Flow Computations (same as Paper 15)].

Report TFD 78-04, Sobieczky, H., Fung, K.-Y., Seebass, A. R. and Yu, N. J., "A New Method for Designing Shock-Free Transonic Configurations," July 1978 (same as Paper 10).

Report TFD 78-03, Sobieczky, H., "A Computational Algorithm for Embedded Supersonic Flow Domains," July 1978.

Report TFD 78-02, Sobieczky, H. and Seebass, A. R., "Adaptive Airfoils and Wings for Shock-Free Supercritical Flight," May 1978.

Report TFD 78-01, Sobieczky, H., "A Computer Program for Analysis of Transonic Flow Past a Wall Ramp," January 1978.

Report TFD 77-01, Sobieczky, H., "Transonic Fluid Dynamics Lecture Notes," October 1977.

<u>Patent Application</u>

"Adaptive Shock-Free Supercritical Aerodynamic Structures and Method for Designing Same," Serial No. 06/049,846 (with Sobieczky), 1979.

UNSTEADY TRANSONIC FLOWS: TIME-LINEARIZED CALCULATIONS

A. Richard Seebass and K.-Y. Fung
Aerospace and Mechanical Engineering, University of Arizona, Tucson, Arizona

An accurate and efficient method of computing unsteady transonic flow is described. The flow is linearized about an experimentally measured or numerically calculated steady state, as represented by a given pressure distribution. For a given mode of motion, the amplitudes and phase lags of the lift and moment coefficients at a given reduced frequency are found by superposition from an indicial response. The computational effort is reduced by treating shock waves as discontinuities, and by applying the correct linear far-field behavior. A novel method of modeling the indicial response provides an analytical formulas for the dependence of the amplitude and phase lag on the reduced frequency.

INTRODUCTION

A combination of technical advances should improve the fuel efficiency of transport aircraft by fifty percent in the next decade. Analogous improvements in the transonic performance of military aircraft should also be realized. These large gains will come from a combination of improvements in engine, structural, and aerodynamic efficiency. More than half will come from improvements in the aerodynamic efficiency, including active control, and the use of composite materials in the primary structure. Part of the improvement in aerodynamic efficiency will result from flight at supercritical Mach numbers with subcritical levels of lift to drag ratio and high lift coefficients at near sonic flight conditions.

This improved transonic performance mandates an accurate prediction of aeroelastic behavior at transonic Mach numbers. Of special concern are flutter boundaries. In 1976 Farmer and Hanson (1) reported that the flutter boundaries of two dynamically identical wings were markedly different at transonic Mach numbers due to very minor differences in wing profile thickness. The results of their measurements are shown in Figure 1, indicating the reduced flutter boundary for the wing with a "supercritical" profile.

Today we understand well the qualitative behavior of inviscid steady and unsteady transonic flows, and we have rudimentary understanding of viscous effects. For flight regimes that involve unseparated flows the main ingredient in the calculation of flutter boundaries is an accurate determination of the steady pressure field. This may be determined either by experiment or by calculation. But once it is known, the response of the wing to pitching, plunging or aileron motion may be found by numerical means. The most essential ingredient in predicting this response is an accurate prediction of the motion of any shock waves present in the flow (see, e.g., (2)). Numerical algorithms that capture shock waves must use relatively fine grid spacing near the shock wave if they are to predict its motion due to the small changes of interest in flutter studies. But this shock motion may be predicted accurately by a time-linearized algorithm using a relatively coarse grid if the calculations are done correctly. This has not generally been the case, with other investigators ignoring this essential effect (3,4,5).

We report here on our two-dimensional, time-linearized computations, which not only properly account for shock wave motion, but are able to resolve them even though the grid used to calculate the flow is relatively coarse. In order to avoid the reflection of the unsteady disturbances from the grid system, only a moderate amount of grid stretching is employed away from the airfoil. To avoid unnecessarily large computational domains, the linearized far-field for an unsteady vortex with a circulation determined by the airfoil's lift is used to evaluate the potential there (6). The airfoil's response to a given mode of motion is determined by superposition from that for an indicial motion. In many cases this indicial response can be modeled in a simple way, providing an analytic result for the dependence of the lift and moment coefficient's amplitudes and phase lags on reduced frequency. A novel feature of this modeling is that of a sequence of harmonic oscillators, each of which improves the previous simulation of the indicial response. This provides an analytical formula for the dependence of the amplitudes and phase lags on the reduced frequency (7).

The computational efficiency of the time-linearized calculation of the amplitudes and phase lags for a range of reduced frequencies is compared with nonlinear and frequency domain computations. The time-linearized calculation of an indicial response can result in a factor of ten or more reduction in computational effort; this is especially significant in three dimensions. The modeling of the indicial response by a sequence of two harmonic oscillators can also reduce computational effort.

GOVERNING EQUATIONS

As noted above, time-linearization about a known steady state is an effective mechanism for determining the unsteady response to a given mode of motion. For flows that are unseparated, and not at incipient separation, an inviscid treatment of the unsteady flow should be adequate for flutter studies. It is important, however, that the nonlinear and viscous aspects of the underlying steady state be determined accurately. This may either be done by experiment, or by a reliable computational algorithm such as Grumfoil (8). In any case, we assume that an accurate steady state pressure distribution has been used to provide the input for the inverse calculation of the airfoil shape that will provide this pressure distribution when the steady state flow is computed using the small perturbation approximation.

As Lin et al. (9) observed more than thirty years ago, within the context of the small perturbation approximation the basic equation governing the unsteady motions is linear unless the reduced frequency, k, is $O(\delta_o)$. Here δ_o is the measure of the perturbation potential and $k = \omega c/U$, where ω is the frequency, c the chord and U the freestream speed. Thus, if we write the velocity potential, Φ, as

$$\Phi = Uc\{x + \delta_o\phi\}$$

where ϕ is the perturbation potential and δ_o is some measure of the disturbance, the governing equation is

$$-(2k/\delta_o)M_\infty^2\phi_{xt} + \{(1 - M_\infty^2)/\delta_o - (\gamma + 1)M_\infty^2\phi_x\}\phi_{xx} \quad (1)$$
$$+ \phi_{yy} = 0,$$

where terms $O(k^2\phi_{tt}/\delta_o)$ and $O(k\phi_t\phi_{xx})$ have been neglected because $k = O(\delta_o)$. (Here the time has been nondimensionalized by the circular frequency and the spatial coordinates by the airfoil chord, and the y coordinate is scaled by $\delta_o{}^{1/2}$.) The second is of little consequence. Neglecting the first is equivalent to disregarding one of the characteristics and assuming disturbances propagate downstream at infinite speed, and has important computational advantages. The boundary condition at the body is

$$\delta_o{}^{3/2}\varphi_y(x,o,t) = \delta Y'(x) + \tilde{\delta}\tilde{Y}_x(x,t) + k\tilde{\delta}\tilde{Y}_t(x,t) \quad (2)$$

where the body is given by

$$y = \delta Y(x) + \tilde{\delta}\tilde{Y}(x,t).$$

Across the airfoil wake the jump in the pressure coefficient must vanish. Thus,

$$[\![\tfrac{1}{2} C_p(x,o,t)]\!] = - [\![\phi_x(x,o,t)$$
$$+ k\phi_t(x,o,t)]\!] = 0,$$

where $[\![(\cdots)]\!]$ indicates the jump across the wake. This implies that in the wake

$$\Delta\phi(x,o,t) = \Gamma(x - kt)/Uc\delta_o. \quad (3)$$

In both these boundary conditions we have retained terms of O(k), which is not consistent with the approximation made in Eq. (1). But as Refs. (10) and (11) demonstrate, this gives good agreement with the results of linear theory for values of k up to, and even above, 1.0. This term is, of course, also retained in the evaluation of the pressure coefficients. As noted in Ref. (2), the appropriate measure of δ_o is $\max(\delta^{3/2},\tilde{\delta}^{3/2},(k\tilde{\delta})^{3/2})$ and normally $\delta^{3/2}$. Far from the airfoil (see (6)),

$$\phi(x,y';t') = \frac{1}{2\pi}\int_0^{t'} f(x,y';t' - t_o')\frac{d\Gamma(t_o')}{dt_o'}\, dt_o' \quad (4)$$

where

$$f(x,y';t') = H(t' + x - \sqrt{(x^2 + y'^2)}) \times$$
$$\cdot\tan^{-1}\frac{\sqrt{(t'^2 + 2xt' - y'^2)} + t'}{y'}$$
$$- \tan^{-1}\frac{\sqrt{(t'^2 + 2xt - y'^2)} - t'}{y'}\},$$

and

$$t' = t(1 - M_\infty^2)/kM_\infty^2\ ,\ y' = y\sqrt{[(1 - M_\infty^2)/\delta_o]}.$$

Here H is the Heaviside unit step function.

In addition to Eq. (1) and the boundary conditions (2)-(4), a shock jump condition needs to be imposed if the shock wave is to be treated as a discontinuity rather than "captured" by the numerical calculations. Because the former is the intent here, we need to note that

$$- (2kM_\infty^2/\delta_o)[\![\phi_x]\!]^2(dx/dt)_s$$
$$- [(1 - M_\infty^2)/\delta_o - (\gamma + 1)M_\infty^2\overline{\phi_x}][\![\phi_x]\!]^2 + [\![\phi_y]\!]^2 = 0, \quad (5a)$$

on

$$(dy/dx)_s = - [\![\phi_x]\!]/[\![\phi_y]\!] \quad (5b)$$

where $[\![(\cdots)]\!]$ and $\overline{(\cdots)}$ indicate the jump in and average of $(\cdots)$ across the shock wave. Equation (5a) insures the conservation of mass. The conservation of momentum is replaced by the irrotationality condition Eq. (5b) or its equivalent, $[\![\phi]\!] = 0$.

Time-linearization

We use the ADI technique introduced by Ballhaus and Steger (12) to compute the steady state solution of Eq. (1), $\phi_o(x,y)$, subject to the steady boundary conditions implied by Eqs. (1)-(4), using the coordinate stretching of Ref. (13). Aside from the far-field condition (4) and the inclusion of terms of O(k) relative to O(1) in (2) and (3), this is equivalent to NASA Ames computer code LTRAN2 of Ballhaus and Goorjian (14). We next linearize about this steady state by assuming that

$$\phi(x,y,t) = \phi_o(x,y) + (\tilde{\delta}/\delta_o^{3/2})\tilde{\phi}(x,y,t) + o(\tilde{\delta}/\delta_o^{3/2}),$$

where $\tilde{\delta}/\delta_o^{3/2} = o(1)$. This gives, with $\delta = \delta_o$.

$$- (2kM_\infty^2/\delta_o)\tilde{\phi}_{xt} + \{[(1 - M_\infty^2)/\delta_o$$
$$- (\gamma + 1)M_\infty^2\phi_{ox}]\tilde{\phi}_x\}_x + \tilde{\phi}_{yy} = 0, \quad (6a)$$

with

$$\tilde{\phi}_y(x,o,t) = \tilde{Y}_x(x,t) + k\tilde{Y}_t(x,t) \quad (6b)$$

and

$$[\![\tilde{\phi}_x(x,o,t) + k\tilde{\phi}_t(x,o,t)]\!] = 0. \quad (6c)$$

With the linearization of the solution about a steady state at time t = 0, we use (4) for the potential far from the airfoil as the circulation departs from its steady state value.

As noted earlier, the proper account shock motions are of prime importance in unsteady transonic flow. We thus use the procedure of Ref. (13) to account for shock motions. Because the shock waves are nearly normal to the freestream we assume that this is the case and satisfy

$$[\![\phi]\!] = 0$$

on the normal shock approximation to Eq. (5), viz.,

$$\frac{dx}{dt}s = +\frac{\gamma + 1}{2k}\left\{\frac{M_\infty^2 - 1}{(\gamma+1)M_\infty^2} + \tilde{\phi}_x\right\}.$$

Again we linearize about the steady state, writing in this approximation

$$x_s(t) = x_{os} + (\tilde{\delta}/\delta_o^{3/2})\chi(t)$$

which gives

$$\frac{d\chi(t)}{dt} = \frac{\gamma + 1}{2k}\tilde{\phi}_x(x_{os}, o, t) \qquad (7)$$

as the equation that keeps track of the shock wave position. Straightforward linearization of $[\![\phi_o + (\tilde{\delta}/\delta_o^{3/2})\tilde{\phi}]\!] = 0$ gives the expression that determines $\tilde{\phi}$ behind the shock from its value ahead of the shock (13):

$$[\![\tilde{\phi}(x_s, t, y)]\!] =$$

$$-\frac{\gamma + 1}{2k}[\![\phi_{ox}(x_s', y)]\!]\int_o^t \tilde{\phi}(x_s', o, \hat{t})d\hat{t}. \qquad (8)$$

This must be integrated in conjunction with (6a). The ADI procedure is again adopted as outlined in Ref. (13), to effect a solution of Eq. (6) in conjunction with Eq. (8), subject to the time-linearized boundary conditions at Eqs. (6a) and (6b).

INDICIAL RESPONSE

One of the major advantages of time-linearization is that, for a given mode of motion, the amplitude and phase lag of the lift or moment coefficient for a given reduced frequency may be computed by a linear superposition of the results obtained for a step change. For example, if the change in lift coefficient as a function of time for a step change in angle of attack, C_{ℓ_α}, is that sketched in Fig. 2, then the lift coefficient for an angle of attack variation, $\alpha(t)$, is

$$C_{\ell_\alpha}(t) = C_{\ell_\alpha}(t)\alpha(o) + \int_o^t C_{\ell_\alpha}(\tau)\frac{d\alpha(t - \tau)}{d\tau}d\tau. \quad (9a)$$

Thus, for a periodic motion $\alpha(t) = \alpha_o + \tilde{\alpha}e^{i\omega t}$,

$$C_\ell(t) = \tilde{\alpha}e^{i\omega t}\left[C_{\ell_\alpha}(\infty) - i\omega\int_o^\infty\left[C_{\ell_\alpha}(\infty) - C_{\ell_\alpha}(\tau)\right]e^{-i\omega\tau}d\tau\right] \quad (9b)$$

$$+ C_{\ell_\alpha}(\infty)\alpha_o.$$

The low frequency approximation made in Eq. (1), viz., that $k^2\phi_{tt}$ was negligible, is, of course, not valid for the high-frequency components of the indicial response calculation. It is, however, perfectly satisfactory for the computation of the indicial response, provided this response is only used to compute motions for which $k = o(1)$. In order to calculate the response for low reduced frequencies, however, we must accurately resolve the indicial response as the motion approaches its asymptotic state. Typically, this requires the computation of the indicial response for 300 chord lengths of airfoil motion. In this time the unsteady perturbations have travelled a little more than 300 chord lengths normal to the freestream. As a consequence, any boundary condition imposed on a $|y|$ = constant boundary that is less than 150 chord lengths away can contaminate the indicial response through a reflection from a boundary. Our experience has been that an erroneous boundary condition such as $\phi = 0$ has to be imposed at $|y|$ greater than 80 chord lengths in order to avoid errors in the phase lag determined from an indicial response. The same must be true for the computation of a harmonic motion, although it would be more difficult to determine that the phase lag was in error in such a computation. This same observation should also be applied to unsteady wind tunnel tests. If there are significant acoustic reflections from the wind tunnel walls, the observed phase lags may be in error. This experimental difficulty warrants further investigation, especially in two-dimensional studies.

On the other hand, we know that with the appropriate steady state value of the potential applied at about twenty chord lengths, the steady state solution is perfectly adequate. With the imposition of the unsteady boundary condition (4), or its time-linearized analog, we find that once again 20 chord lengths will suffice. For low to moderate reduced frequencies, viz., k = 0.1 to 1.0, the acoustic wavelengths associated with the motion are about 1.0 to 10 chords. The grid spacing employed may be stretched, but grid spacing comparable to or larger than the acoustic wavelength will result in acoustic reflections from the grid itself. Thus, while a grid stretching is employed in the calculations, the largest grid spacing used remains a fraction of a chord length.

Harmonic Oscillator Modeling

Typically, the indicial response of the lift coefficient to a step change in angle of attack, flap angle, or imposition of plunging velocity, is like that as shown in Fig. 2. The same is also approximately true for the moment coefficient taken about the airfoil's leading edge (Fig. 3). This suggests that, to a first approximation, the response is nearly exponential and governed by a simple first-order differential equation. And, further, that to a second approximation, the difference between this response and an exponential function can be modeled by a damped harmonic oscillator. Thus, if we let $u(t)$ be a normalized indicial response such that $u(0) = -1$, $u(\infty) = 0$, we should write

$$u(t) = 1 + u_o(t) + u_1(t) + \cdots \qquad (10)$$

where

$$L_o u_o \equiv \dot{u}_o + \lambda u_o = 0$$

and, in general,

$$L_i u_i \equiv \ddot{u}_i + 2p_i\dot{u} + q_i u_i = 0.$$

The constants λ, p_i, q_i are determined to best model the indicial response. That is, the solutions to these equations, viz.,

$$u_o(t) = e^{-\lambda t} \qquad (12a)$$

and

$$u_i(t) = u_i(o)e^{-p_i t}\sin(\Omega t)/\Omega, \qquad (12b)$$

where

$$\Omega = \sqrt{(q_i - p_i^2)},$$

are combined to best approximate the indicial response. To be specific, if we let $\varepsilon_o = u(t) - u_o(t)$, then we choose λ such that

$$I_o(\lambda) = \int_o^\infty [L_o \varepsilon_o]^2 dt \qquad (13)$$

is minimum. Setting $\partial I_o/\partial\lambda = 0$, we find

$$\lambda^{-1} = 2\int_o^\infty \{1 - u(t)\}^2 dt. \qquad (14)$$

In an analogous manner we let $\varepsilon_1 = u(t) - 1 - u_o(t) - u_1(t)$ and choose p_1 and q_1 so that

$$I_1(p_1, q_1) = \int_o^\infty [L_1 \varepsilon_1]^2 dt \qquad (15)$$

is minimized. This gives

$$p_1 = \frac{(\dot{u}(o) - \lambda)^2}{2\int_o^\infty (\dot{u} - \dot{u}_o)^2 dt} \text{ and } q_1 = \frac{\int_o^\infty (\dot{u} - \dot{u}_o)^2 dt}{\int_o^\infty (u - u_o) dt}. \qquad (16)$$

The extent to which the simple first approximation is justified for selected examples is shown in Figs. (4) and (5). In many instances an acceptable determination of the phase lag requires the second approximation. This will be discussed more fully in (7). The constant λ and the $I_o(\lambda)$ of the first approximation can be determined immediately from Eqs. (13) and (14) as the indicial response is being calculated. If I_o is not sufficiently small, then the constants p_1 and q_1 can be calculated from Eqs. (16). If the second approximation is not judged sufficiently accurate because I_1 is not acceptably small, the modeling is abandoned as the computational expense of computing p_1 and q_1 is comparable to that required for three reduced frequencies.

Some time ago it was noted by Tijdeman (15) and the authors (13) that the amplitude of a harmonic response decays like k^{-1} with increasing k. A somewhat more general result is implied by Eqs. (12). If $F(t)$ is a harmonic response, e.g., $C_{\ell_\alpha}(t)$, then with

$$F(t) = F_o(t) + F_1(t) + \cdots, \qquad (17)$$

we find that the first approximation gives

$$F_o/A = (1 + k'^2)^{\frac{1}{2}} \sin(kt - \theta_o) \qquad (18a)$$

where

$$\sin\vartheta_o = k'/(1 + k'^2)^{1/2}. \qquad (18b)$$

Here A is the amplitude of the indicial response to a unit change and $k' = k/\lambda$. The second approximation gives

$$F_1/A - \dot{u}_1(o) k'\Omega' \sin(kt - \vartheta_1) \div$$
$$[\{1 + (k' + \Omega')^2\}\{1 + (k' - \Omega')^2\}]^{1/2} \qquad (19a)$$

where

$$\sin\theta_1 = (k'^2 - \Omega'^2 - 1) \div$$
$$\{[1 + (k' + \Omega')^2][1 + (k' - \Omega')^2]\}^{1/2} \qquad (19b)$$

and $\Omega' = \Omega/\lambda$.

We see immediately from Eq. (18) that in the first approximation the amplitude of the harmonic response is

$$[1 + (k/\lambda)^2]^{-1/2}$$

as indicated in Fig. 4, which behaves like k^{-1} for large k, and that the phase lag is

$$\sin^{-1}\{(k/\lambda)/\{1 + (k/\lambda)^2\}^{1/2}$$

which grows linearly with k/λ for small k/λ, and thereafter is nearly independent of k/λ, as can be seen from Fig. (5).

We limit our discussion to the simple variation of the amplitude and phase lag of the lift and moment coefficients for an NACA 64A006 in pitch with reduced frequency. Earlier, more detailed results depicting the shock motion, etc., are to be found in Refs. (13) and (16). Because we have linearized about a steady, small perturbation solution, we draw no practical conclusions from our study. Tijdeman (personal communication) reports that the application of LTRAN2 to determine the response about an experimental steady state for the F29 airfoil at varying incidence, in conjunction with strip theory and the results of panel methods for subcritical flow to account for three-dimensional effects, was successful in predicting the flutter boundary of the F29 wing.

Figures 4 and 5 give the amplitudes and phase lags of the lift and moment coefficients for an NACA 64A006 airfoil oscillating in pitch at selected reduced frequencies with $M_\infty = 0.86$ and 0.88. Individual results are shown by symbols with the reduced frequency noted below them. Generally, they are well described by the first approximation of the harmonic oscillater model. For $M_\infty = 0.86$ the lift and mid-chord moment results are indistinquishable, but their phase lags are not correctly captured by the modeling of the first approximation. In this case, the initial part of the indicial response is not correctly captured. This is easily dealt with in the model without going to the second approximation (7).

COMPUTATIONAL EFFORT

As noted earlier, a time-linearized calculation requires substantially less computational effort than a nonlinear one. We delineate those differences here, noting that the larger grid spacing that may be used with our shock-fitting procedure implies a computational saving in addition to the considerations discussed here.

If we let T represent the number of time steps required to calculate a time periodic solution in an L×M×N spacial domain, then the total computational effort for a flutter study using either a nonlinear or time-linearized algorithm is proportional to the product TLMN. If we do not time-linearize, this must be done at K reduced frequencies to give a total computational effort that is proportional to KTLMN. If a time-linearized procedure is used to compute a single indicial response, the effort is TLMN. This can be used to generate the mode response for any reduced frequency in about T^2 additional steps, giving a total computational effort proportional to TLMN + (const)$\cdot T^2K$. Typically, T is 500 and L,M,N are about 50, 25, 25, respectively. Thus, a nonlinear analysis at ten reduced frequencies has a computational effort of

$$10\cdot 500\cdot 50\cdot 25\cdot 25 = 10^8.$$

On the other hand, a time-linearized computation requires a computational effort of

$$500\cdot 50\cdot 25\cdot 25 +$$
$$(\text{const})\ (500)^2 10 = 10^7 + (\text{const})\cdot 10^6$$

providing a factor of K reduction over the nonlinear analysis. The constant of proportionality, and the less refined L grid spacing required, also favor the time-linearized algorithm, contributing roughly another factor of ten reduction over the nonlinear procedure.

In two dimensions, the two computational components of the time-linearized calculation, viz., the indicial response and its linear superposition for each reduced frequency, are comparable and an efficient integration algorithm must be used for Eq. (9b).

CONCLUSION

The amplitudes and phase lags of the lift and moment coefficients, at selected reduced frequencies, can be computed accurately and efficiently by time-linearization about a measured or computed pressure field. For three-dimensional studies the linear superposition of the results of a single indicial response substantially reduces the computational effort. Further reductions are achieved by using the linearized far-field for the unsteady flow, and by treating the shock wave as a discontinuity in the computations. In many cases, the indicial response can be modeled by a simple harmonic oscillator, and this provides an analytical result for the dependence of the lift and moment coefficients on reduced frequency, further reducing the computational effort.

ACKNOWLEDGMENTS

This research was supported by ONR Contract Number N00014-76-C-0182 and by AFOSR Grant Number AFOSR-76-2954I. The authors are greatly indebted to Mr. Morton Cooper for his support of their efforts to develop a program in analytical and computational aerodynamics at the University of Arizona.

REFERENCES

1. Farmer, M. G. and Hanson, P. W., "Comparison of Supercritical and Conventional Wing Flutter Characteristics," Proceedings AIAA/ASME/SAE 17th Structures, Structural Dynamics and Materials Conf., King of Prussia, Pa., April 1976, pp. 608-611.
2. Tijdeman, H. and Seebass, R., "Transonic Flow Past Oscillating Airfoils," Ann. Rev. Fluid Mech. 1980, 12, pp. 181-222.
3. Traci, R. M., Farr, J. L., and Albano, E., "Perturbation Method for Transonic Flows About Oscillating Airfoils," AIAA Paper 75-877, 1977.
4. Weatherill, W. H., Sebastian, J. D., and Ehlers, F. E., "Application of a Finite Difference Method to the Analysis of Transonic Flow Over Oscillating Airfoils and Wings," AGARD-CP-226, 1977.
5. Weatherill, W. H., Sebastian, J. D., and Ehlers, F. E., "The Practical Application of a Finite Difference Method of Analyzing Transonic Flow Over Oscillating Airfoils and Wings," NASA Contract Rep. 2933, 1978.
6. Fung, K-Y., "Far-Field Boundary Conditions for Unsteady Transonic Flows," (to appear AIAA J.).
7. Fung, K-Y., "A Time-Linearized Algorithm for Unsteady Transonic Flow," (in preparation).
8. Melnik, R. E., "Turbulent Interactions on Airfoils at Transonic Speeds-Recent Developments," AGARD Symposium on Computation of Viscous-Inviscid Flows, Cororado Springs, October 1980.
9. Lin, C. C., Reissner, E., and Tsien, H. S., "On Two-Dimensional Non-Steady Motion of a Slender Body in a Compressible Fluid," J. Math. Phys. 3, pp. 220-31, 1948.
10. Couston, M. and Angelini, J. J., "Solution of Nonsteady Two-Dimensional Transonic Small Disturbances Potential Flow Equation," In Nonsteady Fluid Dynamics: Proc. ASME Winter Annual Mtg., Dec. 10-15, 1978, San Francisco, pp. 233-44. See also ONERA TP-No. 1978-69.
11. Houwink, R. and van der Vooren, J., "Results of an Improved Version of LTRAN-2 for Computing Unsteady Airloads on Airfoils Oscillating in Transonic Flow." AIAA Paper 79-1553, 1979.
12. Ballhaus, W. F. and Steger, J. L., "Implicit Approximate-factorization Schemes for the Low-frequency Transonic Equation," NASA Tech. Memo TM X-73,082, 1975.
13. Fung, K-Y., Yu, N. J. and Seebass, R., "Small Unsteady Perturbations in Transonic Flows," AIAA J., 16, pp. 815-22, 1978.
14. Ballhaus, W. F. and Goorjian, P. M., "Implicit Finite-difference Computations of Unsteady Transonic Flows About Airfoils," AIAA J., 15, 1728-35, 1977.
15. Tijdeman, H., "Investigations of the Transonic Flow Around Oscillating Airfoils," Doctoral Thesis. Technische Hogeschool, Delft, The Netherlands, 148 pp., 1977.
16. Seebass, A. R., Yu, N. J. and Fung, K-Y., "Unsteady Transonic Flow Computations," AGARD-CP-227, 1978.

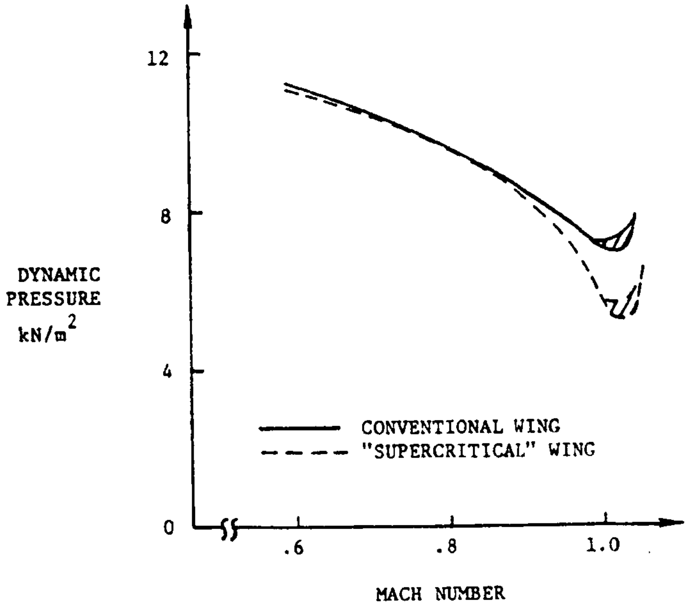

Figure 1. Flutter boundary for two dynamically identical TF-8A wings (Reference (1)).

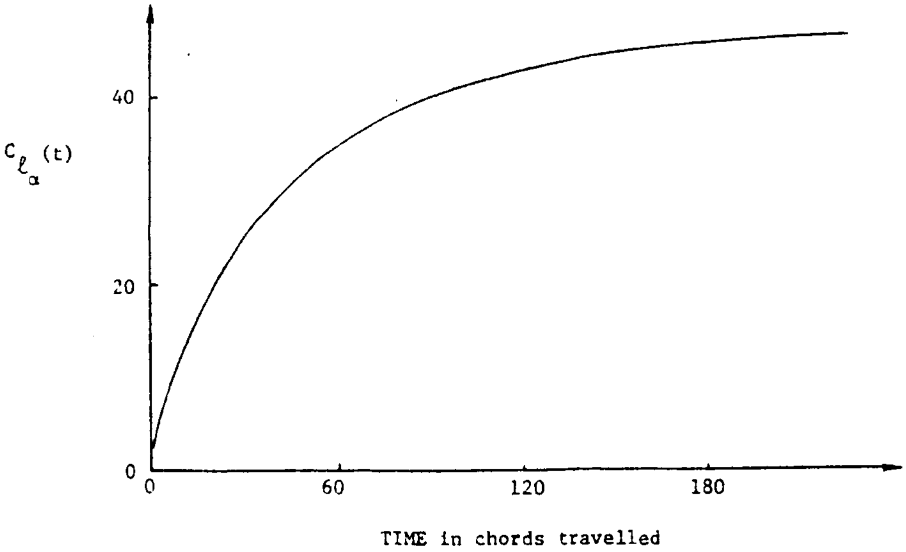

Figure 2. Lift coefficient as a function of time for a step change in angle of attack; NACA 64AC06, $M_\infty = 0.88$.

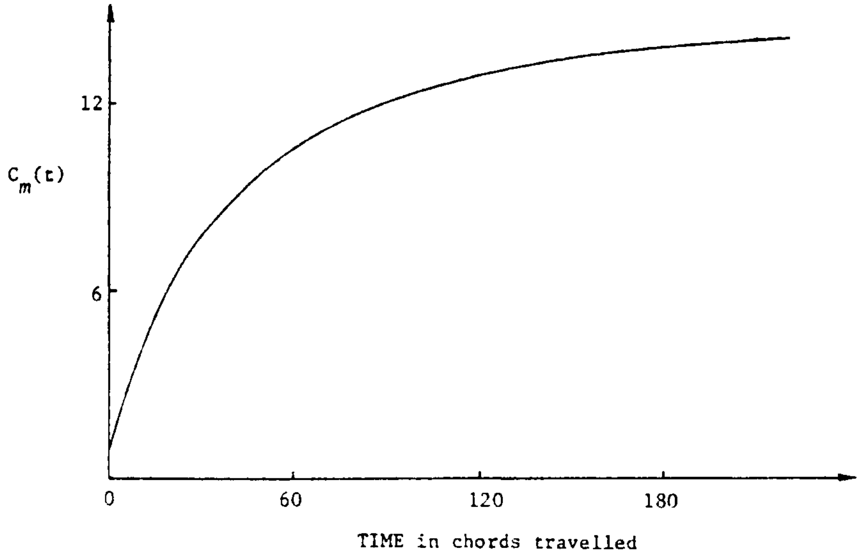

Figure 3. Moment coefficient as a function of time for a step change in angle of attack; NACA 64A006, $M_\infty = 0.88$.

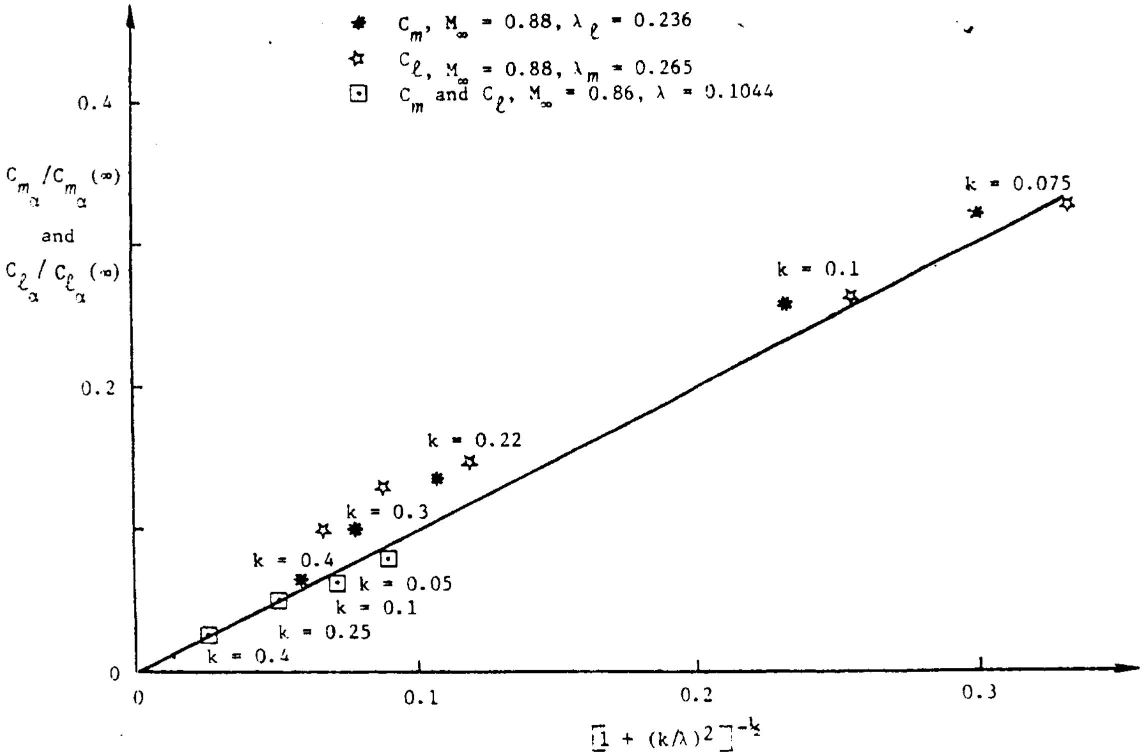

Figure 4. Lift and moment amplitudes normalized by their quasi-steady value as a function reduced frequency for an NACA 64A006 airfoil.

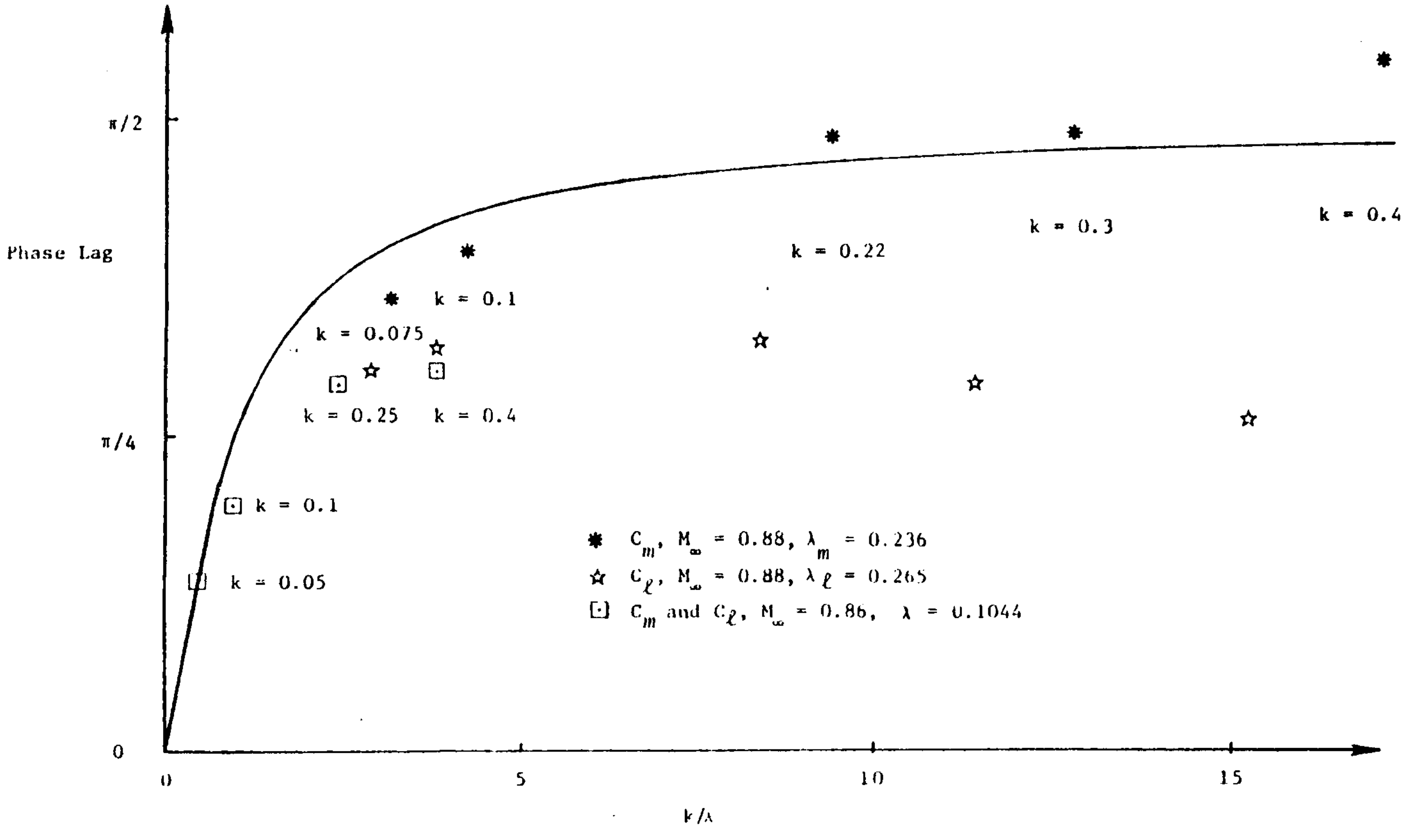

Figure 5. Phase lag for the lift and moment as a function of reduced frequency for an NACA 64A006 airfoil.

AIAA 81-4030

Far Field Boundary Conditions for Unsteady Transonic Flows

K.-Y. Fung*
University of Arizona, Tucson, Ariz.

Analytical results are given for the far field of the unsteady transonic flow due to an instantaneous change in lift at the origin. These results may be superimposed to provide boundary conditions for numerical computational of unsteady transonic flows. A typical numerical experiment using these results shows substantial reductions in the size of the computational domain are possible. In two dimensions this procedure is at least as effective as the nonreflecting conditions suggested by the local characteristic relations. It is also much easier to implement in three dimensions than the nonreflecting conditions.

Introduction

THE computation of unsteady transonic flow is of fundamental importance in determining aeroelastic response and flutter boundaries.[1] At supercritical Mach numbers the flow past airfoils and wings usually includes embedded shock waves; the motion of such shock waves plays an important role in determining the airfoil or wing's response to a given mode of motion. Indeed, there is experimental evidence,[2] and supporting theoretical work,[3] suggesting that serious decrease in the flutter speed with increasing Mach number can occur for some wing designs because of this shock wave motion.

An efficient time-accurate algorithm for solving the transonic unsteady small perturbation equation has been developed by Ballhaus and Goorjian[4] for the important case of low reduced frequencies. Unsteady flows, in one sense, are easier to compute without having the results affected by approximations in the boundary conditions. One can, for example, simply insist that the boundary be far enough away that none of the waves reflected from it have sufficient time to return to the airfoil or wing and contaminate the results. For indicial and periodic motions the computational domain must be large enough that the asymptotic state is achieved before the reflected waves return to their source. This, unfortunately, turns out to be a rather large domain (typically 100 airfoil chord lengths in two dimensions). Magnus,[5] as well as other investigators, have discussed the effects of the boundary conditions on the result of their calculations, with the general conclusion being that they cause serious errors. To remedy this difficulty one may use one of several techniques. The one frequently used for steady flows, viz., grid stretching, may not improve the results, even for low reduced frequencies where the disturbance wavelength of interest is, at most, no more than 10 chord lengths. Any grid spacing larger than a few chord lengths will effectively reflect the incident waves. Another remedy, used, e.g., by Enquist and Majda,[6] is to use boundary conditions that reduce the reflection of incident waves. Such boundary conditions are a local statement that outward going waves should be transmitted through the boundary. Our experience with these boundary conditions indicates that this local approximation is much too crude to allow computational domains of size satisfactory for steady flow calculations. A better procedure is to use the global unsteady far field for the linearized equation, first attempted by Krupp and Cole.[7]

If we assume the far field is governed by a linear equation then the far field for an indicial response can be used to construct that for any response. Additionally, we note that an effective way to proceed with flutter studies is to linearize the steady state about some experimentally or numerically determined steady state.[8] This must be done in a way that accounts for shock motions, as they represent the predominant effect in supercritical flows.[9]

Equation of Flow

For simplicity, we consider the nonlinear flow to be governed by the small perturbation for small reduced frequencies, viz.,

$$-2k\phi_{xt} + \{\kappa - (\gamma+1)\phi_x\}\phi_{xx} + \phi_{yy} + \phi_{zz} = 0 \tag{1}$$

Here the spatial coordinates, the time, and the velocity potential have been nondimensionalized by the chord, the freestream Mach number times the reciprocal of the angular frequency, and the freestream velocity times the chord, respectively; κ is the usual transonic similarity parameter, and k is the reduced frequency, viz., $k = \omega c/U$, i.e., the angular frequency multiplied by the time it takes the airfoil to move one chord length. The appropriate boundary conditions are then

$$\phi_y(x,0,z,t) = \tau[Y_x + kY_t], \qquad \text{on wing}$$

and

$$[\![k\phi_t(x,0,z,t) + \phi_x(x,0,z,t)]\!] = 0, \qquad \text{on wake}$$

where we have included terms of $O(k)$ as suggested by Houwink and van der Vooren,[10] $\tau Y(x,y,z,t)$ is the body shape and $[\![\ ]\!]$ means the jump in the argument.

Unsteady Far Field

We now derive the unsteady far field boundary conditions for Eq. (1). Far from the body the unsteady disturbances will satisfy a linear equation. Considering the whole flowfield to be a small unsteady disturbance superimposed on the steady solution to Eq. (1), we let

$$\phi(x,y,z,t) = \phi^0(x,y,z) + \delta\psi(x,y,z,t) + o(\delta)$$

and

$$Y = Y^0 + (\delta/\tau)Y^u$$

to find

$$-2k\psi_{xt} + \{[\kappa - (\gamma+1)\phi_x^0]\psi_x\}_x + \psi_{yy} + \psi_{zz} = 0 \tag{2}$$

9

Received May 14, 1980; revision received Aug. 11, 1980. This paper is declared a work of the U.S. Government and therefore is in the public domain.

*Assistant Professor, Aerospace and Mechanical Engineering. Member AIAA.

with

$$\psi_y(x,0,z,t) = (Y^u_x + kY^u_t), \qquad \text{on wing}$$

where δ characterizes the size of the unsteady disturbance compared to the basic steady disturbance. While this is now the framework for a time-linearized analysis, we note that the linearized version of Eq. (1) always applies in the far field. As indicated in other studies, e.g., Klunker,[11] the nonlinear term, here correspondingly, $[(\gamma+1)\phi^0_x\psi_x]$ has a doublet like contribution to the steady far field. We will show later that such a term contributes equivalently to the unsteady far field and hence we can neglect it. Only changes in lift contribute to the lowest order; thus, we need only derive the far field for an incremental change in incidence. This we do by solving the following boundary value problem for the upper half-space $(y>0)$

$$-2\Phi_{xt} + \Phi_{xx} + \Phi_{yy} + \Phi_{zz} = 0 \tag{3}$$

with

$$\Phi(x,0,z,t) = \tfrac{1}{2}\Delta\Gamma(z,t_0)H(t-t_0)H(x)$$

Here, the dependent and independent variables are properly scaled. The solution we seek is, of course, antisymmetric in y. The boundary condition in Eq. (3) models a vortex sheet that originates at $x=0$, producing a jump in potential, $\Delta\Gamma(z)$, instantaneously at time $t=t_0$.

Far Field Solutions

We employ the standard techniques of Fourier and Laplace transforms to solve Eq. (3) subject to the boundary condition for a change in the circulation, $\Delta\Gamma(z,t_0)$, at time t_0 for both two-dimensional and three-dimensional flow. We outline the steps briefly here.

Three Dimensions

To solve Eq. (3), we let $\hat{\Phi}(x,y,z,s)$ be the Laplace transform of Φ

$$\hat{\Phi}_{yy} + \hat{\Phi}_{xx} + \hat{\Phi}_{zz} - 2s\hat{\Phi}_x = 0 \tag{4}$$

with

$$\hat{\Phi}(x,0,z,s) = \tfrac{1}{2}\Delta\Gamma(z)(1/s)H(x)$$

The substitution $\hat{\Phi} = e^{sx}\psi$, reduces Eq. (4) to the standard Helmholtz equation, viz.,

$$\psi_{yy} + \psi_{xx} + \psi_{zz} - s^2\psi = 0 \tag{5}$$

with

$$\psi(x,0,z,s) = \tfrac{1}{2}\Delta\Gamma(z)(e^{-sx}/s)H(x)$$

We let $\hat{\psi}(\xi,y,z,s)$ denote the Fourier transform of ψ with respect to x and $\tilde{\psi}(\xi,y,\zeta,s)$ the Fourier transform of $\hat{\psi}$ with respect to z. Applying such transforms to Eq. (5), we find

$$\tilde{\psi}_{yy} - (\zeta^2 + \xi^2 + s^2)\tilde{\psi} = 0$$

with

$$\tilde{\psi}(\xi,0,\zeta,s) = \tfrac{1}{2}\Delta\tilde{\Gamma}(\zeta)\frac{s-i\xi}{s(s^2+\xi^2)}$$

which has the solution

$$\tilde{\psi}(\xi,y,\zeta,s) = \tfrac{1}{2}\Delta\tilde{\Gamma}\frac{s-i\xi}{s(s^2+\xi^2)}\exp[-(\xi^2+\zeta^2+s^2)^{1/2}y] \tag{6}$$

After performing the inverse transforms to Eq. (6) with respect to ζ,ξ,s correspondingly, we have, then, in three-space dimension, that

$$\Phi = \frac{y}{4\pi}\int_{-b/2}^{b/2}\Delta\Gamma(\bar{z},t_0)g(x,y,z-\bar{z},t-t_0)\,\mathrm{d}\bar{z} \tag{7}$$

where b is the wing span and

$$g(x,y,z,t) = H[t+x-(x^2+y^2+z^2)^{1/2}]$$
$$\times[1+x(x^2+y^2+z^2)^{-1/2}]/(z^2+y^2)$$

Because the derivation is for an incremental change $\Delta\Gamma(z,t_0)$ at $t=t_0$, a more suitable form of Eq. (7) for Φ would be

$$\Phi(x,y,z,t) = \frac{y}{4\pi}\sum_{\Gamma(t_0)}^{\Gamma(t)}\int_{-b/2}^{b/2}\Delta\Gamma(\bar{z},t_0)g(x,y,z-\bar{z},t-t_0)\,\mathrm{d}\bar{z} \tag{8}$$

Equation (7) is essentially the steady-state result modified by the Heaviside function which switches on the value given by Eq. (8) when

$$t-t_0 = (x^2+y^2+z^2)^{1/2} - x$$

This implies the far field phase lag is simply $(x^2+y^2+z^2)^{1/2}-x$. Such simple behavior is found only in one- and three-dimensional wave propagation (see, e.g., Lighthill[12]). Equation (8) simply retards the value of the potential Φ so that it is the potential produced by the circulation at an earlier time corresponding to the time for a wave front to travel from the origin, to the location where Φ is being evaluated. Thus, by letting

$$\mathrm{d}\Phi_\Gamma(x,y,z,t_0) = \frac{y}{4\pi}\int_{-b/2}^{b/2}\Delta\Gamma(\bar{z},t_0)[1+x(x^2+y^2$$
$$+(z-\bar{z})^2)^{-1/2}][y^2+(z-\bar{z})^2]^{-1}\mathrm{d}\bar{z}$$

Equation (8) becomes

$$\Phi(x,y,z,t) = \int_{t_0=0}^{t} H(t-t_0+x-\sqrt{x^2+y^2+z^2})\,\mathrm{d}\Phi_\Gamma$$

$$= \int_0^{t-\sqrt{x^2+y^2+z^2}+x}\mathrm{d}\Phi_\Gamma = \Phi_\Gamma[x,y,z,t-(x^2+y^2+z^2)^{1/2}+x]$$

Two Dimensions

In two dimensions we have

$$-2\Phi_{xt} + \Phi_{xx} + \Phi_{yy} = 0 \tag{9}$$

with

$$\Phi(x,0,t) = [\Delta\Gamma(t_0)/2]H(x)H(t-t_0)$$

instead of Eq. (3).

Following the same procedure used in three dimensions, we have the result in two dimensions that

$$\Phi = [\Delta\Gamma(t_0)/2\pi]f(x,y,t-t_0) \tag{10}$$

where

$$f(x,y,t) = H(t+x-\sqrt{x^2+y^2})\left[\tan^{-1}\frac{\sqrt{t^2+2xt-y^2}+t}{y}\right.$$
$$\left.+\tan^{-1}\frac{\sqrt{t^2+2xt-y^2}-t}{y}\right]$$

This result is more complex with the time appearing not only in the unit step function, but also in the argument of the arctangent function. In the limit, as we approach steady state, Eq. (10) becomes

$$f(x,y,\infty) = \frac{y}{|y|}\frac{\pi}{2} + \tan^{-1}\frac{x}{y}$$

which is the steady result of Klunker.[11] For an arbitrary circulation change $\Delta\Gamma(t)$, we must superimpose the results Eq. (10) to find the general two-dimensional far field

$$\Phi(x,y,t) = \frac{1}{2\pi}\int_0^t f(x,y,t-t_0)\frac{\mathrm{d}\Gamma(t_0)}{\mathrm{d}t_0}\mathrm{d}t_0 \tag{11}$$

In the case of harmonic motion, e.g.,

$$\frac{\mathrm{d}\Gamma(t)}{\mathrm{d}t} = \Gamma_{\max}e^{i\omega t}$$

we simply change the lower limit in Eq. (11) to find

$$\Phi(x,y,t)/\Gamma_{\max} = \frac{e^{i\omega t}}{2\pi}\int_0^\infty f(x,y,\tau)e^{-i\omega\tau}\mathrm{d}\tau \tag{12}$$

which gives the phase lag at each location of the far field boundary. The condition given by Krupp and Cole[7] may be viewed as an attempt to approximate the result given by Eq. (12).

We may also use Eq. (10) to examine other far field boundary conditions. For example, the one given in Ref. 6 states that for large y

$$\Phi_y \pm \Phi_x = 0 \tag{13}$$

while analytically we see that

$$\Phi_y \pm \Phi_x = -\frac{(x \mp y)(x+t)+x^2+y^2}{(x^2+y^2)(t^2+2xt-y^2)^{1/2}} \sim (x^2+y^2)^{-1/2}$$

which shows that Eq. (13), while asymptotically correct, is not a suitable replacement for Eq. (10).

Nonlinear Effect

We examine here, following one reviewer's suggestion, the nonlinear effect on the far field by adding to the right-hand side of Eq. (9) a term proportional to $(\phi_x^0\Phi_x)_x$ [see Eq. (2)]. Denoting the solution of Eq. (10) as Φ_h, we may write an integral equation for the solution Φ that

$$\Phi(x,y,t) = \Phi_h - \int_0^\infty F(x,y+\eta,\eta,t)\mathrm{d}\eta$$

$$+\int_0^y F(x,y-\eta,\eta,t)\mathrm{d}\eta + \int_y^\infty F(x,\eta-y,\eta,t)\mathrm{d}\eta \tag{14}$$

where

$$F(x,\alpha,\eta,t) = \int_{-\infty}^\infty\int_{-\infty}^\infty \frac{H(t'+x-x'-\sqrt{\alpha^2+(x-x')^2})}{\sqrt{[t'+(x-x')]^2-[\alpha^2+(x-x')^2]}}$$

$$\times\frac{\partial}{\partial x'}[\phi_{x'}^0(x',\eta)\Phi_{x'}(x',\eta,t-t')]\mathrm{d}t'\mathrm{d}x'$$

We only need to examine Eq. (14) for $y>0$, since $\Phi(x,0,t) = \Phi_h(x,0,t)$. For large x, or large α, we may approximate $F(x,\alpha,\eta,t)$ by evaluating the time integral near its singular point, i.e., $t' = -(x-x')+\sqrt{\alpha^2+(x-x')^2}$. Thus

$$F(x,\alpha,\eta,t) = \int_{-\infty}^\infty \ln\sqrt{\alpha^2+(x-x')^2}\frac{\partial}{\partial x'}[\phi_{x'}^0\Phi_{x'}(x',\eta,t+x$$

$$-x'-\sqrt{\alpha^2+(x-x')^2})\mathrm{d}x'$$

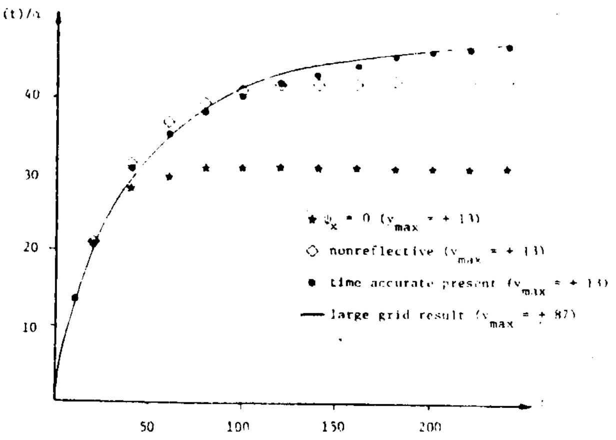

Fig. 1 Indicial pitch response for an NACA 64A006 at $M_\infty = 0.88$.

or

$$F(x,\alpha,\eta,t) = \int_{-\infty}^\infty \frac{x-x'}{[\alpha^2+(x-x')^2]}\phi_{x'}^0\Phi_{x'}(x',\eta,t+x-x'$$

$$-\sqrt{\alpha^2+(x-x')^2})\mathrm{d}x'$$

Since both $\phi_{x'}^0$ and $\Phi_{x'}$ decay as $(x'+\eta^2)^{-1/2}$, we may further approximate $F(x,\alpha,\eta,t)$ by

$$F(x,\alpha,\eta,t)\ \frac{x}{\alpha^2+x^2}\int_{-\infty}^\infty \phi_{x'}^0\Phi_{x'}(x',\eta,t+x-x'$$

$$-\sqrt{\alpha^2+(x-x')^2})\mathrm{d}x' \tag{15}$$

We recognize Eq. (15) as a doublet with strength in proportion to the compressibility effect. At large distances from the airfoil this term is negligible compared to the term we retain in Eq. (10). Thus $\phi(x,y,t)$ approaches $\phi_h(x,y,t)$ asymptotically.

Example

We illustrate the effectiveness of our results by applying them to the time development of the lift on an airfoil subjected to a step change in angle of attack. The time-linearized small perturbation algorithm of Ref. 9 is used as the test bed for the comparison.

Figure 1 compares the lift response of an NACA 64A006 airfoil at $M_\infty = 0.88$, computed using different boundary conditions. Results obtained in a stretched grid with the outer boundary at a $y_{\max}$ of about 100 chord lengths away from the airfoil is compared with results obtained in a grid with a $y_{\max}$ of about 13 chord lengths.

For the large grid we find no significant difference between solutions using different boundary conditions for the times indicated in Fig. 1. In the case of the small grid, we compare solutions obtained by setting $\psi_x = 0$ at $y = \pm y_{\max}$, by using the nonreflecting boundary condition $\sqrt{\kappa}\psi_x \pm \psi_y = 0$ on $y = \pm y_{\max}$, and by using the result of Eq. (11) on $y = \pm y_{\max}$. The solutions are rather insensitive to upstream boundary conditions and are subject to the same downstream conditions, viz., $\psi_x = 0$. The nonreflecting boundary condition of Ref. 6 achieves about 91% of the steady-state lift and gives a substantial improvement over the conventional calculation. Results from the time-accurate boundary condition we have derived here are in very good agreement with those found using the large grid; these are uncontaminated by reflections from the boundary for $t < 200$.

Conclusion

We have derived the far field unsteady solutions for a step change in the lift of an airfoil and a wing. These results can be used to reduce the size of the computational domain required for either time accurate or frequency domain calculations. We have illustrated their application with a time-linearized computation of a step change in the angle of attack of a two-dimensional airfoil.

Acknowledgment

The author thanks Dr. H. Atassi for his technical advice on formulating this problem and Dr. A. R. Seebass for many helpful discussions. The MAC's symbolic manipulation system located at MIT is responsible for some of the integrations and for checking the results. This research was supported by the AFOSR Grant 76-2954G and the ONR Grant N00014-76-C-0182.

References

[1]Tijdeman, H. and Seebass, R., "Transonic Flow Past Oscillating Airfoils," *Annual Review of Fluid Mechanics*, Vol. 12, 1980, pp. 181-222.

[2]Farmer, M. G. and Hanson, P. N., "Comparison of Supercritical and Conventional Wing Flutter Characteristics," *Proceedings AIAA/ASME/SAE 17th Structures, Structural Dynamics and Materials Conference*, King of Prussia, Penn., April 1976, pp. 608-611; see also NASA TMX-72837, May 1976.

[3]Ashley, H., "On the Role of Shocks in the 'Sub-Transonic' Flutter Phenomenon," *Journal of Aircraft*, Vol. 17, March 1980, pp. 187-197.

[4]Ballhaus, W. F. and Goorjian, P. M., "Implicit Finite-Difference Computations of Unsteady Transonic Flows About Airfoils," *AIAA Journal*, Vol. 15, Dec. 1977, pp. 1728-1735.

[5]Magnus, R. J., "Computational Research on Inviscid, Unsteady, Transonic Flow Over Airfoils," Office of National Research, ONR CASD/LVP 77-010, 1977.

[6]Engquist, B. and Majda, A., "Numerical Radiation Boundary Conditions for Unsteady Transonic Flow," *Journal of Computational Physics*, to appear.

[7]Krupp, J. A. and Cole, J. D., "Studies in Transonic Flow IV. Unsteady Transonic Flow," UCLA Eng. Rept. 76104, Oct. 1976.

[8]Tijdeman, H., "Investigations of the Transonic Flow Around Oscillating Airfoils," Doctoral Thesis, Technische Hogeschool Delft, The Netherlands, 1977.

[9]Fung, K.-Y., Yu, N. J., and Seebass, R., "Small Unsteady Perturbations in Transonic Flows," *AIAA Journal*, Vol. 16, Aug. 1978, pp. 815-822.

[10]Houwink, R. and van der Vooren, J., "Results of an Improved Version of LTRAN-2 for Computing Unsteady Airloads on Airfoils Oscillating in Transonic Flow," AIAA Paper 79-1553, July 1979.

[11]Klunker, E. B., "Contribution to Methods for Calculating the Flows About Thin Lifting Wings at Transonic Speeds," NASA TN D-6530, Nov. 1971.

[12]Lighthill, J., *Waves in Fluids*, Cambridge University Press, 1978, pp. 17-21.

12

SIAM J. APPL. MATH.
Vol. 39, No. 2, October 1980

0036-1399/80/3902-0014 $01.00/0

SHOCK WAVE FORMATION AT A CAUSTIC*

K.-Y. FUNG†

Abstract. The behavior of a weak acoustic compression near a caustic surface has been determined for a special class of specified incoming signals. This problem arises in various contexts, including the propagation of sonic booms generated by supersonic aircraft. The solution derives from a mapping of hodograph-like solutions to the physical plane. The maximum amplification for this class of signals of fixed amplitude depends on the width of the incoming signal. The solutions contain reflected shock waves that satisfy the appropriate shock jump conditions, provided the width of the incoming signal is greater than a certain critical value.

1. Introduction. There are many sources of weak shock waves. These include the commonly experienced phenomena of thunder and the sonic boom of supersonic aircraft. At supersonic speeds, aircraft generate a nearly conical wave pattern. These wave fronts propagate along their normals at the local sound speed, i.e., along acoustic rays. Variations in the sound speed (due to temperature changes), aircraft maneuvers, and winds can lead to ray crossing and a focusing of the wavefront. In the case of the sonic boom this results in a so-called "superboom" if the rays form an envelope, or a "super-superboom" if they meet at a point. In the case of a sonic boom, the pressure signature is, nominally, an N-shaped wave. More specifically, a weak shock wave provides an essentially instantaneous rise in pressure; subsequently the pressure falls linearly (in space or time) and is returned to nearly the ambient pressure through a second weak shock wave. The focusing of this weak shock wave is examined here. For simplicity, we phrase the problem in the context of the behavior of a weak shock wave generated by an aircraft in slightly supersonic flight in a flow with a Mach number gradient. Such gradients occur naturally in the troposphere where the ambient temperature decreases nearly linearly with altitude.

Sonic booms as well as weak shock waves from other sources are, under normal circumstances, adequately described by a nonlinear adaptation of geometric acoustics [1], [2], [3]. In geometric acoustics, as in geometric optics, a ray is the path of a signal point on a wave. Neighboring rays form an infinitesimal ray tube. The area of a ray tube will, in some situations, vanish at a point in space-time, which we shall call a focal point. Such focal points may form a hyper-surface in space and time that, in most cases, is an envelope of the rays in physical space. Such a hypersurface is an acoustic caustic, and will be referred to hereafter as a caustic or caustic surface.

The nonlinear adaptation of geometric acoustics needed for signals of finite (but small) strength corrects the phase of a given acoustic signal by an amount proportional to the amplitude of the local signal strength. Except near surfaces, lines, or points of focusing, such as a caustic, this is the only nonlinear correction needed for small but finite amplitude signals.

In the absence of winds, the theory of geometric acoustics states that the Rayleigh acoustic energy, $p'^2A/(\rho a)$, is constant along a ray tube. Here p' is the perturbation pressure, A is the differential ray tube area and ρa, the acoustic impedance, is the product of the local density and sound speed.

This, and the more general conservation law of Blokhintsev [4] applicable in the presence of winds, require that the perturbed quantities such as p' become infinite when

---

* Received by the editors August 6, 1979.

† Department of Aerospace and Mechanical Engineering, University of Arizona, Tucson, Arizona 85721. This research was sponsored by the Office of Naval Research under Grant N00014-76-C-0182.

the differential ray tube area A becomes zero. In these cases, geometric acoustics fails to describe the behavior of a signal and a local treatment is required.

Guiraud [5] and Hayes [6] have given the equation that describes the behavior of the pressure signature near a caustic. Guiraud's derivation is quite lengthy; Hayes' is intuitive and short. Recently, Pechuzal and Kevorkian [7] obtained the same equation as a limiting result of an inner expansion governing the behavior near the caustic. In a coordinate system that is fixed with a wave front, the local behavior at a caustic is not difficult to delineate, and the nonlinear effect needed to provide the correct equation is easily deduced for normal situations. Cramer and Seebass [8] have derived the equation for a focus point, i.e., an arête.

Despite a fairly large number of experimental, numerical and analytical investigations, there has not yet been any truly adequate description of the local behavior of a nonlinear acoustic signal at a caustic. Because the nonlinear behavior at a caustic is a very local one, experimental measurements have proved difficult. Numerical calculations are not very reliable because some of the local details, such as the Guderley patch, if one occurs, are difficult if not impossible to resolve [9]. Analytical studies are difficult because of the inherent nonlinearity of the problem. Perhaps the most informative results are the measurements from the French flight tests discussed by Wanner et al. [10]. Laboratory investigations have used spark generated N-waves [11], [12] artificially stratified steady and unsteady flows [13], [14] and, more recently, weak shock waves generated in shock tubes [15], but have failed to resolve the local details of the flow.

The results presented here derive from a hodograph technique first used by Seebass [16] and later extended by Gill [17]. Their analysis resulted in functions which satisfied the governing partial differential equation and one of the shock jump conditions exactly; but the other jump condition was not satisfied. This paper extends this earlier work by considering a broader class of incoming signals. This provides solutions for compressions of sufficient breadth that the reflected shock wave is never so strong that the flow behind it becomes subsonic.

In this case we are able to satisfy both the partial differential equation and the shock jump relations. More severe incoming compressions are not dealt with as this would require a double-valued hodograph plane, a situation not considered here.

2. Governing equations and boundary conditions. For simplicity we consider the model situation of slightly supersonic flight in an idealized stratified atmosphere with an adiabatic lapse rate and hydrostatic equilibrium, as sketched in Fig. 1. The governing equation is

$$\phi_{yy} - \beta_\infty^2 \phi_{xx} - \frac{\delta M_\infty^2}{l M_a^2}\phi_y = \varepsilon(\gamma+1)M_\infty^2 \phi_x \phi_{xx}, \tag{1}$$

where

$$M_\infty^2 = M_a^2[1-(\gamma-1)\delta(y/l)]^{-1} \quad \text{and} \quad \beta_\infty^2 = M_\infty^2 - 1.$$

Here ϕ is the usual perturbation velocity potential, ε is a small parameter that characterizes the perturbations produced by an aircraft of characteristic length l, δ is the small parameter characterizing the ratio of this length to that determined by the temperature statification, and M_a is the operating Mach number of the aircraft and M_∞ is the local Mach number at infinity. The first two terms of (1) are the usual ones for steady supersonic flow. The third term arises because of the gravitational force and should be retained in a consistent approximation. The last term is the lowest-order nonlinear term and must be retained in transonic flows.

At $y = 0$ we give boundary data that is representative of an incoming signal, say $\phi_y = f(x)$ for $0 < x < l$, with undisturbed upstream parallel flow. We require that the solution vanish in the subsonic domain as $y \to -\infty$. Waves will be reflected from the intervening caustic surface where $M_\infty = 1$ and they must be allowed to pass through $y = 0$ without reflection. This may be thought of as a radiation condition.

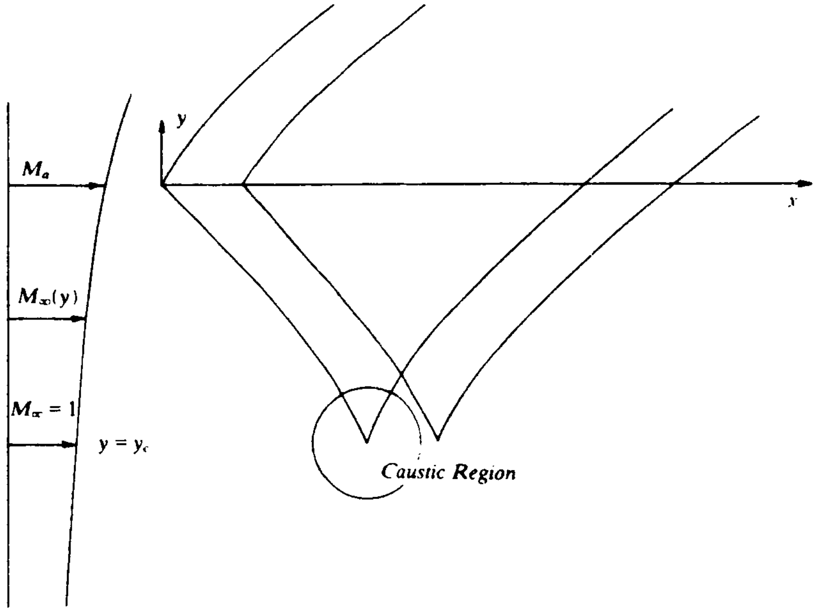

FIG. 1. *Sketch of model problem depicting the linear wave fronts. Our interest is in the local nonlinear behavior in the caustic region.*

Because of the thermal stratification a caustic occurs when $\beta_\infty = 0$, i.e., at

$$y_c = \frac{-l}{(\gamma-1)\delta}(M_a^2 - 1).$$

In order to eliminate the ϕ_y term in (1) we make the transformation

$$\tilde{y} = \left[\left(1 - \frac{\gamma-1}{l}\delta y\right)^{(\gamma-2)/(\gamma-1)} - 1\right]$$

under which (1) becomes

$$\text{(2)} \quad \frac{\delta^2(2-\gamma)^2}{l^2}\phi_{\tilde{y}\tilde{y}} - (1+\tilde{y})^{-(3-\gamma)/(2-\gamma)}\{M_a^2 - (1+\tilde{y})^{-(\gamma-1)/(2-\gamma)} + \varepsilon(\gamma+1)M_a^2\phi_x\}\phi_{xx} = 0.$$

Note that at $y = 0$, $\tilde{y} = 0$ but that at $y = -\infty$, $\tilde{y} = -1$ (for $1 < \gamma < 2$). Thus, the domain of interest is finite in $\tilde{y}$. Except in the subsonic far field where $\tilde{y} \to -1$, $\tilde{y}$ is small. Using a Taylor's Series for small $\tilde{y}$, we may reduce (2) to the simple form

$$\text{(3)} \quad \begin{aligned} &\frac{\delta^2(2-\gamma)^2}{l^2}\phi_{\tilde{y}\tilde{y}} - \left\{(M_a^2 - 1) + \frac{1}{2-\gamma}(\gamma-1)\tilde{y} + \varepsilon(\gamma+1)M_a^2\phi_x\right\}\phi_{xx} \\ &\quad = O(M_a^2-1)^2 + O(\tilde{y}^2) + O(M_a^2-1)\tilde{y}) + \cdots, \end{aligned}$$

valid away from $\tilde{y} = -1$. The caustic now occurs at

$$\tilde{y}_c = -\frac{2-\gamma}{\gamma-1}(M_a^2 - 1)$$

and $\tilde{y}_c$ is $O(M_a^2 - 1)$ which is taken to be small. Hence, the representation of (2) by (3) is valid in the caustic region.

A simple scaling of $\tilde{y}$, x and ϕ reduces (3) to the form

$$\tilde{\phi}_{\eta\eta} - (1 + \eta + \tilde{\phi}_X)\tilde{\phi}_{XX} = 0, \tag{4}$$

where

$$x = \frac{(M_a^2 - 1)^{3/2} l}{(\gamma - 1)\delta} X, \qquad \tilde{y} = \frac{(M_a^2 - 1)(2 - \gamma)}{(\gamma - 1)} \eta,$$

$$\phi = \frac{(M_a^2 - 1)^{5/2} l}{\varepsilon(\gamma + 1) M_a^2 (\gamma - 1)\delta} \tilde{\phi}.$$

The boundary condition at $\eta = 0$ becomes

$$\tilde{\phi}_\eta = \frac{(\gamma - 1) M_a^2 \varepsilon}{(M_a^2 - 1)^{3/2}} F(X), \qquad 0 \leqq X \leqq \lambda, \tag{4a}$$

where $F(X)$ gives the shape of the incoming signal. The other boundary conditions, which are homogeneous, were discussed earlier.

With the vertical coordinate shifted to $1 + \eta = Y$ and, for simplicity, replacing $\tilde{\phi}$ by ϕ, (4) can be reduced to the canonical form

$$(Y + \phi_X)\phi_{XX} - \phi_{YY} = 0. \tag{5}$$

The boundary condition is now prescribed at $Y = 1$, corresponding to $\eta = 0$ or $y = 0$. Equation (5) was derived by Guiraud [5] and also given intuitively by Hayes [6]. It is invariant under the transformation $X \to \alpha X$, $Y \to \alpha^{2/3} Y$, $\phi \to \alpha^{5/3}\phi$. Thus the transonic parameter $(\gamma - 1) M_a^2 \varepsilon / (M_a^2 - 1)^{3/2}$ in (4a) can be absorbed by the scaling $\alpha = (\gamma - 1) M_a^2 \varepsilon / (M_a^2 - 1)^{3/2}$.

A general solution of (5) then has the form

$$\phi = \phi(X, Y; F),$$

where F characterizes the incoming signal shape, and must have $\phi_X \sim Y^{-1/4}$ on the characteristic $X = -\frac{2}{3} Y^{3/2}$ if, as $Y = \to \infty$, the behavior is to be consistent with the linear solution [6] where the ray tube arc is proportional to $Y^{1/2}$ and, with $\phi_X \propto p'$, $\phi_X \sim Y^{-1/4}$ according to the theory of geometrical acoustics.

Pechuzal and Kevorkian [7] have derived (5) from (1) using matched asymptotic expansions with ε as the small parameter. The inner equation, that is, the equation that applies for $\beta_\infty = O(\varepsilon)$, reduces to (5). They give a particular solution applicable to the case where the signal is totally reflected from the sonic line, that is, when the surface $M_\infty = 1$ is replaced by a solid surface.

Equation (5) is a nonlinear partial differential equation of the mixed type. It admits discontinuous solutions that satisfy the jump relation corresponding to continuity of the velocity component tangential to the discontinuity surface

$$[\![\phi_X]\!]^2 (Y + \hat{\phi}_X) = [\![\phi_Y]\!]^2 \tag{6a}$$

along

$$\frac{dY}{dX} = (Y + \hat{\phi}_X)^{-1/2}, \tag{6b}$$

where $[\![\cdot]\!]$ means the jump across the discontinuity and $\hat{}$ the average value of a function evaluated on each side of the discontinuity.

A general approach for solving this equation with general boundary data has not yet been discovered. This equation can be linearized because there are variables in which its characteristics are fixed. Unfortunately, the appropriate boundary conditions in the new coordinates are nonlinear. We digress here to determine the analog of the physical boundary data to (5) in the coordinates in which (5) becomes linear.

3. Hodograph equations. The solution of the nonlinear Tricomi equation (5) that is of main interest is that for an incoming step wave. This signal must be terminated in some appropriate manner, e.g., an N-wave signal, in order for the solution to be finite. The local behavior of the step wave front at the caustic will be insensitive to the overall signal shape. This problem remains to be solved. Gill and Seebass [17] examined a simpler problem, viz., that of an incoming step wave in the hodograph plane, which of course, follows the linear characteristics. Because the image of the characteristic is a simple wave, the incoming signal in the physical plane is a continuous compression. This compression steepens as it approaches the sonic line and finally terminates in a shock wave formed by coalescing compressions that originate on the distorted sonic line. The "solution" they give which satisfies the partial differential equation, but only one of the two shock jump conditions, no doubt gives the general character of this process correctly, but fails to be strictly correct locally. The shock wave that occurs has a subsonic zone behind it and, presumably, they need to consider a double-sheeted Riemann surface to augment their functions to satisfy both shock jump relations.

Using a transformation suggested by the characteristics of (5), we write

$$T = Y + U, \qquad S = X + V,$$

where

$$U = \phi_X \quad \text{and} \quad V = \phi_Y.$$

Then (5) can be replaced by the linear equations

$$TU_S - V_T = 0 \quad \text{and} \quad V_S - U_T = 0. \tag{7}$$

Equations (7) have the solutions (see § 4) of the form

$$\begin{aligned} U(S, T) &= \sum_k \mu_k T^{3k} F_k(\xi), \\ V(S, T) &= -\sum_k \mu_k T^{3k+1/2} G_k(\xi), \end{aligned} \tag{8}$$

where

$$\xi = 9S^2/4T^3.$$

Referring to the scaled physical coordinates, we prescribe a signal $F(X)$ at $Y = 1$, say $F(X) = V_0(X, 1)$ on a set of incoming characteristics. Equation (8) can be used to relate $F(X)$ to $F_k(\xi)$ and $G_k(\xi)$ to determine the coefficients μ_k, provided that $F(X)$ has a simple analytical expression.

To demonstrate this, suppose U is negligible compared to one, then with $T \approx Y$ (8) has the form

$$\begin{aligned} \phi_X(X, 1) &\equiv U_0(X) \doteq \sum \mu_k F_k(\xi)|_{T=1} = \sum \mu_k \tilde{F}_k(X + V(X)), \\ \phi_X(X, 1) &\equiv V_0(X) \doteq -\sum \mu_k G_k(\xi)|_{T=1} = -\sum \mu_k \hat{G}_k(X + V(X)), \end{aligned} \tag{9}$$

where

$$F_k(9S^2/4) \equiv \tilde{F}_k(X + V(X)) \quad \text{and} \quad G_K(9S^2/4) \equiv \tilde{G}_k(X + V(X)).$$

The relation $V_0(X) = V(X + V_0(X))$ holds on the boundary $Y = 1$. Suppose

$$V_0(X) = \begin{cases} 0, & X < 0, \\ 1, & X > 0, \end{cases}$$

then we have the following table:

X	$V_0(X)$	$S(=X+V)$	$V(S)$
$X<0$	0	X	0
$X>0$	1	$1+X$	1

The function $V(S)$ is undefined in the interval $0 < S < 1$. Alternatively, if $V_0(X) = 0$ for $X < 0$ and -1 for $X > 0$, then the function $V(S)$ would be multivalued in the interval $-1 < S < 0$.

These two examples illustrate that if we prescribe simple boundary data in the S,T-plane, the boundary data in the physical plane may not have any physical meaning or a special interpretation is needed there. Signals at different values of Y are different in the S,T-plane because of the nonlinearity in $X = S - V$; therefore, there is no analog of the asymptotic boundary condition in the S,T-plane. Boundary data must be prescribed at a finite distance. This means that the asymptotic prescription given in [1], [2], [5] is inadequate; Pechuzal and Kevorkian [7] pointed this out and have shown how the asymptotic behavior of the solution in the caustic region is to be matched with the incoming signal by means of corrections to the linear characteristics.

If we suppose that $V_0(X)$ is smooth enough so that at $T = 1$, $V(S)$ is single-valued, e.g.,

$$V_0(X) = \begin{cases} 0, & X < 0, \\ -X, & 0 \leqq X \leqq 1, \\ -1, & 1 < X, \end{cases} \quad \text{then} \quad V(S) = \begin{cases} 0, & S < 0, \\ 1, & S > 0, \end{cases}$$

and $V(S)$, while discontinuous, is defined for all S. It is obvious then, that if $V_{0,X} < -1$, $V(S)$ will be multivalued. While this multivalued behavior may be used to find the solution for an incoming wave that is discontinuous in the physical plane, a more difficult problem, we limit our attention to the class of solutions with single-valued incoming signals in the S,T-plane.

We will consider incoming signals of the shape sketched in Fig. 2, characterized by their overall length λ, and the gradient $V_{0,X} = -1 + b$, both evaluated at some $Y = Y_0$. Thus our general solution, as discussed in the previous section, has the form

$$\phi = \phi(X, Y; \lambda; b),$$

where the signal shape F has been replaced by the two parameters λ and b. As we will see, with the relatively simple form of the solutions considered here, viz., continuous solutions in the S,T-plane, valid results are obtained only for b's greater than some critical value, b_c. The parameter λ is not an important one in our study because, for large values of λ, the behavior of the front of the signal becomes independent of λ and our primary interest is in the behavior of the compression.

4. Similar solutions. In this section we delineate the properties of a particular set of solutions, U_k and V_k, that satisfy the equations (7) or the equivalent second-order equations:

$$TU_{SS} - U_{TT} = 0 \quad \text{and} \quad V_{SS} - (V_T/T)_T = 0. \tag{10}$$

Although a unique determination of the μ_k cannot be given without prescribing boundary data and, more importantly, without delineating the complete set of functions for (7), we can study the corresponding solutions for each U_k, as well as some simple combinations of these functions, to see what physical behavior these solutions imply.

If we let $U_k = T^{3k}F_k(\xi)$ and $V_k = T^{3k+1/2}G_k(\xi)$, where $\xi = 9S^2/(4T^3)$, then equations (10) become

$$\xi(1-\xi)F_k'' + \{1/2 - [(-k) + (1/3-k) + 1]\xi\}F_k' - (-k)(1/3-k)F_k = 0 \tag{11a}$$

and

$$\begin{aligned}\xi(1-\xi)G_k'' + \{1/2 - [(1/2-k) + (-1/6-k) + 1]\xi\}G_k'&\\ -(1/2-k)(-1/6-k)G_k = 0.&\end{aligned} \tag{11b}$$

Equations (11) are in the form of the hypergeometric equation

$$\xi(1-\xi)F'' + \{c - [a+b+1]\xi\}F' - abF = 0$$

with the general solution

$$F = A\ {}_2F_1(a, b; c; \xi) + B\xi^{1-c}{}_2F_1(a-c+1, b-c+1; 2-c; \xi), \tag{12}$$

with A and B arbitrary constants. The function ${}_2F_1(a, b; c; \xi)$ is the usual hypergeometric series [18]. Comparing the corresponding parameters a, b, c, of (11) and (12) we find that the restriction on k in order that the series ${}_2F_1$ converge is $k > -\frac{7}{12}$ $(-1 < c-a-b)$. Another bound on k comes from specifying the asymptotic behavior of U_k as T tends to infinity. For the caustic problem, $k = -\frac{1}{12}$ gives the required $T^{-1/4}$ decay $(\phi_x \sim y^{-1/4})$ and $k < -\frac{1}{12}$ an allowable more rapid decay; terms with $k = -\frac{1}{12}$ are included to match the outer solution. If boundary conditions are prescribed at a finite distance, then the second bound for k is relaxed, but the vanishing far-field condition in the subsonic domain is still essential.

To determine the coefficients A and B in (12), we need to study the behavior of the hypergeometric series near the regular singular points $\xi = 0$, 1, ∞. After putting the appropriate values of a, b, c in (12) we have

$$F_k = A\ {}_2F_1(-k, \tfrac{1}{3}-k; \tfrac{1}{2}; \xi) + B\xi^{1/2}\ {}_2F_1(\tfrac{1}{2}-k, \tfrac{5}{6}-k; \tfrac{3}{2}; \xi).$$

The behavior at the three singular points is given by an arbitrary linear combination of the two functions listed in the following table:

$\xi \to 0$	$(1-\xi)^{1/6+2k}\ {}_2F_1(\frac{1}{6}+k, \frac{1}{2}+k; \frac{1}{2}; \xi)$	$\xi^{1/2}(1-\xi)^{1/6+2k}\ {}_2F_1(\frac{2}{3}+k, 1+k; \frac{3}{2}; \xi)$
$\xi = 0$	1	0
$\xi \to 1$	${}_2F_1(\frac{1}{3}-k, -k; \frac{5}{6}-2k; 1-\xi)$	$(1-\xi)^{1/6+2k}\ {}_2F_1(\frac{1}{2}+k, \frac{1}{6}+k; \frac{7}{6}+2k; 1-\xi)$
$\xi = 1$	1	$O(1-\xi)^{1/6+2k}$
$\xi \to \infty$	$\xi^{k-1/3}\ {}_2F_1(\frac{1}{3}-k, \frac{5}{6}-k; \frac{4}{3}; 1/\xi)$	$\xi^{k}\ {}_2F_1(-k, \frac{1}{2}-k; \frac{2}{3}; 1/\xi)$
$\xi = \infty$	0	0

We see that, within the range of k allowed, the only singularity occurs at $\xi = 1$ (i.e., $S = \pm\frac{2}{3}T^{3/2}$). The singular behavior of F_k there is $(1-\xi)^{1/6-2k}$ for $-\frac{7}{12} < k < -\frac{1}{12}$ and $\ln(1-\xi)$ for $k = -\frac{1}{12}(T>0)$. There are two loci in the S,T-plane where $\xi = 1$, namely $S = \mp\frac{2}{3}T^{3/2}$, corresponding to the incoming and the outgoing characteristics. By setting

$$\frac{B}{A} = \frac{-\Gamma(c)}{\Gamma(a)\Gamma(b)} \cdot \frac{\Gamma(a-c+1)\Gamma(b-c+1)}{\Gamma(2-c)},$$

we can remove the singularity on the positive side of the incoming characteristics ($|\xi| < 1$). Using this result, we write (12) in the form

$$F = \mu^*[G(a, b; c; \xi) + \xi^{1-c}G(a-c+1, b-c+1; 2-c; \xi)],$$

where

$$G(a, b; c; \xi) = \frac{\Gamma(a)\Gamma(b)}{\Gamma(c)}\, {}_2F_1(a, b; c; \xi)$$

and μ^* is a complex constant.

Because $\xi = 1$ is a singular point, in order to evaluate ${}_2F_1$ for arguments greater than one we need the analytical continuation of the function F throughout the complex ξ-plane, insisting on smooth behavior in the elliptic domain, viz., $T < 0$ (Re $\xi < 0$). We introduce a cut in the ξ-plane from $\xi = 1$ to infinity on the real axis and choose the branch that makes F continuous everywhere except on the branch line. By this means we can extend our solution to $|\xi| > 1$. By setting

$$\mu^* = \mu[1 + i \tan(2\pi(a+b))],$$

we can eliminate the other singularity on the negative side of the incoming characteristic ($|\xi| > 1$).

Thus solutions of equations (10), with a behavior that we anticipate will prove acceptable in the physical plane, take the form

$$U = \int U_k\, dk = \mathrm{Re}\left[\int \mu_k^* T^{3k} F_k\, dk\right],$$
$$V = \int V_k\, dk = \mathrm{Re}\left[-\int \mu_k^* T^{3k+1/2} G_k\, dk\right], \tag{13}$$

where

$$F_k = G(-k, \tfrac{1}{3}-k; \tfrac{1}{2}; \xi) + \xi^{1/2}G(\tfrac{5}{6}-k, \tfrac{1}{2}-k; \tfrac{3}{2}; \xi)$$

and

$$G_k = G(\tfrac{1}{2}-k, -\tfrac{1}{6}-k; \tfrac{1}{2}; \xi) + \xi^{1/2}G(1-k, \tfrac{1}{3}-k; \tfrac{3}{2}; \xi).$$

Representations of U_k, V_k appropriate to different domains of the S,T-plane are tabulated in [19].

5. Construction of solutions. Were we able to do so, we would now proceed to determine the appropriate equations needed to determine the values of μ_k^* in (13) that would satisfy certain prescribed boundary conditions, although it is unlikely we could solve them analytically. This formidable task is not resolved here. Alternatively, we may try to combine the F_k's and G_k's in such a way that they represent a meaningful solution in the physical plane that corresponds to physically interesting boundary data and satisfies the jump conditions (6) for any discontinuity that may arise. The results are instructive in that their physical interpretation is believed to be more meaningful than any numerical results might be. Furthermore, they provide the basis for further analytical advances.

2C

The function U_k, discussed in § 3, has a jump in S across the incoming characteristic and a singularity of $(1-\xi)^{2k+1/6}$ or $\ln(1-\xi)$ on the reflected characteristic. The jump behaves like the Heaviside unit function multiplied by a decay factor T^{3k}; the function V_k has similar properties with a decay factor $T^{3k+1/2}$.

Suppose we know the shape and the leading power by which the incoming signal amplifies, then k is determined and signal shapes can be constructed as described below. With only the range of k specified, we can examine a finite set of k's and try to find useful combinations of the functions U_k and V_k.

If, for example, we have an incoming step wave at T_0 with k specified,

$$U(S,T_0)=\begin{cases}0, & S+S_0<0,\\ 1, & 0<S+S_0<\lambda,\\ 0, & \lambda<S+S_0,\end{cases}$$

where $S_0=2T_0^{3/2}/3$ then the function $U_k(S,T)$ of (13) gives an increase in U from 0 to 1 at S_0, T_0 for T_0 sufficiently large, while $-U_k(S-\lambda,T)$ provides a decrease in U from 1 to 0. Thus we can construct the solution for a step wave of length λ from the simple combination

$$U(S,T)=U_k(S,T)-U_k(S-\lambda,T). \tag{14}$$

The larger T_0, the closer $U(S,T)$ is to a step function. For the case $k=-\frac{1}{12}$, this is the solution Seebass [16] found using a Fourier transform with the asymptotic boundary condition of an incoming step wave; this solution was examined in some detail by Gill [17]. While the image of the initial part of the wave is obviously a simple wave, as it is the image of a characteristic, the image of the terminal part of the wave is multiple-valued and needs special interpretation. To avoid this difficulty we may construct the solution for an "N-wave." It can be verified that the behavior of the initial rise of these two signals is effectively the same if λ is not small. The "N-wave" behavior of U_x arises naturally in many nonlinear acoustic problems, such as in the sonic boom, and has

$$U(S,T_0)=\begin{cases}0, & S+S_0<0,\\ 1-2\dfrac{S+S_0}{\lambda}, & 0<S+S_0<\lambda,\\ 0, & \lambda<S+S_0.\end{cases}$$

As before $U_k(S,T)$ gives the jump; the integral of U_k with respect to X

$$-\frac{2}{\lambda}\int_{S-\lambda}^{S}U_k(X,T)\,dX$$

gives the linear variation from S_0 to $S_0+\lambda$; and finally, $U_k(S-\lambda,T)$ returns the value of the function to zero at $S_0+\lambda$. Thus

$$U(S,T)=U_k(S,T)-\frac{2}{\lambda}\int_{S-\lambda}^{S}U_k(X,T)\,dX+U_k(S-\lambda,T) \tag{15}$$

represents an incoming N-wave.

The solution of primary interest here is a step or N-wave with a finite step thickness B corresponding to the incoming signals $V_{0,X}=-1+b$. Because the first of these is simpler, and the local behavior of the compression is the same if λ is not small, we limit our discussion to it. Locally the two solutions differ by only a constant.

Proceeding as above, we find the solution

$$U(S, T; B) = \frac{1}{B}\int_{S}^{S+B} U_k(X, T)\,dX - \frac{1}{B}\int_{S-\lambda-B}^{S-\lambda} U_k(X, T)\,dX, \tag{16}$$

which we will discuss in some detail. Notice that

$$\lim_{B\to 0} U(S, T; B) = U_k(S, T) - U_k(S-\lambda, T),$$

which is (14).

Solutions to $U_k(S, T)$ and $V_k(S, T)$ corresponding to (16) with $\lambda = 1$, $B = 0$, $\mu = 0.1$ have been evaluated numerically for many values of k. The main differences between these solutions lie in their behavior near the origin and in different jump behavior. In general the jumps in the values of U and V across the incoming characteristic satisfy

$$[\![U_k]\!]/[\![V_k]\!] = \alpha(k)/T^{1/2},$$

where α is a constant (which can be negative) that depends on k.

The relationships between U_k, V_k, their derivatives and their integrals are found in [19]. Only the values of U_k and V_k have to be calculated to determine any of these functions, as their integrals and derivatives can be expressed in terms of U_k and V_k. For example, (15) and (16) can be reduced to combinations of U_k and V_k.

6. Finite width compression. Here we examine an incoming signal for which the flow behind the shock wave that forms may remain supersonic. In this case we are able to satisfy both shock jump relations. We first construct, by linear superposition, the solution for an incoming signal in the hodograph plane that increases from 0 to 1 linearly in S for fixed T as S varies from $S_0 - B$ to S_0, remains 1 until $S = S_0 + \lambda$, and then decreases, again linearly, to 0 where $S = S_0 + \lambda + B$. The physical plane image of this signal was discussed in § 3, and the behavior sketched in Fig. 2. We then examine the structure of this solution as a function of the signal breadth B (for Gill and Seebass [17], $B = 0$).

For values of B larger than some critical values, B_c, the resulting shock wave is embedded in a supersonic flow. In this case we are able to satisfy the partial differential

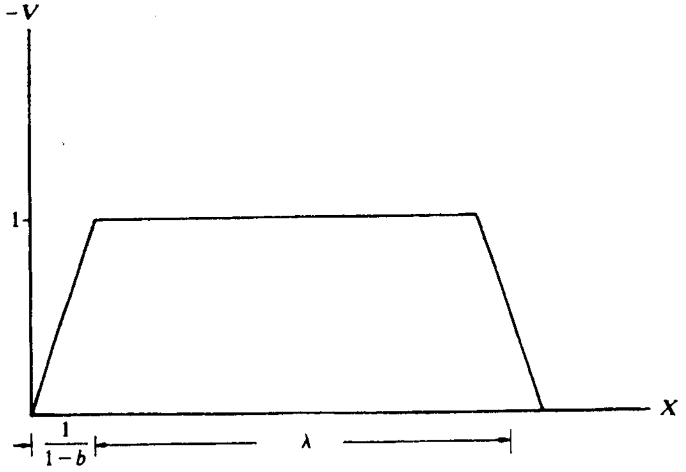

FIG. 2. *Sketch of incoming signal.*

equation and both shock conditions. For B's smaller than B_c, a subsonic zone appears behind the shock wave and we can satisfy only one of the two shock jump conditions. Either jump condition may be chosen as the one to be satisfied, giving, of course, slightly different shock wave shapes. Obviously, for $B\text{'s} < B_c$ we do not find a solution to physical problems posed.

As pointed out in § 2, the boundary data in the hodograph plane that correspond to meaningful physical signals might be multivalued or undefined near discontinuities. If the incoming wave is discontinuous, it must be represented by a multi-valued function in the physical plane. This gives rise to a boundary value problem we do not yet know how to solve in the S,T-plane. Rather than starting with prescribed data in the physical plane, we examine here, in some detail, a continuous solution in the hodograph plane and describe the corresponding behavior in the physical plane.

Consider the finite width step signal of signal length λ in the hodograph plane. For T_0 sufficiently large

$$F(S, T_0) \sim \begin{cases} 0, & S < S_0 - B, \\ \dfrac{1}{B}(S + B - S_0), & S_0 - B < S < S_0, \\ 1, & S_0 < S < S_0 + \lambda, \\ -\dfrac{1}{B}(S - S_0 - \lambda - B), & S_0 + \lambda < S < S_0 + \lambda + B, \\ 0, & S_0 + \lambda + B < S, \end{cases} \tag{17}$$

where

$$S_0 = -\tfrac{2}{3}T_0^{3/2}.$$

For $k = -\frac{1}{12}$, it can be shown by Fourier transforms that the solution

$$\begin{aligned} U_B &\equiv U(S, T; B) \\ &= \frac{1}{B}\int_S^{S+B} U_k(X, T)\, dX - \frac{1}{B}\int_{S-\lambda-B}^{S-\lambda} U_k(X, T)\, dX \\ &= \frac{1}{B}\,\frac{1}{3(k+\frac{1}{2})}\{[\tfrac{3}{2}(S+B)U_k(S+B, T) - \tfrac{3}{2}SU_k(S, T) + TV_k(S+B, T) - TV_k(S, T)] \\ &\qquad - [\tfrac{3}{2}(S-\lambda)U_k(S-\lambda, T) - \tfrac{3}{2}(S-\lambda-B)U_k(S-\lambda-B, T) \\ &\qquad\qquad + TV_k(S-\lambda, T) - TV_k(S-\lambda-B, T)]\} \end{aligned}$$

satisfies (17) asymptotically.

We note that U_B is continuous and finite everywhere in the S,T-plane when $k > -\frac{1}{2}$. This follows because U_B is an integral of U_k and $B \neq 0$. Examining $U_k(S, T)$ at its singular points for $k = -\frac{1}{12}$, the case of interest here,

$$U_{-1/12} \sim S^{-1/6} \quad \text{for } S \to 0,\ T = 0,$$

and

$$U_{-1/12} \sim \ln\left(1 - \frac{3}{2}\,\frac{S}{T^{3/2}}\right) \quad \text{for } S \to \tfrac{2}{3}T^{3/2},\ T > 0.$$

Therefore the behavior of U_B is given by

$$\frac{1}{B}\int_S^{S+B} U_{-1/12}\,dX \sim B^{-1/6}, \qquad S \to 0,\ T=0$$

and

$$\frac{1}{B}\int_S^{S+B} U_{-1/12}\,dX \sim \left(1-\frac{3}{2}\frac{S}{T^{3/2}}\right)\ln\left(1-\frac{3}{2}\frac{S}{T^{3/2}}\right) \qquad S \to \tfrac{2}{3}T^{3/2},\ T>0.$$

Thus U_B is finite and continuous everywhere, with first derivatives that are discontinuous at $S=-\frac{2}{3}T^{3/2}$.

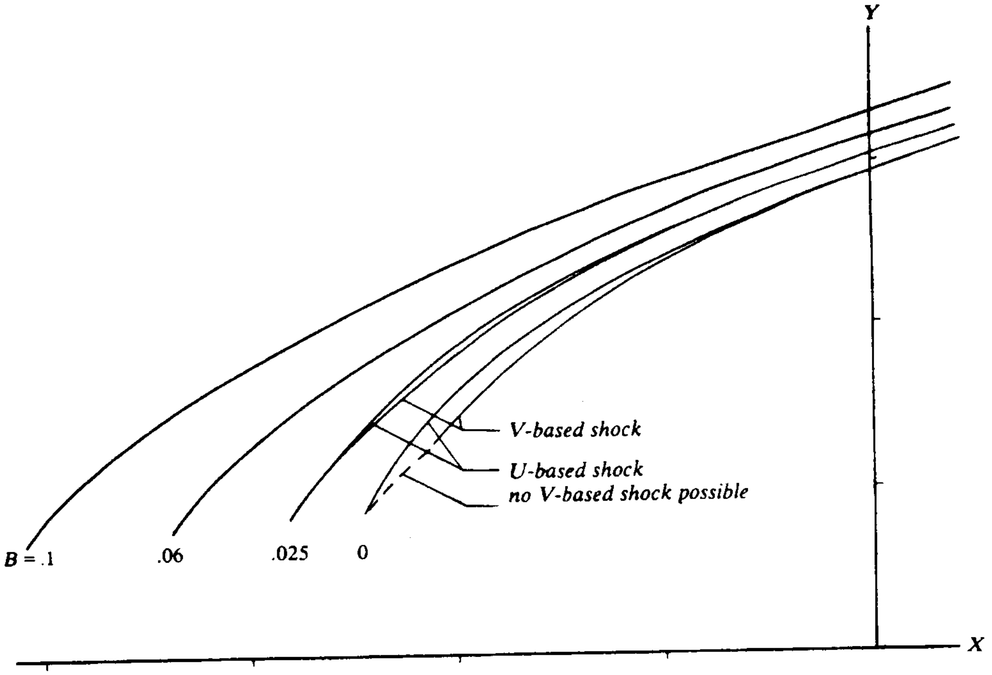

FIG. 3. *Location of the reflected shock wave for four B's*; $k=-\frac{1}{12}$, $\mu=0.1$, $\lambda=20$.

For small B, $U(S, T; B)$ and $\lim_{B\to 0} U(S, T; B)$ are not significantly different in the S,T-plane except where $\lim_{B\to 0} U_B$ is singular and where it has a jump. Here, changes in B significantly alter the behavior of the solutions U and V in the physical plane. These are regions where shock waves form. The transformation from the solutions $U(S, T)$ and $V(S, T)$ to the physical plane requires a high degree of familiarity with these functions. The transformation that gives $U(X, Y)$ and $V(X, Y)$ for fixed values of Y and at specified intervals of X, is accomplished by a digital computer, primarily through Newton's method. Thus we solve the implicit relations

$$\begin{aligned} Y &= T - U(S, T), \\ X &= S - V(S, T) \end{aligned} \tag{18}$$

numerically and to a high degree of accuracy; it is important that we can evaluate U and V to any desired degree of accuracy throughout the S,T-plane.

Notice that U and V have discontinuities in their first derivatives because U_k and V_k are discontinuous. It is essential to know in advance from which region of the

S,T-plane a point X, Y derives; otherwise Newton's method will fail to converge to the correct values, if it converges at all. Constant $Y(S,T)$ contours in the S,T-plane are particularly helpful in designing the numerical code to effect this evaluation. For the results we discuss later, equations (18) are satisfied to one part in 10^{-8}; this limit is set by the accuracy we specify in evaluating the functions.

Above a certain value of Y, $U(X,Y)$ and $V(X,Y)$ become multivalued, indicating the formation of a shock wave. The solution is then made single-valued by introducing a discontinuity so that both the integrals

$$\int^{X} U(t, Y)\,dt, \qquad \int^{X} V(t, Y)\,dt \tag{19a, b}$$

are continuous and single-valued. As noted by Seebass [16], this implies that the jump relations (6) are satisfied if the position of the shock jumps calculated from both integrals coincide. The shock determined by (19a) implies conservation of momentum while that determined by (19b) implies conservation of mass. We carried the integrations in (19) using a pointwise trapezoidal rule with varying intervals. The values of $[\![U]\!]$ and $[\![V]\!]$ were determined by linear interpolation. We have calculated the shock position by both methods and the difference between the two shock positions becomes negligible for values of B greater than a critical value, B_c, when no subsonic zone can be

TABLE 1

Input signal at $Y = 1$ — $B = 0.1$

Signal width $\Delta X = .29480$ — $\lambda = 20$

Signal strength $\Delta U = -.10870$ — $\mu = 0.1$

Y	X_s	$[\![U]\!]$	$[\![V]\!]$	R/L
0.14	−.2046231	$-.321434 \times 10^{-2}$	$.314971 \times 10^{-3}$	.998263
	−.2046225	$-.321199 \times 10^{-2}$	$.314570 \times 10^{-3}$	.998468
0.17	−.200442	−.011451	$.196838 \times 10^{-2}$	.997718
	−.200436	−.011442	$.196547 \times 10^{-2}$	.998058
0.20	−.194564	−.018516	$.402860 \times 10^{-2}$	.997680
	−.194551	−.018501	$.402236 \times 10^{-2}$	.998071
0.30	−.167396	−.037737	.011986	.997954
	−.167352	−.037704	.011968	.998294
0.425	−.122108	−.056853	.022892	.998227
	−.122019	−.056791	.022855	.998549
0.5	−.089789	−.062301	.029384	.999673
	−.089691	−.062219	.029344	1.00020
0.6	−.037158	−.062501	.036056	.999902
	−.037069	−.062421	.036010	1.00015
0.8	.095230	−.061519	.045499	.999982
	.095302	−.061463	.045458	1.00008
1.0	.256577	−.060413	.052557	1.00001
	.256643	−.060364	.052515	1.00006
1.5	.759148	−.057630	.065034	1.00001
	.759198	−.057601	.065001	1.00003

$[\![\ ]\!]$ indicates the jump across the shock wave.

R/L is the ratio of the right to left-hand side of equation (6a).

found behind the shock wave. We conjecture that the solution is an exact one. We know it satisfies the partial differential equations, and, to the accuracy with which we can check them, the shock jump relations. We have not tried to establish the value of B_c, precisely; we do know however that $B_c \approx 0.10$. With $B = 0.06$ the maximum error in satisfying the shock jump relations, as measured by the ratio of the right-hand to the left-hand side of (6a), is 6%; with $B = 0.10$ it is 0.3%.

Detailed numerical calculations have been carried out for five values of B: 0.01, 0.025, 0.04, 0.06 and 0.10. The other parameters, μ and λ, were taken to be 0.1 and 20, respectively, for the convenience of comparing our results with those of Gill and Seebass [17]. Shock locations, and the extent of the subsonic zone based on (19a), called U-based or (19b), called V-based, are depicted in Fig. 3. Note that as the extent of the subsonic region behind the shock wave diminishes the two shock locations become more nearly one curve. This, as was noted earlier, is to be expected because we don't expect our single-valued solution (in the S, T-plane) to be valid if the flow behind the shock is subsonic.

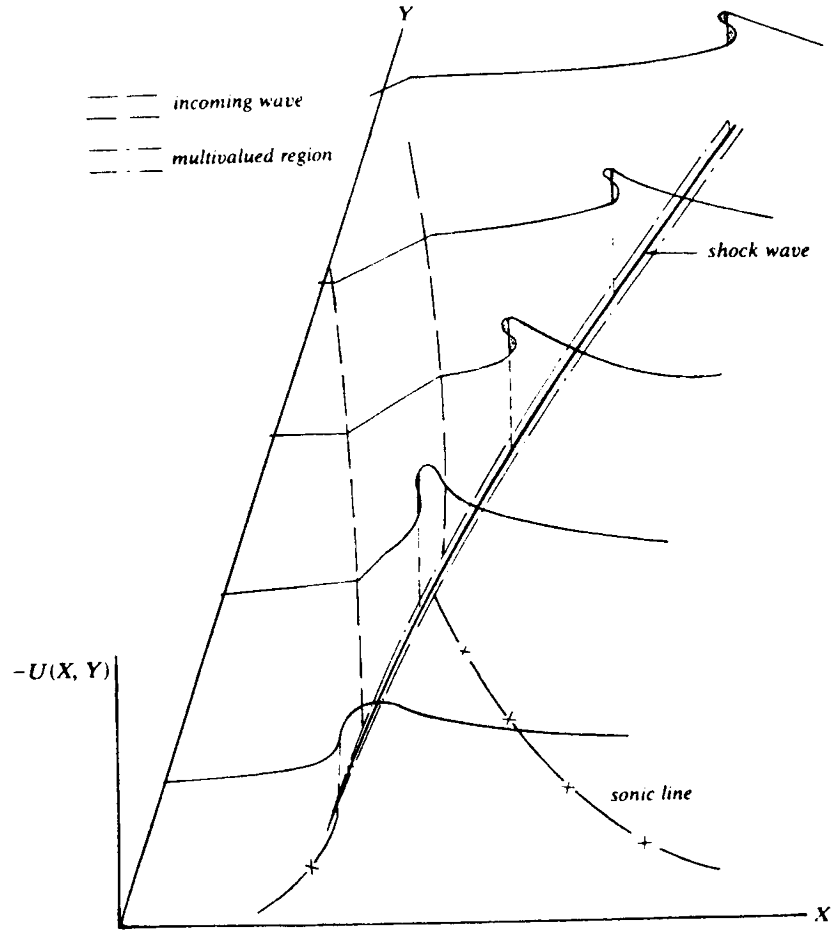

FIG. 4. *An incoming step wave of finite width terminated by the reflected shock wave using the area balance rule in the multivalued region B = .06.*

Table 1 delineates the shock positions and shock jumps U and V, determined using equations (19a) and (19b) for selected values of Y when $B = \mu = 0.1$ and $\lambda = 20$. Also tabulated are the ratios of the right- to left-hand side, R/L, of equation (6a) obtained using (19a) and (19b). The general agreement between the results for the shock position computed both ways and the fact that R/L is 1.0, to the accuracy with which we can calculate the shock jumps using (19a) and (19b), supports the claim that the solution satisfies both shock jump relations.

Figure 4 depicts the value of U as a function of X for fixed values of Y for $B = 0.06$. We see that the distortion of the sonic line gives rise to weak compressions which become much stronger as they meet the incoming compression and then propagate away from the interaction, slowly decreasing in strength.

We now anticipate, but did not do so originally, that if a shock wave arises, and if it has a subsonic portion as sketched in Fig. 5, then a saddle point in speed (or Mach number) will occur. Such behavior occurs on the physical plane when the solution in the hodograph plane is multivalued. Because we have limited our solutions to single-valued functions of S and T we can only expect to find solutions for large enough B, that is, for waves thick enough that the shock wave remains embedded in the supersonic flow.

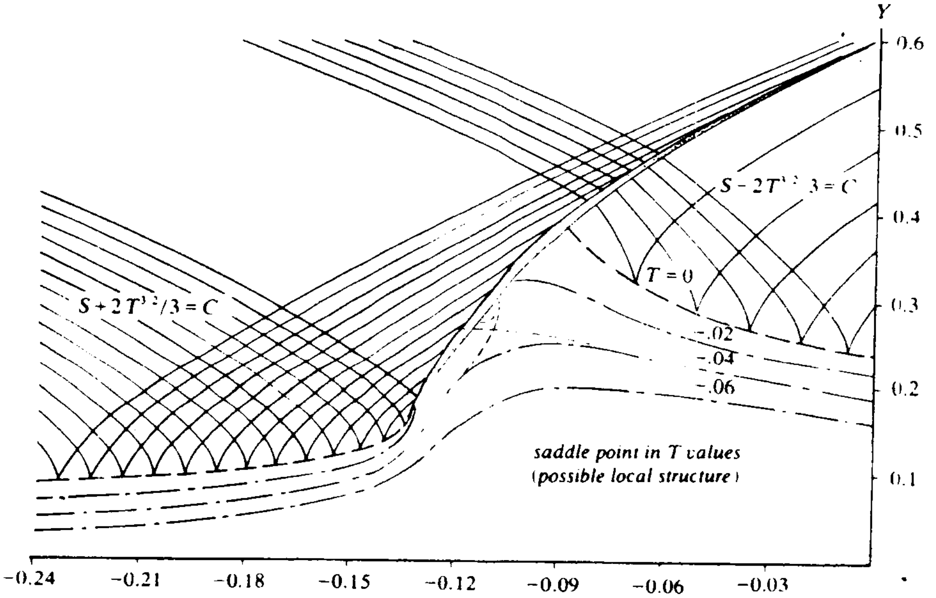

FIG. 5. *Reflected shock wave, sonic line, characteristics.*

A shock will always occur even for large B; it will form further above the sonic line and decrease in strength with increasing B. This follows because the value of V is not zero at the sonic line ($T = 0$), and its maximum values increase in the supersonic domain as $Y^{1/4}$ along the outgoing characteristics. The location of a given U and V in the physical plane is always stretched by V, i.e, $V(X = S - V, Y)$, $U(X = S - V, Y)$. The larger the Y, the more they are stretched. Nevertheless, they weaken because the region of stretching is confined to a thinner and thinner strip, which eventually corresponds to the immediate neighborhood of the singular characteristic.

Starting from the lowest point where the solution becomes multiple-valued, the reflected shock strength increases almost linearly with Y (this behavior is most distinct

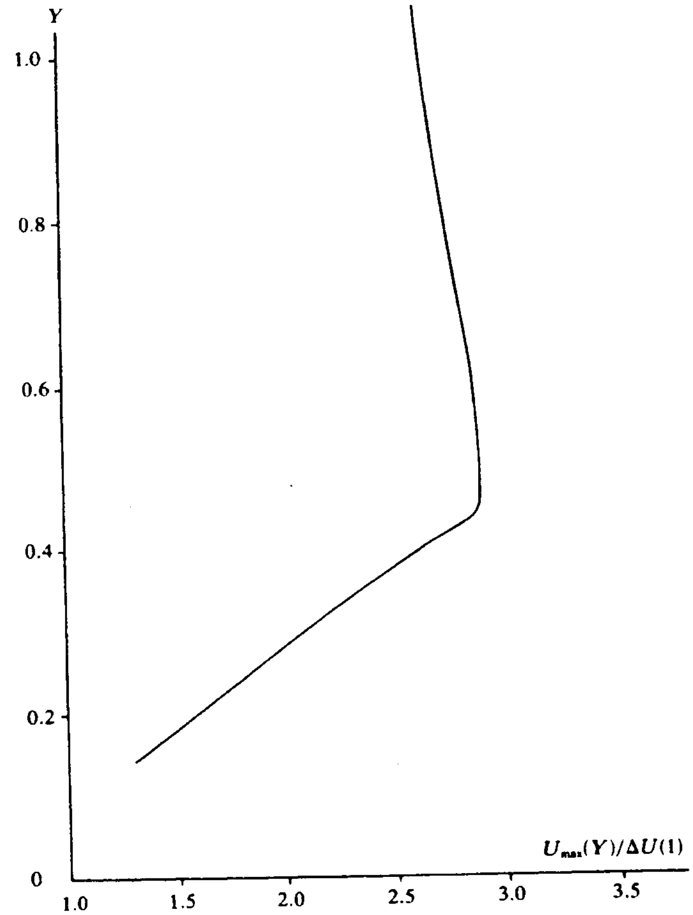

FIG. 6. *Maximum reflected shock strength, divided by the incoming wave strength at* $Y = 1.0$*, as a function of* Y *for* $B = 0.1$.

for large B) to its maximum value at a Y of about 0.4. The shock strength then decreases with Y increasing, as shown in Fig. 6 for $B = 0.10$. This case was used for Table 1.

7. Conclusion. The role of nonlinear effects in the amplification of certain weak acoustic signals at a caustic has been studied through a hodograph-like transformation. Nonlinear distortion of the boundary data plays an important role in determining the appropriate boundary data in the hodograph plane. We have reformulated the equation governing the nonlinear behavior of an acoustic signal at a caustic in a way that avoids supplying asymptotic boundary data. In the new coordinates, the solutions for the inner caustic region are represented by similar solutions whose behavior depends upon a single parameter k. Boundary conditions in the hodograph plane are then related to physically prescribed data. Unfortunately the relation is nonlinear. We have not resolved the problem of determining the corresponding boundary data in the hodograph plane.

Through a study of finite width step waves, with $k = -\frac{1}{12}$, for a small range of step width, we have shown that small changes in asymptotic boundary data near discontinuities in derivatives in the hodograph plane have a substantial influence on the solution's behavior in the physical plane.

The maximum strength of the reflected shock wave decreases monotonically with increasing signal width. When the width is larger than a given critical value, the shock that forms satisfies the jump conditions with a high degree of accuracy. Solutions for other values of k, discussed to some extent here, should prove useful in obtaining acceptable results for more general incoming signals. It seems unlikely, however, that the parameterization in k provides a complete set of solutions. Still, solutions for other incoming signals should be possible. But a single-sheeted Riemann sheet in the hodograph plane won't suffice for these more interesting signals.

For signals whose widths are larger than some critical value, solutions with a discontinuity representing a reflected shock are obtained that are essentially exact. These results represent an advance over previous results and should prove valuable in testing numerical methods designed to solve mixed nonlinear equations.

Acknowledgment. The author is indebted to Professor A. R. Seebass for advice and counsel during the course of this investigation and to Dr. Helmut Sobieczky for stimulating discussions and important suggestions.

REFERENCES

[1] W. D. HAYES, *Sonic boom*, Ann. Rev. Fluid Mech., 3 (1971), pp. 269–288.
[2] A. R. SEEBASS, *Sonic Boom Theory*, J. Aircraft, 6 (1969), pp. 177–184.
[3] R. N. BUCHAL AND J. B. KELLER, *Boundary layer problems in diffraction theory*, Comm. Pure Appl. Math., 13 (1960), pp. 85–114.
[4] D. I. BLOKHINTSEV, *Acoustics of a Nonhomogeneous Moving Medium*, Gustekhizdat, Moscow; USSR 1946. Translated as NACA TM-1399, 1956.
[5] J. P. GUIRAUD, *Acoustique géometrique, bruit ballistique des avions supersoniques et focalisation*, J. Mécanique, 4 (1965), pp. 215–267.
[6] W. D. HAYES, *Similarity Rules for Nonlinear Acoustic Propagation Through a Caustic*, Second Conference on Sonic Boom Research, NASA SP-180 (1968), pp. 165–171.
[7] G. PECHUZAL AND J. KEVORKIAN, *Supersonic-transonic flow generated by a thin airfoil in a stratified atmosphere*, this Journal, 33 (1977), pp. 8–33.
[8] M. S. CRAMER AND A. R. SEEBASS, *Focusing of weak shock waves at an arête*, Part 2, J. Fluid Mech., 88, (1978), pp. 209–222.
[9] N. J. YU AND A. R. SEEBASS, *Computational procedure for mixed equations with shock waves*, Comput. Methods in Nonlinear Mech., (1974), pp. 499–508.
[10] J.-C. WANNER, J. VALLEE, C. VIVIER AND C. THERY, *Theoretical and experimental studies of the focus of sonic boom*, J. Acoust. Soc. Amer., 52 (1972), pp. 13–32.
[11] E. P. CORNET, *Focusing of an N-wave by a spherical mirror*, University of Texas at Austin Report, ARL-TR-72-40, 1972.
[12] W. D. BEASLEY, J. D. BROOKS AND R. L. ROGERS, *A laboratory investigation of N-wave focusing*, NASA TN D-5306 (1969).
[13] C. THERY, *Atomospheric Refraction and Reflection in Sonic Booms*, AGARD CP No. 42 (1962), pp. 13-1 to 13–14.
[14] M. SANAI, T.-Y. TOONG AND A. D. PIERCE, *Ballistic range experiments on superbooms generated by refraction*, J. Acoust. Soc. Amer., 59 (1976), pp. 513–524.
[15] B. STURTEVANT AND V. A. KULKARNY, *The focusing of weak shock waves*, J. Fluid Mech., 73 (1976), pp. 651–671.
[16] A. R. SEEBASS, *Nonlinear acoustic behavior at a caustic*, NASA SP-255, (1971), pp. 87–120.
[17] P. M. GILL AND R. SEEBASS, *Nonlinear acoustic behavior at a caustic*, Progr. Astronautics and Aeronautics, 38 (1975), pp. 353–386.
[18] M. ABRAMOWITZ AND I. A. STEGUN, *Handbook of Mathematical Functions*, Dover, New York, 1968.
[19] K-Y. FUNG, *Shock wave formation at a caustic*, Ph.D. Thesis, Cornell University, Ithaca, NY, 1976.

AIAA 79-1557R

Shock-Free Wing Design

K.-Y. Fung, H. Sobieczky, R. Seebass

Reprinted from

AIAA Journal Volume 18, Number 10, October 1980, Page 1153

ERICAN INSTITUTE OF AERONAUTICS AND ASTRONAUTICS • 1290 AVENUE OF THE AMERICAS • NEW YORK, NEW YORK, N.Y. 10104

VOL. 18, NO. 10 AIAA JOURNAL OCTOBER 1980
ARTICLE NO. 79-1557R

Shock-Free Wing Design

K-Y. Fung,* H. Sobieczky,† and R. Seebass‡
University of Arizona, Tucson, Ariz.

A simple numerical method for generating wing shapes that will be shock free at a specified supercritical Mach number is described. The method involves using a fictitious gas law for the supersonic domain to make the governing equations elliptic. Requirements on this gas law are detailed and a method for computing the real flow in the supersonic domain, given initial data on the embedded sonic surface, is described. The failure of the method to yield a shock-free flow when a limit surface occurs in the supersonic flow, and the difficulties that arise because the initial-value problem for the supersonic domain is ill-posed, are delineated. Finally, a small perturbation algorithm is used to illustrate the procedure and results are given for a simple baseline wing.

Introduction

INCREASED fuel efficiency, and in the case of commercial aircraft, productivity, can be achieved by operating aircraft at supercritical Mach numbers, provided that shock waves can be avoided or made acceptably weak. Two-dimensional procedures for prescribing airfoil sections that are shock free have already provided improvements in aircraft efficiency by employing these airfoils on swept wings. Three-dimensional effects have compromised such designs to some extent, and extensive wind tunnel development tests have been required to recapture the benefits of these "supercritical airfoils."

Sobieczky et al.[1] demonstrated a method of modifying baseline configurations so that they would be shock free at a prescribed Mach number and lift coefficient. This procedure provides a special opportunity for improving aircraft performance through a careful selection of the baseline configuration in order to provide wings and wing-body combinations that are shock free at supercritical Mach numbers, and that have acceptable off-design performance. Yu[2] and Yu and Rubbert[3] have also documented that this procedure is possible and demonstrated its application.

As was first described by Sobieczky,[4] a numerical algorithm is used to solve a fictitious set of equations for the flow past the baseline configuration. These equations are identical to the correct equations for subsonic portions of the flow, but they are modified when the flow becomes supersonic, so that even though the flow speed is larger than the local speed of sound the equations themselves remain elliptic. This procedure generates a numerical solution that satisfies the appropriate equations where the flow is subsonic, and the appropriate boundary conditions on the configuration outside of the supersonic zone. The results of this calculation provide the flowfield at the sonic surface. This surface and flowfield define an ill-posed initial value problem for the supersonic domain that is to be solved using the correct equations. Because this problem is ill-posed in three dimensions any numerical method must, in principle, be unstable. This instability, however, is of no consequence for moderate to high aspect ratios. However, if the detailed definition of the spanwise modifications required to make the wing shock free are comparable to those for the streamwise direction, as they will be for low aspect ratios, then the instability may compromise the calculations.

Fictitious Equations

The flows we seek are to be shock free. As a consequence, they will be irrotational and the governing equation will be the conservation of mass, viz.,

$$\nabla\cdot(\rho\nabla\phi)=0 \tag{1}$$

where

$$\rho/\rho_* = \left\{1+\frac{\gamma-1}{2}\left[1-(\nabla\phi)^2/a_*^2\right]\right\}^{1/(\gamma-1)} \tag{2}$$

or

$$\nabla\phi\cdot\nabla\frac{(\nabla\phi)^2}{2}-a^2\nabla^2\phi=0 \tag{3}$$

where

$$a^2=a_*^2+\frac{\gamma-1}{2}\left[a_*^2-(\nabla\phi)^2\right] \tag{4}$$

Here $(\ )_*$ refers to the critical flow conditions where $q=a$. While the conservative formulation, Eq. (1), is to be preferred over its nonconservative analog, Eq. (3), numerical computations using Eq. (3) should be satisfactory provided that the flow being computed has no shock waves.

In order to generate smooth data on embedded sonic surfaces that are potentially consistent with shock-free flow, we elect to modify the gas laws (2) and (4) so that Eqs. (1) and (3) remain elliptic when $q\geq a_*$. Thus we require

$$\frac{\partial(\rho_f q)}{\rho_f\partial q}>0 \quad \text{if } q>a_* \tag{5a}$$

or

$$a_f>q \quad \text{if } q>a_* \tag{5b}$$

where ρ_f and a_f are a fictitious density and a fictitious sound speed and the partial derivative in Eq. (5a) is taken along a streamline. If we restrict ρ_f and a_f to be functions of q alone, then

$$\frac{\rho_f}{\rho_*}=\exp\left[-\int_{*}^{q}\frac{q\,\mathrm{d}q}{a_f^2(q)}\right]$$

The choice of the fictitious equation or gas law is a tool or technique available to produce a range of designs that are shock free; the initial data found with one gas law may lead to

---

Presented as Paper 79-1557 at the AIAA 12th Fluid and Plasma Dynamics Conference, Williamsburg, Va., July 23-25, 1979; submitted Aug. 13, 1979; revision received March 25, 1980.

Index categories: Aerodynamics; Transonic Flow; Configuration Design.

*Research Assistant Professor. Member AIAA.

†Adjunct Professor, also Research Scientist, DFVLR, Göttingen, West Germany. Member AIAA.

‡Professor. Associate Fellow AIAA.

a limit surface above the wing, while that with another gas law will not. The main consideration in choosing the fictitious equations is that the equation must imply a conservation law and that the conserved quantity must be identical to the mass flux at sonic flow conditions. This insures that the initial data for the supersonic domain is consistent with the conservation of mass in the subsonic flow.

Examples of fictitious gas laws which lead to an elliptic equation include:

$$\rho_f/\rho_* = (a_*/q)^P, \text{ or } a_f = P^{-1/2} q, \; P<1$$

$$\rho_f/\rho_* = \exp\{1/L[(a_*/q)^L - 1]/L\}, \text{ or } a_f = q(q/a_*)^{L/2}, L>0$$

$$\frac{\rho_f}{\rho_*} = \left[\frac{a_*^2}{q^2+\mu(q^2-a_*^2)}\right]^{\frac{1}{2(1+\mu)}}, \text{ or } a_f^2 = q^2+\mu(q^2-a_*^2), \quad \mu>0$$

These gas laws are all of the simple form $\rho=\rho(q)$. It may sometimes be of value to consider an equation that has an explicit spatial dependence in order to alter the shape of the sonic domain. If this is done, care must be taken to insure that a conservation law is implied. Thus we may use $\rho_f = \rho_f(x,y,z)$ and be sure a mass flux is conserved but not, in general, $a_f = a_f(x,y,z)$.

Supersonic Domain

Given a suitable numerical algorithm for solving Eqs. (1) or (3), with the fictitious density or sound speed used for supercritical speeds, we may then locate the embedded surface where $q=a$, and evaluate the velocity components there. Those may be the physical components, viz., u, v, w in the Cartesian coordinates x, y, z or the components U, V, W, in some mapped space X, Y, Z. Because the equations are hyperbolic we choose to work with a first-order system

$$(a^2-u^2)u_x + (a^2-v^2)v_y + (a^2-w^2)w_z - 2uww_x$$
$$-2uvv_x - 2vwv_z = 0 \qquad (6)$$

$$w_x - u_z = 0, \quad w_y - v_z = 0, \quad (u_y - v_x = 0) \qquad (7)$$

with one of the three irrotationality conditions being redundant.

We must then set up a suitable numerical algorithm for the computation of the supersonic flow, marching inward in some fashion toward higher Mach numbers until the stream surface upon which the supersonic surface rests can be continued. In the process two difficulties may arise. The first is that the computation may indicate that the solution has become multivalued because a limit surface intervenes between the sonic surface and the body; then no physically acceptable solution is possible with the initial data supplied. The second is that the inherent instability of the algorithm may become manifest, providing an unacceptable solution. We discuss this problem further shortly.

A nonsubstantive difficulty that may arise with an approach using rectangular coordinates is due to the topology of the supersonic domain. We can expect the supesonic region to wrap around, or more picturesquely, "grab," the wing leading edge, as shown in Fig. 1a. When this occurs, one of the derivatives in the two equations selected from Eqs. (7) may vanish, leading to a singular system of equations. This is most easily avoided by mapping the solution domain to a coordinate system in which this does not occur, as discussed in Ref. 5. The coordinate systems of the computational algorithms to be used may provide the essentials of the mapping. Thus the coordinate systems used in the computational algorithms of Jameson and Caughey[6] and Caughey and Jameson[7] provide natural coordinate systems for the computation of the supersonic domain. In the first of these the wing surface is mapped to the plane $Z'=0$, and we may envision the sonic surface to be as depicted in Fig. 1b.

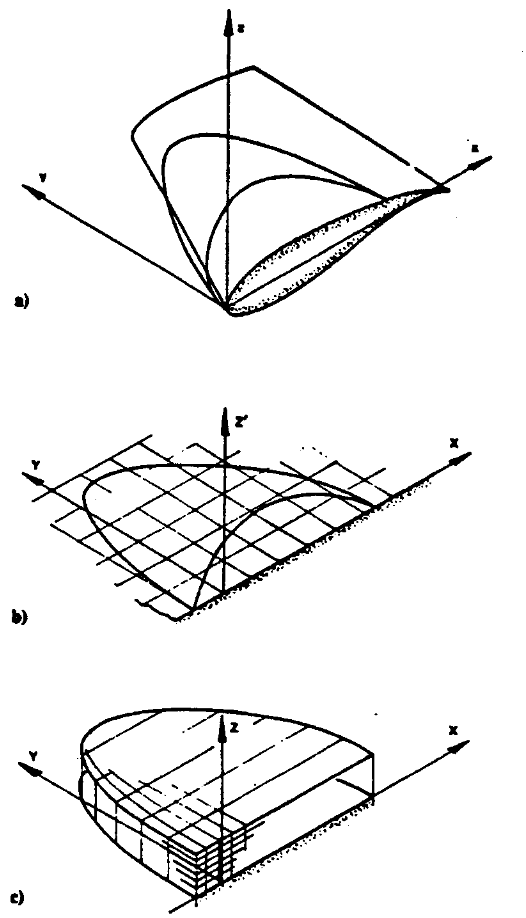

Fig. 1 Local supersonic region in the physical and computational domains.

A subsequent mapping

$$Z = Z'/Z_*'(X,Y)$$

where $Z_*'(X,Y)$ is the sonic surface, then leads to a computational domain like that sketched in Fig. 1c.

In this domain, with U, V and W the X, Y and Z components of the velocity derived from some appropriate potential, we have a system of equations of the form

$$AU_X + BU_Y + CU_Z = 0$$

which we use to advance the solution from one Z level k to the next:

$$U_k = U_{k-1} + [(C^{-1}A)_{k-1/2}(U_X)_{k-1/2}$$
$$+ (C^{-1}B)_{k-1/2}(U_Y)_{k-1/2}]\Delta Z$$

Here we use the subscript $k-1/2$ to indicate a suitably iterated average value of the subscripted quantity and ΔZ is the decrement in the Z coordinate. At each Z station the X and Y derivatives of U are calculated using three-dimensional cubic splines to specify U. Presumably the spline used should be one that avoids introducing, or perhaps even filters out, oscillations in the numerical results.

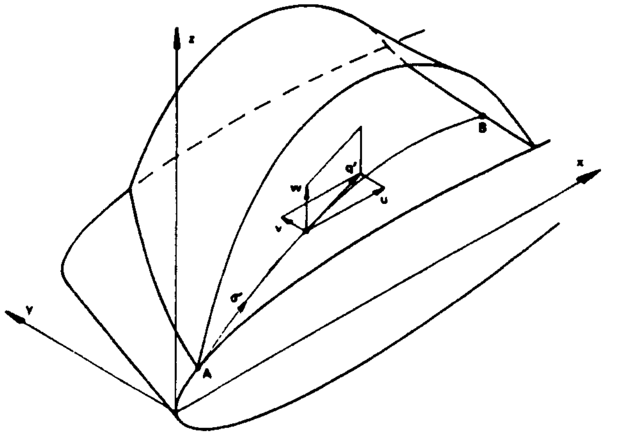

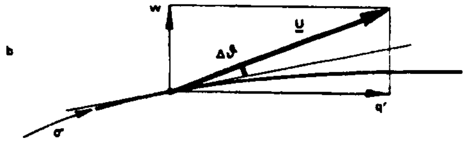

Fig. 2 Change in the flow inclination on the original wing surface that is used to define the new wing surface.

The calculation of U proceeds from one Z level to the next until the original wing surface, in this example $Z=0$, is reached. A new stream surface is then extrapolated from the values of U there, or the computation may be pushed further, to negative Z, and the new stream surface interpolated from the additional values so calculated. If we simply wish to extrapolate the new body surface we may do so in the original physical coordinates x, y, z, or in the mapped coordinates X, Y, Z.

In the original coordinates we may use the new velocity field on the original body (u_b, v_b, w_b) to define the slope in the stream direction,

$$\tan\theta_b = w_b/\sqrt{u_b^2+v_b^2} = w_b/q'$$

As sketched in Fig. 2, the local stream direction is then determined in order to integrate the angular difference $\Delta\theta(\sigma)$ along the arc length σ from A to B. The new body surface may be constructed by marching in the downstream (or upstream) direction and using a cubic spline in the spanwise coordinate to define the body at the computational nodes.

This procedure assumes small surface deviations so that the velocity field's initial surface is also that of the new surface. Extrapolation of the results on the initial surface, and an iterative correction of the new surface found, may be carried out if higher accuracy is required.

Limit Surfaces

Shock-free designs are not always possible for a given baseline configuration, Mach number, and lift coefficient. The initial data generated by given fictitious equations may imply a multivalued solution before the body stream surface intervenes. When this occurs a limit surface will be found in the flowfield. The first occurrence of a limit surface is along a line where U_Z, V_Z, $W_Z=\infty$; the algorithm used to compute the supersonic domain should be constructed so that it can recognize when this occurs, otherwise results may be obtained that have no meaning. Such a surface might look like that

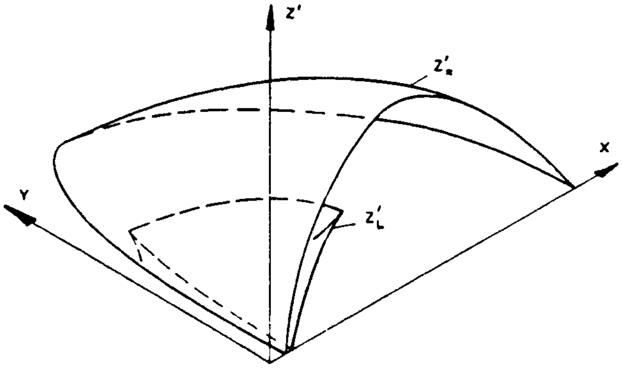

Fig. 3 Sonic surface with a limit surface embedded in the supersonic region.

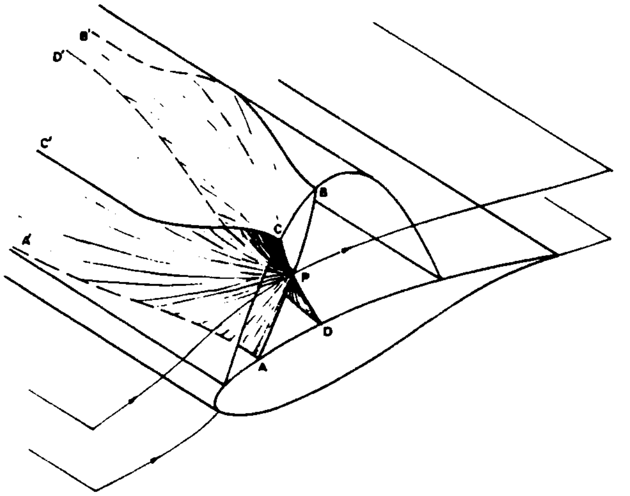

Fig. 4 Sketch of Mach conoids for a two-dimensional flow.

Initial Value Problem

As we mentioned earlier, the initial value problem for the supersonic domain is ill-posed in three dimensions. That is, small changes in the initial data will cause large changes in the solution in the domain of the problem. If we return to the well-posed two-dimensional problem and consider it to be a three-dimensional problem with no variations in the third direction, then we may sketch the Mach conoids, as shown in Fig. 4. The fore and aft Mach conoids define the influence and dependence domains of P. Because we find shock-free solutions the flow is reversible and we may consider the time-like direction to be in either the $\pm q$ direction. When we calculate the solution at P using data from the sonic surface we are effectively replacing the data along AA' by that along BB'. Alternatively, in two dimensions, the normal to the streamline may also be considered time-like and we calculate the solution at P using the data on CB. In three dimensions this alternative approach fails because the solution at P now depends upon the infinite domain $CC'B'B$.

An informative simple example is that of the linear wave equation

$$-\phi_{xx}+\phi_{yy}+\phi_{zz}=0$$

with data given on the $z=0$ plane as sketched in Fig. 5; viz.,

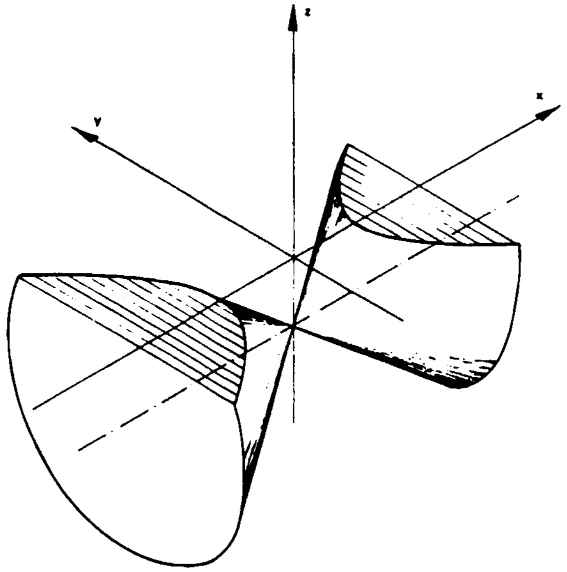

Fig. 5 Mach cones of the linear wave equation and their intersection with the plane where the initial values are given.

We can construct the solution by Fourier superposition of the modal solutions

$$\phi = \exp[i(k_1 x + k_2 y + k_3 z)]$$

in the x and y directions. But then

$$k_3 = \pm\sqrt{k_1^2 - k_2^2}$$

leads to exponential growth in the z direction when the wavenumber in the y direction, k_2, is larger than that in the x direction. In this simple model, then, we may expect the ill-posed nature of the problem to manifest itself when the y variation of the initial data is comparable to or larger than the x variation. Translating this to practical terms, we can expect the inherent instability to cause difficulty for small aspect ratio wings. Payne[10] has used energy arguments to show that exponential growth in the z direction must eventually occur for a large class of functions f and g. We demonstrate this instability in a subsequent section.

Small Disturbance Equations: An Illustration

We illustrate the procedure for computing the supersonic domain, as well as the difficulties that may arise, with the small disturbance equations. The small disturbance approximation introduces difficulties unique to this approximation; these we do not discuss. We first compute the elliptic flowfield using fictitious equations in supersonic regions to maintain elliptic behavior. While we use the Ballhaus-Bailey-Frick line relaxation algorithm as implemented by Mason et al.[8] for our computations, we use a simpler equation in this discussion, viz.,

$$-[\tfrac{1}{2}(K-\phi_x)^2]_x + [\phi_y]_y + [\phi_z]_z = 0 \qquad (8)$$

When $(K-\phi_x) < 0$ we make a change in the difference algorithm that corresponds to changing the first term to

$$[|\phi_x - K|^P/P]_x, \quad P \geq 1 \qquad (9)$$

The sonic surface on an Æ = 6 rectangular wing corresponding to $P = 2$ is shown in Fig. 6. Figure 7 shows the corresponding vertical velocity component of the redesigned airfoil for selected spanwise stations. We note that the more elliptic we make the fictitious gas (i.e., smaller P) the broader that the body will be thinner; this is reflected in the vertical velocity component. For the original parabolic arc section the body slope, and hence the vertical velocity, decrease linearly with x.

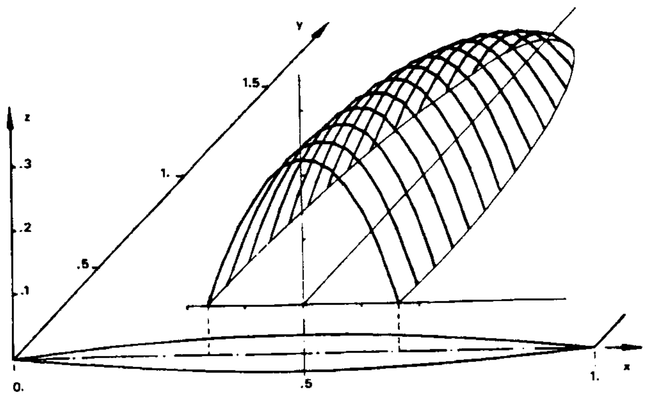

Fig. 6 Sonic surfaces for a rectangular wing with Æ = 6, $P = 2$, $M_\infty = 0.87$.

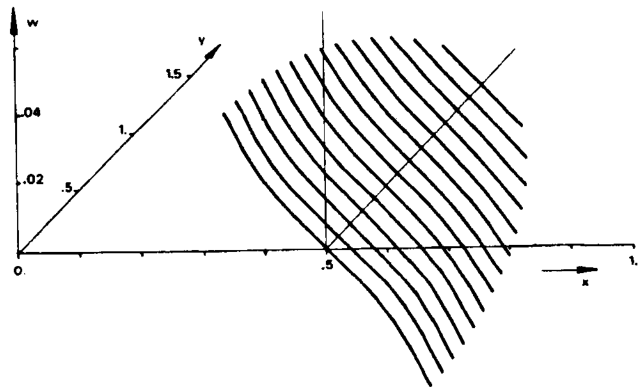

Fig. 7 New surface slopes for the rectangular wing with Æ = 6, $P = 2$, $M_\infty = 0.87$.

The numerical solution then provides values of ϕ, and hence its derivatives, on an embedded sonic surface, $z = z_*(x,y)$, as sketched in Fig. 6. The hyperbolic problem for the supersonic domain is solved using the simplified system of equations corresponding to Eq. (8).

$$-\tfrac{1}{2}[(K-u)^2]_x + v_y + w_z = 0, \quad w_x - u_z = 0,$$

$$w_y - v_z = 0, \quad (u_y - v_x = 0)$$

We may define a new variable $\xi(x,y)$ to replace the coordinate z, and facilitate the computations, e.g.,

$$\xi(x,y) = z/z_*(x,y)$$

In this variable the equations become

$$u_\xi = D^{-1} \begin{bmatrix} (K-u)\xi_x & 0 & 1+\xi_y^2 \\ (K-u)\xi_y & 0 & -(K-u)\xi_x\xi_y \\ -(K-u) & 0 & (K-u)\xi_x \end{bmatrix} \cdot u_x$$

$$+ \begin{bmatrix} 0 & \xi_x & -\xi_x\xi_y \\ 0 & \xi_y & 1+(K-u)\xi_x^2 \\ 0 & -1 & \xi \end{bmatrix} \cdot u_y \qquad (10)$$

where u has the components u, v, w and $D = 1 + \xi_y^2 + (K - u)\xi_x^2$. Our choice of the irrotationality conditions was dictated by the requirement that the determinant of the system D be nonsingular. Any other choice of equations gives $D' = \xi_y D$ and the system is singular when $\xi_y(x,y) = 0$, which always occurs. Limit surfaces occur only if D changes sign. For the system considered here this occurs when $(K-u)\xi_x^2 (<0)$ becomes larger in magnitude than $1 + \xi_y^2$. But D may also vanish because the coordinate system used for the set of equations chosen is not the appropriate one. This failure can be remedied by another choice for the coordinate system and must not be confused with that which occurs when a true limit line is present.

As discussed earlier, the initial value problem we solve is ill-posed. The implied numerical instability becomes more serious when the spanwise gradients are large. Indeed, as we can see from Eq. (10),

$$u_\xi = D^{-1}\{(K-u)\xi_x u_x + (1+\xi_y^2)w_x + \xi_x v_y - \xi_x \xi_y w_y\} \quad (11)$$

$$\qquad - \quad \pm\pm \qquad + \quad - \quad \pm\pm \quad \pm - \mp$$

Consider the sign of the individual terms on the right-hand side for an unswept rectangular wing with a profile symmetrical about the midchord and midspan lines. (The upper/lower sign corresponds to ahead of/behind the midchord line.) Then, because we are solving an elliptic boundary-value problem where the terms have the indicated signs, all of the terms in Eq. (11) except $\xi_x v_y$ give $u_\xi < 0$. The smaller the aspect ratio the larger the local values of $\xi_x v_y$. A similar conclusion holds for v, with a $\xi_y v_y$ term providing a change in v_ξ that increases v and v_y. With a spanwise instability present in the numerics we can anticipate that as it grows in amplitude v_y will grow and affect the magnitude, and eventually the sign, of u_ξ. Figure 8 depicts the surface values $u(x,y,0)$ computed for the supersonic region on rectangular wings of aspect ratios 3 and 2. For an aspect ratio 2 wing numerical instabilities obviously override the generally smooth nature of the flow. Inspection of the other velocity components strongly suggests that the instability has a wavelength four times that of the spanwise grid spacing and amplifies v more rapidly than u or w. The initial data for the two cases are similar, except for the larger y gradients when $AR = 2$.

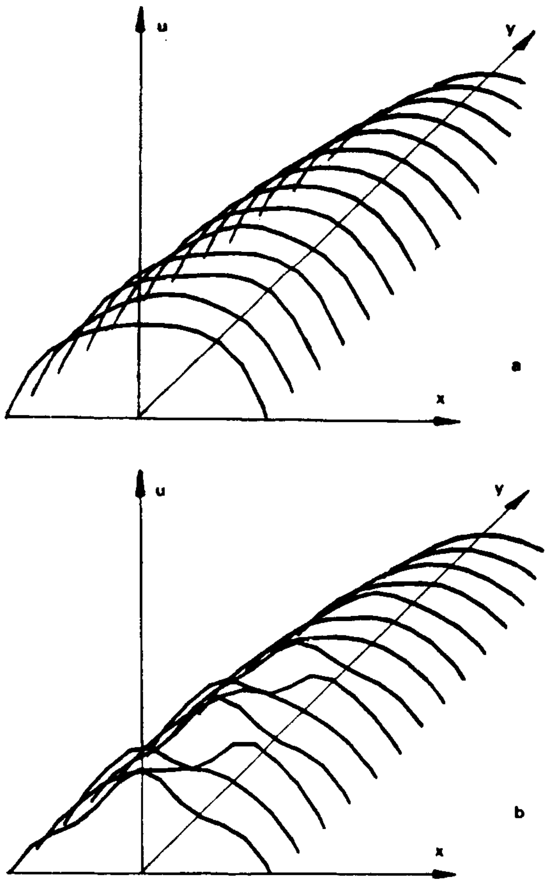

Fig. 8 Effect of numerical instability on the streamwise velocity component for: a) $AR = 3$, $M_\infty = 0.88$; b) $AR = 2$, $M_\infty = 0.89$. There is

Wing Design

The art of aircraft wing design involves many variables and requires knowledge and expertise beyond that of the authors. We believe, however, that by using fictitious equations with suitable baseline configurations various design goals can be met and the wings will be shock free at reasonable flight Mach numbers and lift coefficients. To aid the aircraft designer in understanding this technology we briefly describe the shock-free design process for a simple wing.

The approach outlined in the previous sections results in wings and airfoils with upper surface curvatures that are less than those of the baseline configurations. Additionally, the more acute the intersection of the sonic surface with the body surface, the less the likelihood of a limit surface intervening between the sonic line and the body. For this reason, baseline configurations should have reasonable upper surface curvatures and more thickness than required by the final designs. Designs that are close to the limit of what can be achieved, in terms of Mach number and lift coefficient, will have limit surfaces that nearly penetrate the wing surface. This may occur near the leading edge of the wing or near the aft end of the supersonic region, or in both locations simultaneously.

We will illustrate some of these points with a simple tutorial example. We take a well known airfoil, the 64A4xx, and use it for the wing sections. The planform is chosen to have straight

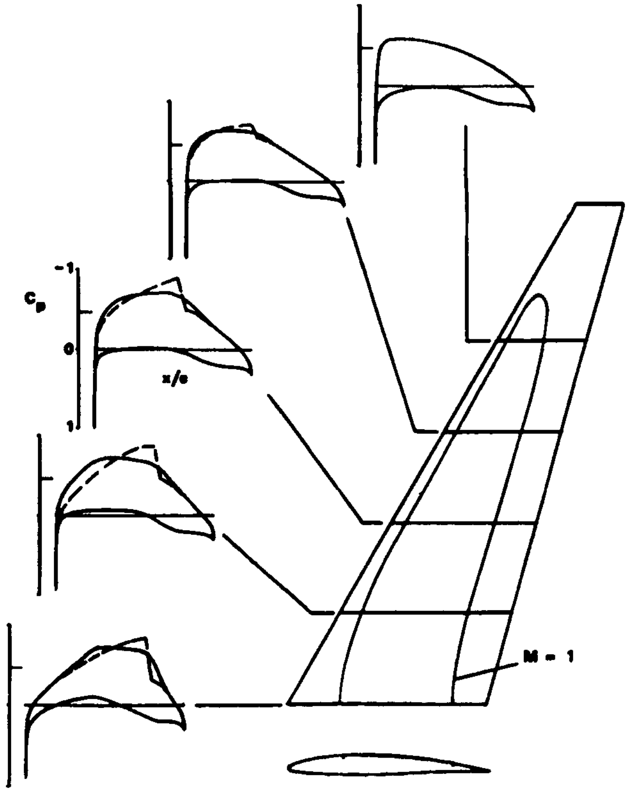

Fig. 9 Intersection of the sonic surface with the wing and pressure coefficients for: the wing designed to be shock free ——; the baseline

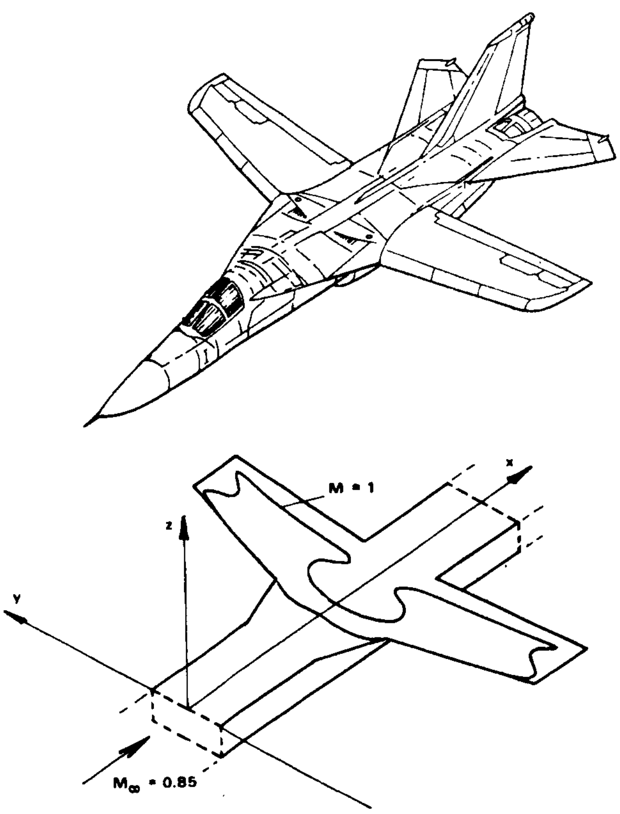

Fig. 10 Sonic surface on the supercritical wing of the AFTI 111 using fictitious equation in the supersonic region.

leading and trailing edges with sweep angles of 30 and 15 deg, respectively. We take the aspect ratio based on wing area to be 8, and the thickness distribution to be elliptical and 10% thick at the wing root. The twist is varied from 4 deg at the root section to 0 deg at midspan, and the angle of attack is 0.4 deg. With a freestream Mach number of 0.80 these conditions will lead [at least for the fictitious equations with $P=2$ in Eq. (9)] to sonic surface data for the system Eq. (10) that are consistent with shock-free flow; that is, no limit surface intervenes before the wing surface is found. Figure 9 shows the intersection of the sonic surface found with the wing, and the center sections of both the baseline configuration and the shock-free design. The design wing is 0.7% of the chord thinner than the baseline wing at the center section. Also shown is a comparison of the pressure coefficient at selected span stations. Both wings have a lift coefficient of 0.50. The small modifications to the baseline wing, over the portion of the upper surface wetted by supersonic flow in the solution of the fictitious equations, results in a wing, that when analyzed numerically, has the shock-free pressure distribution shown. The pressure coefficient on the baseline configuration is also shown for comparison. The inviscid drag evaluation for the original wing gave 96 counts; that for the design wing 86 counts, reflecting the changes in the pressure coefficient. Presumably a viscous calculation that correctly modeled the shock-wave boundary-layer interaction would reflect further improvements.

The selection of a baseline configuration is important to the success of this method. Wings that employ traditional supercritical airfoils will lead to sonic surface data that result in a limit surface. Figure 10 shows the intersection of the sonic surface with the wing for the AFTI 111 wing; again we have used the fictitious equations with $P=2$. The complex nature of this surface, and the occurrence of a limit surface when redesign is attempted, is due to the supercritical design of the AFTI 111 wing. Modifications to the baseline configuration, such as this one, are essential ingredients of any attempt at shock-free design. This is illustrated further in Ref. 9, where analytical functions are used to modify supercritical airfoils.

Conclusion

A procedure for designing wings that are shock free has been described in general terms and illustrated by using the small perturbation equations to modify a simple baseline configuration so that it is shock free. In using this procedure the designer must select the baseline configuration to be modified and the fictitious equations to be used. These determine the flowfield on the sonic surface of the ultimate design. A good choice will allow high Mach numbers and lift coefficients to be obtained. A poor choice will result in a limit surface in the supersonic domain at the design Mach number and lift coefficient. Instabilities in the numerical calculation of the supersonic flow that provides the wing design occur whenever the spanwise gradients are large. These can be suppressed by smoothing both the chordwise and spanwise data at each successive step of the calculation.

Acknowledgments

This research was carried out by the Computational Mechanics Laboratory of the Department of Aerospace and Mechanical Engineering under AFOSR Grant 76-2954G and ONR Grant N00014-76-C-0182.

References

[1] Sobieczky, H., Fung, K-Y., Yu, N. J., and Seebass, A. R., "A New Method for Designing Shock-Free Transonic Configuration," *AIAA Journal*, Vol. 17, July 1979, pp. 722-729.

[2] Yu, N. J., "An Efficient Transonic Shock-Free Wing Redesign Procedure Using a Fictitious Gas Method," *AIAA Journal*, Vol. 18, Feb. 1980, pp. 143-148.

[3] Yu, N. J. and Rubbert, P. E., "Transonic Wing Redesign Using a Generalized Fictitious Gas Method," Boeing Document D-180-25309-1, May 1979.

[4] Sobieczky, H., "Die Berechnung lokaler räumlicher Überschallfelder," ZAMM 58T, 1978.

[5] Sobieczky, H., "A Computational Algorithm for Embedded Supersonic Domains," University of Arizona Engineering Experiment Station Rept. TFD 78-03, 1978.

[6] Jameson, A. and Caughey, D. A., "Numerical Calculations of the Transonic Flow Past a Swept Wing," NASA CR-153297, 1977.

[7] Caughey, D. A. and Jameson, A., "Numerical Calculation of Transonic Potential Flow About Wing-Body Combinations," *AIAA Journal*, Vol. 17, Feb. 1979, pp. 175-181.

[8] Mason, W. H., Mackenzie, D., Stern, M., Ballhaus, W. F., and Frick, J., "An Automated Procedure for Computing the Three-Dimensional Transonic Flow Over Wing-Body Combinations, Including Viscous Effects," Vols. I and II, Air Force Flight Dynamics Laboratory, Wright-Patterson Air Force Base, AFFDL-TR-77, Ohio, 1978.

[9] Sobieczky, H., "Related Analytical Analog and Numerical Methods in Transonic Airfoil Design," AIAA Paper 79-1556, July 1979.

[10] Payne, L. E., private communication, Cornell University, Sept. 1978.

ADAPTIVE AIRFOILS AND WINGS FOR EFFICIENT TRANSONIC FLIGHT

H. SOBIECZKY
DFVLR
GOETTINGEN, FRG.

A.R. SEEBASS
UNIVERSITY OF ARIZONA
TUCSON, USA

PAPER PRESENTED AT THE
12. CONGRESS OF THE
INTERNATIONAL COUNCIL OF THE AERONAUTICAL SCIENCES (ICAS)
MUNICH, GERMANY, OCT. 12.-17., 1980

ADAPTIVE AIRFOILS AND WINGS FOR
EFFICIENT TRANSONIC FLIGHT

by

H. Sobieczky
DFVLR

and

A.R. Seebass
University of Arizona

SUMMARY

A simple design method for two- and three-dimensional shock-free configurations is used for systematic airfoil modification to maintain shock-free flow at varying operating conditions. A mechanical realization is proposed since only minor and local changes of the contour are required.

INTRODUCTION

High speed aircraft design has become one of the most challenging fields of the aeronautical sciences. With availability of large computers new tools for design and analysis of aircraft components became available within the last decade, which encouraged the introduction of new aerodynamic concepts to increase fuel efficiency which is proportional to the ratio of lift over drag, multiplied by the flight Mach number. Rapidly increasing fuel costs within the last years underlined the urgent call for techniques to improve efficiency of the next generation transport aircraft.

A possibility for increasing efficiency by drag reduction is to avoid the occurrence of shock waves which requires a complicated iterative process of aerodynamic shaping carried out using engineering experience, computational facilities and wind tunnels. The resulting wing shapes for the flight regime just below the speed of sound have become known as "supercritical wings", they are designed to be completely or nearly free of recompression shocks at certain operating conditions, while wings with conventional sections have strong shocks and, therefore, additional drag. Theoretically isolated within flow fields containing shocks if the operating conditions are slightly changed [1], such shock-free flows have been considered of not much practical value for some years, but pioneering experiments [2,3] also stimulated the development of computational methods to obtain practically interesting shock-free airfoil shapes [4,5].

These design methods are restricted to two-dimensional flow, they work in the hodograph plane and are, therefore, relatively complicated. A similar method [6] allowed an extension of the approach into physical space [7]. The ability to solve transonic design problems was then coupled to the development of reliable flow analysis algorithms by this approach. It led to efficient design methods which became known as "Elliptic Continuation" or "Fictitious Gas" methods. They form computational tools for the aerodynamic concept of adaptive aircraft geometry for adjusting contours to obtain optimal efficiency even at variable operating conditions.

DESIGN PROCEDURE FOR SHOCK-FREE FLOWS

The purpose of this paper is to illustrate some recent results obtained with a systematic computational procedure for supercritical airfoils and wings which are shock-free at prescribed operating conditions. Since the design method may be developed by extension of any reliable analysis algorithm, we give a short description of the concept with a physical interpretation in order to allow for an implementation of the idea into new and more sophisticated analysis methods becoming operational now and in future.

A local supersonic domain embedded into a subsonic flow field is enclosed in general by a surface consisting of the sonic isotach and a recompression shock. If the flow is shock-free the sonic surface forms a smooth convex bubble situated on the body surface. In this latter case the structure of the flow is qualitatively similar to a subsonic flow: isotachs of velocity higher than velocity at infinity form also bubbles with smooth transition of the flow properties. This relationship of subsonic and shock-free transonic flows gave rise to the following idea to calculate examples of shock-free flow (see Fig. 1):

In a first step we solve a partly fictitious problem by altering the governing isentropic density - velocity, $\rho_{is}(q)$ relation in the domain of supersonic velocities. An artificial compressibility relation $\rho_f(q) > a^*/q$ where $q > a^*$ (a^* the speed of sound) defines a fictitious supersonic flow with subsonic flow quality. The basic differential equation of the complete flow is now of elliptic type, locally describing physically realistic subsonic flows and fictitious supersonic flow. Such a flow will have no recompression shock, the sonic line will qualitatively resemble one of a physically realistic shock-free transonic flow. Examples of such flows may be obtained with use of numerical elliptic solver routines, we observe that only the local supersonic domain is physically not real, the surrounding flow field is a locally correct solution. We ask now for a possibility to use the subsonic part to construct a complete real shock-free flow.

The second step of the procedure consists of an integration of the real supersonic differential equations, with restored density $\rho_{is}(q)$. Initial conditions of this hyperbolic type problem are prescribed along the given sonic surface with velocity directions resulting from the previous solution of the fictitious problem. This ensures a smooth connection between the two physically real parts of the solution. Numerical marching procedures based on the method of characteristics allow an integration of the potential equation, starting at the sonic surface and proceeding toward the body surface. The latter was part of the first step elliptic boundary value problem but the resulting body stream surface from the hyperbolic initial value problem (initial values at the sonic surface) will be different from the given body where wetted by supersonic flow. The body will be flattened providing more space for the real flow than for the fictitious flow to pass because of $\rho_{is} < \rho_f$.

The analytical background[7,8] as well as the numerical aspects[9,10] of this method are described elsewhere, this paper is intended to present some illustrative results in the light of an application to advanced technology computational aircraft design tools.

SELECTION OF ANALYSIS ALGORITHMS, FICTITIOUS GAS MODELS AND BASELINE CONFIGURATIONS

Our design procedure requires in its first step a reliable analysis algorithm for elliptic partial differential equations to solve the subsonic part of the flow and provide flow properties along the sonic surface. Many computational codes are operational for inviscid flow past airfoils. We prefer solvers for the basic equations in conservation form. A finite difference relaxation code was extended to be a design tool[11]. A boundary layer method and - for the analysis version - a method to treat shock - boundary layer interaction was added[12]. Another computer code[13] based on the same analysis algorithm treats viscous interaction between boundary layer and wake[14]. Results obtained with these computer programs will be illustrated in the following.

Wing design codes based on the outlined method have been developed, too, but an implementation of 3D viscous effects still needs to be done. Both non-conservative finite difference and fully conservative finite volume codes have been extended to be shock-free wing design programs[15,16]. With rapid progress in numerical methods more efficient codes will become operational, examples given her are intended to stimulate the engineer to introduce the idea into new computer programs for transonic flow problems.

Given an analysis algorithm for transonic flow we have to introduce the design option by providing an alternate formula for the isentropic flow density

$$\varrho_{is}/\varrho^* = ((\gamma + 1)/2 - (\gamma - 1)/2 \cdot (q/a^*)^2)^{1/(\gamma - 1)}$$

ensuring elliptic partial differential equations. The formula

$$\rho_f/\rho^* = c^p \cdot (q/a^* + c - 1)^{-p}$$

allows a 2-parametric variation of fictitious gas properties and elliptic equations if $p < 1$, $c \geqslant p$. A continuous slope at sonic conditions $q = a^*$, where ρ_{is} is switched to ρ_f, is obtained if $c = p$, but useful results with smooth body surface modifications may also be obtained for $c \neq p$. The value $c = 1$ gives

$$\rho_f/\rho^* = (q/a^*)^{-p} ,$$

results of this gas model have been studied extensively. Gas properties are defined by p and a result is illustrated in Fig. 2 for different values of p to demonstrate the influence of this parameter on the resulting new surface shape. A conventional NACA 0012 airfoil is flattened by the design procedure, we observe that a long flat sonic bubble on the airfoil is obtained by low values of p, here $p = 0$, which describes an incompressible fictitious gas. Surface changes between 2 and 47 percent chord are required, the maximum deviation of the new contour is 0.0054 percent chord.

For higher values of p the surface deformations are smaller and more local, but surface curvature changes become substantial if $p \longrightarrow 1$. This example illustrates the fact that shock-free modification of a given (initial-) configuration for prescribed lift coefficient and flight Mach number does not result in a unique new shape. A variety of shape changes within certain limits is possible and the criterion of choice of the fictitious gas model is the desired resulting pressure distribution on the airfoil. All types between "peaky" and "roof-top" c_p - distributions are possible and selection is at the designer's disposal. Off-design properties of an airfoil or wing are dominated by the occurrence of shock-waves and complicated by viscous interaction, but the design pressure distribution is crucial for prediction of these effects. This leads us to the selection of baseline configurations. Extensive experimental work was performed to arrive at the widely used and well documented NACA airfoils. One of the first results of this method was a series of shock-free modifications of a NACA 64A410 airfoil. The results are illustrated in Fig. 3, in a Mach-c_L-diagram. We see the amount of thickness reduction and the limits for shock-free redesign of this airfoil and chosen gas parameter (p = 0).

A thickness reduction usually tends to shift the occurrence of shock-waves and drag rise toward higher Mach numbers. So a shock-free modification requiring thickness reduction seems not very surprising. A shock-free modification without reduction of the maximum thickness seems important for practical design requirements. Fig. 4 illustrates another result, the verification of a known shock-free inviscid flow (KORN airfoil 75-06-12) with our method. A local surface thickness bump had to be added to the upper surface, a careful variation of its shape and the gas parameter p finally resulted in equal thickness addition and subsequent design thickness reduction so that the original KORN airfoil and its pressure distribution was verified.

These inviscid test results illustrated above lead us to the conclusion that we have computational tools to

- modify conventional configurations to be shock-free at transonic operating conditions,
- specify the type of shock-free flow by a selection of fictitious gas model and initial configuration geometry changes,

- obtain a whole series of neighboring shock-free flow solutions for variable operating conditions.

It is this third capacity of the method we will investigate in the following.

SHOCK-FREE AIRFOIL SERIES:
CONCEPT OF ADAPTIVE CONFIGURATION

Aerodynamic efficiency of a wing is defined by the ratio of lift over drag, multiplied by the flight Mach number. With drag rising sharply if the Mach number approaches unity, efficiency drops and it is therefore a principal goal of high subsonic speed aircraft design to delay drag-rise to higher Mach numbers for prescribed lift. This is usually achieved by delaying the occurrence of shock waves to higher Mach numbers through a careful variation of wing shapes, many analysis computations and very costly wind tunnel experiments.

Our design method seems to be a useful tool to obtain better airfoils and wings for transonic flight. Moreover, the computational definition of surface modifications for varying free stream conditions gives an idea about possible mechanical adjustments of the configuration in order to maintain efficient operation even at different flight conditions.

We choose a design example for illustration of the required surface modifications at varying flight Mach number at constant lift coefficient, Fig. 5. A given airfoil A is designed to be shock-free at Mach = 0.73, c_L = 0.55. We ask for its performance at Mach = 0.75 and c_L = 0.6. Analysis including viscous interaction gives a result with a recompression shock. A bump, added to the upper surface gave an initial configuration 0.3 percent thicker than airfoil A, original thickness was obtained from the subsequent design computation. The new airfoil B is investigated by the analysis version of the code to confirm the design result. Fig. 6 shows off design analysis results, we see that an increase of 0.01 of the drag rise Mach number has been achieved.

Geometry modifications which led from airfoil A to B are depicted in Fig. 7. Addition of a bump (a) which extends from 0 to 85 percent chord and subtraction of a design bump (b) within the supersonic region from 2 to 68 percent chord leaves two small bumps to be added to the original airfoil. These bumps are only 0.0021 and 0.0013 percent chord high. At this point we might think about a technical realization of such a bump addition in order to have both airfoils available for operation. Experiments with a possible use of elastic or pneumatic devices should be carried out. Another concept is a controlled distribution of suction and blowing as already investigated for laminar flow control and similar efforts to influence flow quality. Boundary layer displacement of the flow past airfoil B at design conditions is drawn in Fig. 7 (curve c) for comparison with the required surface modifications.

Another example to investigate sensivity of the calculated shock-free design is shown in Fig. 8. NACA 0012 airfoil was modified to be shock-free using incompressible fictitious gas ($p = 0$). We are interested now in an approximate representation of the calculated surface modifications by a smooth analytical curve. For simplicity we choose a spline function with few supports which is the mathematical model of an elastic beam deformed by single loads. Analysis results are compared with design pressure distribution and to our pleasant surprise we find that this airfoil with an elastic section is practically shock-free, too, even though the pressure distribution and sonic line are different from the original design. The reason for this is obviously related to the multiplicity of possible shock-free designs with different fictitious gas parameters, Fig. 2.

Having proved that desirable flow quality could be achieved by shape changes generated by mechanical devices we go one step further and propose [17] a system for automatically controlling the flow quality, Fig. 9. In the system shown, a flow qualitiy sensor F determines the operating conditions and surface pressure at selected stations and is interrogated by a microcomputer M that determines the proper changes of the effective contour necessary for shock-wave reduction. Our experience with the presented design method enables us to set up the programming of the microcomputer which energizes a servo system S which appropriately alters the effective shape. This is accomplished by servo motors for mechanically adjusting sections of the wing surface, and other mechanical devices on the structure for the opening or closing of apertures on the wing surface to bleed (or add) various amounts of air from (to) the upper surface of the wing. Any combination of the above may also be used. As seen from the illustrated examples, the surface area that needs to be changed is limited and the amount of change required is small.

ADAPTIVE SUPERCRITICAL WINGS

We have outlined a concept of transonic design and illustrated some cases of airfoil flow. At this stage experiments need to be performed to prove both new design results and some realization of adaptive airfoil technology in the wind tunnel.

Parallel to experimental verification an implementation of the idea into new and reliable 3D wing and wing-body configuration analysis codes is necessary. Our experience with wing design is limited to date, also because of a lack of 3D boundary layer and viscous interaction methods. Design studies of inviscid shock-free wings are presently carried out to refine the 3D marching procedure and determine the structure of 3D local supersonic shock-free flow fields. Fig. 10 shows a result obtained by extension of a finite difference analysis code[16] to a design tool. A simple wing based on NACA 64A410 section is modified to be shock-free.

Viscous effects may be accounted for by adding estimated displacement thickness to the initial configuration. Results of a finite volume analysis code[18] design extension for a shock-free supercritical wing with added displacement thickness is shown in Fig. 11. Extent of the supersonic domain on this "flying wing" without body defines the area of possible adaptive surface changes. A thick span loader flying wing seems to be a suitable test bed for experiments with 3D adaptive devices.

CONCLUSION

We have applied the elliptic continuation shock-free flow design method to some illustrative test examples to form a theoretical base for the concept of adaptive wing geometry at variable operating conditions. A system for automatic shape variations of wings based on experience with systematic computational design is proposed. Both special designs and the adaptive shape control system need to be tested experimentally, possibly in combination with new aerodynamic concepts for higher efficiency of transonic aircraft like variable geometry and boundary layer control investigations.

REFERENCES

1 Morawetz, C.S.,"On the Non-Existence of Continuous Transonic Flows Past Profiles, I, II and III", Communications on Pure and Applied Mathematics, (1956, 1957 and 1958), p. 45-68, 107-131 and 139-144.

2 Whitcomb, R.T., "Review of NASA Supercritical Airfoils", Ninth International Congress on Aeronautical Sciences, Haifa, Israel, (1974).

3 Pearcy, H.H., "The Aerodynamic Design of Section Shapes for Swept Wings," Advances in Aeronautical Sciences, Vol. 3, Pergamon Press, (1962), p. 277-322.

4 Garabedian, P.R. and Korn, D.G., "Numerical Design of Transonic Airfoils," Numerical Solution to Partial Differential Equations, Vol. II, Academic Press, New York, (1978), p. 253-271.

5 Boerstoel, J.W., "Design and Analysis of a Hodograph Method for the Calculation of Supercritical Shockfree Airfoils," NLR Rept. TR 77046U, Amsterdam, The Netherlands, (1977).

6 Sobieczky, H., "Entwurf überkritischer Profile mit Hilfe der rheoelektrischen Analogie," DFVLR Rept. DLR-FB 75-43, Göttingen, West Germany, (1975).

7 Sobieczky, H., "Die Berechnung lokaler räumlicher Überschallfelder", ZAMM, 58T, (1978), p. 215-216.

8 Sobieczky, H., "Rheograph Transformation and Continuation Methods," Von Karman Institute for Fluid Dynamics, Lecture Series 1980 - 4, "Mathematical Methods in Fluid Mechanics", (1980).

9 Sobieczky, H., N.J. Yu, K.-Y. Fung, A.R. Seebass, "New Method for Designing Shock-free Transonic Configurations", AIAA Journal, Vol. 17 No. 7 (1979).

10 Fung, K.-Y., H. Sobieczky, A.R. Seebass, "Numercial Aspects of the Design of Shock-free Wings and Wing-Body Combinations." AIAA paper 79-1557 (1979).

11 Jameson, A., "Iterative solution of transonic flows over airfoils and wings, including flows at Mach 1." Comm. Pure Appl. Math. 27 (1974).

12 Nandanan, M., E. Stanewsky, G.R. Inger, "A computational procedure for transonic airfoil flow including a special solution for shock-boundary layer interaction", AIAA paper 80-1389 (1980).

13 Melnik, R.E., Chow, R. and Mead, H.R., "Theory of Viscous Transonic Flow Over Airfoils at High Reynolds Number", AIAA paper 77-680 (1977).

14 Nebeck, H.E., A.R. Seebass, H. Sobieczky, "Inviscid-viscous interactions in the nearly-direct design of shock-free supercritical airfoils", AGARD FDP Symposium on computation of viscous/inviscid interaction (1980).

15 Yu, N.J., "Efficient Transonic Shock-Free Wing Redesign Procedure, Using a Fictitious Gas Method." AIAA Journal, Vol. 18 No. 2 (1980), p. 143-148.

16 Jameson, A. and Caughey, D.A., "Numerical Calculation of the Transonic Flow Past a Swept Wing", New York University ERDA Report COO-3077-140, (1977).

17 Sobieczky, H., A.R. Seebass, "Shock-Free Supercritical Aerodynamic Structure and Method for Designing Same", Invention Disclosure, University of Arizona, Tucson AZ., EES Report TFD 79-02, (1979).

18 Eberle, A., "Eine Methode der finiten Volumen zur Berechnung der transsonischen Potentialströmung um Flügel aus dem Druckmiminumintegral", MBB Report UFE 1407(Ö), (1978).

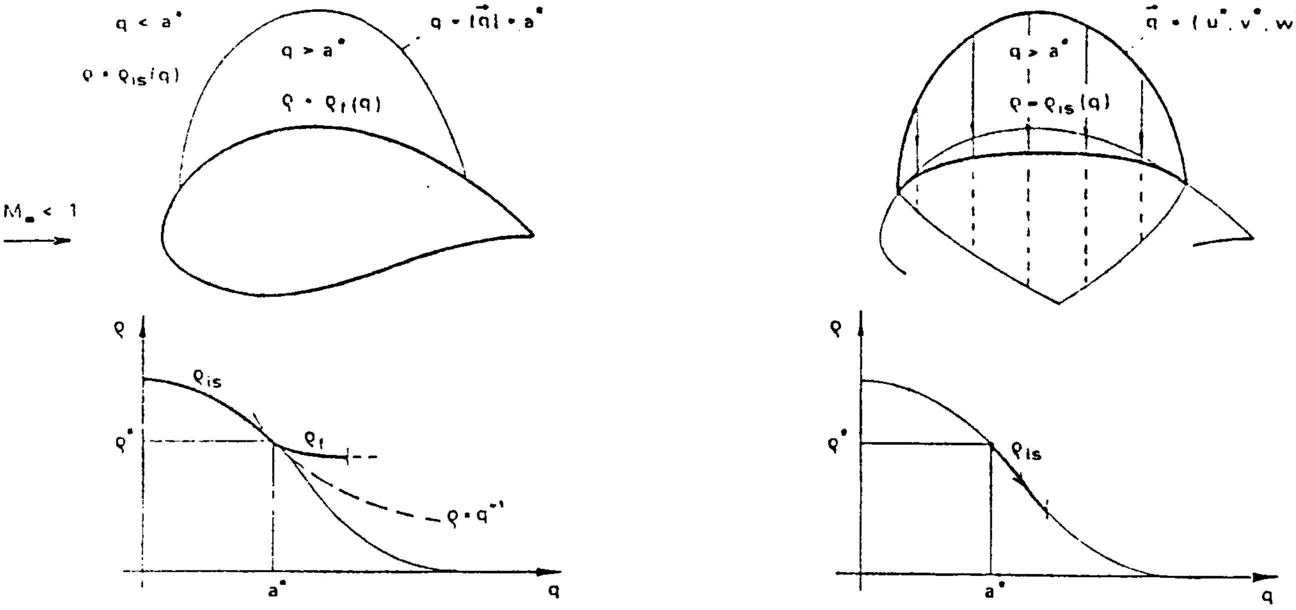

FICTITIOUS COMPRESSIBILITY $\rho_f(q > a^*)$.
ELLIPTIC EQUATIONS FOR $\rho_f > q^{-1}$.
BOUNDARY VALUES, ELLIPTIC SOLVER.

ISENTROPIC COMPRESSIBILITY $\rho_{is}(q > a^*)$.
HYPERBOLIC EQUATIONS FOR $q > a^*$.
INITIAL VALUES, MARCHING PROCEDURE.

Fig. 1 Elliptic continuation shock-free design.
a) First step: Fictitious gas flow analysis
b) Second step: Supersonic domain integration

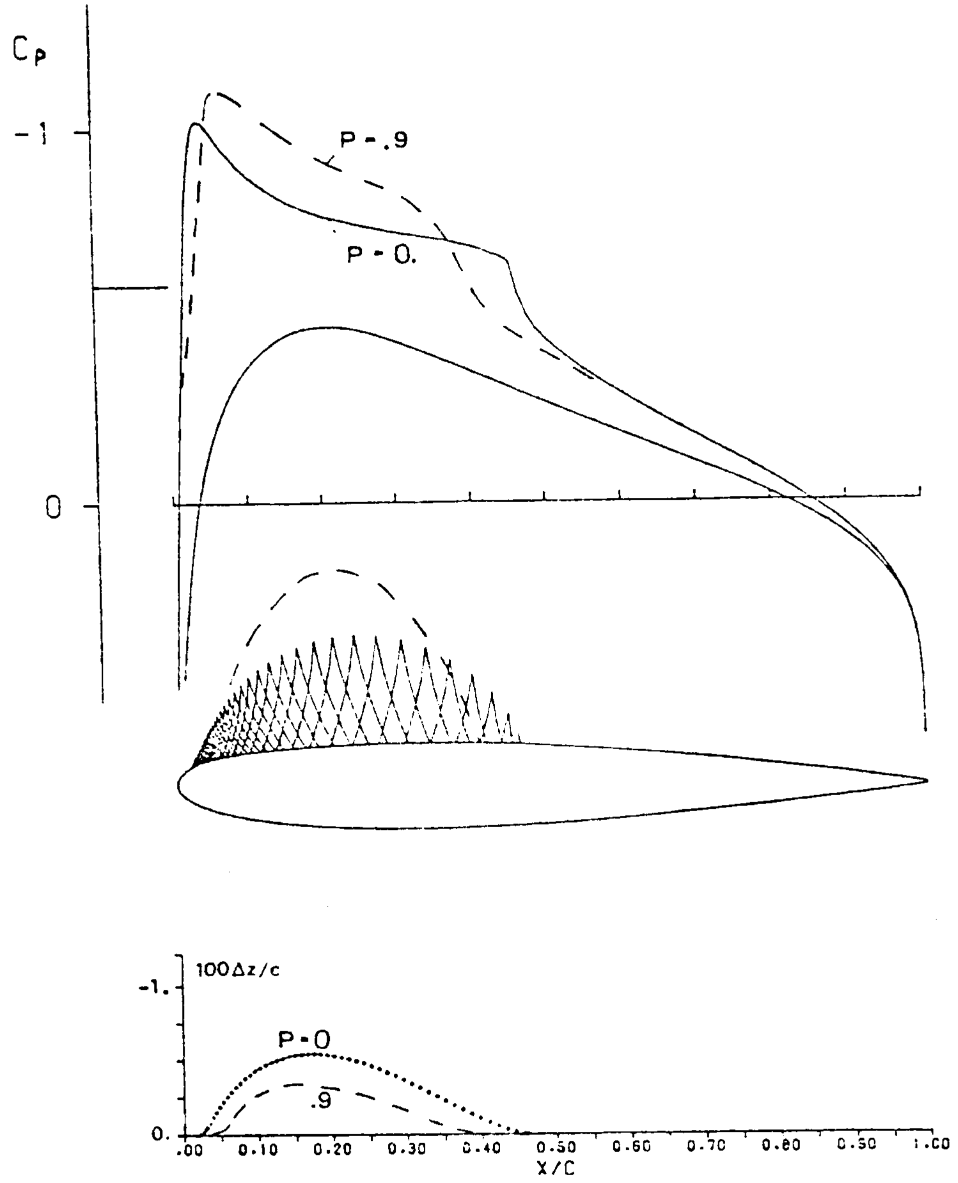

Fig. 2 Surface modifications and structure of local supersonic flow field for different fictitious gas parameters

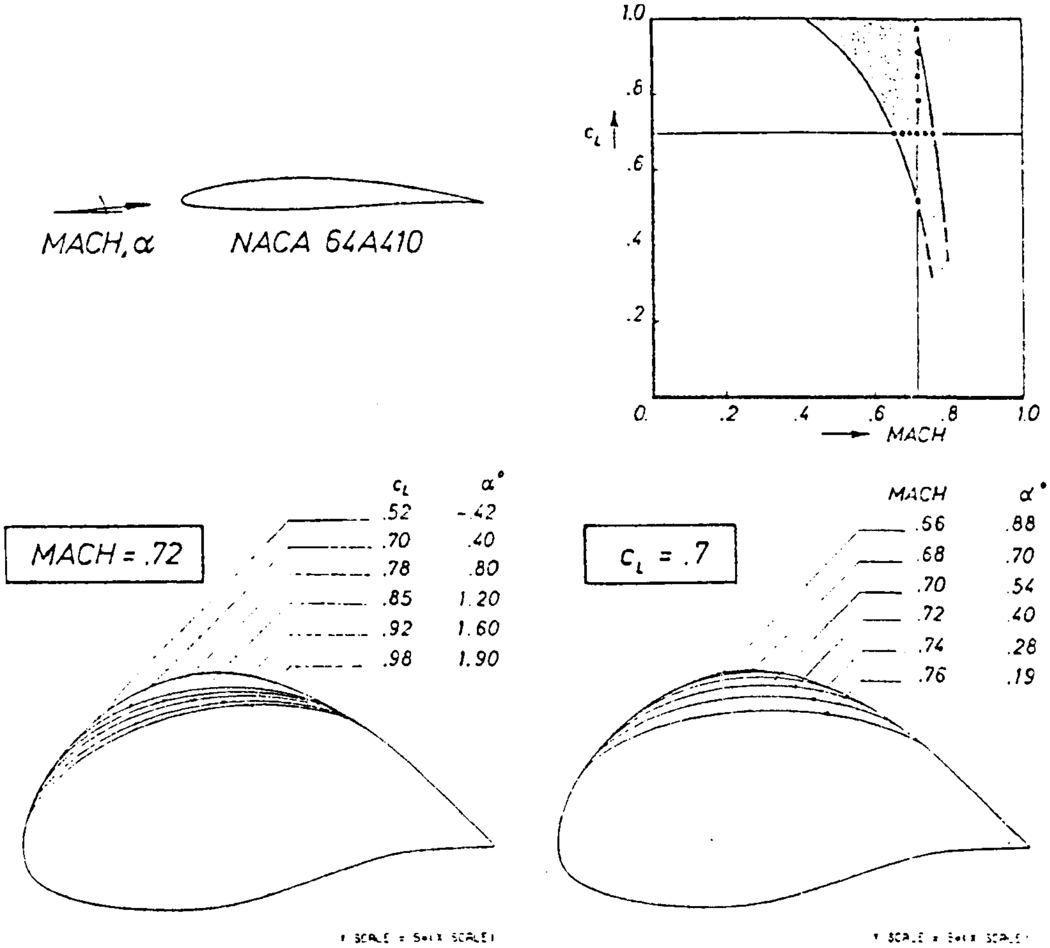

Fig. 3 Inviscid design example: Shock-free flow modifications of NACA 64A410 airfoil.

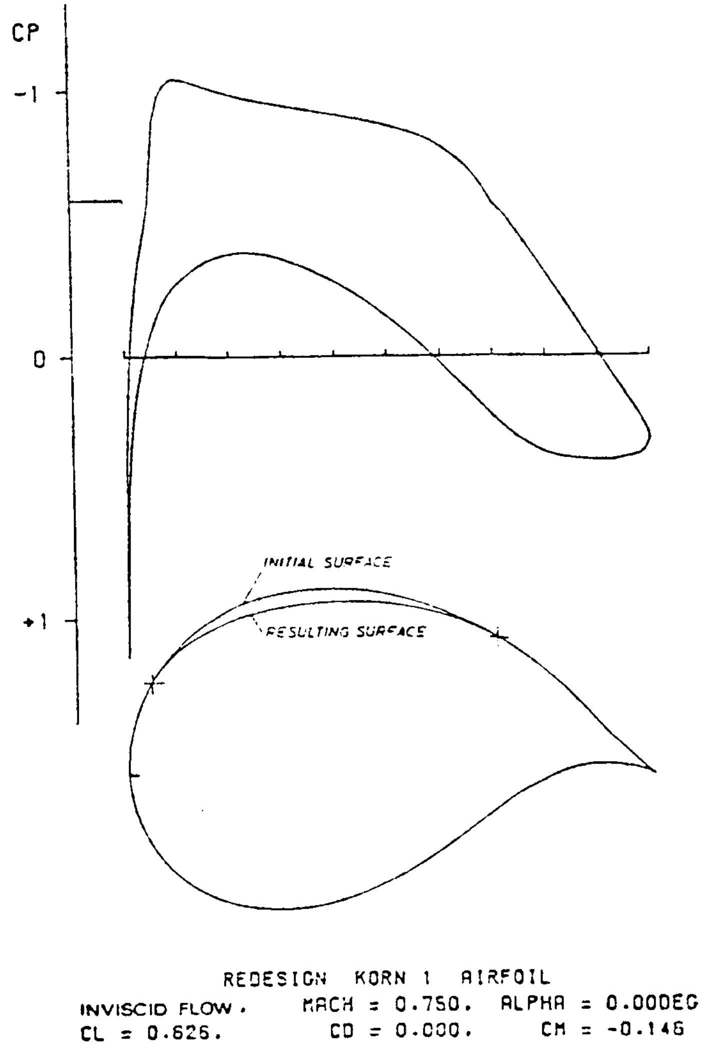

Fig. 4 Design verification of an inviscid shock-free flow: Korn 1 (75-06-12) airfoil.

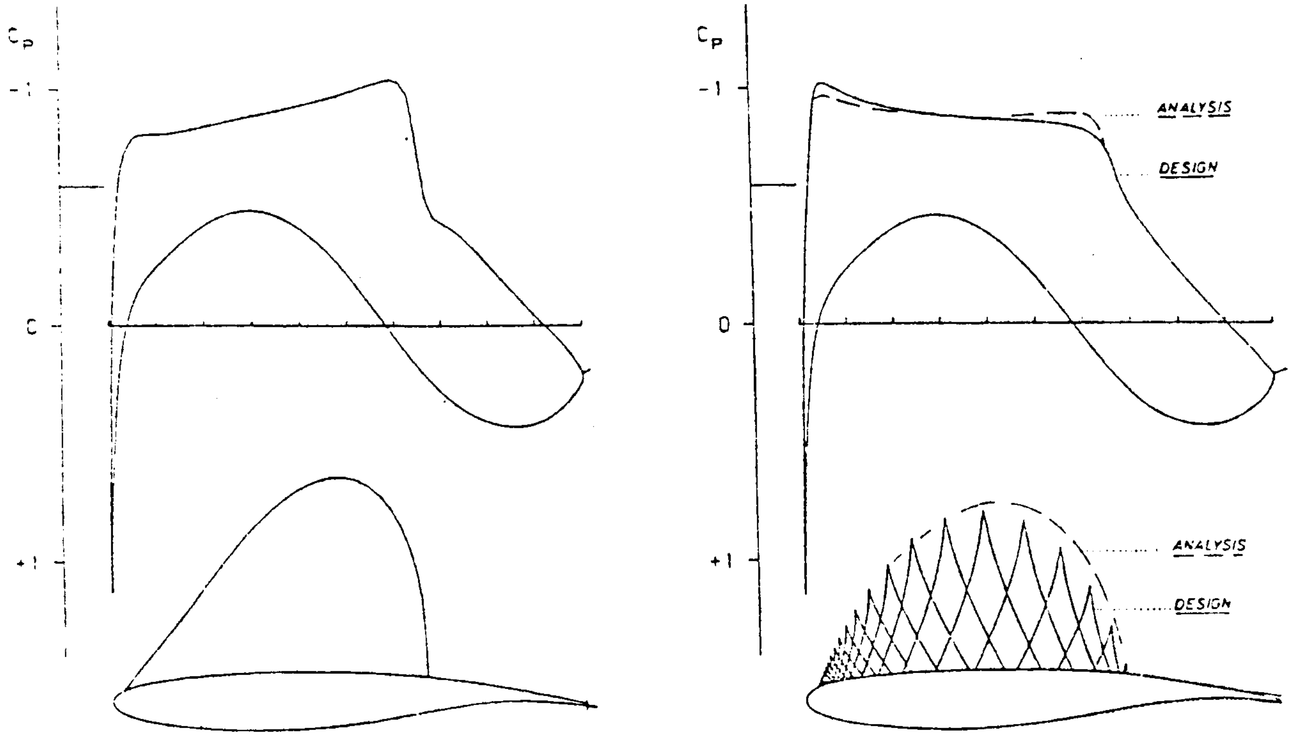

FCR ANALYSIS AIRFOIL A $t/c = .13$
$Re = 40$ MILL. MACH = .75 $\alpha = .198°$
$c_L = .6$ $c_D = .0086$ $c_M = -.1540$

FCR DESIGN + ANALYSIS AIRFOIL B $t/c = .13$
$Re = 40$ MILL. MACH = .75 $\alpha = .234°$
$c_L = .6$ $c_D = .0074$ $c_M = -.1478$

Fig. 5 Shock-free redesign with constant thickness for prescribed Mach number and lift coefficient, including viscous effects.

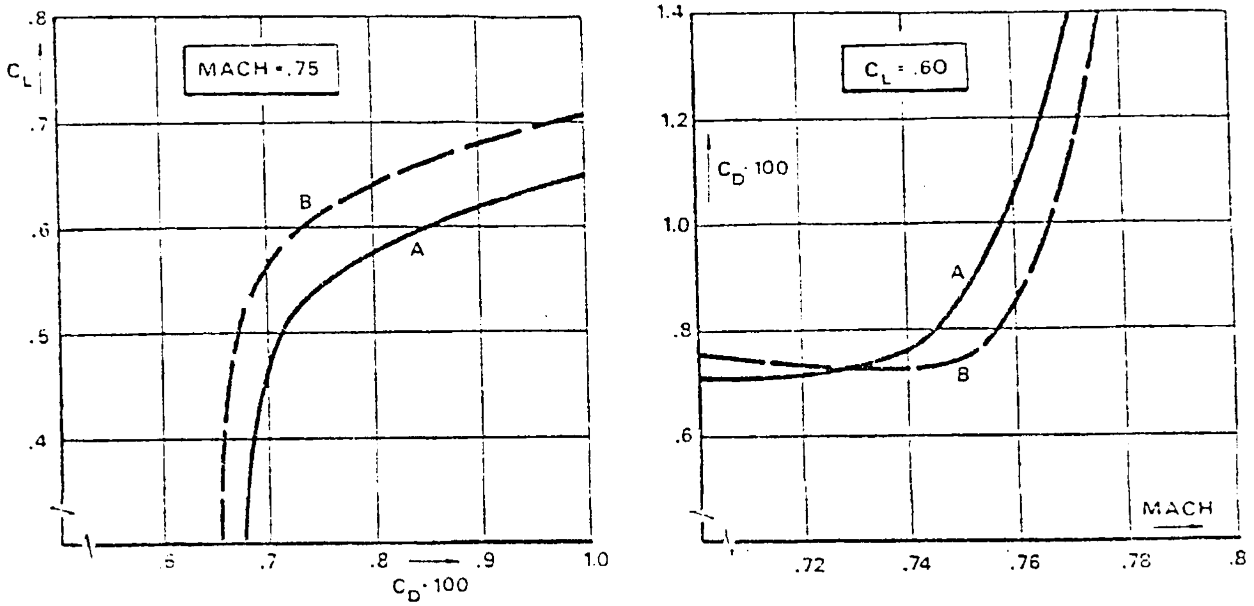

Fig. 6 Comparison of original and redesigned airfoil: lift, drag, Mach number.

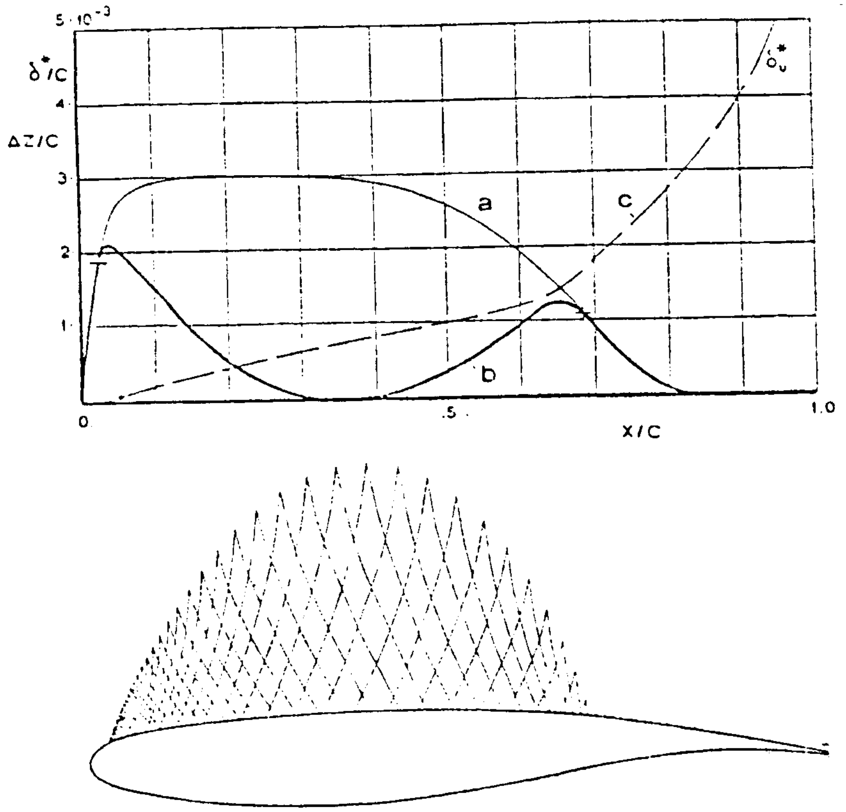

Fig. 7 Surface modifications:
(a) addition for fictitious gas analysis
(b) resulting addition after redesign;
(c) for comparison: upper surface boundary layer displacement thickness.

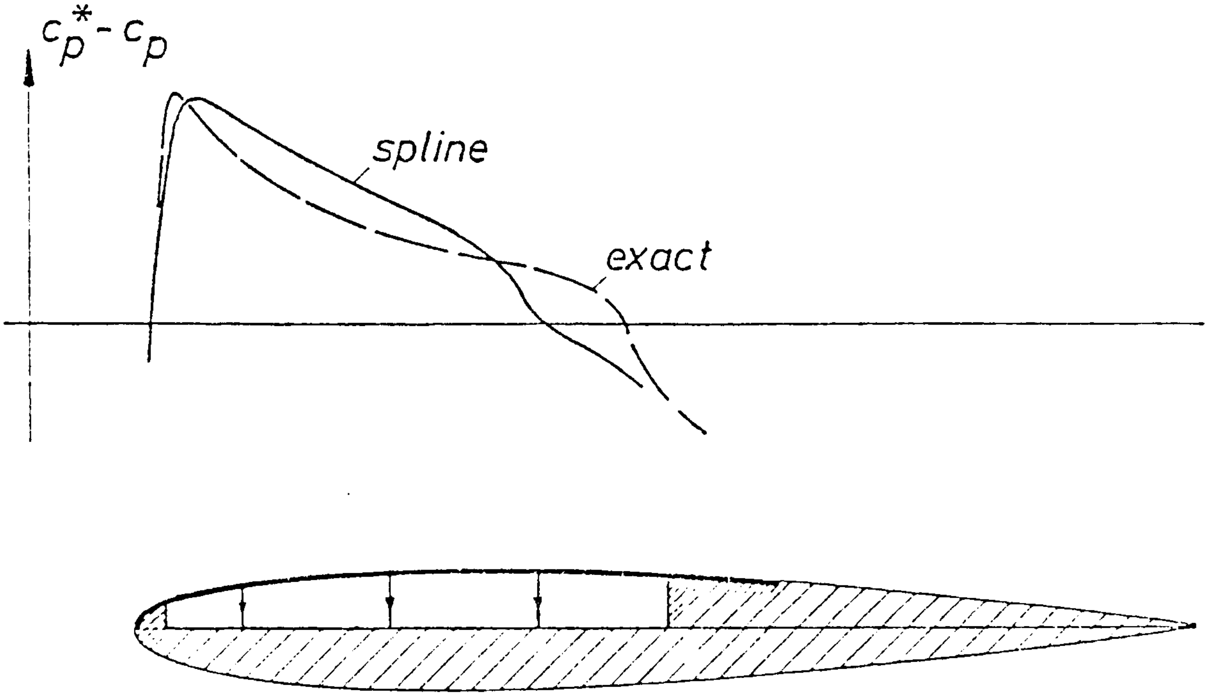

Fig. 8 Shock-free modification of NACA 0012 airfoil, elastic section approximation.

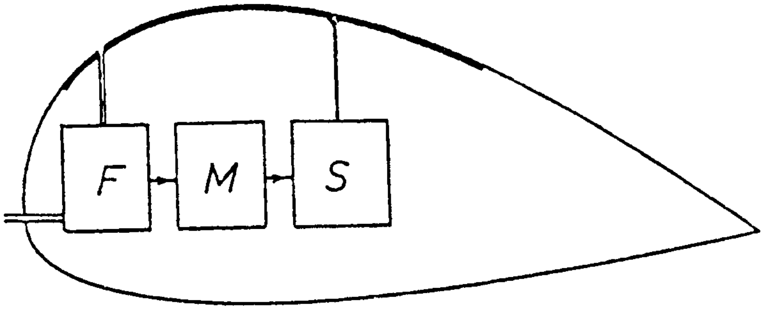

Fig. 9 Adaptive shape control system.

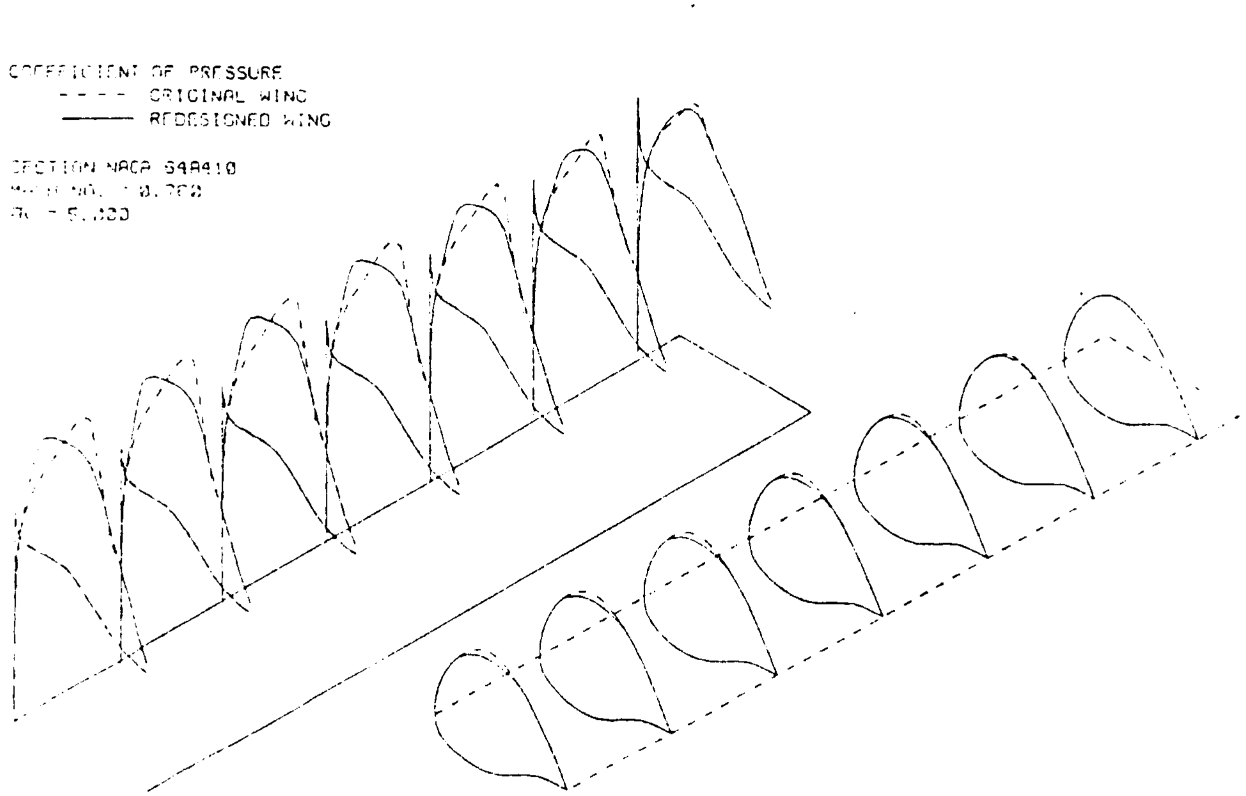

Fig. 10 Shock-free redesign of a rectangular wing with NACA 64A410 section.

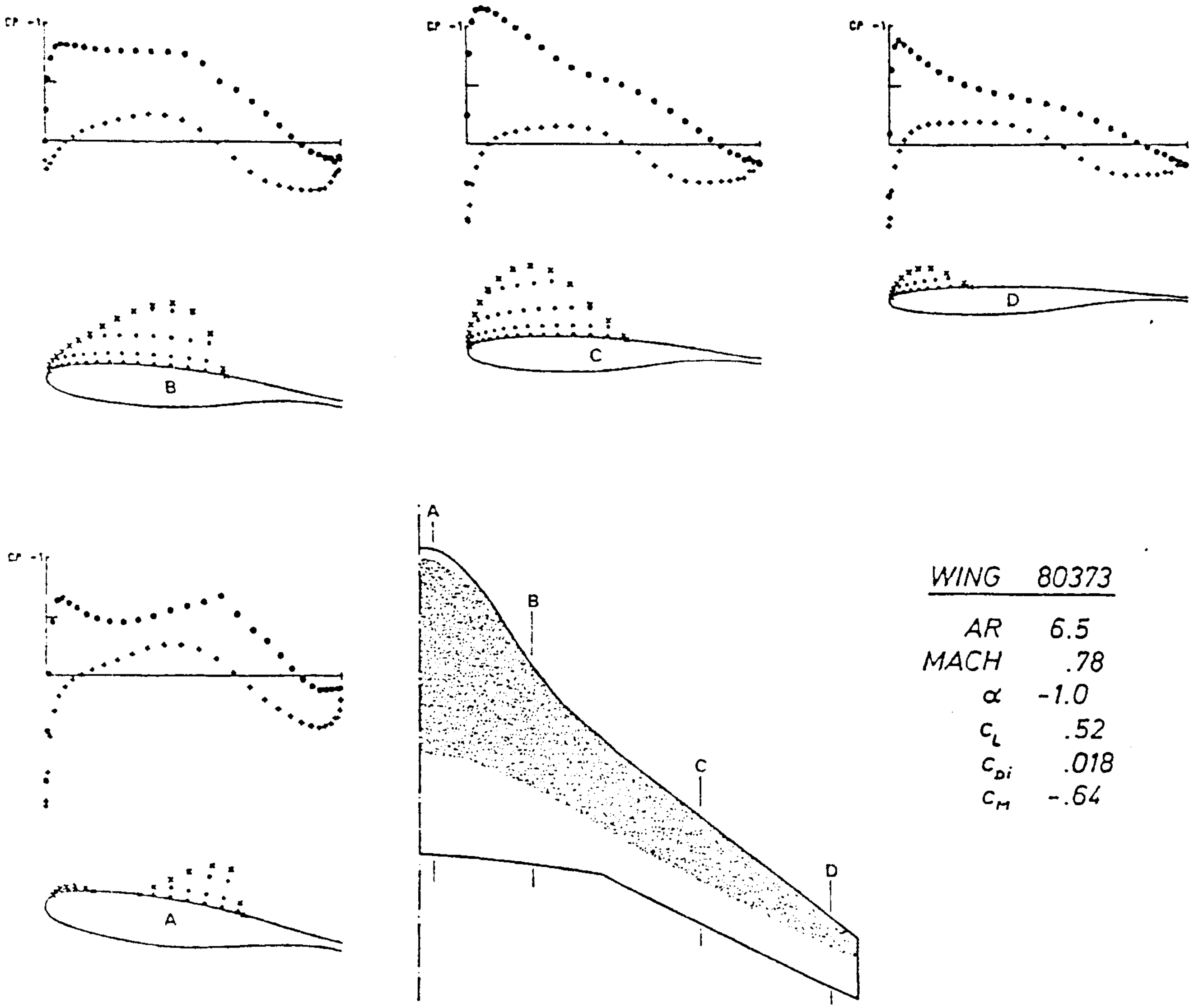

Fig. 11 Shock-free design of a swept wing.
Viscous diplacement model added.

AGARD
ADVISORY GROUP FOR AEROSPACE RESEARCH & DEVELOPMENT

7 RUE ANCELLE 92200 NEUILLY SUR SEINE FRANCE

H. E. Nebeck and A. R. Seebass
University of Arizona
Tucson, Arizona

and

H. Sobieczky
DFVLR
Göttingen, West Germany

INVISCID-VISCOUS INTERACTIONS IN THE NEARLY DIRECT DESIGN OF SHOCK-FREE SUPERCRITICAL AIRFOILS

AGARD Fluid Dynamics Panel Symposium

COMPUTATION OF VISCOUS-INVISCID INTERACTIONS

NORTH ATLANTIC TREATY ORGANIZATION

INVISCID-VISCOUS INTERACTIONS IN THE NEARLY DIRECT DESIGN OF SHOCK-FREE SUPERCRITICAL AIRFOILS

by

H. E. Nebeck and A. R. Seebass
University of Arizona
Tucson, Arizona 85721
and
H. Sobieczky
DFVLR
Göttingen, West Germany

SUMMARY

An especially simple procedure for finding airfoil shapes that have desirable aerodynamic characteristics and that will be shock free at Mach numbers close to the highest values possible is described. The procedure accounts for overall inviscid-viscous interactions that are weak and includes the locally strong interaction at the trailing edge as incorporated in the Grumfoil algorithm.

INTRODUCTION

In the last decade substantial progress has been made in the computation of aerodynamic flow fields in which the global inviscid-viscous interaction is weak. For two-dimensional transonic flows the fundamental interactions, carefully delineated nearly a decade ago by Green (1), are now adequately modeled by computational analysis, provided that the global interaction is weak and that the boundary layer suffers at most mild separations. This is accomplished by coupling a numerical analysis of the inviscid flow, which assumes the main body of the flow is irrotational, hence derivable from a single scalar potential, with a numerical solution of an integral formulation of the boundary layer equations. Much more sophisticated computational tools, such as large eddy simulation, are becoming available but they are not yet efficient enough for their application to design problems.

The application of these analysis tools in design can take many forms. Perhaps the most basic is that of prescribing a pressure distribution and determining the airfoil that will generate this pressure field. This inverse problem is not well-posed and extensive computations are usually required in order to obtain useful results. A variant of this procedure is to prescribe desired changes to an already existing pressure field that is generated by a given airfoil. Here the inverse problem may be linearized about an existing flow and the resulting problem is more amenable to analysis. Another procedure is to use numerical optimization to find which of a family of possible airfoils will provide the best airfoil performance. Here the main limitations are the family of airfoils considered and the computational expense of exploring incremental changes for improvements in performance that are only marginally larger than the errors in the computed performance parameters. A third, but more limited, possibility also exists, namely, determining the changes required in a baseline airfoil to make the flow past it shock free at a prescribed lift coefficient and Mach number. This presumes that an airfoil baseline which meets performance goals for subcritical Mach numbers is known. One then invokes the "fictitious gas" procedure of Sobieczky (2) to find a new shape for the upper surface of the airfoil that will produce shock-free flow at the prescribed conditions. This shape is not unique, nor is it possible to find such shapes for all flow conditions. For a prescribed lift coefficient and airfoil thickness, there is a freestream Mach number above which a shock-free shape is not possible. While the feasibility of this procedure has been amply demonstrated for inviscid flows, indeed, even for three-dimensional flows (3,4), its success for flows with inviscid-viscous interaction has not previously been documented.

The goal of this paper is to demonstrate the ability of the fictitious gas procedure to design advanced shock-free airfoils at little computational expense even when inviscid-viscous interactions are taken into account.

ANALYSIS ALGORITHMS

A number of numerical algorithms have been developed to calculate the transonic flow past an airfoil in the presence of weak inviscid-viscous interactions. One of the early successes was the algorithm of Bauer et al. (5), which we will call BGKJ. It employs a nonconservative formulation of the potential equation, coupled with the integral boundary layer code of Nash and MacDonald (6) and a constant thickness wake model. The nonconservative difference scheme fails to conserve mass and underpredicts the irrotational shock strength. As a consequence, the inviscid version of this algorithm gave results that agreed well with experimental results for the pressure coefficient when compared at the same Mach number and lift coefficient. Collyer and Lock (7) modified the inviscid analysis portion of this program to include a combination of conservative and nonconservative differencing in order to better capture the correct shock pressure rise, and coupled it with Green's lag-entrainment method (8) for computing the turbulent boundary layer. They included the modification of the inviscid flow due to wake curvature but did not model the strong interaction that occurs at the trailing edge. Nandanan, Stanewsky, and Inger (9) have used Jameson's conservative version (10) of the BGKJ algorithm together with Rotta's integral dissipation method (11) and Inger's model of shock-boundary layer interaction (12) to compute flows with weak embedded shock waves. Perhaps the most advanced algorithm of this type in the U.S. is that due to Melnik, Chow, and Mead (13). They coupled Jameson's inviscid algorithm with Green's lag-entrainment method for the boundary layer. The effects of the strong interaction near the trailing edge are also included in the algorithm. This is accomplished by incorporating the results of Melnik and Chow (14) for the multi-layered turbulent boundary layer at a cusped trailing edge. This coupled calculation provides a self-consistent result for the inviscid flow, the boundary layer, and the wake. It also removes the singularity in the inviscid pressure associated with the trailing edge of the airfoil. Wake curvature effects are included and are found to have a significant effect on the results. This algorithm has been called "Grumfoil" by its authors, and we will use the same appellation here. While no shock-boundary layer interaction model is included, the algorithm seems to be accurate for shock strengths for which the irrotational approximation is itself satisfactory.

SHOCK-FREE DESIGN

Inviscid analysis algorithms such as those discussed above have amply demonstrated the generality of Morawetz's (15) result of the mid-1950s, namely, that shock-free flows are mathematically isolated one from another. Despite this isolation they have played an important role in providing moderate increments in aircraft performance. Wind tunnel research by Pearcey at the National Physical Laboratory (16) and Whitcomb (17) at NASA Langley Research Center first demonstrated that such flows could be realized and would have important applications. Subsequently, Garabedian and Korn (18), Nieuwland (19), Boerstoel (20), and Sobieczky (21) developed analytical tools for the prescription of shock-free airfoil shapes. These tools relied on the hodograph transformation, and viscous effects could only be accounted for to the extent that the boundary layer could be computed independently of the inviscid flow. The extension of this capability to the physical plane by the introduction of a fictitious gas for a preliminary calculation of the supersonic portion of the flow field makes it possible to design shock-free airfoils with a proper accounting of the coupled nature of the inviscid and viscous flow fields. This capability requires one crucial approximation that has now been justified by numerical experiment, namely, that the boundary layer displacement thickness is not altered in any consequential way by the difference between the pressure field of the fictitious gas and that of the real gas. Given no essential differences in the boundary layer displacement thickness in the supersonic domain due to the difference between the real and fictitious pressures there, nor any due to the minor change in airfoil thickness, then the inviscid and viscous flow fields must be correct and correctly coupled.

We begin the design process with the selection of a baseline airfoil. Normally, this would be an airfoil that meets subcritical design goals and that has a reasonable amount of upper surface curvature. Here we have used a supercritical section, both for convenience and to see if we can improve its performance somewhat. Our goal here, however, is not advanced airfoil design, but rather, to show that the fictitious gas design procedure is feasible in the presence of coupled inviscid-viscous interactions. We then modify the Grumfoil algorithm to incorporate a fictitious density-flow speed relation when the Mach number exceeds one. Both the baseline airfoil and the fictitious density relationship are at the investigator's disposal and they interact in a way that allows the generation of a limited family of candidate airfoils. Because our concern is with demonstrating the feasibility of the proposed procedure we limit our attention to the simple relation

$$\rho/\rho^* = (a^*/q)^P, \qquad (1)$$

where ρ and q are the fictitious density and real flow speed and ρ^* and q^* are their real sonic values. The exponent P is a parameter that varies the gas law (1). For values of P less than one relation (1) insures that the governing equation, namely,

$$\mathrm{div}(\rho \underline{q}) = 0, \qquad (2)$$

where $\underline{q} = \nabla\phi$, and ϕ is the velocity potential, remains elliptic. For such relations the fictitious mass flow in the supersonic domain is greater than it would be for a real gas. The solution to this fictitious flow problem is used to provide values for the flow deflection on the embedded sonic line. To insure the accuracy of this data we generally insist on convergence to a maximum residual of 10^{-6} on a 160 by 32 grid. This data on the sonic line is used to compute the velocity potential and stream function there. A simple characteristics routine is then used to march down from the sonic line to find the streamline consistent with stream function values at the sonic line airfoil juncture. (This must be done in a way that is consistent with the mass flow added to the flow by the boundary layer displacement effect.) This defines the new body streamline if the characteristics calculation succeeds. It may not, but may rather signal the intervention of a limit line and indicate the failure of the sonic line data to be consistent with shock-free flow. In this event the baseline airfoil and fictitious density law can be modified in an attempt to circumvent the failure. The new airfoil surface will be thinner than the baseline airfoil because the real density is less than the fictitious density and, hence, for the fixed mass flow entering the sonic line, the real gas requires more area. The amount that the airfoil's vertical coordinate is thereby reduced can be added to the baseline airfoil and the process repeated until the baseline airfoil thickness is retained in the shock-free design. Changes in the choice of the gas law, here simply limited to changes in P, also have an effect on airfoil thickness, albeit a small one. Further progress in airfoil design requires an understanding of the relationship between the baseline airfoil and the fictitious gas law chosen. We do not explore that question further here.

The designed airfoil must now be analyzed by the original algorithm to see how well it performs. The boundary layer calculation used in the design process was based upon the pressure gradient of the fictitious gas calculation. The designed airfoil will have a somewhat different pressure gradient. If the displacement thickness were correct, then only the pressure field in the supersonic domain is altered. However, this change in the pressure field alters the boundary layer displacement thickness and, to some degree, the extent of the supersonic domain. We find in practice, however, that the error in the displacement thickness is so small that we need not correct for it.

RESULTS

We selected the VFW airfoil Va2 for our baseline as characteristic of the wing sections that will be used on future commercial transport aircraft. This airfoil, which is 12.5% thick, has a design Mach number, M_∞, of 0.73 and a design lift coefficient, C_ℓ of 0.525. Our coordinates are slightly different from those for the Va2 and we have used our own designation, 47070M, for this baseline airfoil. As this airfoil is already an advanced design we only examined a modest increment in design conditions, namely, M_∞ = 0.75 and C_ℓ = 0.550 at a flight Reynolds number of 35 million. Figure 1 depicts the pressure distribution and sonic line - shock wave shape for the baseline airfoil at the new flight conditions. It has a drag of 67 counts. When we repeat this calculation using the fictitious density law (1) with P = 0.9, we find results like those depicted in Figure 2. Because we are solving an elliptic equation we obtain a smooth pressure distribution and well behaved sonic line. Although it has no physical meaning we note the drag is now 61 counts. None of this can be wave drag because we solved an elliptic equation and we must attribute it to viscous effects. The undulations in the upper surface pressure near the leading edge are due to irregularities in the airfoil shape and the boundary layer's transition to turbulent flow.

We now use the flow speed and deflection angle on the sonic line to calculate the flow in the supersonic domain in the manner described above. This defines the new body surface. Since it is thinner than the original body, we choose to repeat the process with a baseline airfoil shape that is the original airfoil plus a multiple of the difference between the original and the shape calculated using the design procedure outlined above. The pressure distribution and sonic line for the fictitious flow past this airfoil are depicted in Figure 2. Performing the design process on this new baseline results in an airfoil that has essentially the same thickness as the original baseline airfoil. We now compute the flow past this new airfoil (47073) to see if we have indeed found improved performance.

The results of this final calculation are shown in Figure 3. Shock-free flow has been achieved. The calculation was done with the lift coefficient set to 0.550. The drag coefficient, not too surprisingly, is the same as that calculated using the fictitious gas. Figure 4 compares the redesigned airfoil and the original baseline airfoil with the vertical scale magnified five times so that the small differences between the two airfoils can be observed. The improvement in lift to drag ratio over the baseline at M_∞ = 0.75 is 10%. The entire design process required about 500 CPU seconds on a CDC 7600. It could be repeated to recover the very small loss in airfoil thickness.

The success of the design procedure depends on the boundary layer displacement thickness for the fictitious gas analysis being essentially the same as that for the real gas analysis of the new airfoil. Figure 5 compares the displacement thickness for the original airfoil, 47070M, that for the fictitious gas flow past a thickened airfoil 47070B, and that of the final design, 47073. There are very minor differences between the displacement thickness for the 47070B and the 47073 airfoils at about 62% of the chord. This is more readily noticed in Figure 6, which compares the skin friction coefficients for the three airfoils. This small difference in the displacement thickness manifests itself in a small difference in the subsonic portion of the pressure distributions of Figures 2 and 3 just downstream of the sonic line airfoil juncture. The difference is so small that it can really only be discerned when the two pressure distributions are overlayed. The supersonic pressure is, of course, always different.

If we compare the off-design performance of the two airfoils we discover that the improvement in the drag divergence Mach number is not even 0.01. Figures 7 and 8 compare the pressure distributions and the sonic line shapes for the two airfoils at M_∞ = 0.74 and 0.76. From these results it is easy to see how the new design achieves the modest improvement in drag at M_∞ = 0.75. The variation in the drag coefficient with Mach number at the design lift coefficient and with the lift coefficient at the design Mach number for the two airfoils is depicted in Figures 9 and 10. If we repeat the design process at a higher Mach number, and with a somewhat thicker baseline airfoil, we find another new airfoil, 47081, which achieves a 0.015 increment in the drag rise Mach number. The drag coefficient as a function of Mach number for the 47081 is also shown in Figure 9. Figure 11 depicts the pressure distribution and sonic line shape for the 47081 airfoil and Figure 12 compares this airfoil with the 47070M baseline airfoil. While the improvement in drag rise Mach number is very small, there can be no doubt that, other things being equal, such small improvements are of major importance in the design of a commercial transport. There is a limit to the Mach number at which shock-free designs can be found for a fixed lift and airfoil thickness. With the 47070M as a baseline this would seem to be about M_∞ = 0.77 for C_ℓ = 0.550 and 12.5% thickness.

CONCLUSION

We have described a computationally efficient method for finding airfoil shapes with desirable aerodynamic properties that are also shock-free at supercritical Mach numbers. The process of making them shock free can be successfully carried out even in the presence of coupled inviscid-viscous interactions. The shock-free design process is as reliable as the analysis algorithm used to compute the flow field. A wide range of airfoil shapes can be found, depending on modifications to a selected baseline and on the choice of the gas law. There is a limit to the maximum drag divergence Mach number that can be achieved for a prescribed airfoil thickness and lift coefficient. Our experience with this process in inviscid flow gives us confidence that these limits can be achieved with an artful selection of baseline airfoils and fictitious gas laws.

ACKNOWLEDGEMENTS

This research was supported by Grant Number AFOSR-76-2954I from the Air Force Office of Scientific Research and by Grant Number N00014-76-C-0182 from the Office of Naval Research.

REFERENCES

1. Green, J. E. "Some Aspects of Viscous-Inviscid Interactions at Transonic Speed, and Their Dependence on Reynolds Number," AGARD CP-83-71, 1971, pp. 2-1, 2-12.
2. Sobieczky, H. "Die Berechnung lokaler Räumlicher Überschallfelder," ZAMM, 58T, 1978, pp. 215-216.
3. Sobieczky, H., Yu, N. J., Fung, K-Y., and Seebass, A. R. "New Method for Designing Shock-free Transonic Configurations," AIAA J., Vol. 17, No. 7, July 1979, pp. 722-729.
4. Fung, K-Y., Sobieczky, H., and Seebass, R. "Shock-Free Wing Design," AIAA J., (to appear). Also AIAA Paper 79-1557.
5. Bauer, F., Garabedian, P. R., and Korn, D. G. "Supercritical Wing Sections," Lecture Notes in Economics and Mathematical Systems, No. 66, Springer-Verlag, 1972.
6. Nash, J. F. and MacDonald, A. G. J. "The Calculation of Momentum Thickness in a Turbulent Boundary Layer at Mach Numbers up to Unity," ARC CP-93, London, 1967.
7. Collyer, M. R. and Lock, R. C. "Prediction of Viscous Effects in Steady Transonic Flow Past an Airfoil," Aero. Quart., August 1979, pp. 485-505.
8. Green, J. E., Weeks, D. J., and Broomen, J. W. F. "Prediction of Turbulent Boundary Layers and Wakes in Compressible Flow by a Lag Entrainment Method," RAE Tech. Report, 72231, 1973.
9. Nandanan, M., Stanewsky, E., and Inger, G. R. "A Computational Procedure for Transonic Airfoil Flow Including a Special Solution for Shock Boundary Layer Interaction," AIAA Paper 80-1389, 1980.
10. Jameson, A. "Numerical Computation of Transonic Flow with Shock Waves," Symposium Transsonicum II, Springer-Verlag, New York, 1975.
11. Rotta, J. C. "Turbulent Boundary Layer Calculation with the Integral Dissipation Method," Computation of Turbulent Boundary Layers, 1968 AFOSR-IFP Stanford Conference, Vol. 1, pp. 177-181.
12. Inger, G. R. and Cantrell, J. C. "Application of Shock-Turbulent Boundary Layer Interaction Theory to Transonic Aerodynamics," 4th U. S.-F. R. G. Meeting on Viscous and Interacting Flow Field Effects, BMVG-FBWT 1979, pp. 100-115.
13. Melnik, R. E., Chow, R., and Mead, H. R. "Theory of Viscous Transonic Flow Over Airfoils at High Reynolds Number," AIAA Paper 77-680, 1977.
14. Melnik, R. E. and Chow, R. "Asymptotic Theory of Two-dimensional Trailing Edge Flows," NASA Conference on Aerodynamic Analysis Requiring Advanced Computers, NASA SP-347, 1975, pp. 177-249.
15. Morawetz, C. S. "On the Non-Existence of Continuous Transonic Flows Past Profiles, I, II, and III," Communications on Pure and Applied Mathematics, 1956, 1957, and 1958, p. 45-68, 107-131, and 139-144.
16. Pearcey, H. H. "The Aerodynamic Design of Section Shapes for Swept Wings," Advances in Aeronautical Sciences, Vol. 3, 1962, pp. 277-322.
17. Whitcomb, R. T. and Clark, L. R. "An Airfoil Shape for Efficient Flight at Supercritical Mach Numbers," NASA TM X-1109, July 1965.
18. Garabedian, P. R. and Korn, D. G. "Numerical Design of Transonic Airfoils," Numerical Solutions to Partial Differential Equations, Vol. II, Academic Press, New York, 1978, pp. 253-271.
19. Nieuwland, G. Y. "Transonic Potential Flow Around a Family of Quasi-Elliptical Airfoil Sections," NLR Report TR-T 172, 1967.

20. Boerstoel, J. W. "Design and Analysis of a Hodograph Method for the Calculation of Supercritical Shock-free Airfoils," NLR Report TR-77046 U, 1977.

21. Sobieczky, H. "Entwurf überkritischer Profile mit Hilfe der rheoelektrischen Analogie," DFVLR Report DLR-FB 75-43, 1975.

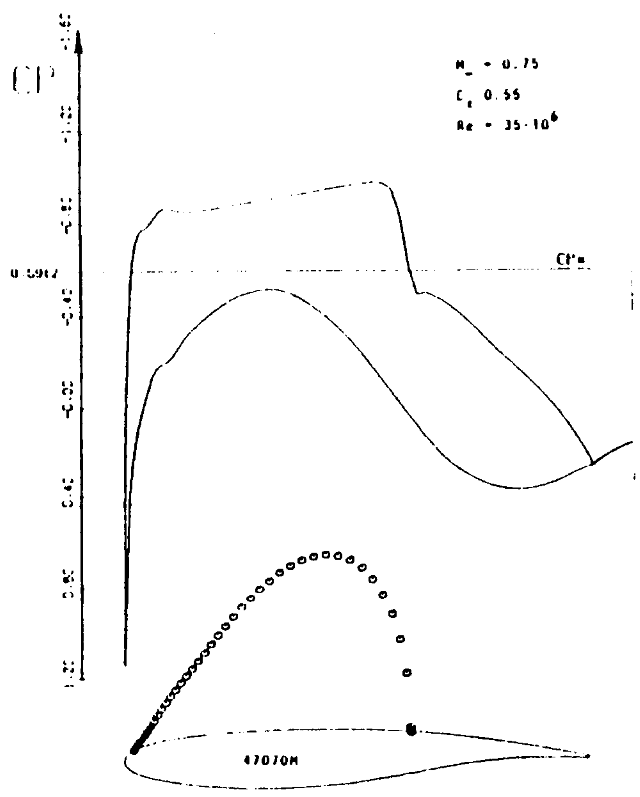

Figure 1. Grumfoil analysis of the baseline airfoil 47070M.

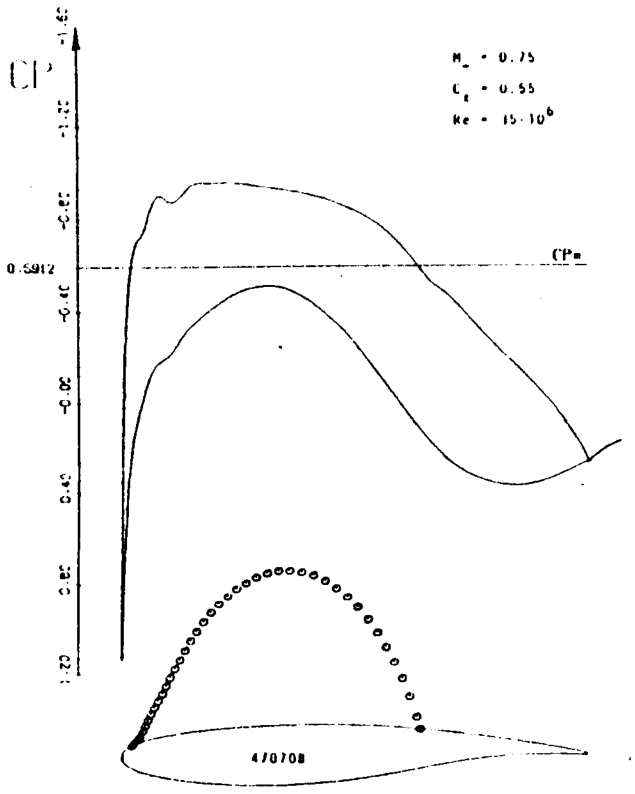

Figure 2. Grumfoil fictitious gas (P = 0.9) analysis of the baseline airfoil plus a bump (47070B).

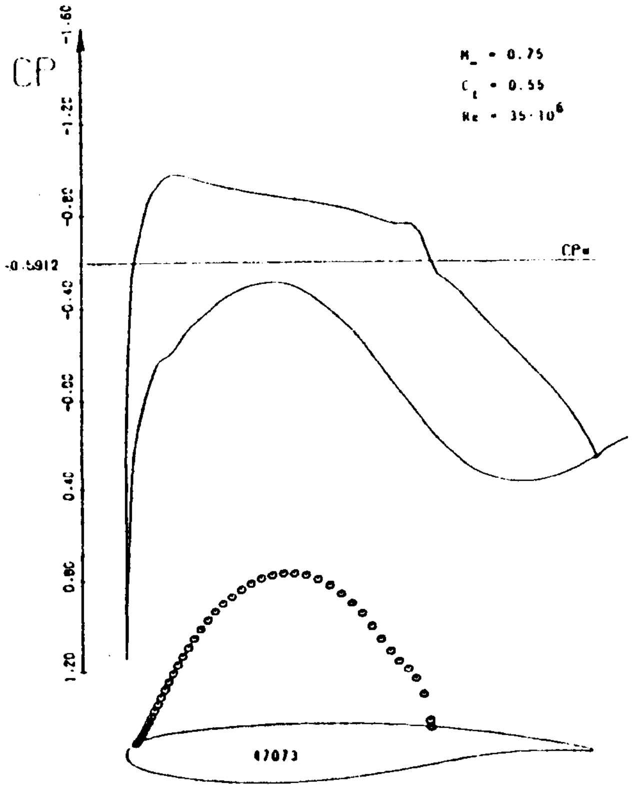

Figure 3. Grumfoil analysis of the shock-free design airfoil (47073).

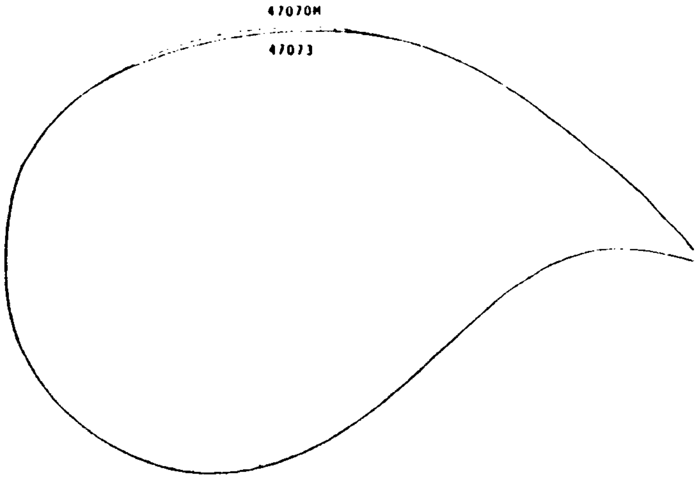

Figure 4. Comparison of the baseline and shock-free design airfoils. The vertical scale is magnified five times.

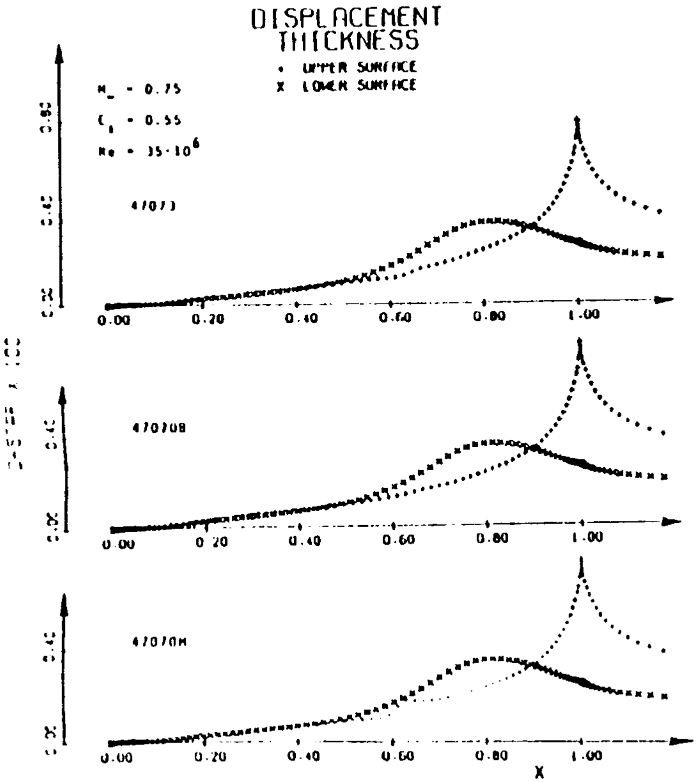

Figure 5. Displacement thickness for the three airfoils of Figures 1-3.

Figure 6. Skin friction coefficients for the three airfoils of Figures 1-3.

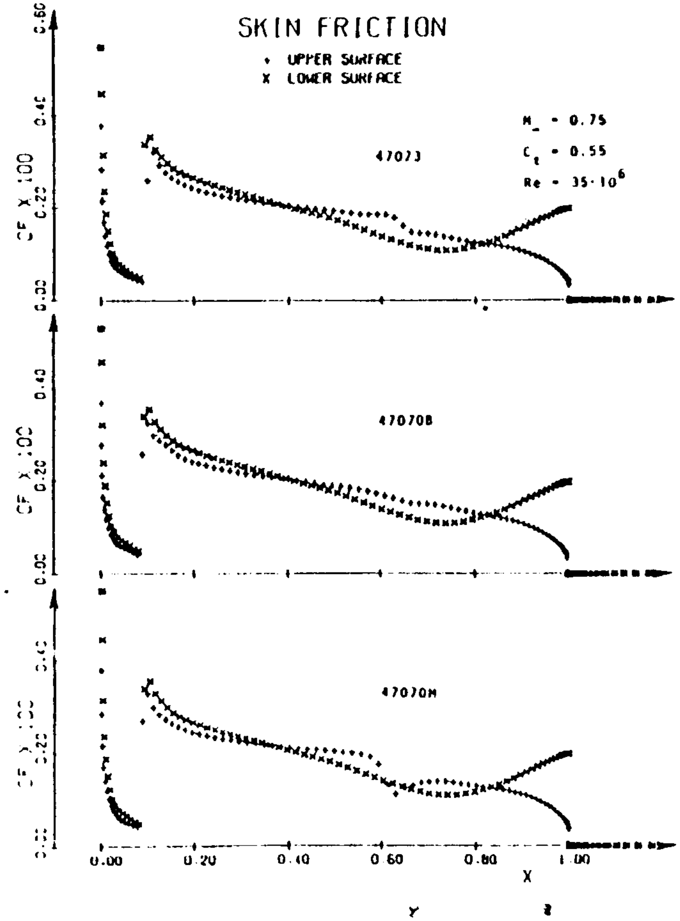

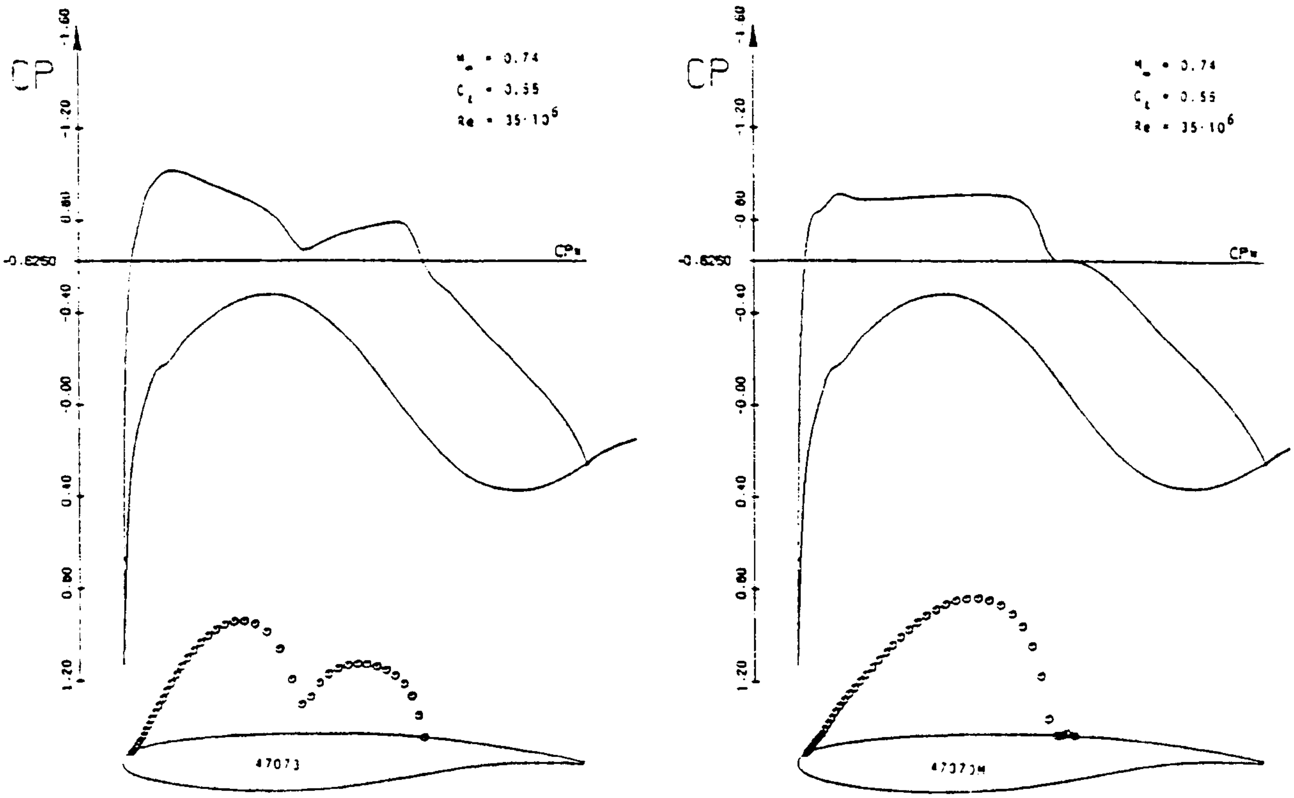

Figure 7. Pressure distributions and sonic line - shock wave shapes for the baseline and shock-free airfoils at M_∞ = 0.74.

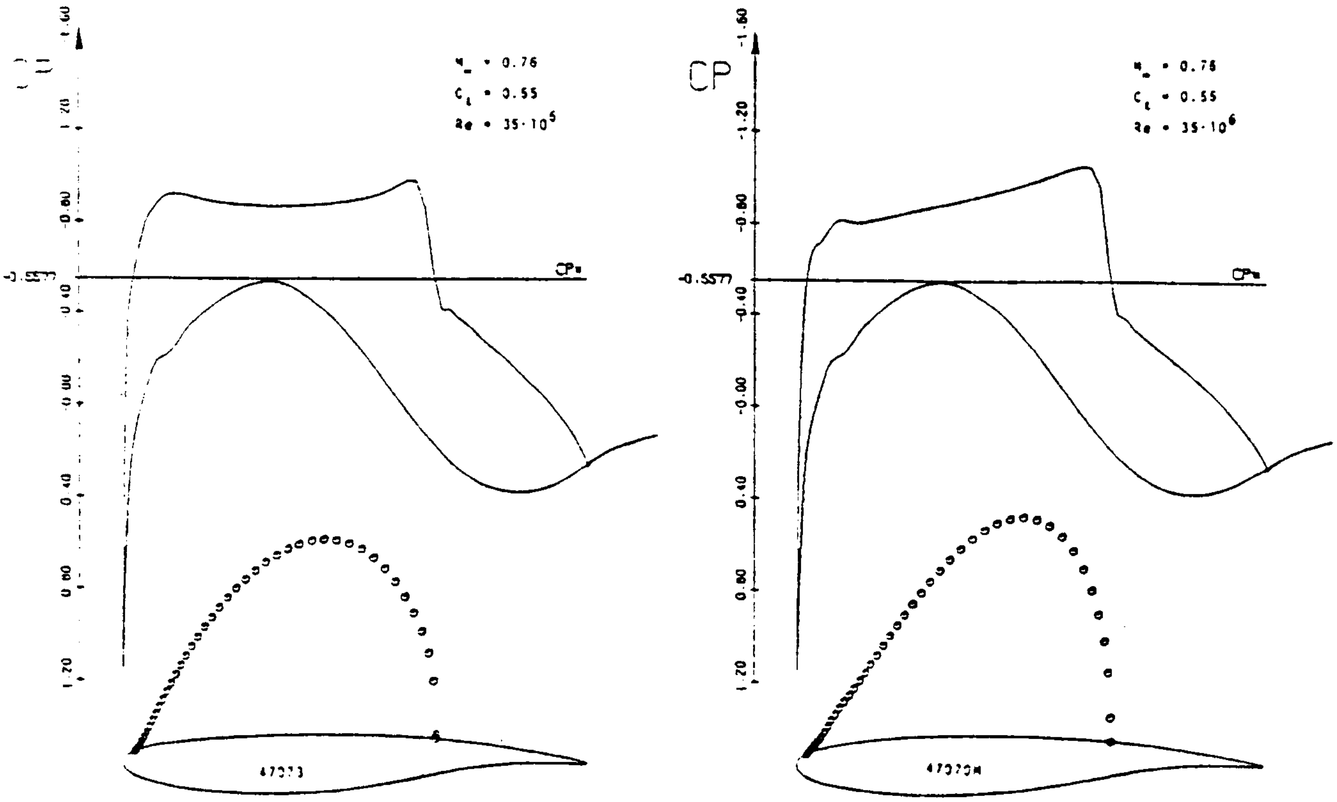

Figure 8. Pressure distributions and sonic line - shock wave shapes for the baseline and shock-free airfoils at M_∞ = 0.76.

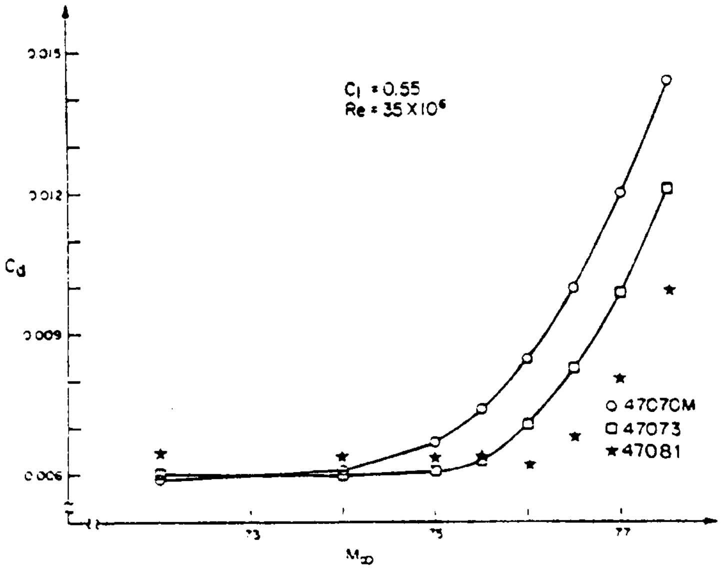

Figure 9. Drag coefficient as a function of Mach number for the 47070M, 47073, and 47081 airfoils at C_l = 0.55, Re = 35·10^6.

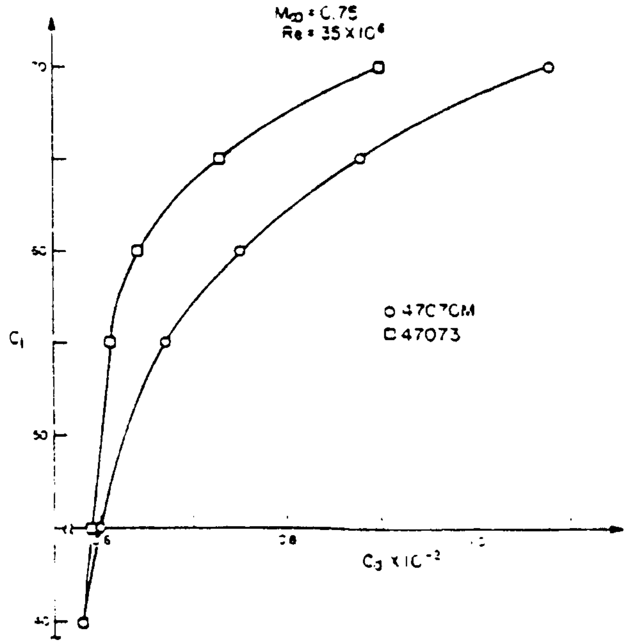

Figure 10. Lift coefficient as a function of drag coefficient of the 47070M, 47073, 47081 airfoils at M_∞ = 0.75, Re = 35·10^6.

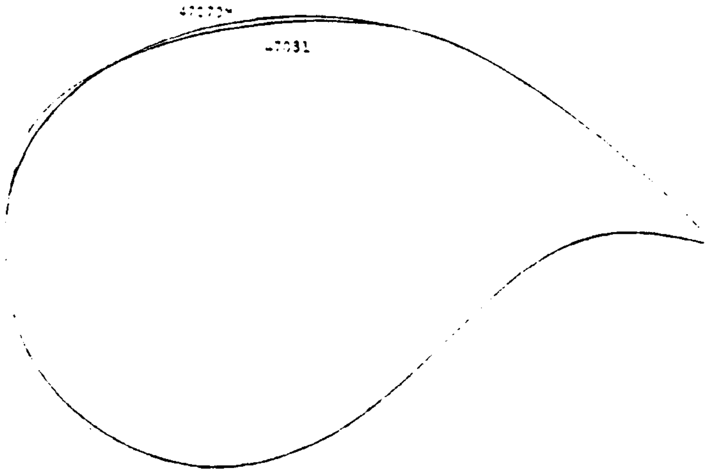

Figure 12. Comparison of the 47070M and 47081 airfoils. The vertical scale is magnified five times.

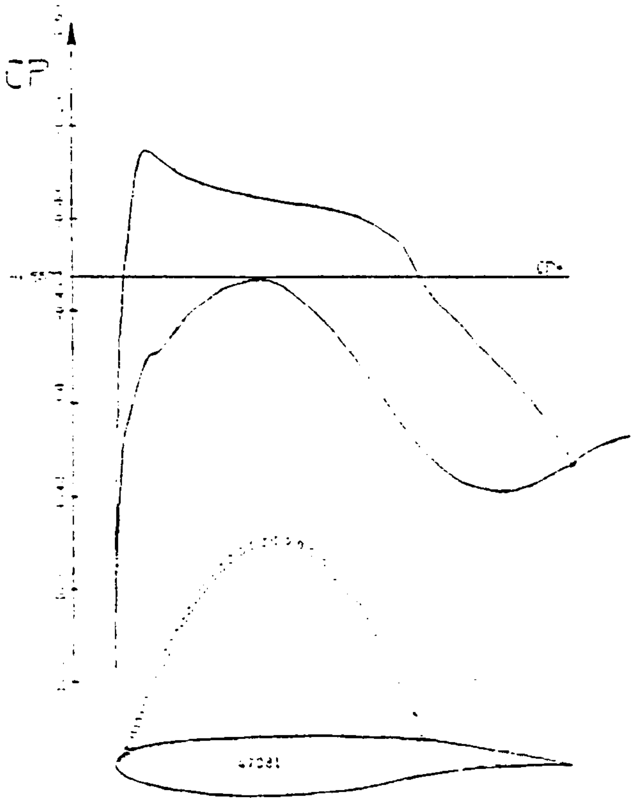

Figure 11. Pressure distribution and sonic line shape for the 47081 airfoil at $M_\infty = 0.76$, $C_l = 0.55$, $Re = 35 \cdot 10^6$.

ARTICLE NO. 80-4035

Analysis of Two-Dimensional Incompressible Flows by a Subsurface Panel Method

Jack Moran,* Kevin Cole,† and David Wahl‡
University of Minnesota, Minneapolis, Minn.

A new approach to panel methods is explored for two-dimensional steady incompressible flows. The method uses linear distributions of sources and vortices on straight-line panels, but satisfies boundary conditions on the actual body surface, at nodes that are also end points of the panels. The result is continuity in body-surface velocity distribution, without recourse to numerical quadrature for the velocity influence coefficients. The method is unusually sensitive to the distribution of the nodes. For example, it almost always fails to give acceptable results when the nodes are distributed randomly. However, the continuity of the velocity distribution makes possible a unique node redistribution scheme, which may be iterated to give accurate results reliably.

Background

PANEL methods are now widely used for calculating linear potential flows past aerodynamic bodies. The steps involved in setting up a panel method are as follows:

1) Represent the perturbation potential by a distribution of sources, doublets, and/or vortices of unknown strength over the body surface and its wake.

2) Approximate the body and wake surfaces by the union of panels of relatively simple geometry.

3) Parameterize the singularity strength on the panels; e.g., represent it by a polynomial of degree two or less.

4) For each unknown parameter in the representation of the singularity strength, demand that the potential and/or velocity field satisfy an appropriate boundary condition at some control point.

5) Solve the resulting system of linear algebraic equations for the parameters underlying the singularity strength.

Once these steps are completed, the velocity and potential may be evaluated anywhere in the flow by summing contributions from the individual panels.

Almost invariably, approximations made in the formulation of panel methods lead to singularities at the panel boundaries, and so restrict the usable output of the methods to points near the panel center. This is certainly the case if the panels are plane or piecewise plane. However, even when curved panels are used, spurious singularities sometimes result.[1-3] The integrals which give the potential and velocity fields due to the singularity distributions on the panels cannot be evaluated in closed form unless they are approximated through series expansion by integrals over plane or piecewise-plane surfaces. In effect, the source, doublet, or vortex distribution over a curved surface is replaced by a series of multipole distributions over a plane surface. At the panel edges, each term of the expansion is even more singular than the one preceding.

A related problem of existing panel methods, at least in three-dimensional situations, is the rather complicated way in which they approximate the body surface. Since panel edges are not available as control points, there is generally just one control point per panel, and thus (approximately) one unknown per panel as well. Quadrilateral panels are therefore preferred to triangles, since the latter would double the number of unknowns for a given number of points at which data on the body shape are specified. However, to avoid numerical quadrature, the surfaces on which the singularities are distributed should be plane, and a curved three-dimensional surface cannot be approximated by a continuous system of plane quadrilaterals. Some methods simply allow gaps between neighboring panel edges; others use a piecewise-planar quadrilateral (four triangles surrounding a planar parallelogram whose corners are the midpoints of the sides of the quadrilateral).

The use of (roughly) one control point per panel also complicates the parameterization of the singularity strength. Recent methods are based on quadratic doublet distributions. In order to specify the ten coefficients of the quadratics without creating discontinuities at panel or subpanel boundaries, one method uses a singularity spline based on a least-squares fit of the quadratic in one panel to the doublet strength in twenty surrounding panels.

A more local support for the singularity splines is desirable for a number of reasons. First, the more local the spline, the easier it is to match the singularity strength at boundaries between distinct networks of singularity distributions (e.g., at wing-body junctions). Also, a wide support suggests that the effective mesh size is much larger than the distance between nodes. Finally, a more local spline would probably simplify and, hence, expedite the analysis.

The objective of the present research, therefore, is to develop a panel method with the following characteristics: 1) the velocity distribution on the body surface should be continuous, even at panel edges; 2) integrals giving the velocity field should be evaluated in closed form; and 3) both the body surface and the singularity strength should be specified by splines of local support. Thus far we have succeeded in implementing a two-dimensional version of a method which promises to meet all three objectives. This paper reports our progress.

Analysis

We want to determine the aerodynamics of an airfoil of specified geometry immersed in a uniform steady incompressible inviscid flow. A general representation of the perturbation velocity potential may be constructed by

---

Received May 7, 1979; revision received Aug. 27, 1979. Copyright © American Institute of Aeronautics and Astronautics, Inc., 1979. All rights reserved. Reprints of this article may be ordered from AIAA Special Publications, 1290 Avenue of the Americas, New York, N.Y. 10019. Order by Article No. at top of page. Member price $2.00 each, nonmember, $3.00 each. **Remittance must accompany order.**

Index categories: Computational Methods; Aerodynamics.

*Associate Professor, Dept. of Aerospace Engineering and Mechanics.

†Graduate Student, Dept. of Aerospace Engineering and Mechanics.

‡National Science Foundation Summer Intern, Dept. of Aerospace Engineering and Mechanics.

distributing sources and vortices over a surface S:

$$\phi_P = \frac{1}{2\pi}\int_S (\sigma_Q \ln r_{QP} - \gamma_Q \theta_{QP})\,ds \tag{1}$$

Here P is a typical field point, Q a point on S, and r_{QP}, θ_{QP} polar coordinates of P relative to Q. The quantities σ_Q and γ_Q are the strengths per unit length of the source and vortex distributions, respectively, at Q.

For any given source and vortex distributions, Eq. (1) satisfies the conditions of continuity and irrotationality and also the boundary condition at infinity. To make Eq. (1) the solution of a particular flow problem, it is only necessary that it also meet the flow-tangency condition on the airfoil surface and the circulation condition.

Before we can proceed further, we must specify the surface S—the "panels" of the method—on which the sources and vortices are distributed. Equation (1) is essentially equivalent to Green's third identity, according to which the potential outside S is representable by a source distribution of strength $\partial\phi/\partial n$ and a doublet distribution of strength ϕ on S. The restrictions on the validity of Eq. (1) are therefore the same as those on Green's third identity; namely, that ϕ is a continuous single-valued solution of Laplace's equation outside the surface S on which the sources and vortices are distributed. A safe choice for the panel surface, therefore, is the surface of the body under study.

However, it is difficult to evaluate the requisite integrals if the panel surface is curved. In the subsurface panel method, therefore, we distribute the sources and vortices on straight-line panels, whose endpoints are nodes on the body surface, as shown in Fig. 1, but continue to satisfy the flow-tangency condition on the actual body surface. This distinction between the panel and body surfaces is consistent with the limits on the validity of Green's identity, provided the flow has an analytic continuation across the body surface to the panels if, as is usually the case, the panels lie within the body. Since the panel surface can be made to approximate the body surface as closely as desired simply by increasing the panel density, this condition is not expected to be overly restrictive. However, it does necessitate the special treatment of (if not exclude from consideration) flows that are truly singular; in particular, flows past bodies with convex corners or sharp edges (aside from edges at which a Kutta condition removes the singularity).

Even with the panel surface S of Eq. (1) specified, the flow tangency and circulation conditions do not determine the source and vortex strengths uniquely. It is possible to specify one of them almost arbitrarily and then to determine the other so that Eq. (1) meets all the conditions it should. A convenient way to supply a closure condition is to specify a fictitious velocity field inside the surface S. In our work, this fictitious field has zero velocity. Then σ and γ are, respectively, the normal and tangential components of the total (not perturbation) velocity on the outside of the panel surface.

In order to discretize the problem, we approximate the source and vortex distributions as linear over each panel. Such distributions may be parameterized in terms of the source and vortex strengths at the vertices of the panels, which in turn equal the velocity components normal and tangential to the panels at their vertices. Since the vertices are also nodes on the body surface, these are components of the total fluid velocity on the body surface.

Specifically, let the jth panel be the straight line between the jth and $(j+1)$th nodes, ℓ_j its length, and ξ the distance from the jth node, as shown in Fig. 2. Then we take

$$\sigma(\xi) = \sigma_0 + (\sigma_\ell - \sigma_0)(\xi/\ell_j), \quad \gamma(\xi) = \gamma_0 + (\gamma_\ell - \gamma_0)(\xi/\ell_j) \tag{2}$$

in which, because the singularity strengths at $\xi = 0$ and ℓ_j are components of the total fluid velocity at the jth and $(j+1)$th nodes, respectively,

$$\begin{pmatrix}\sigma_0\\ \gamma_0\end{pmatrix} = [R(\theta_j - \beta_j)]\begin{pmatrix}V_{n_j}\\ V_{t_j}\end{pmatrix}$$

$$\begin{pmatrix}\sigma_\ell\\ \gamma_\ell\end{pmatrix} = [R(\theta_{j+1} - \beta_j)]\begin{pmatrix}V_{n_{j+1}}\\ V_{t_{j+1}}\end{pmatrix} \tag{3}$$

Here V_{n_j} and V_{t_j} are the velocity components normal and tangential to the body surface at the jth node, θ_j the inclination of the body surface at the same point, β_j the inclination of the jth panel, and $[R]$ a rotation matrix:

$$[R(\theta)] = \begin{bmatrix}\cos\theta & \sin\theta\\ -\sin\theta & \cos\theta\end{bmatrix} \tag{4}$$

This parameterization allows us to achieve our first major objective, continuity of the body-surface velocity. The velocity field due to any one panel does blow up at the ends of that panel. However, with our parameterization, the singularities due to neighboring panels cancel exactly, as is shown in the Appendix.

Note, on the other hand, that the source and vortex strengths themselves are not continuous from one panel to the next. The singularity strengths are, as previously pointed out, velocity components normal or tangential to the panel. At a node, the source and vortex strengths on the panels which meet there are components of the same velocity, the local body-surface velocity. But, because panels generally meet at an angle, the components of that velocity normal and tangential to the panels differ, and so, then, do the local source and vortex strengths.

Since V_{n_j} is known at each node from the flow-tangency condition, our unknowns are the nodal tangential velocity components. These we determine by satisfying an integral equation for V_t at each node,

$$V_{t_i} = \frac{1}{2\pi}\int_S [\sigma_Q \hat{t}_i \cdot \nabla_i \ln r_{Qi} - \gamma_Q \hat{t}_i \cdot \nabla_i \theta_{Qi}]\,ds + V_\infty \cdot \hat{t}_i \tag{5}$$

which is derived by differentiating Eq. (1). Contributions to Eq. (5) from the panels adjacent to the ith node must be subjected to a limiting process, in which the field point approaches the ith node from the outside S; see the Appendix for some of the details.

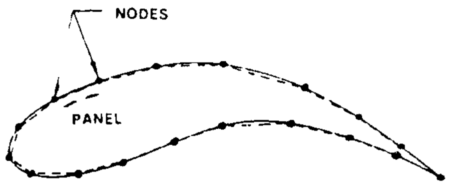

Fig. 1 Subsurface paneling.

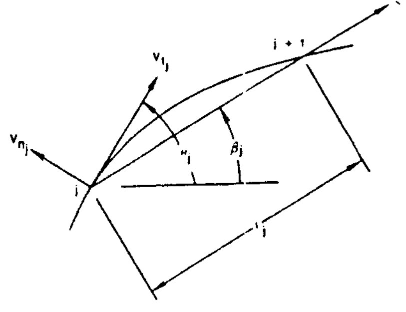

Fig. 2 Nomenclature used in formulas for source and vortex strengths.

An alternative approach is to require the velocity tangential to the body surface to vanish on the inside of each node. Because of the jumps in velocity across the panels, the resultant formula is exactly equivalent to Eq. (5), and we shall refer to Eq. (5) both as an "integral equation for the external tangential velocity" and a "requirement of vanishing internal tangential velocity."

Circulation Condition

For sharp-tailed airfoils, the circulation is fixed by the Kutta condition, that the velocity be finite at the trailing edge. Unless the trailing edge is cusped, this implies that the trailing edge is a stagnation point. Although we can show that, in principle, our solution yields finite velocities at sharp-but-not-cusped trailing edges if, and only if, the flow stagnates there, simply replacing Eq. (5) at the trailing-edge nodes by the stagnation condition

$$V_{t_j}=0 \text{ at trailing-edge stagnation points} \qquad (6)$$

yielded obviously incorrect results, including pressures higher on the leeward side of the trailing edge than on the windward.

Similarly poor results were obtained when we attempted a variety of alternative circulation conditions, including equation of the tangential velocities at the trailing-edge nodes and requiring the trailing-edge bisector to be a streamline, with such conditions used in place of Eq. (5) at one or both trailing-edge nodes. What such formulations seem to ignore is that the circulation condition is a requirement that the solution must satisfy over and above the integral equation approximated by Eq. (5). In any case, we obtain good results only by solving an overdetermined system comprised of an equation like Eq. (5) for each node and a circulation condition. For bodies with trailing-edge stagnation points, we use Eq. (6) in place of Eq. (5) at the trailing-edge nodes.

For bodies with sharp trailing edges, the circulation condition used is that the velocity component normal to the trailing edge bisector vanishes at a point very close to the trailing edge; specifically, at a distance from the trailing edge of about 10^{-5} times the average length of the two panels adjacent to the trailing edge. For the present case of steady two-dimensional flow, it makes little difference whether this point is inside or outside the airfoil.

The rationale for this form of the circulation condition was the suppression of the trailing-edge singularity which would follow from failure to satisfy the Kutta condition. However, the singularity is only logarithmic, and, as we discoverd by accident, the results change very little if we simply delete the logarithmically near-singular terms in calculating the velocity at the control point near the trailing edge. On the other hand, no logical alternative circulation condition suggested itself. In particular, we cannot simply require tangential velocities at the two trailing-edge nodes to be equal and opposite. This is already accomplsihed, in effect, by setting Eq. (5) or (6) at the two nodes.

Real airfoils—certainly if viscous displacement effects are taken into account—do not have sharp trailing edges. A cutoff trailing edge is usually modeled by hypothesizing a constant-pressure wake to emanate from the edge. Thus we require that the tangential velocities at the nodes on either side of the trailing edge be equal and opposite. The trailing edge is closed by a single panel, on which the velocity is determined solely by requiring the velocity to be continuous at its two nodes, where it is tangential to the main airfoil surfaces. Thus, the trailing-edge panel supports a fairly strong source distribution. Equation (5) is imposed at the trailing-edge nodes, which implies that the internal velocity tangential to the main airfoil surface vanishes at those nodes (as well as all the others).

The various forms of circulation condition for sharp, cusped, and cutoff trailing edges are summarized in Fig. 3, in which the $X'd$ arrows indicate velocity components that are set to zero.

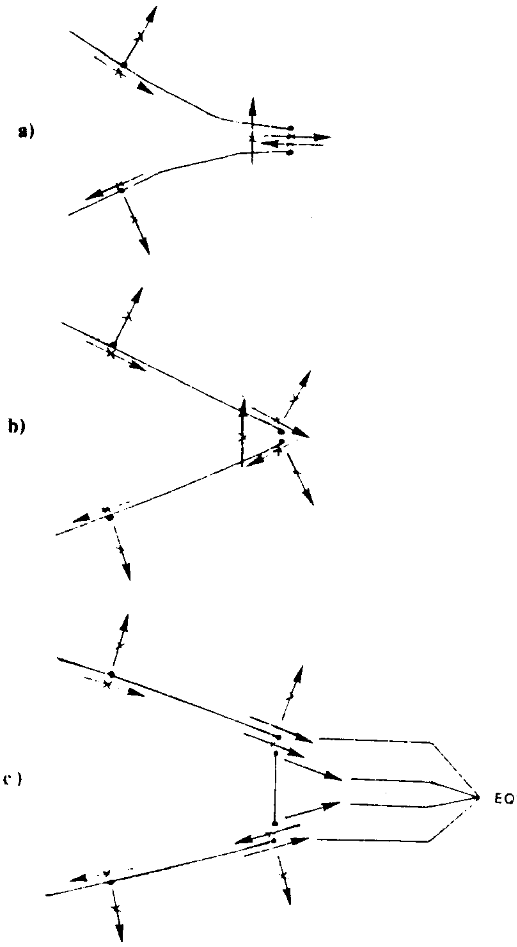

Fig. 3 Summary of boundary conditions imposed at trailing edges of various types: a) cusped, b) sharp but not cusped, and c) cutoff.

As noted above, adding the circulation condition to the system which governs the nodal tangential velocities overdetermines those unknowns. To solve the resultant system, we generally follow Bristow[3] in introducing an extra unknown for each extra equation, namely, a constant error term in all equations like Eq. (5), the constant varying from one element to another in multielement problems. We also provide, in our program, the option of using a least-squares technique. Generally, the two methods give quite comparable results. Bristow's is much cheaper, and so is preferred, but the least-squares method is occasionally more reliable in the node redistribution process to be described below.

Input Requirements

It should be noted that, to obtain a solution for the source and vortex strengths, the only data which must be known about the body shape are its coordinates and slope at the nodes. No assumption or approximation is made concerning the body shape between nodes. Thus, the only approximation made in the analysis is that the source and vortex strengths are assumed to vary linearly with distance along the panels. By invoking the momentum and moment-of-momentum theorems, we reduce force and moment calculations to integrals over the panels rather than over the body surface, so that that part of the calculations, too, is independent of the form of the body surface between nodes. Further, the assumed linearity of the velocity distribution on the panels makes it possible to evaluate in closed form the integrals over the panels required for the force and moment.

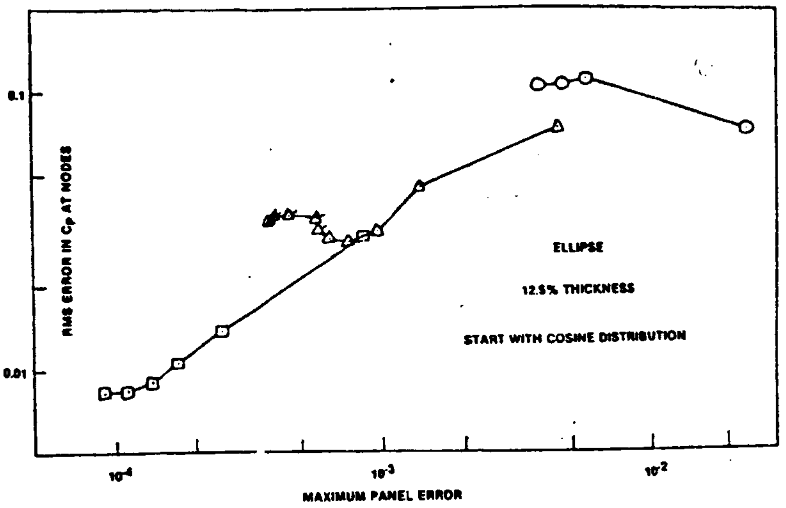

Fig. 4 History of root-mean-squared error during node redistribution process for ellipse of thickness ratio 0.125. Nodes initially distributed by cosine formula Eq. (11). Circles, 16 panels; triangles, 32 panels; squares, 64 panels.

Error Estimation

A unique feature of our method, made possible by the continuity of its results for the velocity distribution, is a capacity for checking its own accuracy a posteriori. As noted above, the only approximation made in the analysis is the assumption that the velocity distribution is linear on the panels. Once the nodal tangential velocities V_{t_i} are calculated, Eq. (5) can be adapted to calculate the velocity induced by the panels and the onset flow at the middle of the ith panel, $\hat{V}_i$. Then the nonlinearity of the velocity distribution on the ith panel is measured by

$$\Delta V_i = \hat{V}_i - \tfrac{1}{2}(V_i + V_{i+1}) \tag{7}$$

in which V_i, V_{i+1} are the (now known) velocities at the end points of the ith panel.

Now the contribution of any panel to any quantity of interest (the potential or velocity, for example) at any field point is calculated by integrating over the panel the products of the source and vortex strengths with appropriate kernel functions, or, what is the same thing, the dot product of the velocity distribution on the panel with some vector kernel K. The error incurred in this calculation due to the nonlinearity of the velocity distribution on the panel is, therefore,

$$\int_{i\text{th panel}} \Delta V_i \cdot K ds - \ell_i \Delta V_i \tag{8}$$

where ℓ_i is the length of the ith panel. This product, $\ell_i \Delta V_i$, is called the panel error function. Again, note that it can be calculated for each panel a posteriori, once the V_{t_i} have been determined, whether or not the exact solution is known.

From calculations of flows past ellipses, Joukowski airfoils, and Karman-Trefftz airfoils, using various numbers and distributions of nodes, we found the root-mean-squared error in the pressure coefficients at the nodes to correlate fairly well with the maximum value of the panel error functions. This suggested a node redistribution algorithm, in which a solution is obtained with a given set of nodes, which are then relocated so as to even out variations of the panel error function and so to reduce the maximum panel error. Since the nonlinearity of the velocity distribution on the ith panel is of order ℓ_i^2,

$$\ell_i \Delta V_i = 0(\ell_i^3) \tag{9}$$

Thus we stretch the panels so that their new lengths ℓ_i' are given by

$$\ell_i' = c\ell_i / \sqrt[3]{\ell_i \Delta V_i} \tag{10}$$

in which c is chosen so as to fix the locations of the starting and ending points of the group of nodes being redistributed.§

Results obtained with this node redistribution algorithm for symmetric flow past an ellipse of thickness ratio ⅛ are shown in Fig. 4. For three different numbers of panels (16, 32, and 64) the nodes were initially distributed according to a cosine law

$$x_i = \cos\frac{\pi(i-1)}{N-1} \quad \text{for } i=1,\ldots,N \tag{11}$$

The root-mean-squared errors in C_p at the nodes observed in successive redistributions of the nodes are shown connected by solid lines.

In every case shown in Fig. 4, the redistribution algorithm reduced the maximum panel error; i.e., the history of the algorithm goes from right to left in Fig. 4. Usually it also reduced the rms error in the nodal C_p, although, given the order-of-magnitude basis of the algorithm, it would be too much to expect such a reduction every time. Indeed, the initial result in the 16-panel case was somewhat better than the final results, at least according to the measure of rms error in C_p at the nodes. However, with higher numbers of nodes, the algorithm improved the nodal C_p by factors of 3-5. (At least part of the worsening of the rms error with redistribution of 16 nodes is due to the fact that the initial distribution did not concentrate so many points near the stagnation points, where C_p is more rapidly varying.)

Because the algorithm cannot be guaranteed to optimize the node distribution, its efficient utilization required some experimentation. Since the objective is to reduce the maximum panel error by smoothing out variations in the redistribution panel error from one panel to another, the redistribution process is generally terminated when the ratio of the maximum panel error to the minimum is less than some fixed number on every network. Our experience shows little improvement in the solutions when this max/min ratio is reduced below about 4.0. This is illustrated in Fig. 4, in which the iterations were pursued in the 32-panel case until the max/min ratio was under 1.2. Points for which the ratio was under 4.0 are flagged. Note that the iterations do appear to be converging (though not necessarily to an "optimum" solution so far as the rms error in nodal C_p is concerned). This has been the case in all our calculations, at least when we use, as a

---

§Such a group of nodes, with fixed starting and ending points, is called a *network* in what follows. For example, separate networks are used for a wing's upper and lower surfaces, with their leading and trailing edges being fixed in the node redistribution process.

closure condition, stagnation conditions within the panels. An alternative approach, in which the closure condition was that the velocity inside the panels equaled that of the onset flow (so that the source and vortex strengths were components of the perturbation velocity normal and tangential to the panels), yielded divergent results for the case that is the subject of Fig. 4.

To avoid oscillations which otherwise were found in some cases, the node movement is under-relaxed by a constant factor when and if necessary to avoid an increase in the average node movement from one trial to the next. Even so, as will be seen later, we occasionally find that the maximum panel error increases with node redistribution. This usually indicates that further redistribution would not improve the solution significantly. Therefore, if the maximum panel error increases, we terminate the redistribution process and reject the distribution which yields the higher panel error.

Calculations similar to those reported in Fig. 4 were performed in which the initial node distribution was random. The histories of the rms error were quite similar to those shown in Fig. 4, except that the initial errors were much higher. In three trials with different initial distributions of 32 nodes, the rms error in the nodal C_p decreased during the node redistribution process from 0.3-0.4 to about 0.04.

While the final results obtained with the node redistribution algorithm are usually quite acceptable, the very magnitude of the improvement it brings is evidence that the subsurface panel method is extremely sensitive to the node distribution. This is brought home still more graphically by Fig. 5, which shows the history of the pressure distributions calculated at various stages of the node redistribution process. In that case, the ellipse initially exhibited a lift coefficient of about 1.5!

Studies of flows past a variety of other airfoils—including NACA four-digit airfoils and other formula-generated sections as well as Karman-Trefftz airfoils of varying thickness, camber, and trailing-edge angle—confirm the implications of Figs. 4 and 5, both as to the sensitivity of the subsurface panel method to the node distribution and the effectiveness of the node redistribution algorithm. The troubles of the basic method are not restricted to initially random distributions. The results of Figs. 6 and 7 were obtained starting with the "reasonable" distribution of Eq. (11). The implausible crossing over of the pressure distribution near the trailing edge shown in Fig. 6 is seen in Fig. 7 to lead to a 25% deficiency in the calculated lift coefficient, even when 64 panels are used. A possibly related anomaly was encountered near the sharp-but-not-cusped trailing edge of the highly cambered Karman-Trefftz airfoil to which Fig. 8 refers. In both cases, the anomaly was eliminated after a single application of the node redistribution algorithm.

Our final example, a multi-element airfoil, is displayed in Fig. 9 to demonstrate the prowess of the program used to implement the method.

Discussion and Conclusions

The effect of node distribution on results is not often discussed in the literature. Hess[1] gives a few results which indicate the effect can sometimes be substantial, but not nearly to the extent observed in the present study. From private communication with several of the authors of the present paper's references, and some limited experiments of our own with the classical constant-singularity-strength flat-panel method,[4] the subsurface panel method seems to be unusually sensitive to node distribution.

The cause of our oversensitivity to node distribution is not known. It is not the case, as has been suggested, that we are not satisfying the Kutta condition; the velocities we calculate are properly directed near the trailing edge. Nor does it seem to have to do with the $O(s \ln s)$ behavior of the velocity near the nodes. Similar results were obtained when we used cubic distributions of sources and vortices to reduce the singularity

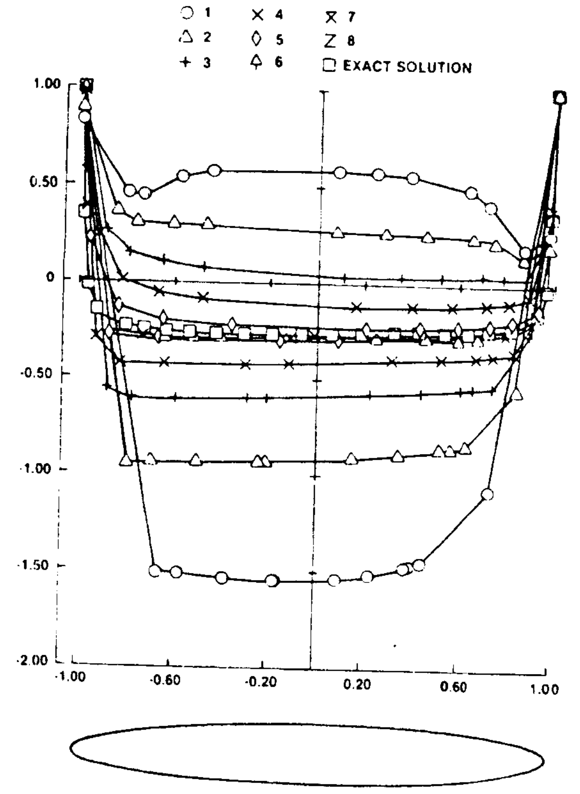

Fig. 5 Pressure distributions in successive stages of node redistribution process for ellipse of thickness ratio 0.125, starting with random distribution, 24 panels. Numbers indicate successive solutions.

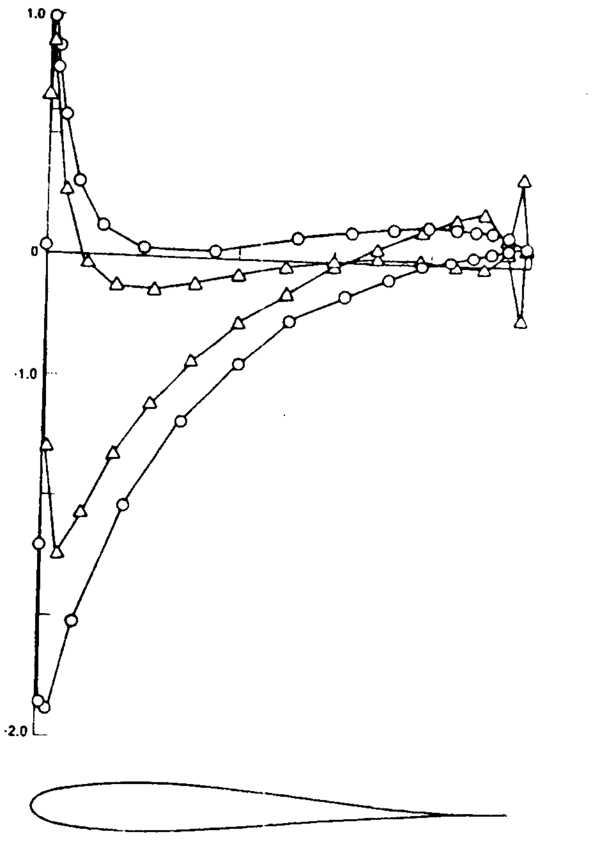

Fig. 6 Pressure distributions on simple uncambered airfoil with thickness proportional to $\sqrt{x}(1-x)^2$, angle of attack = 5 deg. Triangles obtained with cosine node distribution, circles after 4 node redistributions, 32 panels.

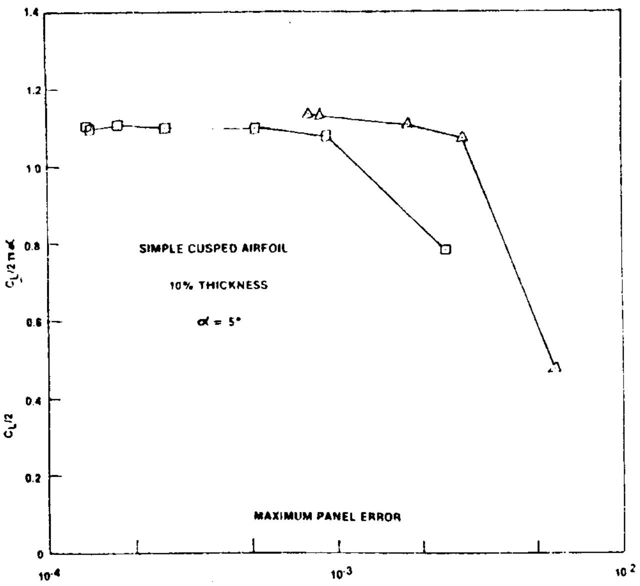

Fig. 7 History of lift coefficient during node redistribution process for airfoil of Fig. 6. Nodes initially distributed by cosine formula Eq. (11). Triangles, 32 panels; squares, 64 panels.

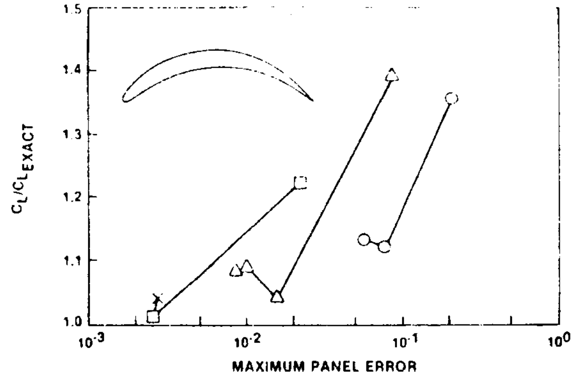

Fig. 8 History of lift coefficient during node redistribution process for highly cambered Karman-Trefftz airfoil (22% camber, 10% thickness) at zero angle of attack. Nodes initially distributed by equally spacing angular variable in circle plane. Circles, 16 panels; triangles, 32 panels; squares, 64 panels.

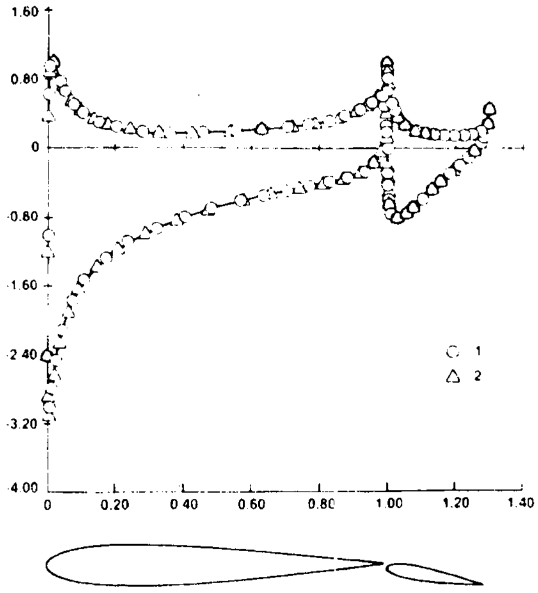

Fig. 9 Pressure distributions on two-element airfoil consisting of NACA 0012 sections: nose of flap 1% of wing chord below wing trailing edge; flap chord 30% of wing chord; flap deflection 10 deg, angle of attack 3 deg. Numbers indicate successive stages of redistribution process.

to $O(s^2 \ln s)$ and to make dV_n/ds vanish at the nodes (along with V_n itself). On the other hand, if we compute, a posteriori, the velocity induced by the panels at points along the body surface, we find that our worst solutions are characterized by a large amount of leakage.

In order to eliminate this problem, we tried to control the normal velocity component in a way that would account for the velocity induced by all the panels rather than just the local flow-tangency condition. Simply replacing Eq. (5) by one which would set the panel-induced normal velocity component to zero leads, as is fairly well known, to an ill-conditioned matrix and to oscillations in the velocity from node to node. Similar results were obtained when we sought to minimize, with respect to the tangential velocity components V_{t_i}, the integral along the inside of the panels of either the square of the velocity component normal to the panels or the square of the magnitude of the velocity. An attempt to make the potential constant inside the panels also led to an ill-conditioned matrix. As would be expected our parameterizing the source and vortex strengths with derivatives of the potential diminished the diagonal dominance of the matrix, enough to give oscillatory answers. Less well understood are the failures of the results to improve when the equation set was amplified by the addition of requirements that the net source strength vanish, or that the integral of $\partial\phi/\partial n$ along the inside of the body surface vanish (which is required to make the solution of the internal problem unique when its boundary condition is that the tangential velocity vanish on the inside of the body surface).

Late in the course of the research reported herein, it was recognized that the parameterization of the source and vortex strengths in terms of the nodal velocity components as described by Eqs. (2-4) was not unique in so far as obtaining a continuous velocity field is concerned. As noted in the Appendix, the V_{n_j} and V_{t_j} in Eq. (3) can be replaced by arbitrary functions of the node indices without altering our conclusions so far as continuity is concerned. In particular, we can devise a continuous version of the Douglas-Neumann method[4] by replacing the V_{t_j} by say, a constant Γ and the V_{n_j} by variables S_j, and determining those unknowns so as to make the panel-induced normal velocity component cancel the normal component of the onset flow at every node, and to satisfy a Kutta condition (such as equality of tangential velocity components at the trailing edge). The results we obtained with this method were even worse than those reported herein possibly because of reduced diagonal dominance in the coefficient matrix. As shown in the Appendix, the diagonal coefficient of the matrix associated with Eq. (5) (the coefficient of V_{t_i}) is

$$-1 + 1/2\pi(\nu_{i-1} + \nu_i)$$

in which $(\nu_{i-1} + \nu_i)$ is the angle subtended at the ith node by the $(i-1)$th and $(i+1)$th nodes, an angle that is generally less than π, much less so at the leading- and trailing-edge nodes. In our subsurface version of the Douglas method, the corresponding coefficient is simply

$$(\nu_{i-1} + \nu_i)$$

which can be relatively small.

Kemp[5] has devised a panel method very similar to the present one, in that it yields a continuous body-surface velocity distribution. His "loading vector" is essentially the nodal tangential velocity V_{t_i} of the present method, and he sets the nodal normal velocity component V_{n_i} in accordance with the local flow tangency condition, as do we. A major difference is that Kemp determines the V_{t_i} so that the velocity induced by the panels is normal to the panels at their midpoints. Following publication of his report, we performed some limited experiments with Kemp's method. For symmetric flows past ellipses, we found it considerably more accurate than the present method. However, it seems to share our sensitivity to node distribution, yielding spurious results when the nodes were distributed randomly on the ellipse, and for an airfoil with a cusped trailing edge. Our node redistribution algorithm did not help in such cases. Of course, it could be that our implementation of Kemp's method was in error. In any case, satisfaction of boundary conditions at panel midpoints, while no problem in two dimensions, complicates the treatment of three-dimensional problems. As will be discussed in the epilogue which follows, use of the nodes as the sole control points leads to a very attractive singularity spline.

It is hoped that the evidence presented on the utility of the node redistribution scheme is convincing. In every case we have tried, it has enabled us to overcome the sensitivity of the method to the starting node distribution. Except when we play with random distributions, five or fewer iterations are sufficient to reach our criteria for terminating the redistribution process. Of course, this means that the method may require as much as six times the computation time of other methods for the same number of nodes, without any improvement in accuracy relative to higher-order methods like those of Hess,[1] Johnson and Rubbert,[2] and Bristow.[3] Therefore, the method is of practical interest only as a prototype of a method for three-dimensional flows.

Epilog

Whatever their worth for two-dimensional flows, panel methods are much more interesting in three-dimensional situations, where their ability to treat complicated geometries far exceeds that of currently available field methods. A three-dimensional version of the subsurface panel method described herein would enhance these advantages considerably. We have such a version in the debugging stage and enumerate here some of its features, since it may be of interest to know how much of the existing two-dimensional analysis which is the subject of this paper can be carried over to the three-dimensional case.

The method is based on distributions of sources and vortices (see Ward[6] for the basic equation) on plane triangular panels whose vertices are nodes on the body surface. Their strengths are components of the total fluid velocity on the outside of the panels and are assumed to vary linearly over the panels. The parameters of the source and vortex strengths are then the three components of the body-surface velocity distribution at the nodes which are vertices of the panel.

Since the velocity component normal to the body surface is known, we have two unknown singularity-strength parameters per node. For a given set of nodes, this gives us about twice as many unknowns as would be dealt with by other panel methods. This disadvantage may be overcome by the extremely local nature of our singularity splines; on any panel, our source and vortex strengths depend only on parameters associated with the vertices of that panel. Thus, as noted earlier, our effective mesh size may be considerably smaller than that of another panel method which uses the same node distribution.

The use of triangular panels greatly simplifies the geometry problem. All we must know about the body are its coordinates and the direction of its surface normal at each node. No approximation need be made for the body shape between nodes, even in calculating forces and moments. To be sure, we do require continuity of the body surface velocity, which excludes from current consideration flows past wings of zero thickness and other idealized problems.

The method yields a continuous body-surface velocity distribution. This will allow an estimate of the deviation from linearity of the velocity distribution on the panels, just as the two-dimensional case. At this point, we do not know wh would be the optimal way to use such information to impro the node distribution, but that remains well within the reali of possibility. For example, we could use the prese algorithm directly to redistribute the nodes in a given ro and/or column. If the number of iterations required to ci cumvent the sensitivity of this method to node distributio which must be assumed to be as bad in the two-dimension case, can be kept to the five or fewer required in the tw dimensional case, the simplification of the singularity spline and elimination of the geometry problem should make th subsurface approach quite competitive in three-dimension situations.

Appendix

Let $V_j(x,y;\theta)$ be the contribution of the jth panel to th component of velocity in the direction θ at $P(x,y)$. T evaluate V_j, it is helpful to introduce local coordinate oriented with the jth panel:

$$x^* = (x-x_j)\cos\beta_j + (y-y_j)\sin\beta_j$$

$$y^* = (y-y_j)\cos\beta_j - (x-x_j)\sin\beta_j \qquad \text{(A1)}$$

Then, if u^* and v^* are the velocity components at P along the (x^*, y^*) axes,

$$V_j = u^*\cos(\theta-\beta_j) + v^*\sin(\theta-\beta_j) \qquad \text{(A2)}$$

Differentiating Eq. (1) and taking the source and vortex strengths to follow the linear laws of Eqs. (2), we find

$$\begin{pmatrix} u^*(x^*,y^*) \\ v^*(x^*,y^*) \end{pmatrix} = \begin{pmatrix} u_0 & v_0 & u_1 & v_1 \\ v_0 & -u_0 & v_1 & -u_1 \end{pmatrix} \begin{pmatrix} \sigma_0 \\ \gamma_0 \\ \sigma_1 \\ \gamma_1 \end{pmatrix} \qquad \text{(A3)}$$

where

$$u_0(x^*,y^*) = \frac{1}{2\pi} - \left(1-\frac{x^*}{\ell_j}\right)f_\ell - \frac{y^*}{\ell_j}f_t$$

$$u_1(x^*,y^*) = \frac{1}{2\pi} - \frac{x^*}{\ell_j}f_\ell + \frac{y^*}{\ell_j}f_t$$

$$v_0(x^*,y^*) = \left(1-\frac{x^*}{\ell_j}\right)f_t - \frac{y^*}{\ell_j}f_\ell$$

$$v_1(x^*,y^*) = \frac{x^*}{\ell_j}f_t + \frac{y^*}{\ell_j}f_\ell \qquad \text{(A4)}$$

and

$$f_\ell = (1/2\pi)\ln(r_{j+1}/r_j) \qquad \text{(A5)}$$

$$f_t = (1/2\pi)\nu_j \qquad \text{(A6)}$$

Here r_j is the distance from the jth node to $P(x,y)$ and ν_j is the angle subtended at P by the jth panel.

When P approaches either the jth or $(j+1)$th node, f_ℓ blows up and f_t depends on the direction of approach. However, if we consider the jth and $(j-1)$th panels in combination, then, near the jth node, we find

$$2\pi(V_{j-1}+V_j) = \ln r_j\{\sigma_{0_j}\cos(\theta-\beta_j)$$

$$-\sigma_{t_{j-1}}\cos(\theta-\beta_{j-1}) - \gamma_{0_j}\sin(\theta-\beta_j) + \gamma_{t_{j-1}}\sin(\theta-\beta_{j-1})\}$$

$$+\nu_j\{\gamma_{0_j}\cos(\theta-\beta_j)+\sigma_{0_j}\sin(\theta-\beta_j)\}$$

$$+\nu_{j-1}\{\gamma_{0_{j-1}}\cos(\theta-\beta_{j-1})+\sigma_{0_{j-1}}\sin(\theta-\beta_{j-1})\}$$

$$+\text{terms regular near the } j\text{th node} \qquad \text{(A7)}$$

Here subscripts j and $j-1$ have been put on the source and vortex strengths to indicate the panel with which they are associated; recall that the singularity strengths are not continuous from one panel to the next.

On substituting for the σ's and γ's in Eq. (A7) from Eq. (3), we find that the logarithmically singular terms cancel one another, while the remaining terms reduce to

$$V_{j-1}+V_j=1/2\pi(\nu_j+\nu_{j-1})[V_{n_j}\sin(\theta-\theta_j)+V_{t_j}\cos(\theta-\theta_j)]$$

$$+\text{terms regular near the } j\text{th node} \qquad \text{(A8)}$$

While ν_j and ν_{j-1} are indeterminate as P approaches the jth node, their sum approaches the angle subtended at the jth node by the $(j-1)$th and $(j+1)$th nodes. Thus the velocity due to the linear singularity distributions Eqs. (2), with parameters given by Eq. (3), is continuous on and outside the panels. Near the nodes, it has an $s\ln s$-type behavior. It is easy to show that these same results would obtain if V_{n_i} and V_{t_i} in Eq. (3) were replaced (consistently) by arbitrary functions of the node indicator i.

To apply these results to Eq. (5), simply let θ in Eq. (A8) become θ_i. Then the integral in Eq. (5) becomes

$$1/2\pi(\nu_i+\nu_{i-1})V_{t_i}+\text{terms regular near the } i\text{th node}$$

Therefore, in forming the coefficient matrix which governs the nodal tangential velocity components, we simply set $\ln r_j$ and ν_j equal to zero whenever they threaten to become singular and indeterminate, respectively, and compensate by adding $(\nu_i+\nu_{i-1})/2\pi$ to the coefficient of V_{t_i}.

Acknowledgment

This research was supported in part by NASA Ames Research Center, under Grant NSF-2316. A large fraction of the work was completed while the first author was a guest of A. R. Seebass, first at the University of Arizona and then at the University of Washington. It was a pleasure to acknowledge many simulating conversations with Seebass and his colleagues, and also the additional support given the research during that phase of it by the Office of Naval Research, under Contract N00014-76-0182.

References

[1] Hess, J. L., "Higher Order Numerical Solutions of the Integral Equation for the Two-Dimensional Neumann Problem," *Computational Methods in Applied Mechanics and Engineering*, Vol. 2, 1973, pp. 1-15.

[2] Johnson, F. T. and Rubbert, P. E., "Advanced Panel-type Influence Coefficient Methods Applied to Subsonic Flows," AIAA Paper 75-50, 1975.

[3] Bristow, D. R., "Recent Improvements in Surface Singularity Methods for the Flowfield Analysis about Two-Dimensional Airfoils," AIAA Paper 77-641, 1977.

[4] Hess, J. L., "The Problem of Three-Dimensional Lifting Potential Flow and its Solution by Means of Surface Singularity Distribution," *Computational Methods in Applied Mechanics and Engineering*, Vol. 4, 1974, pp. 283-319.

[5] Kemp, W. B. Jr., "A Vector-Continuous Loading Concept for Aerodynamic Panel Methods," NASA TM 80104, 1979.

[6] Ward, G. N., *Linearized Theory of High-Speed Flow*, Cambridge University Press, 1955, pp. 40-42.

80

Ann. Rev. Fluid Mech. 1980. 12: 181-222

TRANSONIC FLOW PAST OSCILLATING AIRFOILS[1]

*8157

H. Tijdeman
Nationaal Lucht-en Ruimtevaartlaboratorium, Amsterdam, The Netherlands

R. Seebass
Departments of Aerospace and Mechanical Engineering, and Mathematics,
University of Arizona, Tucson, Arizona 85721

INTRODUCTION

Under certain conditions structures like airplane wings and tail surfaces may experience vibrations of an unstable nature. This phenomenon, called "flutter," is an aeroelastic phenomenon governed by the interaction of the elastic and inertial forces of the structure with the unsteady aerodynamic forces generated by the oscillatory motion of the structure itself. In general, two or more vibration modes are involved, e.g. bending and torsional vibrations of a wing, which, under the influence of the unsteady aerodynamic forces, interact with each other in such a way that the vibrating structure extracts energy from the passing airstream. This leads to a progressive increase in the amplitude of vibration and may end with the disintegration of the structure.

For a given wing structure the aerodynamic forces increase rapidly with flight speed, while the elastic and inertial forces remain essentially unchanged. Normally there is a critical flight speed, the "flutter speed," above which flutter occurs. Because of the potentially disastrous character of this phenomenon, flutter speeds of aircraft must be well outside their flight envelope. In many cases this requirement is the determining factor in the construction of wings and tail surfaces. Because the vibration characteristics of the structure at zero airspeed can be determined accurately by current numerical methods or by ground vibration tests, the

---

[1] The authors thank the NLR, the AFOSR, and the ONR for their support of this review and related studies.

0066-4189/80/0115-0181$01.00

81

accuracy of the flutter prediction depends mainly on the knowledge of the unsteady aerodynamic forces.

In subsonic and supersonic flight unsteady aerodynamic forces can be predicted reasonably well by theoretical and numerical means. For transonic flight, with its mixed subsonic-supersonic flow patterns, prediction methods are less advanced. The current practice for wings of general planform is still rather arbitrary, with interpolations and extrapolations being made on the basis of calculated airloads for pure subsonic and supersonic flow. And, in many cases, one must resort to very expensive wind tunnel experiments.

Currently there is a renewed interest in transonic flight for both military and civil aircraft. For military aircraft this stems from the need for a new generation of air combat aircraft, like the F-16 and F-17, which require an optimal maneuverability at transonic speeds. In civil aviation there is a great need for more efficient aircraft, made possible by technological advances that include the so-called supercritical wing. Such wings make it possible to cruise at transonic speeds without the usual drag penalty associated with the presence of shock waves. This is achieved by shaping the wing geometry in such a way that the transition from local flow regions with supersonic flow to the adjacent subsonic regions does not take place with strong shock waves as it does on the conventional-type wings, but with only very weak shock waves or even without them.

In the present review we describe the nature of transonic flows past oscillating airfoils and discuss recent developments in unsteady transonic flow calculations. We place emphasis on plane flows because most of the published studies deal with this type of flow. The first section starts with a general description of the flow past airfoils. Experimental results are then reviewed and used to illustrate the interaction between the steady and unsteady flow fields, the periodic motion of shock waves, and the effects of frequency and amplitude of oscillation. In the subsequent section we discuss the inviscid equations forming the basis of the various theoretical methods and review techniques for their solution, all essentially numerical. Viscous effects and calculation methods are then described. Finally, in the last section we assess the present status of the field and the future developments expected.

The reader should be aware of four related reviews. Landahl (1976) reviews the unsteady aspects of transonic flow, while a recent review of unsteady fluid dynamics by McCroskey (1977) also has informative sections on unsteady transonic flow and unsteady boundary layers. Computational aspects of steady and unsteady transonic flows are reviewed by Ballhaus (1978) and the dissertation of Tijdeman (1977) contains a more complete discussion of many of the topics addressed here.

FLOW PAST AIRFOILS

Steady Flow

A brief survey of the behavior of steady transonic flows past airfoils provides an introduction to the discussion of the transonic flow past oscillating airfoils. When the free-stream Mach number of a purely subsonic flow past a symmetrical airfoil is increased, the flow pattern usually develops in the manner sketched in Figure 1. The so-called critical Mach number M^* is reached when the maximum local Mach number in the flow becomes unity. Beyond the critical Mach number a supersonic region appears on the airfoil, which, in general, is terminated by a nearly normal shock wave through which the flow speed is reduced from supersonic to subsonic. With a further increase of the free-stream Mach number, the shock wave moves aft and the size of the supersonic region and the shock strength both increase. After the pressure jump through the shock wave has become sufficiently large, so-called shock-induced separation

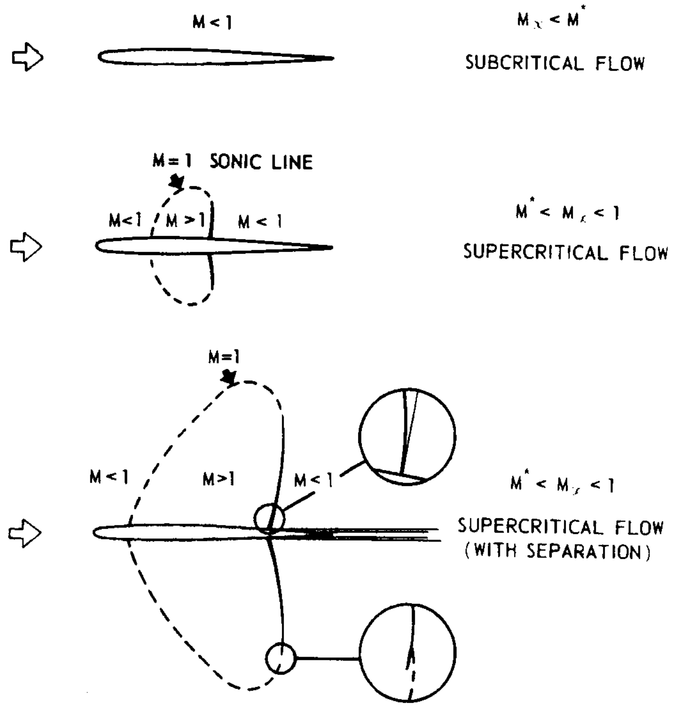

Figure 1 Influence of Mach number on flow pattern.

of the boundary layer occurs. For a turbulent boundary layer, this shock-induced separation starts when the local Mach number just upstream of the shock wave is about 1.25 to 1.3. When the boundary layer downstream of the shock wave separates completely, the flow around the airfoil is

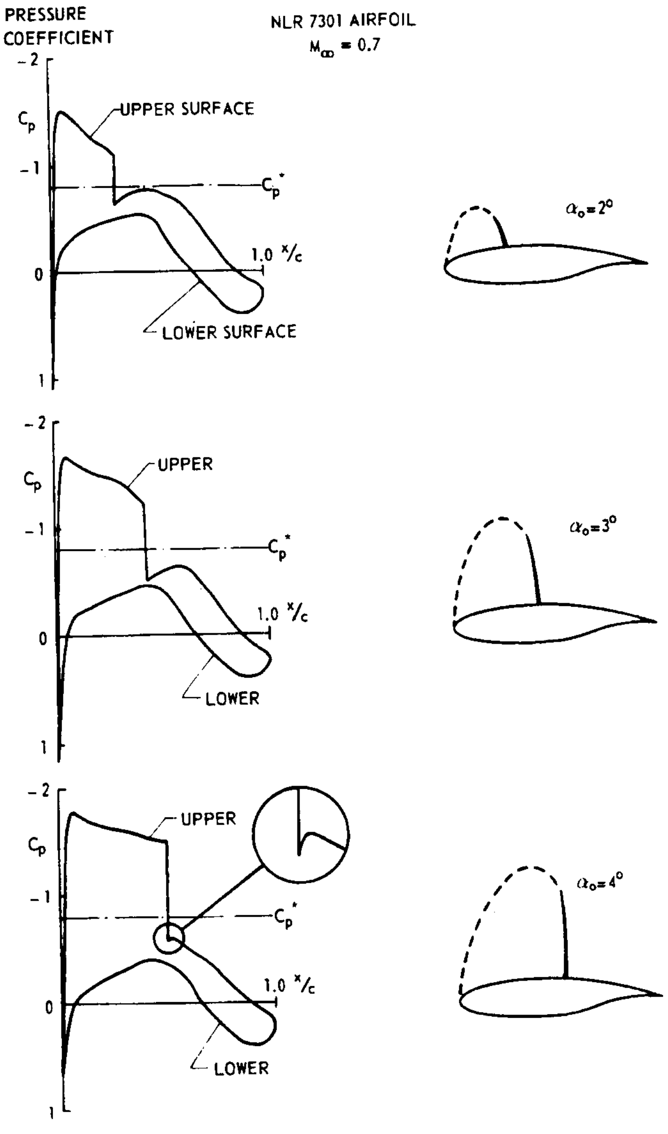

Figure 2 Influence of incidence on pressure distribution and flow pattern in transonic flow.

changed considerably, and often unsteady-flow phenomena such as "buffet" and "buzz" start to occur.

When an airfoil's incidence is increased at a supercritical Mach number, the flow changes in the manner sketched in Figure 2. Initially the airfoil carries a well-developed supersonic region on its upper surface, terminated by a shock wave. When the incidence is increased, the speed over the upper surface increases and the supersonic region and the shock wave develop in much the same way as described above for increasing free-stream Mach number. This example shows that small variations in incidence may lead to considerable changes in the pressure distribution, shock position, and shock strength.

Across the nearly normal shock wave that occurs on the airfoil, the velocity is reduced from supersonic to subsonic. In two-dimensional inviscid flow the foot of the shock wave must be normal to the airfoil. For a convex airfoil the pressure will increase and the Mach number will decrease with distance above the airfoil ahead of the shock wave. The pressures behind the shock, given by the Rankine-Hugoniot relations, must still balance the flow curvature demanded by the airfoil. This can only be accommodated if the shock wave has infinite curvature at its foot (Zierep 1966). This results in a rapid expansion there (logarithmically infinite pressure gradient); this expansion can often be noticed in surface pressure distributions of airfoils, where it manifests itself as the so-called Zierep cusp, or Oswatitsch-Zierep singularity, as sketched in Figure 2.

Usually transonic flow patterns are characterized by the presence of nearly normal shock waves on either the upper or the lower surface of the airfoil, or on both surfaces at the same time. Occasionally even two shock waves, one behind the other, occur. An exception to this rule is the flow around a so-called supercritical (shock-free) airfoil at its design condition. This type of airfoil is shaped in such a way that, for a specific combination of incidence and free-stream Mach number, the "design condition," the transition of the supersonic region to the adjacent subsonic regions takes place without a noticeable shock wave. This requires a careful tailoring of the airfoil so that a smooth recompression is obtained. Changes in the Mach number and angle of attack affect this tailoring, and away from the design condition the flow will normally have at least a weak shock wave. The flow past a supercritical airfoil in its design condition, shown in Figure 3, clearly reveals that small changes in incidence are sufficient to disturb the shock-free flow condition. An important question with respect to the practical application of supercritical airfoils is how gradually the transition from shock-free flow to the neighboring flow conditions with shock waves takes place, or, in other words, what are the margins within which the Mach number and incidence can be

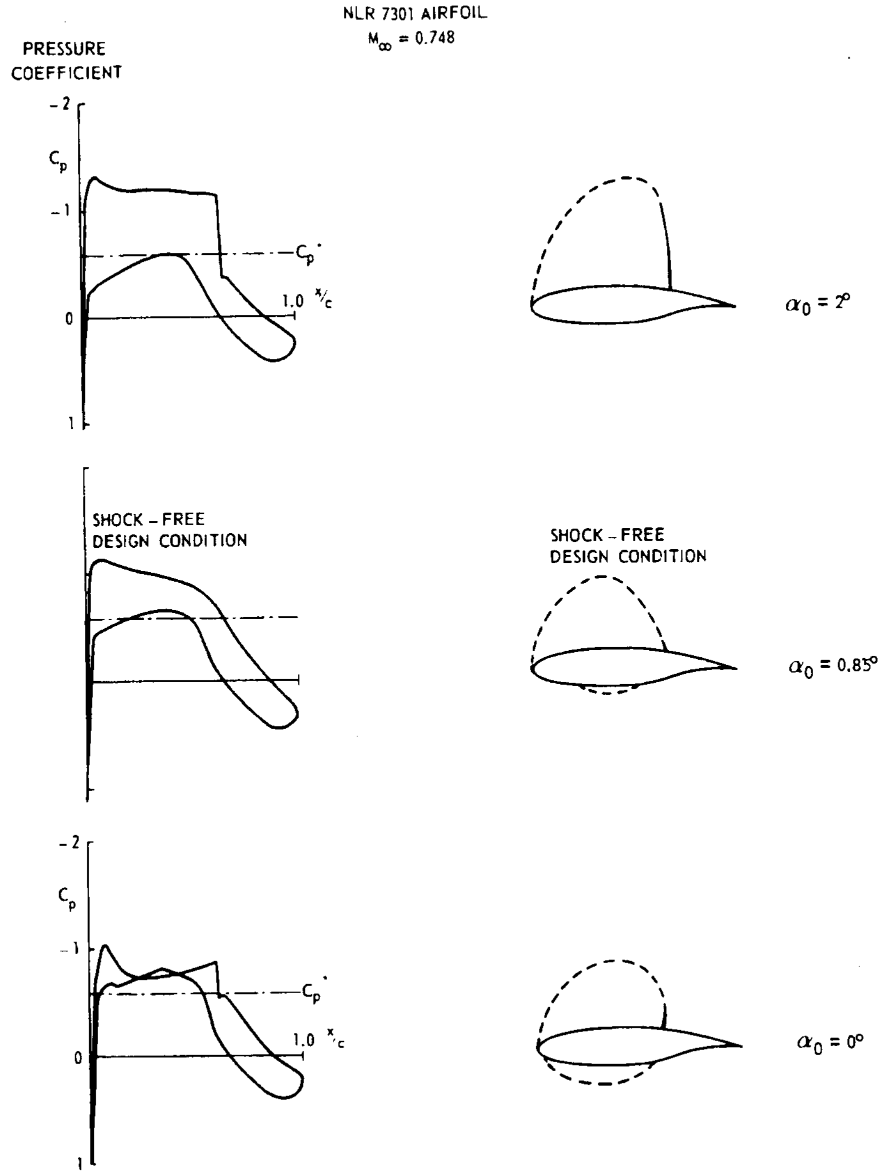

Figure 3 Influence of incidence on pressure distribution and flow pattern of a "shock-free" airfoil.

varied around the design condition without a serious deterioration of the favorably low-drag property of the shock-free flow condition.

An aspect that cannot be discarded when considering the flow past airfoils concerns the effects of viscosity. In an attached flow viscous effects are confined to a thin layer adjacent to the surface of the airfoil, the "boundary layer," and to its wake. In the boundary layer the velocity rises rapidly from zero at the surface to the local flow velocity at the outer edge. The boundary layer starts at the leading edge as a laminar boundary layer, which in cases of practical interest changes from laminar to turbulent after a small fraction of the chord (typically 5–10%). The presence of the boundary layer changes the effective contour of the airfoil and, thus, has an effect on the pressure distribution and the aerodynamic loading. The magnitude of this effect depends, among other things, on the Reynolds number, which is an important parameter for the growth of the boundary-layer thickness and the location of the transition point. The behavior of the boundary layer is of even more importance in transonic flow than in subsonic flow, since here it has a considerable influence on the position and strength of the shock wave.

Unsteady Flow

When an airfoil performs sinusoidal oscillations around a given mean position, the circulation and, hence, the lift force and local pressures show periodic variations. In order to keep the total vorticity constant (according to Helmholtz's theorem), each time-dependent change in circulation around the airfoil is compensated by the shedding of free vorticity from the trailing edge. This vorticity, which has the same strength as the change in circulation but is of opposite sign, is carried downstream by the flow as sketched in Figure 4. Due to the velocities induced by the free vortices around the airfoil, the instantaneous incidence of the airfoil is changed in such a way that the oscillating part of the lift lags behind the motion of the airfoil.

The main parameter governing the unsteady flow is the so-called reduced frequency k, defined as $k = \omega l/U_\infty$, which is proportional to the ratio of the chord length $2l$ and the wavelength L (see Figure 4). The reduced frequency is a measure of the unsteadiness of the flow; for

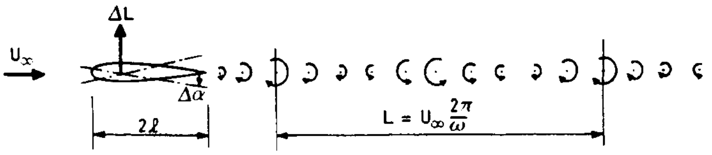

Figure 4 Flow around an oscillating airfoil.

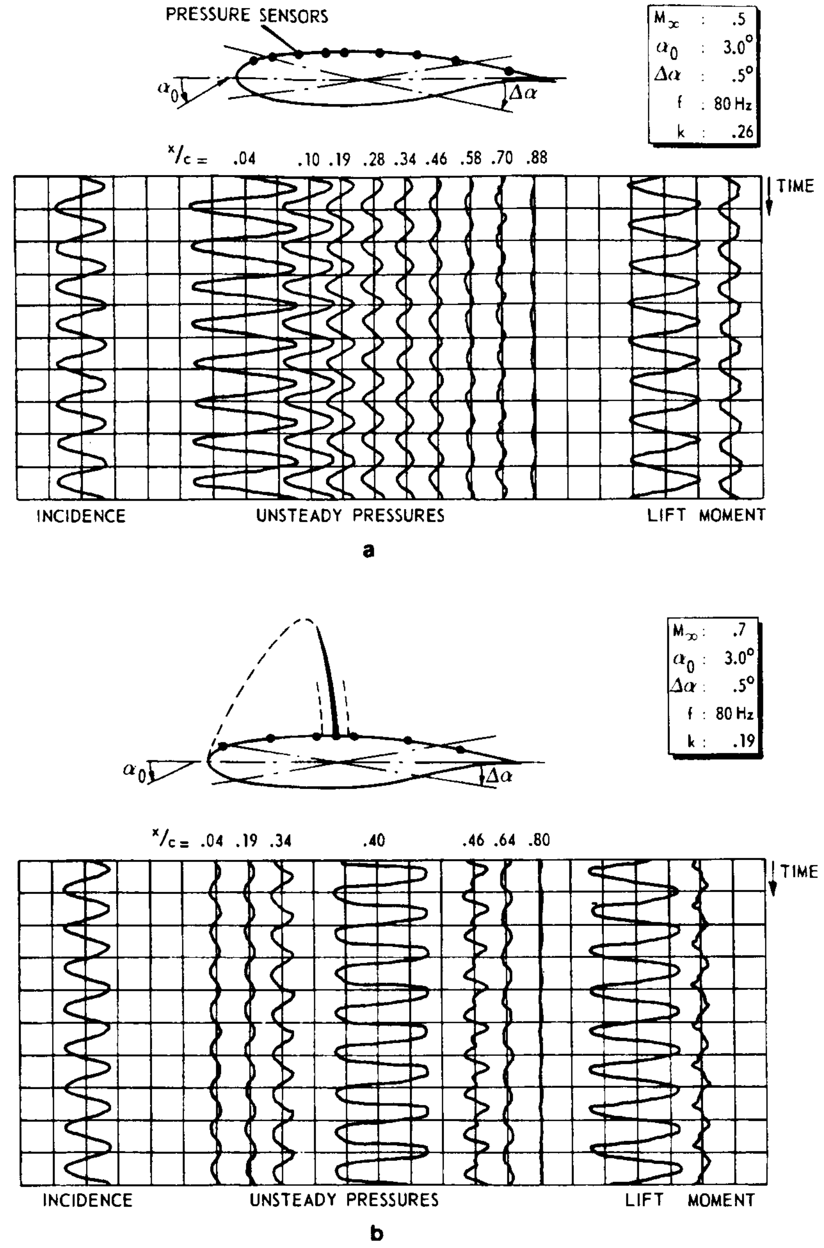

Figure 5 Unsteady pressure signals and overall loads on an oscillating airfoil: (*a*) subsonic flow; (*b*) transonic flow.

similarity of the flow past an oscillating full-scale airfoil and its wind-tunnel model representation it is required that the reduced frequencies be the same.

Figure 5*a* shows the time histories of the local pressures and the resulting lift and moment on an airfoil performing oscillations in pitch in a subsonic flow. Both the pressures and the overall loads show almost sinusoidal variations around their mean values. In this case the pressures and loads may be described by the first harmonic of a Fourier series, viz.,

$$p = p_s + \Delta p' \cos \omega t + \Delta p'' \sin \omega t = p_s + |\Delta p| \cos (\omega t - \varphi)$$

where p and p_s denote the local and mean pressures, while $\Delta p'$ and $\Delta p''$ are the components of the fundamental. The coefficient $\Delta p'$ can be interpreted as the actual pressure perturbation at the instant the oscillating airfoil reaches its maximum deflection, while $\Delta p''$ represents the pressure perturbation at the instant the airfoil passes its midposition.

This way of describing unsteady pressures or loads is valid only if the aerodynamic quantities vary sinusoidally in time, or, in other words, as long as a linear relationship exists between the displacement of the airfoil and the unsteady pressures. This is usually the case for moderately subsonic and supersonic flow, at least as long as the flow remains attached. For transonic flow, however, this is no longer true, particularly in the region of a shock wave, as illustrated in Figure 5*b*. In such cases one has to give the complete time history of the signals or to add higher harmonics to the Fourier series.

Nonlinear Character of Unsteady Transonic Flow

The combined influence of airfoil thickness, incidence, and amplitude of oscillation is different for moderately subsonic and supersonic flow than for transonic flow. For subsonic and supersonic flow both the equations and the corresponding boundary conditions can usually be linearized. This implies that the problem of an oscillating airfoil can be decomposed into a steady problem (thickness + incidence) and the unsteady problem of an infinitely thin plate oscillating in a uniform flow. The unsteady-flow problem can be treated independently of the steady-flow problem. The main parameters for the unsteady flow then are the reduced frequency k, the free-stream Mach number M_∞, and the mode of vibration.

For transonic flows at low to moderate reduced frequencies the equations governing the motion cannot be linearized. This implies that the unsteady flow field can no longer be treated independently of the steady flow field. For the aeroelastician this means a considerable complication. In addition to the aforementioned parameters for subsonic and supersonic flow, he has to consider also the mean steady flow field around the airfoil, which is determined by the geometry of the airfoil and its mean incidence with respect to the oncoming flow. For a normal flutter investigation in subsonic and supersonic flow, unsteady airloads already have to be computed for 50 to 100 combinations of reduced frequency, free-stream Mach number, and vibration mode. For the transonic flow regime this number increases considerably because then the computations have to be performed for different values of the incidence. The complication becomes even worse if it is not possible to linearize the unsteady transonic-flow problem by assuming the unsteady flow to be a small perturbation superimposed upon a given mean steady flow field. Then the unsteady airloads are no longer linear functions of the amplitude of motion, which implies that in aeroelastic calculations, where the unsteady aerodynamic forces have to be combined with inertial, stiffness, and damping forces of the aircraft structure, linear systems of equations no longer apply. So it is quite evident that from the practical point of view there is a strong demand for some sort of linearization. Of course, in theory, this linearization can always be enforced by making the amplitude of oscillation small enough, but the question arises whether the amplitudes that occur in practice will be that small.

OBSERVATIONS FROM EXPERIMENTS

Results Available

The first transonic-flutter accidents occurred during World War II with aircraft of advanced design at that time that were able to penetrate the transonic regime during a diving flight. These accidents gave the transonic regime its veil of mysticism and contributed to the many myths about the difficulties associated with crossing the "sound barrier." At that time it was impossible to get aerodynamic data for the transonic speed range because there were no transonic wind tunnels and there was little or no support from theory. During the first fifteen years after the war, the knowledge of transonic flows improved considerably through experience gained with research aircraft, like the Bell X-1, and the development of transonic wind tunnels with slotted and porous walls. The latter greatly enlarged the possibilities for obtaining aerodynamic data under controlled conditions. From that period stem a number of unsteady aerodynamic load measurements on oscillating wind tunnel models. The majority of these experiments had an ad hoc character and were directly related to problems encountered in flight.

The first measurements of local unsteady pressures on an oscillating wind tunnel model in transonic flow were made by Erickson & Robinson (1948). Their method, in which electrical pressure cells installed flush with the model surface are used, was applied successfully by Wyss & Sorenson (1951) and their colleagues at the then NACA. Although they actually measured the pressures on oscillating control surfaces and on airfoils and wings oscillating in pitch, only overall aerodynamic coefficients were published, along with some typical oscillograph records of local pressure fluctuations. The first detailed unsteady pressure distributions in the transonic regime were reported by Lessing, Troutman & Meness (1960) and by Leadbetter, Clevenson & Igoe (1960).

A series of exploratory wind tunnel investigations on some characteristic airfoil sections was initiated by the NLR in the late sixties. With the aid of a special technique in which scanning valves and pressure tubes were used (Bergh 1965), steady and unsteady pressures were measured on the conventional NACA 64A006 airfoil with oscillating trailing-edge flap, on the shock-free NLR 7301 airfoil oscillating in pitch (Tijdeman & Bergh 1967, Tijdeman & Schippers 1973, Tijdeman 1977), and on the same airfoil with an oscillating control surface (Schippers 1978). Parallel with this basic research program, unsteady pressure distributions were measured on a variety of three-dimensional wings, under contract with aircraft industries (see, for example, Bergh, Tijdeman & Zwaan 1970, Tijdeman 1976). About the same time Triebstein (1969, 1972) performed experiments on a rectangular wing with and without control surface. In his tests he also applied the measuring technique with tubes and scanning valves. In France, successful tests on a supercritical airfoil section with control surface were reported by Grenon & Thers (1977), who used a large number of miniature pressure sensors placed inside the model. Recently, a similar technique was applied by Davis & Malcolm (1979), who performed exploratory tests on the conventional NACA 64A010 airfoil and the NLR 7301 airfoil of Figure 3. In the NASA experiments a sophisticated test rig that makes it possible to drive the models into pitch as well as plunge motions was used; moreover, the tests could be performed at large Reynolds numbers. Finally, a preliminary series of measurements on an NACA 64A010 airfoil oscillating in pitch has been reported (Davis 1979).

Interaction Between the Steady and Unsteady Flow Fields

Some of the results for an airfoil with flap (Tijdeman 1977) will be recalled here to demonstrate the mechanism of the interaction between the steady and unsteady flow fields. This example is chosen because it lends itself well to physical interpretation.

Low-speed steady and unsteady pressure distributions on the symmetrical NACA 64A006 airfoil with flap are shown in Figure 6-1. Figure 6-1*a* shows the steady pressure distributions along the upper surface of the airfoil for three flap angles, viz., − 1.5, 0, and 1.5 degrees, respectively.

From these steady distributions, the "quasi-steady" pressure differences,

$$\Delta C_p = \frac{C_p(\delta_0 - \Delta\delta) - C_p(\delta_0 + \Delta\delta)}{2\Delta\delta},$$

are determined, and the resulting chordwise distribution is shown in Figure 6-1*b*. This quasi-steady pressure distribution can be interpreted as the "unsteady" pressure distribution when the oscillations are infinitely slow. Figure 6-1*c* depicts the first harmonic of the unsteady pressure distribution for a frequency of 120 Hz and an amplitude of about one degree. The unsteady pressure distribution very much resembles the quasi-steady distribution; both show the characteristic peaks at the leading edge of the airfoil and at the hinge axis at 75% chord. For the unsteady example the results of "thin-airfoil theory," assuming an infinitely thin

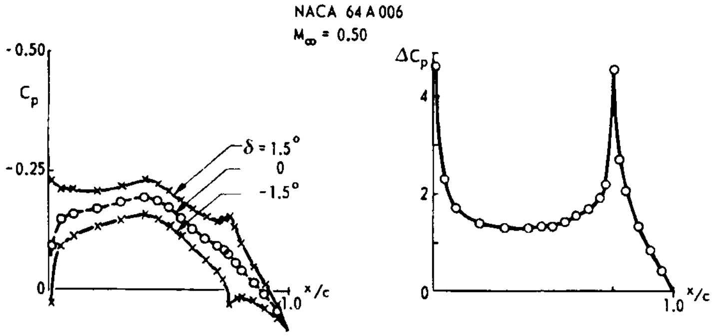

a: STEADY

b: QUASI-STEADY ; k = 0

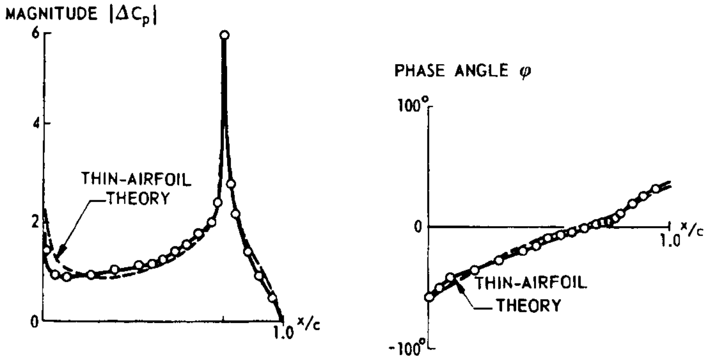

C : UNSTEADY ; f = 120 Hz ; k = 0.392

Figure 6-1 Steady, quasi-steady, and unsteady pressure distributions in low subsonic flow.

wing in a uniform main flow, are also given. At this low speed, the agreement with the experimental amplitude and phase distributions is satisfactory, which indicates that the unsteady-flow problem can be treated independently of the steady flow pattern around the airfoil.

Results for the same configuration in high subsonic flow are shown in Figure 6-2. Around the 50% chord point, where the flow is almost critical, a bulge occurs in the magnitude of the measured distribution of both the quasi-steady and unsteady pressures. This bulge and the phase variation are not predicted by the thin-airfoil theory. Another characteristic feature is that the phase lag on the front part of the airfoil is consistently larger than that given by the theory.

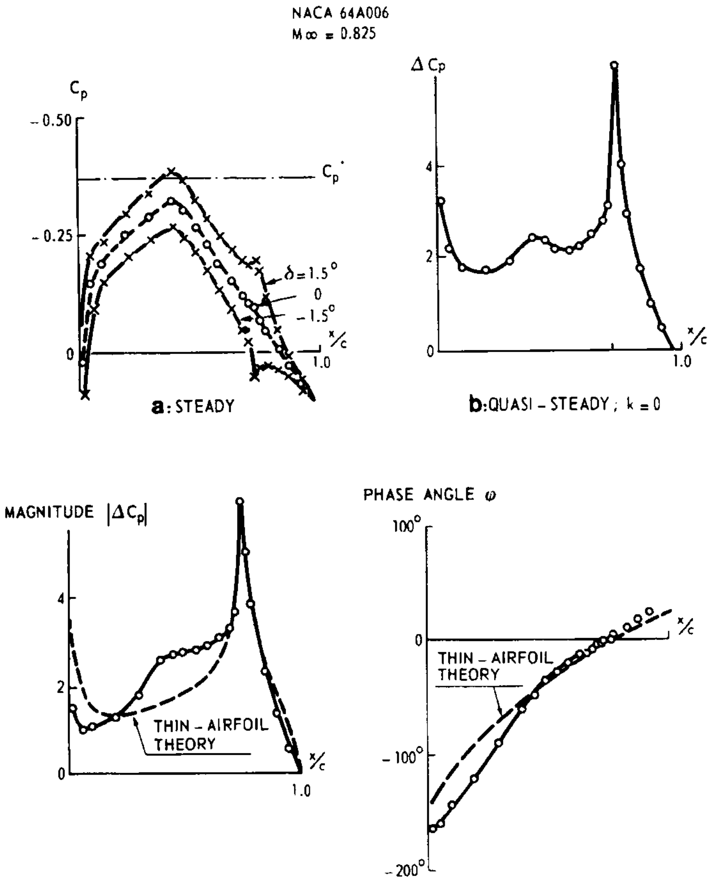

a: STEADY

b: QUASI - STEADY ; k = 0

c: UNSTEADY ; f = 120 Hz ; k = 0.248

Figure 6-2 Steady, quasi-steady, and unsteady pressure distributions in high subsonic flow.

Results that are typical for a transonic flow with a nearly normal shock wave are given in Figure 6-3. It is clear from this pressure distribution that a change in flap angle is followed by a shift in shock position, and this leads to a peak in the magnitude of the quasi-steady and unsteady pressures in the vicinity of the shock. This peak, which is a significant contribution to the overall unsteady lift and moment, cannot, of course, be predicted by a fully linear theory. Note that the pressure perturbations in front of the shock wave are smaller than those predicted by theory,

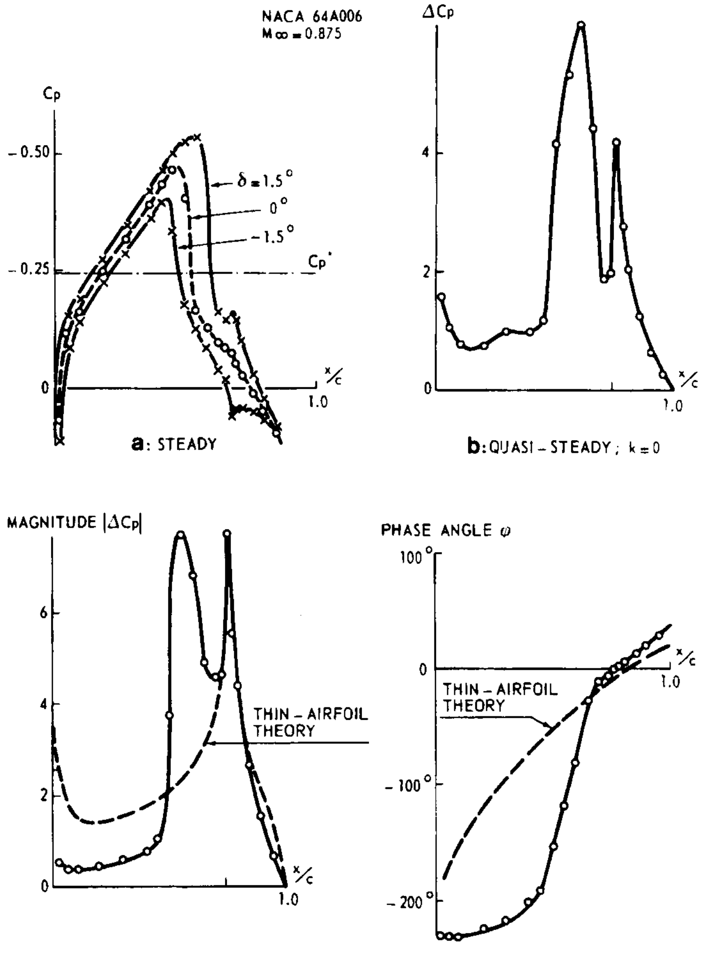

C: UNSTEADY; f = 120 Hz; k = 0.234

Figure 6-3 Steady, quasi-steady, and unsteady pressure distributions in slightly supercritical flow.

and that the measured phase variation shows a sharp change in gradient in the region of the shock wave.

To illustrate that the observed effects in the preceding examples for high subsonic and transonic flow are caused by the interaction of the steady and unsteady flow field, a graphical experiment has been performed. A pulsating pressure disturbance is assumed to be located at the airfoil's hinge axis. Acoustic waves propagate from this disturbance into the surrounding nonuniform flow. The acoustic wave patterns, as obtained with the well-known construction of Huygens for the airfoil under consideration, are shown in Figure 7. This figure displays the position of the wavefronts after equal time intervals Δt for two different Mach numbers. The part of the figure above the airfoil depicts the time histories of the wavefronts in the actual flow field. Below the airfoil the same wavefronts are shown, but now for a steady uniform flow field in which the local Mach number everywhere is equal to the free-stream Mach number. The corresponding travel times (time lags) are given in the diagrams at the bottom of Figure 7. At $M = 0.8$ the flow is subcritical and the upstream-moving wavefronts encounter more "head wind" in the actual flow than in the

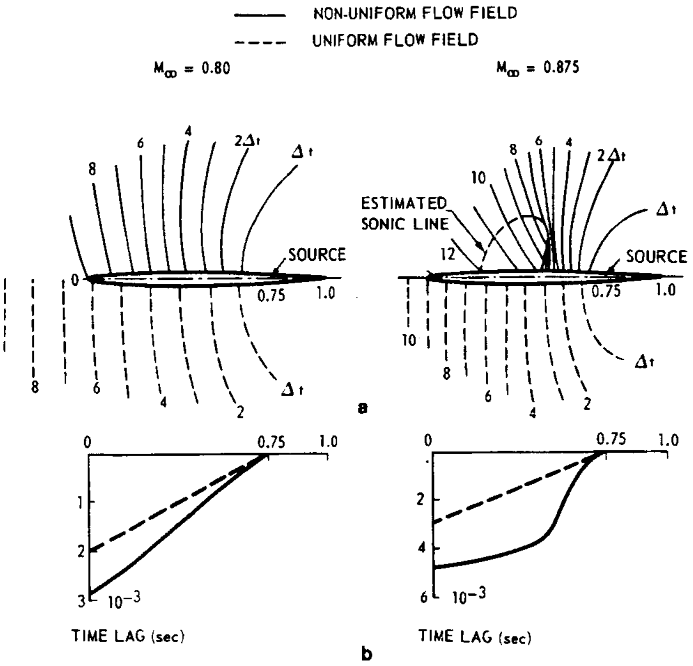

Figure 7 Upstream propagation of wavefronts generated by a source at the hinge axis: (*a*) wave propagation; (*b*) time lag derived from wave pattern.

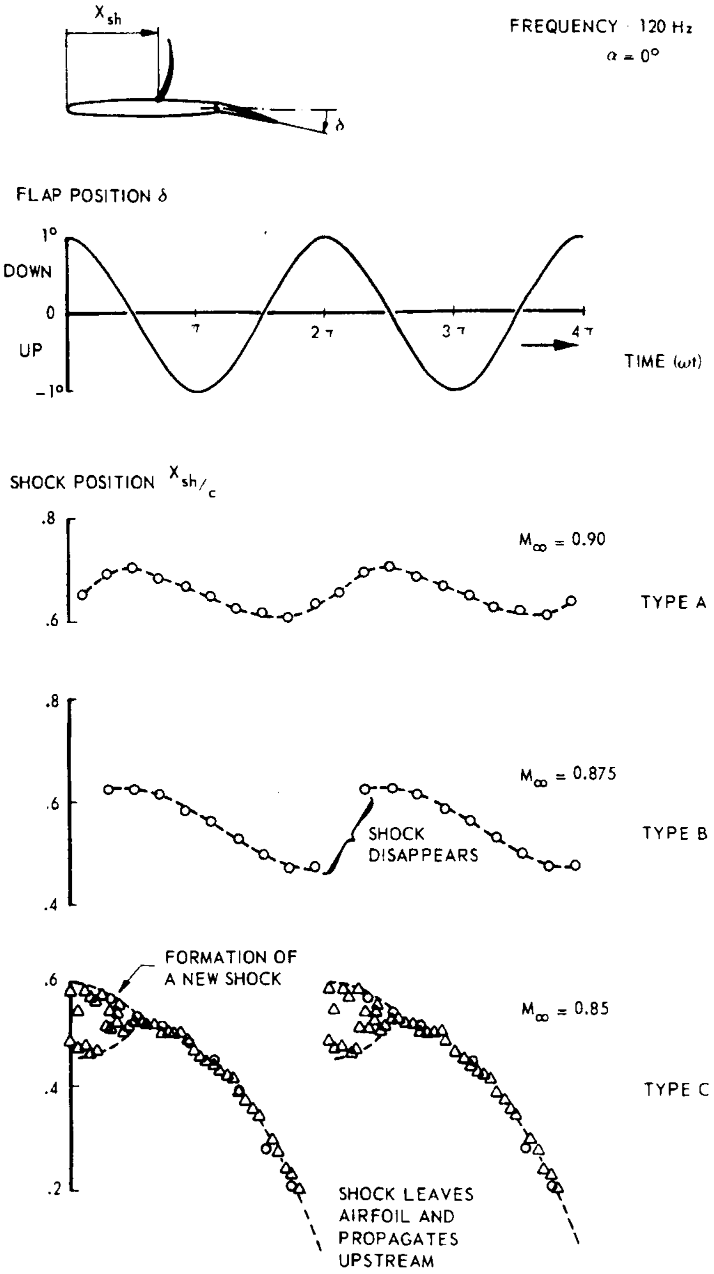

Figure 8 Observed types of periodic shock-wave motion.

96

uniform flow, as can be seen from the closer spacing of the fronts and from the time-lag curves. Moreover, the velocity gradients normal to the chord in the actual flow cause a forward inclination of the wavefronts. When it is recognized that the spacing of the wavefronts is a measure of the intensity of the local pressure perturbation gradient, while the time lag is a measure for the phase shift, it becomes clear that the high subsonic effects observed in Figure 6-2 can be attributed mainly to the influence of the nonuniform steady flow field. At $M = 0.875$, when a supersonic region is present and terminated by a shock wave, the inclination of the wavefronts is essential to enable the waves to penetrate the region of supersonic flow. Some portions of the upstream-moving wavefronts close to the airfoil surface merge into the shock while other portions bend around the top of the shock and penetrate the supersonic region. This is reflected in the time-lag curve. Since the energy content of the wavefronts penetrating the supersonic region has decreased, due to geometric dilatation, only small pressure changes occur in front of the shock wave. These findings correlate very well with the effects observed in the wind tunnel results presented in Figures 6-2 and 6-3. Note that the main contribution to the peak at the shock position is due to the oscillatory displacement of the shock waves, which is not included in this simple graphical result.

Periodic Motion of Shock Waves

From the preceding discussions it should be clear that the periodic motion of shock waves makes an important contribution to the overall unsteady airloads. Optical flow studies on an airfoil with flap (Tijdeman 1976) have shown that in the oscillating case three different types of periodic shock-wave motions can be distinguished. They have the following main characteristics, which are depicted in Figure 8.

SINUSOIDAL SHOCK-WAVE MOTION (TYPE A) This type resembles, more or less, the shock-wave motions discussed by Lambourne (1958) and Nakamura (1968). The shock moves almost sinusoidally and remains present during the complete cycle of oscillation, although its strength varies. Due to the dynamic effect, phase shifts exist between the model motion and shock position and between shock strength and shock position. The maximum shock strength is not reached during the maximum downstream position of the shock, as in quasi-steady flow, but during its upstream motion.

INTERRUPTED SHOCK-WAVE MOTION (TYPE B) This motion is similar to Type A, but now the magnitude of the periodic change in shock strength becomes larger than the mean steady shock strength and, as a consequence, the shock wave disappears during a part of its backward motion.

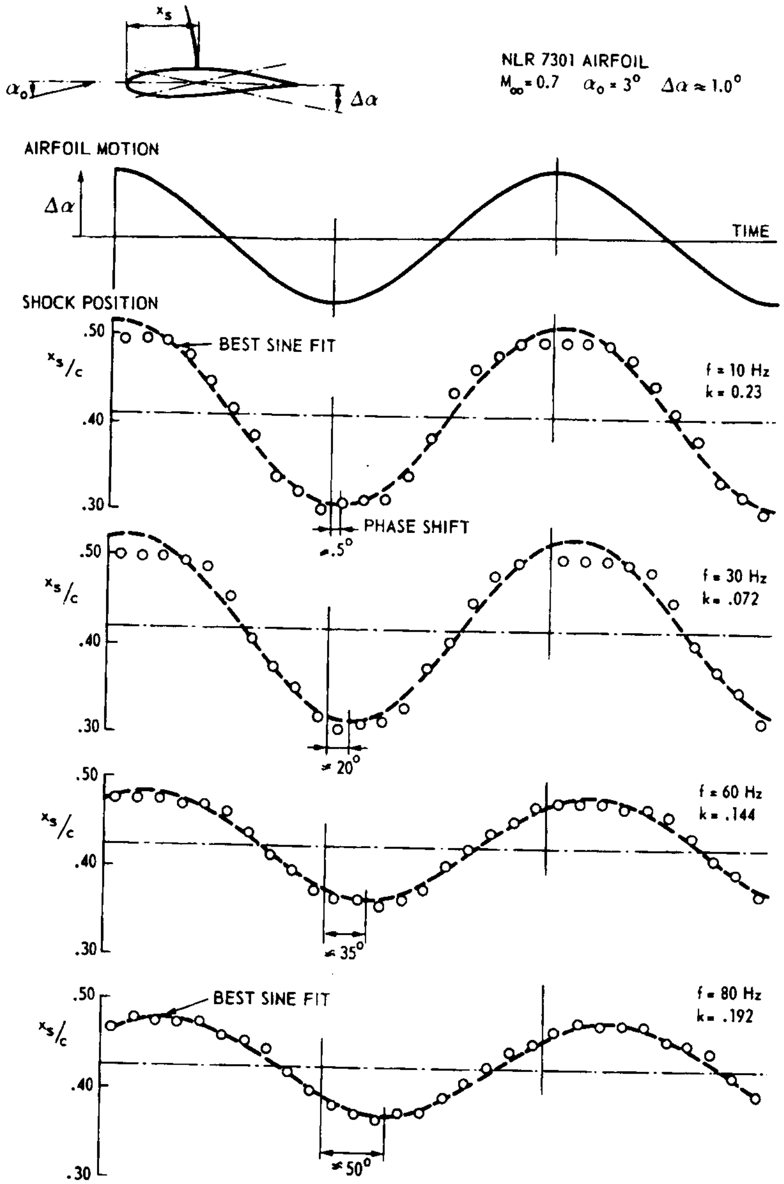

Figure 9 Periodic shock-wave motion for various frequencies.

9.50

UPSTREAM-PROPAGATED SHOCK WAVES (TYPE C) At slightly supercritical Mach number a third type of periodic shock-wave motion is observed, which differs completely from the preceding types. Periodically a shock wave is formed on the upper surface of the airfoil. This shock moves upstream while increasing its strength. The shock wave weakens again, but continues its upstream motion, leaves the airfoil from the leading edge, and propagates upstream into the oncoming flow as a (weak) free shock wave. This phenomenon is repeated periodically and alternates between upper and lower surface.

The type of shock-wave motion that occurs in a given situation depends on the Mach number, its chordwise distribution ahead of the shock wave, and on the amplitude and frequency of the motion of the airfoil. The types of shock-wave motions mentioned above are observed not only on oscillating airfoils, but also on steady airfoils with severe flow separation downstream of the shock waves (see, for example, Finke 1975, McDevitt 1979). Under these conditions the shocks do not always remain normal, but cyclically become lambda-type shocks.

Optical flow studies on an airfoil oscillating in pitch (Tijdeman 1977) reveal that the amplitude of the shock-wave motion decreases with frequency, as shown in Figure 9. This is consistent with the observation made in the next section dealing with the theoretical developments. As a consequence, the large pressure peaks generated by the periodic shock motion become smaller with increasing frequency, or, in other words, the contribution of the shock waves to the overall unsteady airloads, which forms one of the dominant effects in transonic flow, will be largest at low to moderate frequencies.

Another interesting feature, observed in the mentioned experiments and in those of Grenon & Thers (1977), is that an almost linear relationship is found between the frequency of oscillation and the phase shift between the motion of the airfoil and the motion of the shock wave for low to moderate reduced frequencies. This means that there is a constant time lag between the motion of the airfoil and the shock-wave motion. This corresponds with the findings of Erickson & Stephenson (1947), who observed a fixed relation between the phase lag of the shock motion and the time required by a pressure impulse to travel from the trailing edge to the shock wave.

In a flow pattern with a well-developed shock wave, the shock motion takes place nearly sinusoidally, with an amplitude of the shock motion that is proportional to the amplitude of the motion of the airfoil. Further, in spite of the presence of the oscillating shocks, the overall lift also varies almost sinusoidally while the moment sometimes shows irregularities (Figure 5*b*). Locally, underneath the foot of the moving shock wave, the pressure signal is highly nonlinear. However, as illustrated in the data of Figure 10 from Schippers (1978), the distributions of the higher harmonics of the pressure signals along the chord show the characteristic that they do not contribute noticeably to the overall lift and only slightly to the moment. This behavior can be explained very well by considering the pressure changes at such a point to be entirely due to a sinusoidal oscillation of a shock that spends part of its time on each side of the point (Tijdeman 1977). Neglecting the local pressure gradient, then, gives a field whose higher harmonics do not contribute to the net lift and only to second order in shock amplitude to the net moment.

Effect of Frequency and Amplitude of Oscillation

As mentioned earlier, it is important for the aeroelastician to know to what extent a linear relationship holds between unsteady airloads and

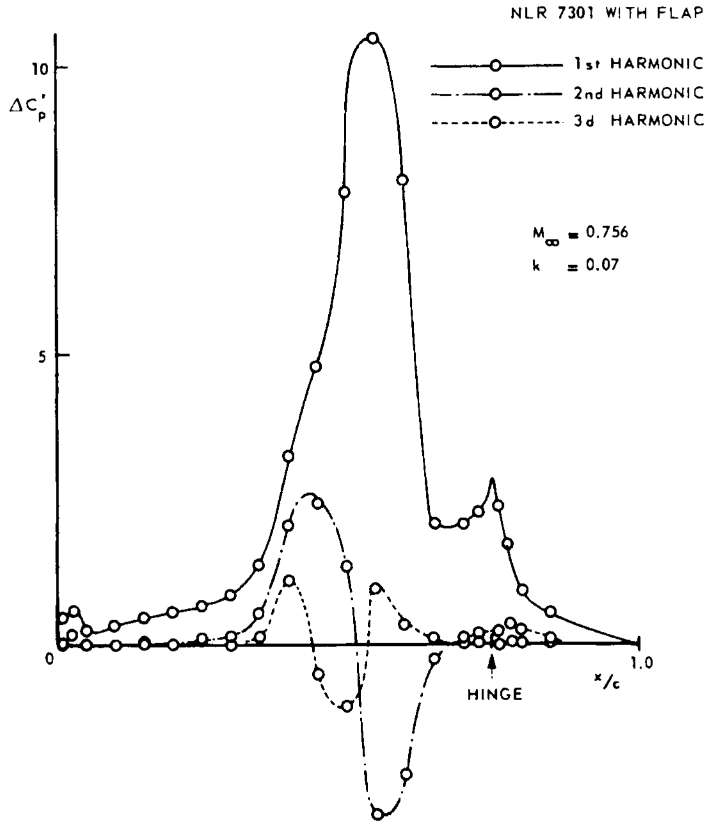

Figure 10 Unsteady pressure distribution showing the first three harmonics.

the amplitude of motion of the airfoil. For his purpose, linearization of the unsteady airloads makes sense only as long as small, but still practical changes in incidence or flap angle (say of the order of 0.5 and 1 degree, respectively) give rise to linear changes in the aerodynamic loads. Also, he must have a procedure for selecting a minimum number of suitable mean steady flow conditions for which the unsteady airloads should be determined. At this moment the experimental and theoretical evidence is not yet conclusive in this respect, but there are a number of observations that certainly throw some light on the problem.

Theoretical analysis (see the next section) shows that the unsteady transonic flow problem becomes a linear one for sufficiently high frequencies. From this, coupled with the observation that the amplitudes of periodic shock-wave motions are largest at low frequency, we can expect that the nonlinear characteristics of unsteady transonic flows will manifest themselves mainly at low to moderate frequencies and in quasi-steady flow. Therefore, we can expect that the behavior of the slopes of the steady lift and moment curves versus incidence or flap angle may serve as an effective guide to detect possible nonlinear regions and to select the mean incidences or flap angles around which linearization is possible.

As noted above, we may also expect that at sufficiently high frequency the measured results will approach the results of thin-airfoil theory. Unfortunately, the experiments show that this does not happen within the frequency range of interest for flutter investigations ($k \lesssim 0.5$). Figure 11 compares some of the results of Davis & Malcolm (1979), whose studies cover a considerable range of frequencies, with a thin-airfoil theory. It is clear that the unsteady airloads cannot be calculated with a linear theory that does not account for the mean steady flow field. However, if the

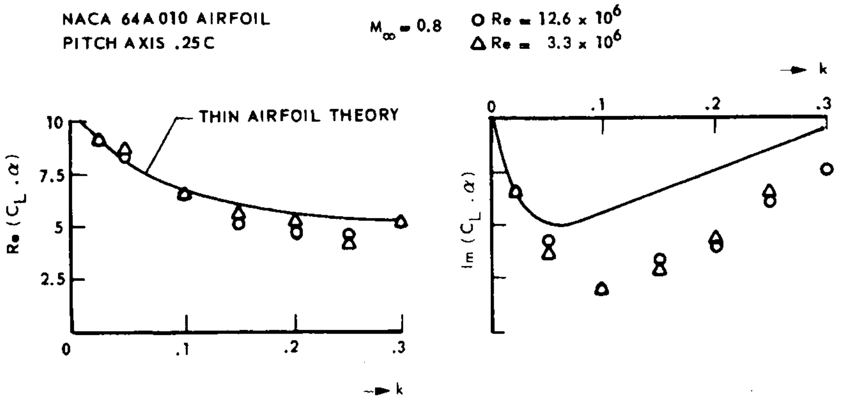

Figure 11 Effect of frequency on unsteady airloads.

amplitude of oscillation is small, we can expect that in most cases linearization for a practical range of amplitudes of oscillation should be possible as long as the flow remains attached. This expectation is confirmed very well by the tests Davis and Malcolm performed on the NACA 64A010 airfoil in a flow condition with a well-developed supersonic region terminated by a relatively strong shock wave. They found a linear relationship between the real and imaginary parts of the lift coefficient with amplitude for 0.25, 0.50, and 1.0 degrees, and further demonstrated that the unsteady airloads for a motion that was a linear combination of two other modes were a linear combination of the airloads for those modes.

THEORETICAL AND NUMERICAL METHODS

In this section we discuss the theoretical and numerical methods developed in recent years to calculate the inviscid transonic flow past oscillating airfoils, stressing the conclusions we may deduce from them. The discussion proceeds from the so-called Euler equations, which can be considered as the most complete set of equations describing inviscid flow problems, through increasingly less complete models to the small-perturbation equation.

Euler Equations

Because the flows of interest here occur at high Reynolds numbers, viscous effects are, for the most part, confined to the boundary layers and wakes. For flows in which the boundary layer remains attached over most of the airfoil, the inviscid flow is the correct first approximation for most of the flow field.

For inviscid flows, the conservations of mass, vector momentum, and energy give a system of four first-order partial differential equations in five scalar unknowns. These equations are usually referred to as the Euler equations. An additional equation relating the state variables is required. The system of equations is hyperbolic and quasilinear. Weak solutions to a hyperbolic system, viz., solutions with discontinuous behavior, may be found numerically if the difference equations are deduced from the conservative form of the equations, that is, from the equations in the form of a space-time divergence of a vector unknown. The physics governing the structure of shock waves is one of a balance between viscous and inertial terms involving viscous dissipation in the wave. Thus, the difference schemes are usually constructed so that the truncation error is predominately dissipative rather than dispersive. In such calculations the mesh size must be small in order that the viscosity implied by the truncation error be small compared with the length scale typical of flow in the vicinity of "captured" shock waves.

Numerical solutions of the Euler equations have been carried out by a number of investigators. Warming, Kutler & Lomax (1973) describe an effective third-order and consequently dissipative, finite-difference scheme with minimal dispersion. Beam & Warming (1976) report comparable results for a dispersive-dominant algorithm, with a switch from central to one-sided differencing where appropriate. The desire to compute steady flow fields originally motivated such computations. Some of the first methods used were explicit in time, time-accurate solutions being computed until a steady flow was achieved. A series of publications by Magnus & Yoshihara (1975, 1976, 1977) and Magnus (1977a, 1977b, 1978) provide many useful results for oscillating airfoils and include studies of the influence of various approximations on the accuracy of the solution. Other interesting results were reported by Beam & Warming (1974), who made a computation for small unsteady perturbations to an already established steady flow, by Laval (1975), and by Lerat & Sidès (1977).

Magnus & Yoshihara (1975) gave detailed unsteady pressure distributions for an airfoil oscillating in pitch; subsequently (1976) they gave analogous results for an airfoil with an oscillating flap, including here an ad hoc procedure to account for the shock–boundary-layer interaction. More recent studies were for the NLR 7301 supercritical airfoil (Magnus 1978). The results, among other things, reproduce the three types of shock motion observed experimentally. To illustrate this, Figure 12 depicts the instantaneous surface pressure distributions for pitch oscillations of an NACA 64A410 airfoil displaying a Type A shock motion. An interesting feature that appears in all numerical results is that the lift and moment vary nearly sinusoidally, despite the presence of strong shock waves. Figure 13 illustrates this behavior for an NACA 64A006 airfoil with an oscillating flap.

The paper of Magnus (1977a), which summarizes his previous studies using the Euler equations and comments on errors introduced by the boundary conditions used, is of considerable interest. For the low to moderate reduced frequencies, the finite computational domain often leads to the reflection of disturbances from the far-field boundary and their interference with the flow field near the airfoil before a harmonic motion is established. In Magnus' studies the far-field data were determined from vortex and doublet singularities located somewhere near the airfoil. Another approximation invoked in these studies was that the unsteady boundary conditions were applied at the steady-state location of the oscillating airfoil. Substantial differences are found when the correct boundary conditions are imposed, with the incorrect boundary conditions causing larger disturbances in the flow. Other studies, e.g. those of Lerat & Sidès (1977) and Steger (1978), avoid this approximation at the computational expense of time-dependent mappings. It is clear from these studies that it is essential to impose boundary conditions on the airfoil unless the amplitude of the unsteady motion is small, and to use a computational region that applies boundary conditions that either allow

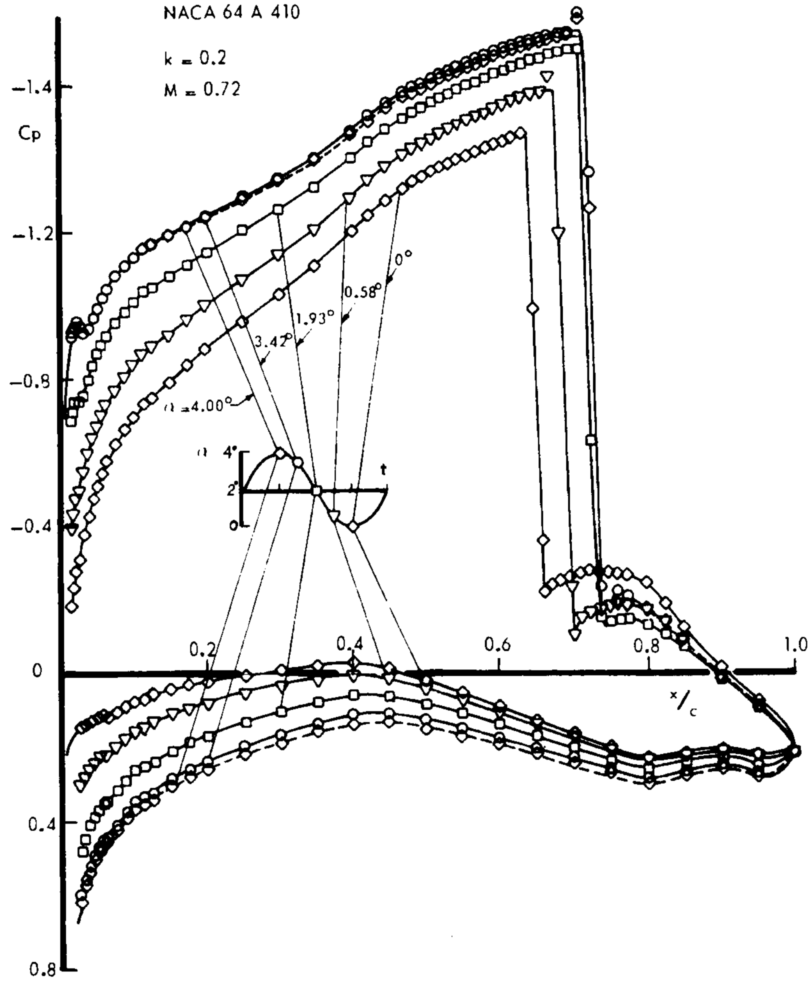

Figure 12 Instantaneous pressure distributions for an NACA 64A410 airfoil pitching around midchord calculated using the Euler equations.

waves to pass through it, or that is sufficiently large that incorrect boundary conditions on its extremities do not cause unacceptable errors.

Explicit calculations such as those discussed above require substantial central processing (CPU) time. Three or four cycles of a harmonic motion may require a comparable number of hours on a CDC 7600. Their main inefficiency occurs at the low to moderate reduced frequencies of practical interest, where improved computational times can be achieved using implicit methods. Beam & Ballhaus (1975) report that the numerical effort per time step for the implicit solution of the Euler equations is four times that required for their explicit solution. For reduced frequencies below about 0.2, however, the larger time step allowed by an implicit calculation results in reduced computational times.

The Potential Approximation

The flows of primary interest here are, for the most part, irrotational, with vorticity introduced by viscous effects in the boundary layers and

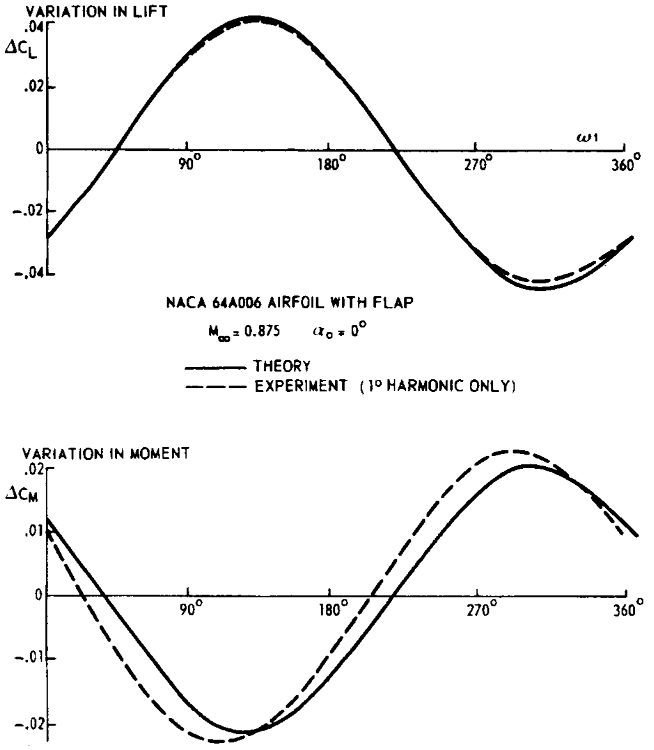

Figure 13 Time histories of the unsteady airloads calculated using the Euler equations.

shock waves. In the inviscid approximation shock-free flows that are originally irrotational will remain so; flows with shock waves will have a rotational component downstream of the shock wave. Crocco's theorem implies that in steady flow the vorticity behind the shock wave will be proportional to the cube of the change in the pressure coefficient across the shock wave multiplied by the speed of sound and divided by the vertical extent of the shock wave. For many practical situations this means that the flow behind the shock wave, and hence the overall inviscid flow, will be affected to a nonnegligible extent by the vorticity introduced by the shock wave. However, the assumption of irrotational flow makes it possible to simplify the problem to one with only a single unknown, the velocity potential. This leads to a considerable reduction in CPU time and storage requirements.

Under the assumptions mentioned above, the following equation for the velocity potential, Φ, can be derived:

$$\Phi_{tt}+(\nabla\Phi)_t^2+\tfrac{1}{2}\nabla\Phi\cdot\nabla(\nabla\Phi)^2-a^2\nabla^2\Phi=0, \tag{1}$$

where

$$a=a_\infty^2-(\gamma-1)[\Phi_t+\tfrac{1}{2}(\nabla\Phi)^2-\tfrac{1}{2}U^2],$$

and the symbols have their usual dimensional meaning. This is subject to the boundary condition that the flow remains tangential to the airfoil surface:

$$F_t+(\nabla\Phi)\cdot\nabla F=0$$

on

$$F=y-\delta Y(x)-\tilde{\delta}\tilde{Y}(x,t)=0.$$

Here δ and $\tilde{\delta}$ are amplitude parameters for the steady and unsteady motions.

Numerical algorithms for the steady potential equations, due principally to Jameson (1974, 1978), are now highly developed and provide reliable results for shock-free flows. Isogai (1977) has solved (1) using a nonconservative time-marching algorithm with unsteady boundary conditions applied at the airfoil's mean surface, a mean steady-state far-field, and an approximate vortex-wake condition. Results for a supercritical airfoil at its design condition oscillating in pitch (Isogai 1978) are shown in Figure 14. The more nearly linear behavior of the unsteady pressure distribution with an increase in frequency is clearly evident.

More recently, Chipman & Jameson (1979) have developed a conservative alternating-direction algorithm that uses a time-varying coordinate system to satisfy the exact boundary conditions. A conservative calculation will capture "shock" waves that conserve mass but add momentum to the flow to balance the wave drag on the body. These will be stronger discontinuities than Rankine-Hugoniot shock waves for a given Mach number ahead of the "shock" wave (van der Vooren & Slooff 1973). More definite comparisons of numerical solutions to (1) with those for the Euler equations are needed to determine quantitatively the adequacy of the potential approximation when shock waves appear in the flow. Isogai's computations indicate, as expected, that the results are unreliable if the cube of the pressure jump across the shock wave is not small.

The calculation of one cycle of harmonic motion requires the equivalent of a minute or so of CDC 7600 CPU time; the number of cycles required to achieve harmonic results will depend on the reduced frequency, with even the lower frequencies requiring at least three cycles.

The Small-Disturbance Approximation

The most basic approximation in inviscid aerodynamics is that of a small disturbance. With the assumption of small disturbances, the vorticity

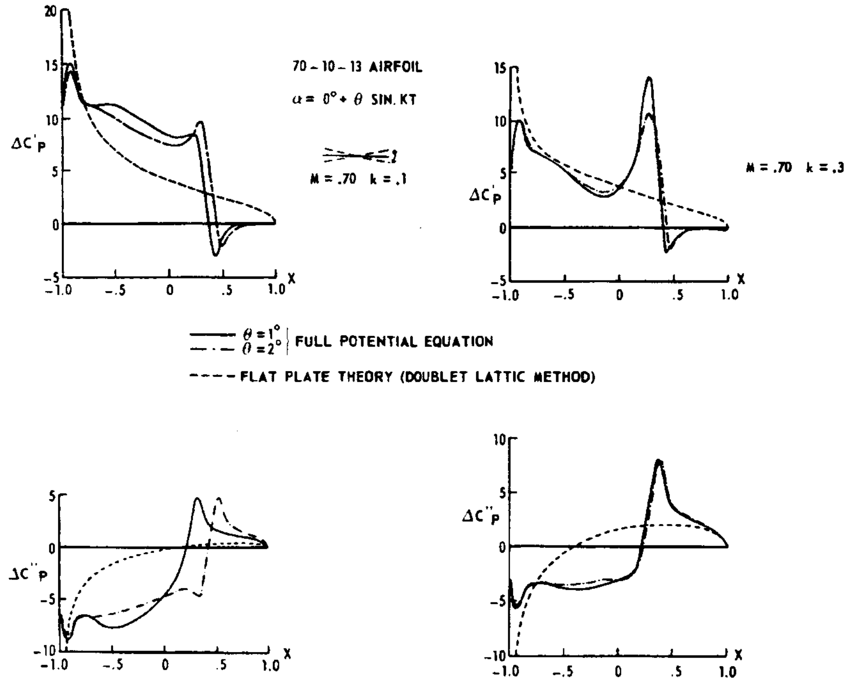

Figure 14 Unsteady pressure distributions on a 70-10-13 supercritical airfoil oscillating in pitch around the design condition calculated using the potential equations.

introduced by a shock wave will be small and the flow may be assumed irrotational. The least trivial balance of terms then leads to the equation

$$\frac{k^2M_\infty^2}{4\delta_0}\phi_{tt}+\frac{k}{\delta_0}M_\infty^2\phi_{xt}-\left\{\frac{1-M_\infty^2}{\delta_0}-(\gamma+1)M_\infty^2\left[\phi_x+\frac{1}{2}\frac{\gamma-1}{\gamma+1}k\phi_t\right]\right\}\phi_{xx}-\phi_{yy}=0, \qquad (2)$$

where the perturbation velocity potential ϕ is defined by

$$\Phi = Uc[x+\delta_0\phi],$$

where Φ is the velocity potential. Here the time has been nondimensionalized by the circular frequency and the coordinates by the airfoil chord, and the vertical coordinate scaled by $\delta_0^{\frac{1}{2}}$. Application of the mean-surface boundary conditions requires that

$$\delta_0^{\frac{3}{2}}\phi_y(t,x,0) = -\delta\frac{Y'(x)}{c}-\tilde{\delta}\left[\frac{\tilde{Y}'(x,t)}{c}+\frac{k}{2c}\tilde{Y}_t(x,t)\right], \qquad (3)$$

and hence that

$$\delta_0^{\frac{3}{2}} = \max(\delta,\tilde{\delta},k\tilde{\delta}).$$

For $k = O(1)$ a linear theory applies. This theory is fully developed in the monograph by Landahl (1961) and will not be discussed further here as the cases of most practical concern are those of small reduced frequency. The theoretical limit of interest here is that with $k = O(\delta_0)$. In practice, however, k is often large enough that contributions of this size, viz., $O(k)$, are important, and retaining them provides a bridge to the linear theory. Neglecting the first term of (2) makes the equation parabolic and is equivalent to disregarding one of the characteristics and requiring disturbances to be propagated downstream with infinite speed. There are numerical advantages to doing this. Couston & Angélini (1978) and Houwink & van der Vooren (1979) have shown that marked improvements are obtained at larger values of k when terms of order k are retained in the transport of shed vorticity, the boundary condition (3), and the pressure coefficient.

In the strict limit $k = O(\delta_0)$, that is, for low reduced frequencies, a fully nonlinear theory applies and the conservation of mass takes the form

$$-(k/\delta_0)M_\infty^2\phi_{xt}+\{(1-M_\infty^2)/\delta_0-(\gamma+1)M_\infty^2\phi_x\}\phi_{xx}+\phi_{yy}=0, \qquad (4)$$

a result first given by Lin, Reissner & Tsien (1948). The corresponding "shock" jump relations are

$$\frac{-kM_\infty^2}{\delta_0}[\![\phi_x]\!]^2\left(\frac{dx}{dt}\right)_s - \left\{\frac{1-M_\infty^2}{\delta_0} - (\gamma+1)M_\infty^2\bar{\phi}_x\right\}[\![\phi_x]\!]^2 + [\![\phi_y]\!]^2 = 0, \qquad (5)$$
$$\left(\frac{dy}{dx}\right)_s = -[\![\phi_x]\!]/[\![\phi_y]\!]$$

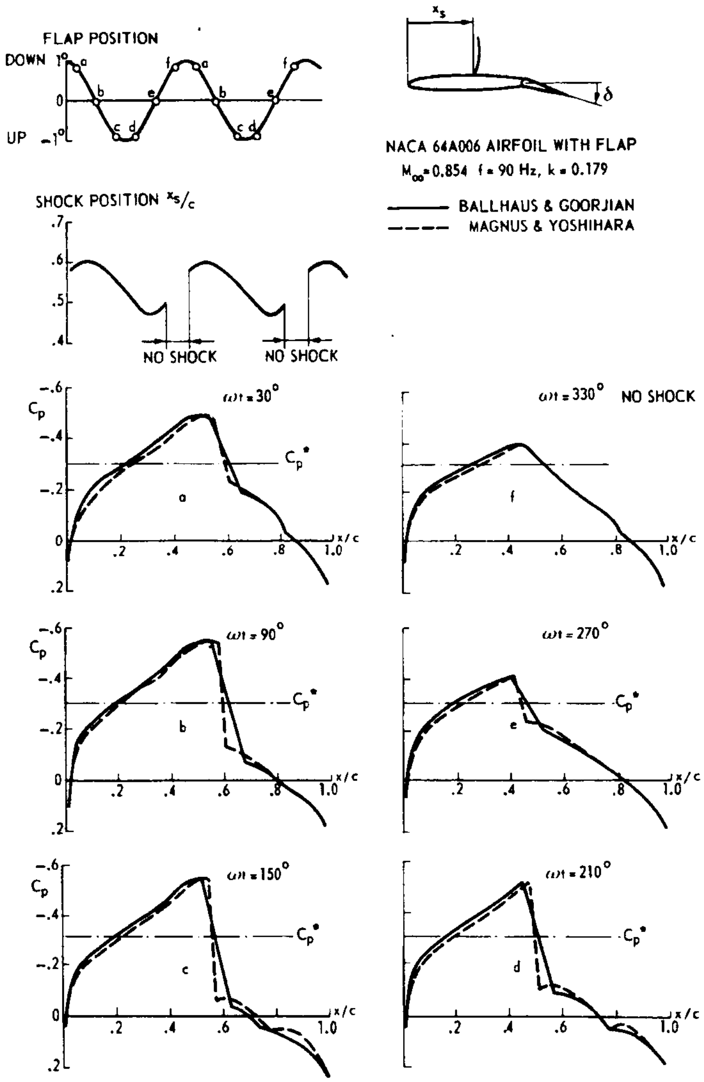

Figure 15 Instantaneous pressure distributions on the upper surface, showing type-B shock motion, calculated using the Euler and the small-disturbance equations.

with $\bar{\phi}_x$ the average value of ϕ_x, and $[\![\phi_x]\!]$ the jump in ϕ_x, across the discontinuity.

Explicit procedures for the solution of (5) are unstable unless the time step is much smaller than that required to resolve low-frequency motions. A fully implicit alternating-direction algorithm with a time-step limitation consistent with that required for accuracy has been developed by Ballhaus & Steger (1975). The far-field boundary conditions used are mean steady-state values on all but the downstream boundary where $\phi_x = 0$. This

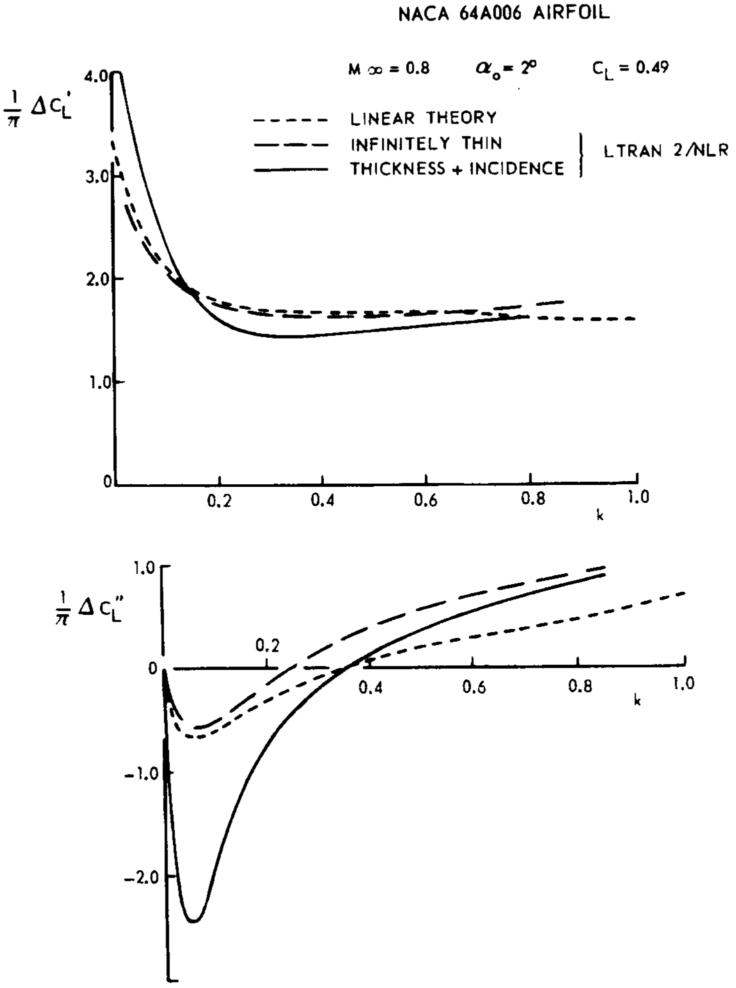

Figure 16 Unsteady lift coefficients for a pitching airfoil showing the effect of reduced frequency.

algorithm resolves shock waves and their motion well, provided the flow changes from supersonic to subsonic across the shock. Using this algorithm Ballhaus & Goorjian (1977) were able to reproduce observed features of experimental studies. To illustrate this, Figure 15 gives the time history of pressure distributions, which reveal a Type B shock-wave motion. Another interesting feature, shown in Figure 15, is that good agreement with results obtained with the Euler equations can be achieved. This is accomplished by introducing arbitrary powers of the Mach number into the equations and boundary conditions to "tune" the results to provide this agreement.

As another example of small-disturbance theory, Figure 16 shows the two components of the lift coefficient for a pitching airfoil as a function of reduced frequency. These computations, by Houwink & van der Vooren (1979), include wake vorticity transport in the Ballhaus-Steger algorithm. They agree reasonably well with the linear theory that applies for $k = O(1)$, but which also retains the ϕ_{tt} term. Figure 16 clearly shows that results for the airfoil with thickness and incidence approach the results for the infinitely thin plate as the frequency increases. Calculations of this type may be useful to determine, for a given airfoil, the frequency range within which a transonic computation method should be applied.

Time-Linearization

The small-disturbance equation (2) can be linearized by assuming the unsteady flow field to be a small perturbation superimposed upon a given mean steady flow field, or, in other words,

$$\phi(x, t) = \phi_0(x, y) + (\tilde{\delta}/\delta)\tilde{\phi}(x, y, t) + o(\tilde{\delta}/\delta)$$

where

$$\tilde{\delta}/\delta = o(1).$$

The linearized version of (5) must be retained to account for shock motion. The steady flow field may be defined either by experimental or numerical means, providing an accurate description of the shock wave's geometry and strength. Because of the ease of the practical implementation in aeroelastic computations, time-linearization is attractive for the flutter specialists. Their main interests are the magnitude and phase of the lift and moment perturbations for the relevant modes of motion. Since the unsteady loads are supposed to be linear, they can be solved in two ways, namely, in the frequency domain or in the time domain. In the frequency domain a steady equation with the frequency as parameter has to be solved for each frequency of interest. In the time domain the time history of the aerodynamic response to a step input (indicial response) has to be calculated. The results for a harmonic motion of the required frequencies then can be obtained by linear superposition, using Duhamel's integral. Solutions in the time domain have been obtained by Beam & Warming (1974), who considered small unsteady disturbances to a basic steady state defined by the Euler equations. The results compare favorably with the linear results obtainable from the theory of Heaslet, Lomax & Spreiter (1948). Noting the advantage of the indicial approach, Beam & Warming further observe that a ramp change (i.e. linear growth for an appropriate time) can be used in place of a step change, avoiding some difficulties in the numerical computations.

Ballhaus & Goorjian (1978) have used the nonlinear algorithm of Ballhaus & Steger (LTRAN2) to calculate indicial responses. They must use an amplitude that is small enough to produce linear results and yet large enough for the response to be computed correctly, a minor difficulty that is avoided by a strict time-linearization. Fung, Yu & Seebass (1978) have given a time-linearized version of the LTRAN2 algorithm that includes explicitly the effects of shock-wave motion through the time-linearized analog of (5). Steady-state shock jumps are obtained from another modification of Ballhaus' algorithm that uses shock fitting (Yu, Seebass & Ballhaus 1978). A detailed comparison of nonlinear and time-linearized calculations (Seebass, Yu & Fung 1978) verifies that the latter is accurate when $\tilde{\delta}/\delta$ is $\leqq 10^{-1}$. If shock-wave motion is not included, the lift and moment variations are incorrect. It also appears that most indicial responses are approximately exponential for the frequency range of most interest and behave as $\exp(-t/\tau)$, where τ is usually large, say 15. This implies that the amplitude of any response is the asymptotic change times $[1+(2k\tau)^2]^{-\frac{1}{2}}$, while the phase angle is $2k\tau[1+(2k\tau)^2]^{-\frac{1}{2}}$. This behavior is consistent with the experimental observation noted earlier, viz., that the amplitude of shock-wave excursions is proportional to k^{-1} for moderate reduced frequencies, and the phase shift is proportional to k for low reduced frequencies (K.-Y. Fung, private communication).

Time-linearized algorithms for the frequency domain have been developed by Ehlers (1974), with subsequent studies by Weatherill, Sebastian & Ehlers (1977, 1978), by Traci, Farr & Albano (1975), and by Fritz (1978). They solve for $\tilde{\phi}$ using a relaxation procedure. Computations in the frequency domain have an inherent limitation on $kM_\infty^2/(1-M_\infty^2)$ that depends on the mesh size. This is a consequence of the generation of standing-wave solutions, which Weatherill, Sebastian & Ehlers (1978) have unsuccessfully tried to eliminate by various means. This restriction is a serious one. More importantly, none of these studies allows for shock-wave motion, although in principle the procedure of Fung, Yu & Seebass (1978) can be carried over to the frequency domain.

To conclude this section on theoretical methods, a few words have to be said on the integral-equation method, since this type of approach has been highly successful for unsteady flow problems governed by linear equations. Such methods were probably the first to provide results for transonic flows with shock waves. The integral method is more suited for the time-linearized equations and, as described by Nixon (1978) for the low-frequency small-disturbance equation, shock-wave motions can be included. A disadvantage is that time-linearized calculations require an effective definition of the steady-state solution. Because finite-difference type time-accurate methods are frequently competitive with other methods of finding the required steady-state solution, one most probably will select a time-accurate procedure to determine the steady-state solution. However, in that case it is more convenient to continue the study of the unsteady response with the same method, instead of switching over to the integral-method approach.

Before the recent advances in computational methods, local linearization proved to be a useful but limited tool (for a review see Spreiter & Stahara 1975; for some recent results see Dowell 1977). Better tools, namely finite-difference algorithms, are now available.

Remarks on the Kutta Condition

With the approximation of inviscid flow, we must impose a Kutta condition at the trailing edge in order to obtain a unique solution. The imposition of the Kutta condition in the form of continuity of the pressure at the trailing edge requires that neither the average velocity nor the jump in velocity be zero if the circulation is to change with time. Consequently, in the strict inviscid limit the flow must follow either the upper or the lower surface of the airfoil at the trailing edge. Which surface it follows depends upon the past history of the motion. More specifically, the rate of change of circulation, Γ (measured counterclockwise), is given by

$$\begin{aligned}\frac{d\Gamma}{dt} &= \frac{d}{dt}\oint \mathbf{q}\cdot d\mathbf{r} = \oint \frac{d\mathbf{q}}{dt}\cdot d\mathbf{r} + \oint \frac{dq^2}{2} = -\oint\left(\frac{dp}{\rho} - \frac{dq^2}{2}\right) \\ &= -\frac{(q_u+q_l)}{2}(q_u-q_l), \qquad (6)\end{aligned}$$

where the right-hand side is to be evaluated at the trailing edge and the velocities are those sketched in Figure 17*a*.

Though this view is satisfactory from a computational standpoint, it is rather too narrow. The Kutta condition is an idealization of the behavior for infinite Reynolds numbers. The correct picture is given by Sears (1976), who notes that for viscous flow, Equation (6) applies provided *u* and *l* are

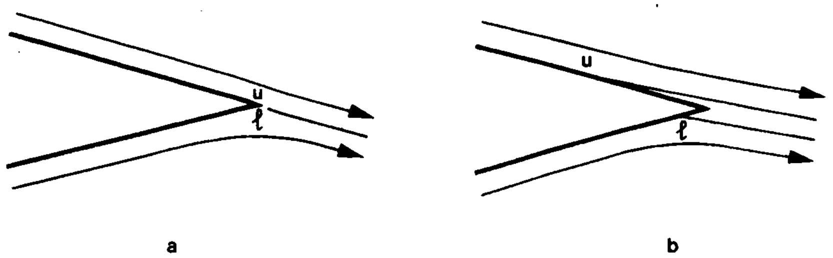

Figure 17 Flow patterns at the trailing edge for inviscid and viscous unsteady flow.

the instantaneous locations of the upper and lower points of boundary-layer separation adjusted for their motion, as shown in Figure 17*b*. Unsteady computations using the Euler equations normally impose some requirement equivalent to the (steady) Kutta condition, e.g. that the flow leaving the trailing edge bisect the trailing-edge angle. While this is inconsistent with results given above (Basu & Hancock 1978), the error involved in doing so is usually inconsequential, nor are time lags of consequence at the frequencies of interest here (see, for example, McCroskey 1977).

Viscous Flows

Viscosity determines, through the Kutta condition and the presence of a boundary layer and a wake, the basic structure of the flow past airfoils. The important parameter here is the Reynolds number, which has a significant influence on the thickness of the boundary layer, on the location of transition and separation points, and on the way in which the boundary layer interacts with a shock wave. A relatively simple method to determine the viscous flow past airfoils is the use of a combination of an algorithm to compute the inviscid flow field with an algorithm to compute the boundary layer. For steady, attached flows such methods are available: first, the inviscid flow field is determined; next the boundary layer is computed and the displacement thickness of the boundary layer is added to the airfoil contour. For this new airfoil the inviscid flow field is calculated again, followed by a new calculation of the boundary layer and so on. An illustration of a result obtained in this way with the method of Bauer et al (1975) is given in Figure 18. This figure reveals that both the steady and the associated quasi-steady pressure distributions are significantly altered by the presence of the boundary layer and that a considerably improved agreement with experiment is obtained. For quasi-steady flow (Figure 18*b*) the effect of the boundary layer is even of the same order of magnitude as the effect of wing thickness. This indicates that reliable predictions of the unsteady airloads on actual airfoils can be obtained

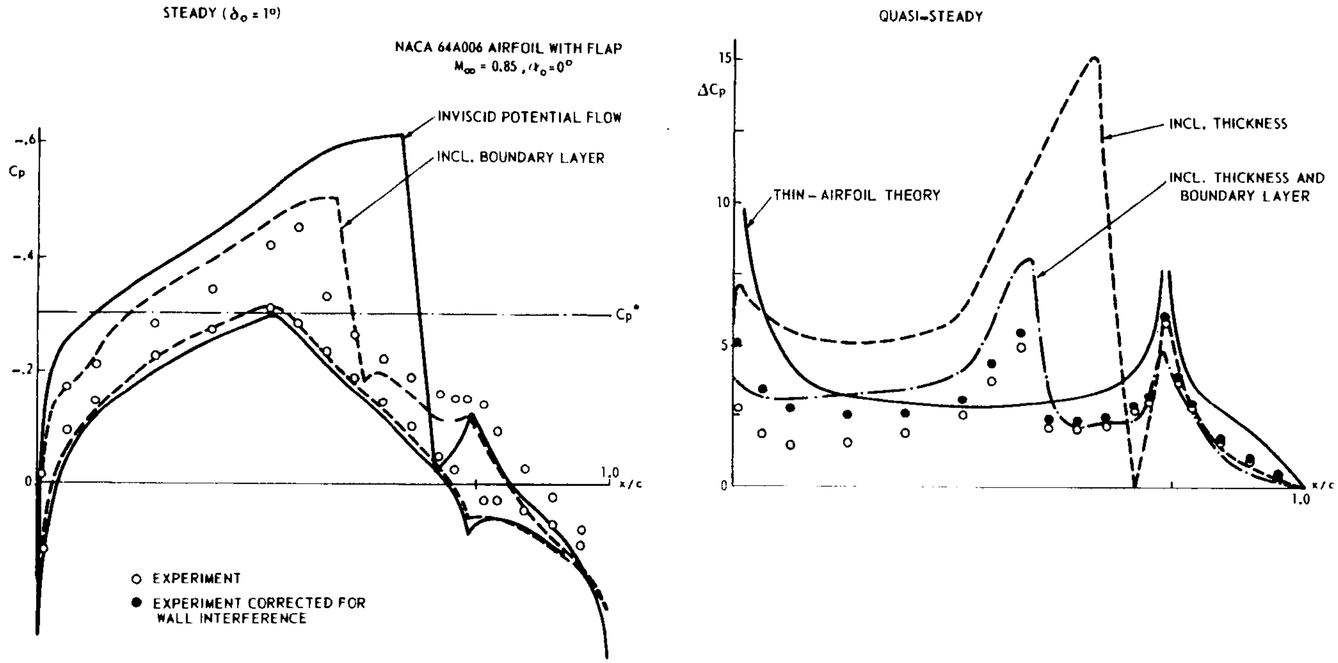

Figure 18 Effect of thickness and boundary-layer displacement on steady and quasi-steady pressure distribution in transonic flow.

only if the boundary layer is included. Provided the flow remains unseparated, computations as shown here for quasi-steady flow are satisfactory also for unsteady flow, as was demonstrated recently by Grenon, Desoper & Sidès (1979). Computations for steady flow that model viscous effects at the trailing edge and the shock–boundary-layer interaction have been reported by Melnik, Chow & Mead (1977); they achieve good agreement with experimental measurements. To take the shock-wave–boundary-layer interaction into account the unsteady methods are still limited to the simple ad hoc procedure devised by Magnus & Yoshihara (1976). They incorporate, in a quasi-steady manner, a wedge-nosed displacement ramp at the foot of the shock wave, providing a qualitative improvement in inviscid results.

There is much yet to be learned about both the steady and unsteady coupling of the boundary layer with the inviscid flow. The main problem areas are the modeling of the interaction between shock waves and boundary layers (Melnik, Chow & Mead 1977 have made considerable progress in this respect) and the accurate treatment of the flow past the trailing edge. Further, a better physical understanding of turbulence is essential if the more complex models are to provide acceptable results for modeling separated flows.

The equations that govern the complete viscous flow are the Navier-Stokes equations for a compressible medium. Questions regarding the existence and uniqueness of the solutions to these equations, even when the medium is incompressible, are generally unanswered. From an engineering point of view, flows of practical interest have turbulent boundary layers, and the Reynolds-averaged form of the Navier-Stokes equations, in conjunction with suitable turbulence models, is an appropriate and necessary basic approximation. The main difficulties that arise are in determining the adequacy of turbulence models, delineating their ability to produce reliable results over a range of conditions, and providing the central processing time needed, and storage required, to effect a numerical solution of the equations. Comprehensive reviews of such calculations may be found in Peyret & Viviand (1975) and MacCormack & Lomax (1979).

Algorithmic advances for the Reynolds-averaged Navier-Stokes equations have recently improved computational efficiency by more than an order of magnitude. One marked improvement was the time-split method due to MacCormack (1976) that separates the equations into a hyperbolic part, which is treated explicitly with a local characteristic method, and a parabolic part, which is solved by an implicit method. The efficiency of this algorithm is sufficient to allow complex three-dimensional flows to be calculated (Hung & MacCormack 1978). Beam & Warming (1978)

116

have extended an earlier algorithm for the Euler equations to the Reynolds-averaged equations, and Steger (1978) has implemented this algorithm with unsteady grid generation and the "thin-layer" version of these equations. The "thin-layer" approximation is essentially the boundary-layer approximation, except that the normal momentum equation is retained, obviating difficulties in matching viscous and inviscid calculations (see Baldwin & Lomax 1978).

In the framework of the Reynolds-averaged Navier-Stokes equations, Seegmiller, Marvin & Levy (1978) studied the flow past an 18% thick circular-arc airfoil in a channel at Mach numbers of 0.76 and 0.79 for a Reynolds number based on a chord of 10^7. This study is part of a continuing investigation to determine the adequacy of numerical algorithms. They use the time-split algorithm of MacCormack. Separate turbulence models are used for the boundary layer ahead of the shock, the separation bubble following the shock, the wake of the separation bubble, and the outer boundary layer and wake. Each is modeled with a simple scalar

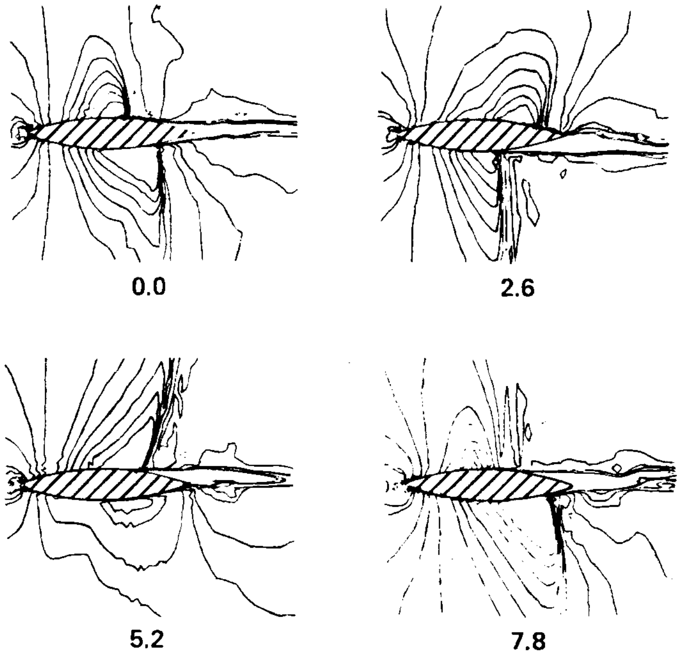

Figure 19 Computed Mach contours for flow past an 18% thick circular-arc airfoil at $M_\infty = 0.754$, Re = 10^7, from Levy (1978).

eddy diffusivity. This numerical simulation yielded an unsteady solution when the Mach number was 0.76, but a steady solution was found again when the Mach number was increased to 0.79. This unsteady motion, an alternate fore-aft motion of the shock wave with shock-induced separation on each side of the airfoil, was also observed experimentally over a narrow range of Mach numbers for the Reynolds number used in the calculations. The numerical results reproduce well (within 20%) the frequency of this oscillation at the lower Mach number. Figure 19, from Levy (1978), depicts the Mach contours exhibiting this behavior for a free-stream Mach number of 0.754. Velocity profiles at various chordwise stations were found to be in qualitative agreement with those measured. The main difficulties encountered in this numerical simulation were the inadequacy of the turbulence modeling near the trailing edge and a tendency of the numerical algorithm to capture strong (supersonic to subsonic) shocks where weak (supersonic to supersonic) shocks were observed. The time to carry out a cycle of the unsteady computation on a CDC 7600 was 1.8 hours.

In an exploratory study, using the "thin-layer" algorithm mentioned above, Steger & Bailey (1979) simulated the aileron buzz observed in flight tests of the P-80 and subsequently documented in the Ames 16-foot wind tunnel. These coupled aeroelastic computations were able to reproduce the Mach number of the observed onset of buzz at two angles of attack. This result, and that discussed above, demonstrate that contemporary algorithms and computer hardware are able to simulate complex flow phenomena.

CONCLUDING REMARKS

During the past five years sufficient experimental observations and measurements have been made to provide a good understanding of the transonic flow past oscillating airfoils. Furthermore, recent studies have provided results essential for the design of transonic aircraft. The main limitations of these experiments are their failure, for the most part, to duplicate full-scale Reynolds numbers and an inability to duplicate free-flight conditions due to wind tunnel wall interference. Experimental studies, both in progress and planned for the future, will be more nearly at full-scale Reynolds number, and eventually these Reynolds numbers will be obtained with minimum wall interference in new facilities now under development.

Paralleling this progress has been a rapid development of reliable, and in the small-perturbation approximation, efficient numerical algorithms for the computation of inviscid flows. Numerical results from these methods are in qualitative agreement with the experimental observations, with the main discrepancies in quantitative prediction as a consequence of the inviscid approximation. For steady flows coupled inviscid–boundary-layer calculations of unseparated flows obtain quantitative agreement with experimental measurements. We can expect this to be true for unsteady flows in the near future. The numerical simulation of unsteady separated flows is demonstrably possible, but the two orders of magnitude improvement in computer speed that is projected for a special-purpose aerodynamic computer will be essential for this simulation to have practical consequences.

It is the authors' opinion that the satisfactory prediction of unsteady airloads for aeroelastic applications is within reach. This can be accomplished by "tuning" inviscid boundary conditions to model an experimentally determined steady flow and then computing its unsteady response using an inviscid small-perturbation algorithm. Thus, the time is ripe to start with the incorporation of the new methods in aeroelastic practice as recently demonstrated by Ashley (1979). Of course, the use of two-dimensional methods is justified only for large aspect-ratio wings. To treat the low aspect-ratio configuration the next, and not difficult, step has to be made, namely, the development of prediction methods for three-dimensional flows.

Literature Cited

Ashley, H. 1979. On the role of shocks in the "sub-transonic" flutter phenomenon. *AIAA Pap. 79-0765*

Baldwin, B. S., Lomax, H. 1978. Thin layer approximation and algebraic model for separated turbulent flows. *AIAA Pap. 78–257*

Ballhaus, W. F. 1978. Some recent progress in transonic flow computations. *Numerical Methods in Fluid Dynamics*, ed. H. J. Wirz, J. J. Smolderen, pp. 155–235. New York: McGraw-Hill

Ballhaus, W. F., Goorjian, P. M. 1977. Implicit finite-difference computations of unsteady transonic flows about airfoils. *AIAA J.* 15:1728–35

Ballhaus, W. F., Goorjian, P. M. 1978. Computation of unsteady transonic flows by the indicial method. *AIAA J.* 16:117–24

Ballhaus, W. F., Steger, J. L. 1975. Implicit approximate-factorization schemes for the low-frequency transonic equation. *NASA Tech. Memo X-73,082*

Basu, B. C., Hancock, G. J. 1978. The unsteady motion of a two-dimensional aerofoil in incompressible inviscid flow. *J. Fluid Mech.* 87:159–78

Bauer, F., Garabedian, P., Korn, D., Jameson, A. 1975. Supercritical wing sections II. *Lect. Not. Econ. Math. Syst. No. 108*. Berlin: Springer

Beam, R. M., Ballhaus, W. F. 1975. Numerical integration of the small-disturbance potential and Euler equations for unsteady transonic flow. *NASA SP-347*, Part II, pp. 789–809

Beam, R. M., Warming, R. F. 1974. Numerical calculations of two-dimensional, unsteady transonic flows with circulation. *NASA Tech. Note D-7605*

Beam, R. M., Warming, R. F. 1976. An implicit finite-difference algorithm for hyperbolic systems in conservation-law form. *J. Comput. Phys.* 22:87–110

Beam, R. M., Warming, R. F. 1978. An implicit factored scheme for the compressible Navier-Stokes equations. *AIAA J.* 16:393–402

Bergh, H. 1965. A new method for measuring the pressure distribution on harmonically oscillating wings. *Proc. 4th ICAS-Congress, Paris, 1964*, ed. R. Dexter. London: MacMillan. See also *NLR MP.224*, 1964

Bergh, H., Tijdeman, H., Zwaan, R. J. 1970. High subsonic and transonic effects on pressure distributions measured for a swept wing with oscillating control surface. *Z. Flugwiss.* 18(9/10): 339–46

Chipman, R., Jameson, A. 1979. Fully conservative numerical solutions for unsteady irrotational transonic flow about airfoils. *AIAA Pap. 79-1555*

Couston, M., Angélini, J. J. 1978. Solution of nonsteady two-dimensional transonic small disturbances potential flow equation. In *Nonsteady Fluid Dynamics: Proc. ASME Winter Annual Mtg.*, Dec. 10–15, 1978, San Francisco, pp. 233–44. See also *ONERA TP-No. 1978-69*

Davis, J. A. 1979. Unsteady pressures on an NACA 64A410 airfoil: experimental and theoretical results. *AIAA Pap. 79-0330*

Davis, S., Malcolm, G. 1979. Experiments in unsteady transonic flow. *AIAA Pap. 79-0769*

Dowell, E. H. 1977. A simplified theory of oscillating airfoils in transonic flow: Review and extension. *Proc. AIAA Dynamics Specialist Conf., San Diego, 1977*, pp. 209–24

Ehlers, F. E. 1974. A finite difference method for the solution of the transonic flow around harmonically oscillating wings. *NASA Contract Rep. 2257*

Erickson, A. L., Robinson, R. C. 1948. Some preliminary results in the determination of aerodynamic derivatives of control surfaces in the transonic speed range by means of a flush type electrical pressure cell. *NACA RM A8H03*

Erickson, A. L., Stephenson, J. D. 1947. A suggested method of analyzing for transonic flutter of control surfaces based on available experimental evidence. *NACA RM A7F30*

Finke, K. 1975. Shock oscillations in transonic flows and their prevention. *Symp. Transsonicum II*, ed. K. Oswatitsch, D. Rues, pp. 57–65. Berlin: Springer

Fritz, W. 1978. Transsonische Strömung um harmonisch schwingende Profile. *Dornier GMBH Rep. 78/16 B*

Fung, K-Y., Yu, N. J., Seebass, R. 1978. Small unsteady perturbations in transonic flows. *AIAA J.* 16:815–22

Grenon, R., Desoper, A., Sidès, J. 1979. Effets instationnaires d'une gouverne en écoulement bidimensionnel subsonique et transsonique. *AGARD CP-262*

Grenon, R., Thers, J. 1977. Étude d'un profil supercritique avec gouverne oscillante en écoulement subsonique et transsonique. *AGARD CP-227*

Heaslet, M. A., Lomax, H., Spreiter, J. R. 1948. Linearized compressible-flow theory for sonic flight speeds. *NACA Rep. 956*

Houwink, R., van der Vooren, J. 1979. Results of an improved version of LTRAN-2 for computing unsteady airloads on airfoils oscillating in transonic flow. *AIAA Pap. 79-1553*

Hung, C. M., MacCormack, R. W. 1978. Numerical solution of three-dimensional shock wave and turbulent boundary-layer interaction. *AIAA J.* 16: 1090–96

Isogai, K. 1977. Calculation of unsteady transonic flow over oscillating airfoils using the full potential equation. *Proc. AIAA Dynamics Specialist Conf., San Diego, 1977*

Isogai, K. 1978. Numerical study of transonic flow over oscillating airfoils using the full potential equation. *NASA Tech. Pap. 1120*

Jameson, A. 1974. Iterative solution of transonic flows over airfoils and wings, including flows at Mach 1. *Comm. Pure Appl. Math.* 27: 283–309

Jameson, A. 1978. Transonic flow calculations. In *Numerical Methods in Fluid Dynamics*, ed. H. J. Wirz, J. J. Smolderen, pp. 1–87. New York: McGraw-Hill

Lambourne, N. C. 1958. Some instabilities arising from the interaction between shock waves and boundary layers. *AGARD Rep. 182*

Landahl, M. T. 1961. *Unsteady Transonic Flow*. New York/London: Pergamon

Landahl, M. T. 1976. Some developments in unsteady transonic flow research. *Symp. Transsonicum II*, ed. K. Oswatitsch, D. Rues. Berlin: Springer

Laval, P. 1975. Calcul de l'écoulement instationnaire transsonique autour d'un profil oscillant par une méthode à pas fractionnaires. *ONERA TP No. 1975-115*

Leadbetter, S. A., Clevenson, S. A., Igoe, W. B. 1960. Experimental investigation of oscillatory aerodynamic forces, moments and pressures acting on a tapered wing oscillating in pitch at Mach numbers from 0.40 to 1.07. *NASA TN-D1236*

Lerat, A., Sidès, J. 1977. Calcul numérique d'écoulements transsoniques instationnaires. *AGARD Spec. Mtg. on Unsteady Airloads in Separated and Transonic Flow, Lisbon, April 1977*. See also *ONERA TP No. 1977-19E*

Lessing, H. C., Troutman, J. L., Meness, G. P. 1960. Experimental determination of the pressure distribution on a rectangular wing oscillating in the first bending mode for Mach numbers from 0.24 to 1.30. *NASA TN-D344*

Levy, L. L., Jr. 1978. Experimental and computational steady and unsteady transonic flows about a thick airfoil. *AIAA J.* 16: 564–72

Lin, C. C., Reissner, E., Tsien, H. S. 1948.

On two-dimensional non-steady motion of a slender body in a compressible fluid. *J. Math. Phys.* 3:220–31

MacCormack, R. W. 1976. An efficient numerical method for solving the time-dependent compressible Navier-Stokes equations at high Reynolds number. *NASA Tech. Memo X-73, 129*

MacCormack, R. W., Lomax, H. 1979. Numerical solution of compressible viscous flows. *Ann. Rev. Fluid Mech.* 11: 289–316

McCroskey, W. J. 1977. Some current research in unsteady fluid dynamics. *Trans. ASME, March 1977, J. Fluids Eng.*, pp. 8–39

McDevitt, J. B. 1979. Supercritical flow about a thick circular-arc airfoil. *NASA Tech. Memo 78549*

Magnus, R. J. 1977a. Computational research on inviscid, unsteady, transonic flow over airfoils. *ONR CASD/LVP 77-010*. 68 pp.

Magnus, R. J. 1977b. Calculations of some unsteady transonic flows about the NACA 64A006 and 64A010 airfoils. *AFFDL Tech. Rep. 77-46*

Magnus, R. J. 1978. Some numerical solutions of inviscid, unsteady, transonic flows over the NLR 7301 airfoil. *ONR CASD/LVP*. 37 pp.

Magnus, R. J., Yoshihara, H. 1975. Unsteady transonic flows over an airfoil. *AIAA J.* 13:1622–28

Magnus, R. J., Yoshihara, H. 1976. Calculation of the transonic oscillating flap with "viscous" displacement effects. *AIAA Pap. 76-327*

Magnus, R. J., Yoshihara, H. 1977. The transonic oscillating flap. *AGARD-CP-226*

Melnik, R. E., Chow, R., Mead, H. R. 1977. Theory of viscous transonic flow over airfoils at high Reynolds number. *AIAA Pap. 77-680*

Nakamura, Y. 1968. Some contributions on a control surface buzz at high subsonic speeds. *J. Aircraft* 5:118–25

Nixon, D. 1978. Calculation of unsteady transonic flows using the integral equation method. *AIAA J.* 16:976–83

Peyret, R., Viviand, H. 1975. Computation of viscous compressible flows based on the Navier-Stokes equations. *AGARDograph No. 212*

Schippers, P. 1978. Results of unsteady pressure measurements on the NLR 7301 airfoil with oscillating control surface. *NLR TR 78124 C*

Sears, W. R. 1976. Unsteady motion of airfoils with boundary layer separation. *AIAA J.* 14:216–20

Seebass, A. R., Yu, N. J., Fung, K-Y. 1978. Unsteady transonic flow computations. *AGARD-CP-227*

Seegmiller, H. L., Marvin, J. G., Levy, L. L. Jr. 1978. Steady and unsteady transonic flow. *AIAA J.* 16:1262–70

Spreiter, J. R., Stahara, S. S. 1975. Unsteady transonic aerodynamics—An aeronautics challenge. *Proc. Unsteady Aerodynamics Symp.*, Univ. of Arizona, Vol. II, pp. 553–82

Steger, J. L. 1978. Implicit finite-difference simulation of flow about arbitrary two-dimensional geometries. *AIAA J.* 16:679–86

Steger, J. L., Bailey, H. E. 1979. Calculation of transonic aileron buzz. *AIAA Pap. 79-0134*

Tijdeman, H. 1976. High subsonic and transonic effects in unsteady aerodynamics. *Part of AGARD Rep. 636*: see also On the motion of shock waves on an airfoil with oscillating flap. *Symp. Transsonicum II*, ed. K. Oswatitsch, D. Rues, pp. 43–56. Berlin: Springer

Tijdeman, H. 1977. *Investigations of the Transonic Flow Around Oscillating Airfoils*. Doctoral thesis. Technische Hogeschool Delft, The Netherlands. 148 pp.

Tijdeman, H., Bergh, H. 1967. Analysis of pressure distributions measured on a wing with oscillating control surface in two-dimensional high subsonic and transonic flow. *NLR-TR F.253*

Tijdeman, H., Schippers, P. 1973. Results of pressure measurements on an airfoil with oscillating flap in two-dimensional high subsonic and transonic flow (zero incidence and zero mean flap position). *NLR TR 73078 U*

Traci, R. M., Farr, J. L., Albano, E. 1975. Perturbation method for transonic flows about oscillating airfoils. *AIAA Pap. 75-877*

Triebstein, H. 1969. Instationäre Druckverteilungsmessungen an einem schwingenden Tragflügel im subsonischen und transsonischen Geschwindigkeitsbereich. *DLR FB 69-49*

Triebstein, H. 1972. Instationäre Druckverteilungsmessungen an einem harmonisch schwingenden Flügelmodell in drei-dimensionaler, kompressibler Strömung. *Z. Flugwiss.* 21(11):400–12; see also *DLR FB 72-55*

van der Vooren, J., Slooff, J. W. 1973. On inviscid isentropic flow models used for finite difference calculations of two-dimensional transonic flows with embedded shocks about airfoils. *NLR MP 73024 U*

Warming, R. F., Kutler, P., Lomax, H. 1973. Second- and third-order noncentered difference schemes for nonlinear hyperbolic equations. *AIAA J.* 2:189–96

Weatherill, W. H., Sebastian, J. D., Ehlers, F. E. 1977. Application of a finite difference method to the analysis of transonic flow over oscillating airfoils and wings. *AGARD-CP-226*

Weatherill, W. H., Sebastian, J. D., Ehlers, F. E. 1978. The practical application of a finite difference method for analyzing transonic flow over oscillating airfoils and wings. *NASA Contract Rep. 2933*

Wyss, J. A., Sorenson, R. M. 1951. An investigation of the control surface flutter derivatives of an NACA 65-213 airfoil in the Ames 16-foot high speed wind tunnel. *NACA RM A51J10*

Yu, N. J., Seebass, A. R., Ballhaus, W. F. 1978. Implicit shock-fitting scheme for unsteady transonic flow computations. *AIAA J.* 16:673–78

Zierep, J. 1966. Theorie der Schallnahen und der Hyperschallströmungen. Karlsruhe: G. Braun

J. Fluid Mech. (1979), *vol.* 95, *part* 2, *pp.* 223–240
Printed in Great Britain

Lifting three-dimensional wings in transonic flow

By M. S. CRAMER

Department of Engineering Science and Mechanics, Virginia Polytechnic
Institute and State University, Blacksburg, Virginia 24061

(Received 5 September 1978)

The far field of a lifting three-dimensional wing in transonic flow is analysed. The boundary-value problem governing the flow far from the wing is derived by the method of matched asymptotic expansions. The main result is to show that corrections which are second order in the near field make a first-order contribution to the far field. The present study corrects and simplifies the work of Cheng & Hafez (1975) and Barnwell (1975).

1. Introduction

This paper is concerned with the transonic flow over thin lifting wings. In particular, the flow far from the wing is discussed. A number of authors have studied the transonic flow far from wings and bodies. One of the most important contributions to our understanding of these flows is the transonic area rule. This area rule (see, e.g. Oswatitsch 1952) states that the transonic flow far from a wing-body combination is the same as that produced by an equivalent body of revolution having the same axial distribution of cross-sectional area. This rule has been established for slender bodies by Oswatitsch (1952) and Cole & Messiter (1957). Spreiter & Stahara (1971) extended this to non-slender wings, i.e. wings having an aspect ratio of order one. Ashley & Landahl (1965) also extended the theory to include wings at an angle of attack comparable to their thickness. Generally, the area rule is deduced by deriving the boundary-value problem governing the flow far from the wing or body; this boundary-value problem is seen to be identical to that for a slender body of revolution, provided that the streamwise rate of change of cross-sectional area is the same for both.

Hayes (1954) has pointed out that the transonic area rule fails when the volume of the wing is sufficiently small. Cheng & Hafez (1972, 1973, 1975) and Barnwell (1973, 1975) have studied the effect of lift on the transonic area rule. The study presented here treats the case of a lifting wing with no thickness. With this simple case it is easy to illustrate the basic theory and the main effect of lift on the far field. The boundary-value problem governing the flow far from the wing is obtained through a straightforward application of the method of matched asymptotic expansions.

Our main interest here is in the basic theory of lifting wings in transonic flow; for a more complete discussion of the flow from a physical point of view, and of extensions to the basic theory, we refer the reader to the references cited above.

In §6 we review and discuss the previous investigations of Cheng & Hafez (1975) and Barnwell (1975). In most respects our work agrees with the above authors. However, there are important differences in our expressions for the boundary condition

0022-1120/79/4336-7770 $02.00

123

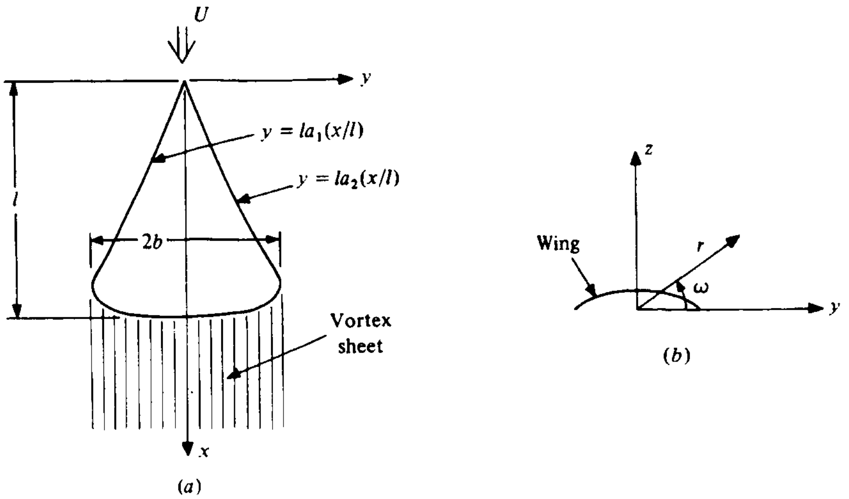

FIGURE 1. Sketch of wing and co-ordinate system. (a) Plan view; (b) rear view, $r \equiv (z^2+y^2)^{\frac{1}{2}}$.

for the outer flow; the disagreement with the results of Cheng & Hafez is due to fundamental differences in the matching.

2. Mathematical formulation

The co-ordinate system used is sketched in figure 1; the origin is taken at the nose of the wing, the x axis is aligned with the undisturbed uniform flow, and the z axis is taken as approximately perpendicular to the wing surface. A typical wing has been sketched; it has a length l and a span of $2b$. The equations defining the wing are

$$z = \mathscr{Z}(x,y;l;b;\alpha) = \alpha l Z\left(\frac{x}{l},\frac{y}{l};\frac{b}{l}\right)$$

for $a_1(x/l) \leqslant y/l \leqslant a_2(x/l)$; the functions a_1 and a_2 give the leading edges of the wing as well as the outer edges of the trailing vortex sheet. The function Z is taken to be some sufficiently smooth function of x and y. Because it defines a single surface in space, the wing has no thickness. The aspect ratio is taken to be of order one; i.e. b/l will be assumed to be of order one. To eliminate unnecessary writing, the independent variables x, y and z will be scaled by l; otherwise the quantity $b/l = O(1)$ will appear throughout the calculations. For the sake of simplicity Cheng & Hafez (1975) assume that Z is such that there are no singularities at the leading edges. In fact, they assume that the velocity perturbations are zero at the leading edges and the outer edges of the trailing vortex sheet; here we assume this as well. By making this assumption we avoid the difficulties associated with leading edge singularities and separation addressed by Barnwell (1975). The small parameters of the problem are α, which gives a measure of the angle of attack of the wing, and M_0^2-1, which indicates that the flow is transonic; here $M_0 \equiv U/a_0$, where U is the speed of the undisturbed uniform flow and a_0 is the ambient sound speed.

The flow is assumed to be irrotational; a velocity potential ϕ^* therefore exists and the inviscid equations of motion of a perfect gas may be written

$$\nabla\phi^* . \nabla\left(\frac{\nabla\phi^* . \nabla\phi^*}{2}\right) = a^2\nabla^2\phi^*,$$

where

$$a^2 \equiv a_0^2 + \frac{\gamma-1}{2}\left[U^2 - \frac{\nabla\phi^* . \nabla\phi^*}{2}\right],$$

a is the local speed of sound in the gas and the γ is the ratio of specific heats. The last equation is just the Bernoulli equation for steady isentropic flow. The velocity potential ϕ^* contains a part due to the uniform stream and a part due to the perturbation of the wing. It will be convenient to work with the equation for the perturbation potential, ϕ, defined by

$$\phi^* \equiv Ux + \phi.$$

In terms of ϕ, the equation of motion is

$$\left.\begin{aligned} U^2\phi_{xx} + U\frac{\partial}{\partial x}|\nabla\phi|^2 + \nabla\phi . \nabla\left(\frac{|\nabla\phi|^2}{2}\right) &= a^2\nabla^2\phi, \\ a^2 = a_0^2 - (\gamma-1)\left[U\phi_x + \frac{|\nabla\phi|^2}{2}\right]&, \end{aligned}\right\} \tag{1}$$

exactly. The boundary condition on the wing is

$$\phi_z = (U+\phi_x)\mathscr{Z}_x + \phi_y\mathscr{Z}_y \tag{2}$$

on $z = \mathscr{Z}(x,y;l;b;\alpha)$. As $x^2+y^2+z^2 \to \infty$, it is further required that $|\nabla\phi| \to 0$.

In the following sections, solutions to (1) and (2) are sought which are valid for small α and M_0^2-1. In § 3 the solution valid near the wing is derived; this will be called the inner solution. Because the inner solution neglects certain nonlinear terms in (1), it fails to give a valid description of the flow at large distances from the wing. An approximation to (1) which is valid at large distances from the wing is derived in § 4. There it is shown that, to lowest order, the flow is governed by the small disturbance transonic equation; the region in which this is valid is called the outer region. The boundary condition satisfied by the first term of the outer expansion is obtained by a matching with the inner solution; this is done in § 5. There it is seen that every term in the inner solution contributes to the boundary condition for the outer problem; the resultant boundary condition for the outer problem will therefore be an infinite sum of terms. The outer expansion will be written

$$\phi = Ulf_0\,\Phi_0(\tilde{x},\hat{r},\omega) + o(f_0),$$

where $\tilde{x}$ and $\hat{r}$ are just scaled values of x and r (see figure 1*b*); the function Φ_0 will be shown to satisfy

$$\left.\begin{aligned} \Phi_{0\hat{r}\hat{r}} + \frac{1}{\hat{r}}\Phi_{0\hat{r}} + \frac{1}{\hat{r}^2}\Phi_{0\omega\omega} &= \frac{M_0^2-1}{f_0}\Phi_{0\tilde{x}\tilde{x}} + (\gamma+1)\Phi_{0\tilde{x}}\Phi_{0\tilde{x}\tilde{x}}, \\ \Phi_0(\tilde{x},\hat{r},\omega) &\sim \frac{a(\tilde{x})}{\hat{r}} + b(\tilde{x})[\ln^2\hat{r} + \cos^2\omega] + c(\tilde{x})\ln\hat{r} + d(\tilde{x}) + \dots, \end{aligned}\right\} \tag{3}$$

as $\hat{r} \to 0$, and $\hat{r}^{-1}\Phi_{0\omega}$, $\Phi_{0\hat{r}}$, $\Phi_{0\tilde{x}} \to 0$, as $\hat{r} \to \infty$. Here the dots indicate terms which are of order $\hat{r}\ln^3\hat{r}$ and higher in $\hat{r}$. An analogous result has been obtained by Cole & Messiter (1957) for the case of a slender axisymmetric body in transonic flow, see, e.g. their equation 5.9. Note also that the terms shown in (3) are singular as $\hat{r}\to 0$, whereas the unwritten terms vanish in this limit. In §5, it is further assumed that Φ_0 may be uniquely determined by a specification of the singularities at the axis; we may therefore truncate the infinite series and write the boundary condition as

$$\Phi_0 \sim \frac{a}{\hat{r}}+b[\ln^2\hat{r}+\cos^2\omega]+c\ln\hat{r}+d$$

as $\hat{r}\to 0$.

3. Inner solution

In the inner region the velocity potential ϕ and the independent variables x, y and z may be scaled as follows:

$$\phi = Ul\varphi, \quad x = l\tilde{x}, \quad y = l\tilde{y}, \quad z = l\tilde{z},$$

provided $b/l = O(1)$; where $\tilde{x}$, $\tilde{y}$ and $\tilde{z}$ are of order one in the inner region. Equations (1) and (2) may now be written as

$$\left.\begin{aligned} M_0^2\left[\varphi_{\tilde{x}\tilde{x}}+\frac{\partial}{\partial\tilde{x}}|\nabla\varphi|^2+\nabla\varphi\,.\,\nabla\left(\frac{|\nabla\varphi|^2}{2}\right)\right] &= \frac{a^2}{a_0^2}\nabla^2\varphi,\\ \frac{a^2}{a_0^2} &= 1-(\gamma-1)\,M_0^2\left(\varphi_{\tilde{x}}+\frac{|\nabla\varphi|^2}{2}\right) \end{aligned}\right\} \tag{4}$$

with

$$\varphi_{\tilde{z}} = \alpha[(1+\varphi_{\tilde{x}})\,Z_{\tilde{x}}+\varphi_{\tilde{y}}\,Z_{\tilde{y}}] \quad \text{on} \quad \tilde{z} = \alpha Z(\tilde{x},\tilde{y}), \tag{5}$$

where all derivatives are now with respect to $\tilde{x}$, $\tilde{y}$, $\tilde{z}$.

Equations (4) and (5) will now be perturbed for small α and M_0^2-1; the inner expansion is written

$$\varphi^i = g_0\,\varphi_0+g_1\,\varphi_1+O(g_2), \tag{6}$$

where the g_i's are the as yet undetermined inner gauge functions. When (6) is substituted into (4) and (5) and when the coefficients of like powers of α and M_0^2-1 are equated, there results a set of boundary-value problems, each of which is of the form

$$\left.\begin{aligned} \nabla_2^2\psi &= \mathscr{F}(\tilde{y},\tilde{z})\\ \psi_{\tilde{z}}(\tilde{y},0\pm) &= f\pm(\tilde{y}), \quad a_1\leqslant\tilde{y}\leqslant a_2, \end{aligned}\right\} \tag{7}$$

where $\nabla_2^2 \equiv \partial^2/\partial\tilde{z}^2+\partial^2/\partial\tilde{y}^2$; here $\tilde{x}$ only appears as a parameter and its dependence has not been explicitly shown. At this point it is useful to review the method of solution of (7); this will not only give a simple formula for the solution, but will also clarify certain of its features.

Solutions to (7) are not unique; the operator is elliptic, but boundary values are only specified on a slit $\tilde{z} = 0\pm$, $a_1 \leqslant \tilde{y} \leqslant a_2$. It is easily seen that any two solutions of (7) differ by, at most, a harmonic function. In this paper the arbitrary harmonic function is determined by matching to the outer solution. We first decompose the solution to (7) as follows:

$$\psi = \psi_p+\psi_H, \tag{8}$$

where ψ_p satisfies

$$\nabla_2^2 \psi_p = \mathscr{F}(\tilde{y}, \tilde{z})$$

and ψ_H satisfies

$$\nabla_2^2 \psi_H = 0,$$

$$\psi_{H\tilde{z}} = f^{\pm} - \psi_{p\tilde{z}} \quad \text{on} \quad \tilde{z} = 0\pm, \quad a_1 \leqslant \tilde{y} \leqslant a_2.$$

In terms of the complex variables $\zeta \equiv \tilde{y} + i\tilde{z}$ and $\bar{\zeta} \equiv \tilde{y} - i\tilde{z}$, the above equation for ψ_p may be written

$$\psi_{p\zeta\bar{\zeta}} = \tfrac{1}{4}\mathscr{F}(\zeta, \bar{\zeta});$$

thus ψ_p may be obtained by integrating with respect to ζ and $\bar{\zeta}$:

$$\psi_p = \frac{1}{4}\iint \mathscr{F}(\zeta, \bar{\zeta})\, d\zeta\, d\bar{\zeta} + \mathscr{H}_p,$$

where $\mathscr{H}_p$ is any harmonic function and is composed of the two arbitrary functions of integration. Because the function $\mathscr{F}$ is given, the indefinite integral $\iint \mathscr{F} d\zeta\, d\bar{\zeta}$ can be calculated explicitly. At this stage, it is convenient, but not necessary, to choose $\mathscr{H}_p$; the choice of $\mathscr{H}_p$ will only affect ψ_H and not the final result for ψ. This will be chosen such that ψ_p is some simple known function, say Ψ, e.g. when $\mathscr{F} \equiv 0$, $\mathscr{H}_p$ will be taken to be zero as well. We now discuss the harmonic part of the solution ψ_H. Because no conditions at infinity are given, ψ_H will be arbitrary; we may always rewrite ψ_H as

$$\psi_H = \psi'_H + \mathscr{H}_H,$$

where ψ'_H is defined by

$$\nabla_2^2 \psi'_H = 0,$$

$$\psi'_{H\tilde{z}} = f^{\pm} - \Psi_{\tilde{z}} \quad \text{on} \quad \tilde{z} = 0\pm, \quad a_1 \leqslant \tilde{y} \leqslant a_2,$$

and

$$\psi'_H \sim b_0 \ln \tilde{r} + b_1 + \ldots \quad \text{as} \quad \tilde{r} \to \infty.$$

The function $\mathscr{H}_H$ may be any function satisfying

$$\nabla_2^2 \mathscr{H}_H = 0,$$

$$\mathscr{H}_{H\tilde{z}} = 0 \quad \text{on} \quad \tilde{z} = 0\pm, \quad a_1 \leqslant \tilde{y} \leqslant a_2.$$

The solution for ψ'_H is well known (see, e.g. Ashley & Landahl 1965):

$$\psi'_H = \frac{1}{2\pi}\int_{a_1}^{a_2} [\psi'_{H\tilde{z}}] \ln r_1\, dy + \frac{1}{2\pi}\int_{a_1}^{a_2} [\psi'_H] \frac{\tilde{z}}{r_1^2}\, dy_1 + K,$$

where $r_1 \equiv \{(y_1 - \tilde{y})^2 + \tilde{z}^2\}^{\frac{1}{2}}$ and the square brackets indicate the jump in the quantity across the slit. Thus, ψ_H is given by

$$\psi_H = \frac{1}{2\pi}\int_{a_1}^{a_2} [f - \Psi_{\tilde{z}}] \ln r_1\, dy_{11} + \frac{1}{2\pi}\int_{a_1}^{a_2} [\psi_H] \frac{\tilde{z}}{r_1^2}\, dy_1 + K + \mathscr{H}_H$$
$$- \frac{1}{2\pi}\int_{a_1}^{a_2} [\mathscr{H}_H] \frac{\tilde{z}}{r_1^2}\, dy_1.$$

When this is substituted in (8) and the fact that $[\psi_H] = [\psi - \Psi]$ is used, we have

$$\psi = \Psi + \frac{1}{2\pi}\int_{a_1}^{a_2} [f - \Psi_{\tilde{z}}] \ln r_1\, dy_1 + \frac{1}{2\pi}\int_{a_1}^{a_2} [\psi - \Psi] \frac{\tilde{z}}{r_1^2}\, dy_1 + K$$
$$+ \mathscr{H}_H - \frac{1}{2\pi}\int_{a_1}^{a_2} [\mathscr{H}_H] \frac{\tilde{z}}{r_1^2}\, dy_1. \tag{9}$$

Thus, (9) gives the desired solution to (7) in terms of the known functions $f^{\pm}(\tilde y)$ and $\mathscr{F}(\tilde y,\tilde z)$ and the unknown harmonic function $\mathscr{H}_H$. It is clear from the above results that when $\mathscr{F}$ is not identically zero, the particular solution will induce a source or doublet distribution on the slit; this is due to the fact that the second and third terms in (9) contain $[\Psi_{\tilde z}]$ and $[\Psi]$ in their integrands. In the theory presented here the constant K and the harmonic function $\mathscr{H}_H(\tilde y,\tilde z)$ may also be functions of $\tilde x$ and α.

We now return to the equations (4) and (5); when (6) is substituted in (4) and (5), we find that

$$\nabla_2^2\varphi_0 = 0, \quad \varphi_{0\tilde z} = Z_{\tilde x}(\tilde x,\tilde y) \quad \text{on} \quad \tilde z = 0\pm, \quad a_2 \leqslant \tilde y \leqslant a_2,$$

provided we choose $g_0 = \alpha$. The solution to this is given by (9), with $\Psi \equiv 0$:

$$\varphi_0 = \frac{1}{2\pi}\int_{a_1}^{a_2}[\varphi_{0\tilde z}]\ln r_1\,dy_1 + \frac{1}{2\pi}\int_{a_1}^{a_2}[\varphi_0 - \mathscr{H}_0]\frac{\tilde z}{r_1^2}\,dy_1 + K_0(x) + \mathscr{H}_0(x,y,z).$$

Because $\varphi_{0\tilde z}$ is continuous across the wing the first integral may be dropped. Furthermore, the above boundary-value problem is satisfied by functions φ_0 which are antisymmetric in $\tilde z$, i.e.

$$\varphi_0(\tilde z) = -\varphi_0(-\tilde z).$$

Here we will assume that both φ_0 and $\mathscr{H}_0$ have this symmetry; hence, $K_0(\tilde x) \equiv 0$ and

$$\varphi_0(\tilde x,\tilde y,\tilde z) = \frac{1}{2\pi}\int_{a_1}^{a_2}[\varphi_0 - \mathscr{H}_0]\frac{\tilde z}{r_1^2}\,dy_1 + \mathscr{H}_0.$$

In order to obtain higher order terms in the inner expansion, it will be convenient to anticipate some of the results of matching to the outer solution. The inner expansion of the outer solution is essentially the inner boundary condition for the outer problem; this must be matched to the large $\tilde r$ expansion of φ_0:

$$\varphi_0 \sim \frac{1}{2\pi}\frac{\sin\omega}{\tilde r}\int_{a_1}^{a_2}[\varphi_0 - \mathscr{H}_0]\,dy_1 + \mathscr{H}_0 + O(\tilde r^{-2}),$$

where $\mathscr{H}_0$ has not yet been expanded and $\sin\omega = \tilde z/\tilde r$, $\cos\omega = \tilde y/\tilde r$. We require that this boundary condition contain at least the doublet

$$\frac{1}{2\pi}\frac{\sin\omega}{\tilde r}\int_{a_1}^{a_2}[\varphi_0]\,dy_1;$$

this will only be possible if, at large $\tilde r$, $\mathscr{H}_0 = O(\tilde r^{-1})$, at most. Thus, the matching gives the large $\tilde r$ behaviour of $\mathscr{H}_0$; $\mathscr{H}_0$ therefore satisfies

$$\nabla^2\mathscr{H}_0 = 0, \quad \mathscr{H}_{0\tilde z} = 0 \quad \text{on} \quad \tilde z = 0, \quad a_1 \leqslant \tilde y \leqslant a_2,$$

$$\mathscr{H}_0 = O(\tilde r^{-1}) \quad \text{as} \quad \tilde r \to \infty,$$

which implies that

$$\mathscr{H}_0 = \frac{1}{2\pi}\int_{a_1}^{a_2}[\mathscr{H}_0]\frac{\tilde z}{r_1^2}\,dy_1.$$

Thus,

$$\varphi_0(\tilde x,\tilde y,\tilde z) = \frac{1}{2\pi}\int_{a_1}^{a_2}[\varphi_0]\frac{\tilde z}{r_1^2}\,dy_1. \tag{10}$$

This gives φ_0 in terms of its jump across the wing and trailing vortex sheet. This jump is not known *a priori*; (10) leads to an integral equation for $[\varphi_0]$. Because the primary concern here is the flow far from the wing, it will be assumed that this integral equation has been solved and that $[\varphi_0]$ is known everywhere on the wing and in the trailing vortex sheet.

For the purposes of matching, the large $\tilde{r}$ behaviour of φ_0 is of interest; this is

$$\varphi_0 \sim \frac{F(\tilde{x})}{2\pi}\frac{\sin\omega}{\tilde{r}} + O\left(\frac{1}{\tilde{r}^2}\right), \tag{11}$$

where

$$F(\tilde{x}) \equiv \int_{a_1}^{a_2} [\varphi_0]\, dy_1.$$

This is immediately recognized as the potential due to a line doublet.

We now discuss the solution for φ_1. Substitution of the inner expansion (6) in (4) yields

$$\begin{aligned}\varphi_{\tilde{y}\tilde{y}} + \varphi_{\tilde{z}\tilde{z}} = {} & \alpha^2 \frac{\partial}{\partial\tilde{x}}\left[\frac{\gamma+1}{2}\varphi_{0\tilde{x}}^2 + \varphi_{0\tilde{y}}^2 + \varphi_{0\tilde{z}}^2\right] + \alpha g_1\left\{2\frac{\partial}{\partial\tilde{x}}\left[\frac{\gamma+1}{2}\varphi_{0\tilde{x}}\varphi_{1\tilde{x}}\right.\right. \\ & \left.\left. + \varphi_{0\tilde{y}}\varphi_{1\tilde{y}} + \varphi_{0\tilde{z}}\varphi_{1\tilde{z}}\right] + (\gamma-1)\varphi_{0\tilde{x}}\nabla_2^2\varphi_1 + (M_0^2-1)\alpha\varphi_{0\tilde{x}\tilde{x}}\right\} \\ & + \alpha^3\left\{\frac{\gamma+1}{2}\varphi_{0\tilde{x}}^2\varphi_{0\tilde{x}\tilde{x}} + \frac{\gamma-1}{2}\varphi_{0\tilde{x}\tilde{x}}(\varphi_{0\tilde{y}}^2 + \varphi_{0\tilde{z}}^2) + \varphi_{0\tilde{y}}^2\varphi_{0\tilde{y}\tilde{y}} + \varphi_{0\tilde{z}}^2\varphi_{0\tilde{z}\tilde{z}}\right. \\ & \left. + 2\varphi_{0\tilde{x}}\varphi_{0\tilde{y}}\varphi_{0\tilde{x}\tilde{y}} + 2\varphi_{0\tilde{x}}\varphi_{0\tilde{z}}\varphi_{0\tilde{x}\tilde{z}} + 2\varphi_{0\tilde{y}}\varphi_{0\tilde{z}}\varphi_{0\tilde{y}\tilde{z}}\right\} \\ & + O[(M_0^2-1)\alpha^2,\ (M_0^2-1)g_1] + o(\alpha^3, \alpha g_1),\end{aligned} \tag{12}$$

where use has been made of the fact that $\nabla_2^2\varphi_0 = 0$ and that $g_0 = \alpha$. In a similar manner the boundary condition (5) may be expanded to yield

$$\begin{aligned}\varphi_{\tilde{z}} = {} & \alpha Z_{\tilde{x}} - \alpha^2\{Z_{\tilde{x}}\varphi_{0\tilde{x}} + (Z\varphi_{0\tilde{y}})_{\tilde{y}}\} + \alpha g_1\{Z_{\tilde{x}}\varphi_{1\tilde{x}} + Z_{\tilde{y}}\varphi_{1\tilde{y}} - Z\varphi_{1\tilde{z}\tilde{z}}\} \\ & + \alpha^3\left\{ZZ_{\tilde{x}}\varphi_{0\tilde{x}\tilde{z}} + \left(\frac{Z^2}{2}\varphi_{0\tilde{y}\tilde{z}}\right)_{\tilde{y}}\right\} + o(\alpha^3, \alpha g_1),\end{aligned} \tag{13}$$

at $\tilde{z} = 0$. Here the usual Taylor series' expansions have been used to transfer the boundary condition from the wing surface to the $\tilde{z} = 0$ plane. In order to save space, the left-hand sides of both equations (12) and (13) have been left in terms of the exact potential φ; these of course, must be expanded in (6) when the actual calculations are performed.

At this stage, it is necessary to discuss the size of the $(M_0^2-1)\alpha\varphi_{0\tilde{x}\tilde{x}}$ term appearing in (12). In many theories of transonic aerodynamics, the matching of the near- and far-field solutions establishes a relationship between $M_0^2 - 1$ and the thickness or angle of attack of the wing or body. If, in the present case, we were to make no assumption about the size of $M_0^2 - 1$, the matching would show that

$$M_0^2 - 1 = O(\delta^2),$$

where δ is the ratio of the inner and outer length scales and is related to the angle of attack, α, through the equation

$$\alpha = \frac{\delta}{|\ln\delta|^{\frac{1}{2}}}.$$

In the following, we shall anticipate this result and use it wherever it is convenient; the reason for doing this is to keep the discussion of the inner expansion as concrete as possible.

We may now identify g_1 and the boundary-value problem for φ_1; this is

$$\nabla_2^2 \varphi_1 = \frac{\partial}{\partial \tilde{x}}\left[\frac{\gamma+1}{2}\varphi_{2\tilde{x}}^2 + \varphi_{0\tilde{y}}^2 + \varphi_{0\tilde{z}}^2\right] \tag{14}$$

with

$$\varphi_{1\tilde{z}}(\tilde{y}, 0\pm) = Z_{\tilde{x}}\,\varphi_{0\tilde{x}} + (Z\varphi_{0\tilde{y}})_{\tilde{y}}$$

for $a_1(\tilde{x}) \leqslant \tilde{y} \leqslant a_2(\tilde{x})$ provided we take $g_1 = \alpha^2$. In appendix A, the result (9) has been used to solve equations (14) for φ_1. Under the assumptions stated there φ_1 may be written

$$\varphi_1 = \frac{1}{2\pi}\int_{a_1}^{a_2}[\varphi_{0\tilde{y}}]\,Z\,\frac{\tilde{y}-y_1}{r_1^2}\,dy_1 + \tfrac{1}{2}(\varphi_0^2)_{\tilde{x}} - \frac{1}{2\pi}\int_{a_1}^{a_2}[\varphi_0]\,Z_{\tilde{x}\tilde{x}}\ln r_1\,dy_1$$
$$+\frac{\gamma+1}{2}\left\{\Psi'''' - \frac{1}{2\pi}\int_{a_1}^{a_2}[\Psi_{\tilde{z}}'''']\ln r_1\,dy_1\right\} + \mathscr{K}(\tilde{x}),$$

and the large $\tilde{r}$ expansion of φ_1 is

$$\varphi_1 \sim \frac{S'(\tilde{x})}{2\pi}\ln\tilde{r} + \mathscr{K}(\tilde{x}) + \frac{\gamma+1}{32\pi^2}(F'^2)'(\ln^2\tilde{r} + \cos^2\omega) + O\left(\frac{\ln\tilde{r}}{\tilde{r}}, \frac{1}{\tilde{r}}\right),$$

where Ψ'''' and $\psi_{\tilde{z}}''''(\tilde{y}, 0\pm; \tilde{x})$ are given by equations (A 7) and (A 5) respectively, and

$$S'(\tilde{x}) \equiv \frac{dS(\tilde{x})}{d\tilde{x}} \equiv G(\tilde{x}) + \frac{\gamma+1}{2}I(\tilde{x}),$$

$$G(\tilde{x}) \equiv -\int_{a_1}^{a_2}[\varphi_0]\,Z_{\tilde{x}\tilde{x}}\,dy_1, \quad I(\tilde{x}) \equiv -\int_{a_1}^{a_2}[\Psi_{\tilde{z}}'''']\,dy_1,$$

and $\mathscr{K}(\tilde{x})$ is an arbitrary function of $\tilde{x}$; it may also have a weak, e.g. logarithmic, dependence on α.

Inspection of (A 10) shows that φ_1 contains a source-like term as well as one which depends nonlinearly on the lift $F'(\tilde{x})$. Because $[\varphi_0] \neq 0$ on the trailing vortex sheet, $G(\tilde{x}) \neq 0$ there; hence, the source has an afterbody associated with it. The results obtained here are equivalent to those obtained previously by Cheng & Hafez (1975).

It is clear from equations (11) and (A 10) that the inner expansion (6) breaks down at large values of $\tilde{r}$; this is because nonlinear terms in (4) play an important role far from the wing. In the next section the nonlinear equation governing the flow far from the wing is derived.

4. Outer region

Far from the wing the $\tilde{y}$ and $\tilde{z}$ co-ordinates must be stretched relative to the $\tilde{x}$ co-ordinate; thus, we define the outer variables $\hat{y}$ and $\hat{z}$ by

$$\hat{y} \equiv \delta(\alpha)\tilde{y}, \quad \hat{z} \equiv \delta(\alpha)\tilde{z},$$

where $\delta = o(1)$ as $\alpha \to 0$. The outer expansion is written

$$\varphi^0 = f_0(\alpha)\,\Phi_0(\tilde{x}, \hat{y}, \hat{z}) + o(f_0).$$

For the sake of simplicity we shall assume that Φ_0 is also a weak function of α or $\delta(\alpha)$, e.g. logarithmic in δ. The results we obtain will be in accord with those found by Cheng & Hafez (1975). The advantage of the procedure used here is that we need only to discuss a one term outer expansion. Barnwell (1975) has approached the outer expansion from a different point of view; he primarily discusses three terms of an outer expansion having gauge functions which may be written

$$f_0, \frac{f_0}{\sqrt{|\ln\delta|}}, \frac{f_0}{[\ln\delta|}, \ldots,$$

where the coefficients of these gauge functions are now independent of α. The dots indicate the higher-order gauge functions; an inspection of higher-order terms suggests that this is an infinite sequence of terms of the general form $f_0/|\ln\delta|^{\frac{1}{2}n}$, where n takes on integral values. The relationship between the two approaches is clear; the outer expansion of Barnwell results from expanding our $\Phi_0(\tilde{x}, \tilde{r}, \omega; \ln\delta)$ for small δ. One can show that the results obtained by either approach are equivalent to the appropriate order.

When this scaling and outer expansion are substituted into the exact equation of motion (4), this equation becomes

$$\delta^2 f_0(\Phi_{0\hat{y}\hat{y}} + \Phi_{0\hat{z}\hat{z}}) = (M_0^2 - 1) f_0 \Phi_{0\tilde{x}\tilde{x}} + f_0^2 \frac{\partial}{\partial\tilde{x}}\left(\frac{\gamma+1}{2}\Phi_{0\tilde{x}}^2\right) + o(\delta^2 f_0, (M_0^2-1) f_0, f_0^2).$$

We now require that the four terms which are shown explicitly balance in the outer region; thus

$$\delta = \sqrt{f_0} \quad \text{and} \quad M_0^2 - 1 = O(f_0) = O(\delta^2),$$

and the equation satisfied by Φ_0 is

$$\Phi_{0\hat{y}\hat{y}} + \Phi_{0\hat{z}\hat{z}} = \frac{M_0^2 - 1}{\delta^2}\Phi_{0\tilde{x}\tilde{x}} + \frac{\partial}{\partial\tilde{x}}\left(\frac{\gamma+1}{2}\Phi_{0\tilde{x}}^2\right). \tag{15}$$

The outer equation is immediately recognized as the three-dimensional, small disturbance, transonic equation. The boundary condition for this equation must come from a matching with the inner solution; this we carry out in the next section. In addition to providing the boundary condition for the outer problem, the matching determines the scale factor δ explicitly in terms of α.

5. The matching

In this section the inner and outer expansions are matched. For the sake of simplicity, Van Dyke's (1964) matching principle is used. The more sophisticated technique of intermediate expansions gives results identical to the ones presented here.

The two term inner expansion reads

$$\varphi^i = \alpha\varphi_0 + \alpha^2\varphi_1 + o(\alpha^2),$$

where φ_0 and φ_1 have been given explicitly by equations (10) and (A 9), respectively. The one term outer expansion is given by

$$\varphi^0 = f_0\Phi_0(\tilde{x}, \hat{y}, \hat{z}) + o(f_0),$$

where $\hat{y} = \delta(\alpha)\tilde{y}$, $\hat{z} = \delta(\alpha)\tilde{z}$ and $\delta = f_0^{\frac{1}{2}} = o(1)$. As we have already discussed, we will regard Φ_0 as depending logarithmically on δ; furthermore, we shall take $\Phi_0 = O(1)$ as $\alpha \to 0$. To match these two expansions, the inner expansion must be cast in the outer variables and expanded to order f_0. Because $\tilde{r} = \hat{r}/\delta$, the large $\tilde{r}$ expansion of φ_0 and φ_1 will be useful. The resultant expansions are

$$\varphi_0 \sim \delta \frac{F}{2\pi} \frac{\sin\omega}{\hat{r}} + O\left(\frac{\delta^2}{\hat{r}^2}\right),$$

$$\varphi_1 \sim \frac{S'}{2\pi} \ln\frac{\hat{r}}{\delta} + \mathscr{K} + \frac{\gamma+1}{2} \frac{(F'^2)'}{16\pi^2} \left(\ln^2\frac{\hat{r}}{\delta} + \cos^2\omega\right) + O\left(\frac{\delta}{\hat{r}} \ln\frac{\hat{r}}{\delta}, \frac{\delta}{\hat{r}}\right).$$

We now introduce

$$\mathscr{K}^* \equiv \mathscr{K} - \frac{S'}{2\pi} \ln\delta + \frac{\gamma+1}{2} \frac{(F'^2)'}{16\pi^2} \ln^2\delta;$$

in order that $\Phi_0 = O(1)$ as $\alpha \to 0$, we require that $\mathscr{K}^* = O(1)$ as $\alpha \to 0$. Thus, the outer expansion of the inner solution reads:

$$(\varphi^i)^0 \sim \alpha\delta \frac{F}{2\pi} \frac{\sin\omega}{\hat{r}} + \alpha^2 \left\{ \left[\frac{S'}{2\pi} - (\gamma+1) \frac{(F'^2)'}{16\pi^2} \ln\delta \right] \ln\hat{r} + \mathscr{K}^* + \frac{\gamma+1}{2} \frac{(F'^2)'}{16\pi^2} (\ln^2\hat{r} + \cos^2\omega) \right\}. \qquad (16)$$

Here we have dropped the terms of order $\alpha\delta^2 = \alpha f_0$ which resulted from the expansion of φ_0 and the terms of order $\alpha^2\delta\ln\delta$ and $\delta\alpha^2$ which resulted from the expansion of φ_1. The first of these is clearly $o(f_0)$ and, if we anticipate the result, $\alpha^2 = \delta^2/|\ln\delta|$ as discussed in § 3, the second set of terms is also seen to be $o(f_0)$.

When the outer solution is written in terms of the inner variables $\tilde{r}$, ω, $\tilde{x}$ we have

$$(\varphi^0)^i = f_0 \Phi_0(\tilde{x}, \delta\tilde{r}, \omega); \qquad (17)$$

thus the boundary condition for the outer problem is applied as $\hat{r} \to 0$. The matching principle requires that (16) and (17) match as $\alpha \to 0$; hence

$$f_0 \Phi_0(\tilde{x}, \hat{r}, \omega) \sim \delta\alpha \frac{F}{2\pi} \frac{\sin\omega}{\hat{r}} + \alpha^2 \left\{ \left[\frac{S'}{2\pi} - (\gamma+1) \frac{(F'^2)'}{16\pi^2} \ln\delta \right] \ln\hat{r} + \mathscr{K}^* + \frac{(\gamma+1)}{2} \frac{(F'^2)'}{16\pi^2} (\ln^2\hat{r} + \cos^2\omega) \right\}. \qquad (18)$$

Fraenkel (1969) has pointed out that terms containing logarithms, *viz.* the term having α^2 as a coefficient in (18), should be matched as a single term. With this in mind, we see that the appropriate choice for $f_0 = \delta^2$ is $\alpha^2|\ln\delta|$, which further implies that $\delta = \delta(\alpha)$ is given implicitly by

$$\alpha^2 = \delta^2/|\ln\delta|. \qquad (19)$$

Thus, the matching requires that, as $\hat{r} \to 0$,

$$\Phi_0(\tilde{x}, \hat{r}, \omega) \sim \frac{1}{|\ln\delta|^{\frac{1}{2}}} \frac{F}{2\pi} \frac{\sin\omega}{\hat{r}} + \left[\frac{S'}{2\pi} \frac{1}{|\ln\delta|} + (\gamma+1) \frac{(F'^2)'}{16\pi^2} \right] \ln\hat{r} + \frac{\mathscr{K}^*}{|\ln\delta|} + \frac{1}{|\ln\delta|} \frac{\gamma+1}{2} \frac{(F'^2)'}{16\pi^2} (\ln^2\hat{r} + \cos^2\omega). \qquad (20)$$

According to the analysis presented so far, this is the boundary condition for the outer problem. When the third-, fourth-, and higher-order terms of the inner expansion are calculated, they also make a contribution to this boundary condition; in fact, the actual boundary condition is an infinite sum of terms. This is to be expected as we seek the asymptotic expansion of Φ_0 as $\hat{r} \to 0$ rather than its value at $\hat{r} = 0$. As an example, we could continue the inner expansion (6) to include third- and fourth-order terms

$$\varphi^i = g_0\,\varphi_0 + g_1\,\varphi_1 + g_2\,\varphi_2 + g_3\,\varphi_3 + o(g_3)$$

where an inspection of equations (12) and (13) shows that $g_2 = (M_0^2 - 1)\,\alpha$ and $g_3 = \alpha^3$. The procedure of this paper could be applied to these higher-order terms to determine their contribution to the boundary condition (20). It may be shown that when φ_2 and φ_3 are included in the inner expansion we must add the following quantity to (20):

$$\frac{\mathscr{k}}{|\ln\delta|^{\frac{1}{2}}}\left\{\frac{F''}{4\pi}\hat{r}\sin\omega\ln\hat{r} + \delta\mathscr{H}_2'\right\} + \frac{1}{|\ln\delta|^{\frac{3}{2}}}\left\{\frac{\gamma+1}{8\pi}\hat{r}\sin\omega[\tfrac{2}{3}(F'B')'\ln^3\hat{r}\right.$$
$$+ (F'(A' - B' - 2\ln\delta B'))'\ln^2\hat{r} + (F'(\tfrac{3}{2}B' - A' + 2\mathscr{K}^{*\prime}$$
$$\left. + B'\ln\delta))'\ln\hat{r} - (F'B')'\cos^2\omega] + \delta\mathscr{H}_3^*\right\}.$$

Here $\mathscr{k} \equiv M_0^2 - 1/\delta^2$, $A \equiv S'/2\pi$, $B \equiv \gamma + 1(F'^2)'/32\pi^2$ and $\mathscr{H}_2^*$ and $\mathscr{H}_3^*$ are harmonic functions proportional to $\hat{r}/\delta$. In like manner we could also determine the contributions of higher-order terms; these contribute terms of even higher order in $\hat{r}$. In order to simplify the boundary condition for the outer problem, we now make the assumption that the outer problem is well-posed provided that the singularities in Φ_0 at $\hat{r} = 0$ are specified. Because the higher-order terms, i.e. the terms $g_i\,\varphi_i$, $i \geqslant 2$, in the inner expansion contribute terms which vanish as $\hat{r} \to 0$, we may truncate the boundary condition to include only those shown in equation (20). Thus, the outer problem may be written

$$\Phi_{0\hat{r}\hat{r}} + \frac{1}{\hat{r}}\,\Phi_{0\hat{r}} + \frac{1}{\hat{r}^2}\,\Phi_{0\omega\omega} = \frac{M_0^2 - 1}{\delta^2}\,\Phi_{0\tilde{x}\tilde{x}} + (\gamma+1)\,\Phi_{0\tilde{x}}\,\Phi_{0\tilde{x}\tilde{x}},$$

where, as $\hat{r} \to 0$,

$$\Phi_0(\tilde{x}, \hat{r}, \omega) \sim \frac{1}{|\ln\delta|^{\frac{1}{2}}}\frac{F}{2\pi}\frac{\sin\omega}{\hat{r}} + \left[\frac{S'}{2\pi}\frac{1}{|\ln\delta|} + (\gamma+1)\frac{(F'^2)'}{16\pi^2}\right]\ln\hat{r}$$
$$+ \frac{\mathscr{K}^*}{|\ln\delta|} + \frac{1}{|\ln\delta|}\left(\frac{\gamma+1}{2}\right)\frac{(F'^2)'}{16\pi^2}(\ln^2\hat{r} + \cos^2\omega), \tag{21}$$

and, as $\hat{r} \to \infty$, $\hat{r}^{-1}\Phi_{0\omega}$, $\Phi_{0\hat{r}}$, $\Phi_{0\tilde{x}} \to 0$.

Here we recognize the first term as a doublet and the second term as a source having strength $(S'/2\pi)(1/|\ln\delta|) + (\gamma+1)(F'^2)'/16\pi^2$. The first part of the source is due to the nature of the second-order velocity perturbations on the wing and the part depending nonlinearly on the lift is due to the fact that the flow in the neighbourhood of the wing, i.e. $\tilde{r} = O(1)$, appears as a source flow when viewed from the far field. We note also that in theories of transonic flow not involving lift, the solution to the outer problem only depends on $M_0^2 - 1/(\gamma+1)\,\delta^2$, i.e. the similarity parameter of the problem. Here the solution also depends on $(\gamma+1)$ and $\ln\delta$; hence, in lift dominated flows, no simple similarity rule holds. Furthermore, it is clear that no conventional area or equivalence rule applies for the wings treated here. We refer the reader to Cheng & Hafez (1975) and Cheng (1977) for a further discussion of equivalence rules applied to lifting wings.

Throughout this paper we have confined ourselves to wings having zero thickness. The effect of a wing's thickness is easily incorporated and we will now give a brief discussion of it. The equation of a wing having thickness can be written

$$\tilde{z} = \alpha Z \pm \tau Z_v$$

where the subscript v will always denote functions associated with thickness effects. The inner expansion corresponding to (6) would be

$$\varphi^i = \alpha\varphi_0 + \tau\varphi_v + \alpha^2\varphi_1 + \dots .$$

If we now proceed as we did in § 3, we should find that

$$\varphi_v = \frac{1}{\pi}\int_{a_1}^{a_2} Z_{vx} \ln r_1 \, dy_1 + \mathscr{K}_v,$$

and, as $\tilde{r} \to \infty$,

$$\varphi_v \sim \frac{1}{2\pi} S_v \ln \tilde{r} + \mathscr{K}_v + O\left(\frac{1}{\tilde{r}}\right),$$

where

$$S_v \equiv 2\int_{a_1}^{a_2} Z_{v\tilde{x}} \, dy_1.$$

When this is cast in terms of the outer variables we have

$$(\varphi_v)^0 \sim \frac{1}{2\pi} S_v \ln \hat{r} + \mathscr{K}_v^* + O\left(\frac{\delta}{\hat{r}}\right),$$

where $\mathscr{K}_v^* \equiv \mathscr{K}_v - (S_v/2\pi)\ln\delta \equiv O(1)$. Thus, the thickness would contribute

$$\tau[(S_v/2\pi)\ln\hat{r} + \mathscr{K}_v^*]$$

to equation (18). Inspection shows that the thickness and lift have an equal effect on the outer problem provided $\tau = O(f_0) = O(\delta^2)$, where δ is related to α by (19). An examination of higher-order terms shows that this is the only additional singularity generated by the introduction of the thickness; thus, provided $\tau = O(\delta^2)$, the thickness contributes $\tau/\delta^2[S_v/2\pi \ln\hat{r} + \mathscr{K}_v^*]$ to the boundary condition in (21). Generally, when $\tau \neq O(\delta^2(\alpha))$, where $\delta(\alpha)$ is given by (19), we may neglect either the lift or thickness when calculating the outer flow. For example, when $\tau = O(\alpha)$, the matching requires that $f_0 = \tau$, $\delta = \tau^{\frac{1}{2}}$ and that the boundary condition is

$$\Phi_0 \sim \frac{S_v}{2\pi}\ln\hat{r} + \mathscr{K}_v^*$$

as $\hat{r} \to 0$. When $\tau = O(\alpha^3)$, the matching yields the same results as in the zero thickness case; in this case the thickness effects may be considered negligible for the purposes of calculating the far field.

6. Discussion of previous investigations

In this section we discuss the investigations of Barnwell (1975) and Cheng & Hafez (1975), comparing their results and procedures to ours. Both papers give derivations of the boundary-value problem governing the flow far from a lifting wing; their procedures are seen to differ considerably in both appearance and content from each other and the present study.

We first discuss the work of Barnwell. It should first be mentioned that Barnwell uses a body oriented co-ordinate system in contrast to the wind oriented system used here; hence care should be exercised in comparing Barnwell's work to either ours or Cheng & Hafez's. Barnwell also provides a discussion of the effect of leading edge separation; this complication will not be discussed here. Barnwell first presents an inner expansion which contains gauge functions which are logarithmic in the ratio of the inner and outer length scales. Although our inner expansion proceeded in integral powers of α and M_0^2-1, we allowed $\mathscr{H}$ and $\mathscr{H}_H(\tilde{y},\tilde{z})$ in (9) to depend on α; thus, the resultant inner expansion is seen to be equivalent to that of Barnwell. A further examination of Barnwell's inner expansion shows that Barnwell has omitted the following term,

$$\frac{\bar{r}}{\lambda^4}\frac{\partial^2\phi_1}{\partial\bar{z}^2}g = -\frac{\bar{r}}{\lambda^4}\frac{\partial^2\phi_1}{\partial\bar{y}^2}g,$$

from his boundary condition (19). This produces an error in the strength of the equivalent source given by $H(\bar{x})$ in his equation (68).

Barnwell also presents a very careful study of the outer solution. As we mentioned in §4 he finds the equations governing three terms of the outer expansion; in his notation these terms are

$$\epsilon_1\,\Phi_1+\epsilon_2\,\Phi_2+\epsilon_3\,\Phi_3,$$

where ϵ_1, ϵ_2 and ϵ_3 are the outer gauge functions and Φ_1, Φ_2 and Φ_3 are independent of any small parameters. The lowest-order term satisfies the small disturbance transonic equation and Φ_2 and Φ_3 satisfy linear equations which have coefficients dependent on the lower-order Φ_i's and their derivatives. To match the inner and outer expansions he needs a small $\bar{r}$ expansion of the Φ_i's. To obtain this he uses the iterative technique of Cole & Messiter (1957) to solve the differential equations governing Φ_1, Φ_2 and Φ_3 for small values of $\bar{r}$; this assures us that the inner expansion of the outer solution satisfies the outer equations. For the sake of simplicity, we have presented a more intuitive approach to this than that presented by Barnwell. Essentially, we have tacitly assumed that a small $\hat{r}$ expansion of our outer solution will contain all the terms necessary to match. It is easy to show that when such an iterative procedure is applied to our outer solution, a boundary condition results which is identical to the one presented here. Once Barnwell obtains his expansion of the outer solution he matches this to the large $\bar{r}$ expansion of the inner solution. Except for the error in the source strength mentioned above his results are in agreement with those given here.

As a final remark we note that Barnwell states that an intermediate expansion is necessary in order to match the inner and outer expansions. He bases this on an examination of the large $\bar{r}$ expansion of the inner solution (his equation 67) and the small $\bar{r}$ expansion of the outer solution (his equation 68). Because the leading term in (67) is a dipole and the leading term in (68) is a source, he concludes that an intermediate expansion is necessary. In §5 we used a rule concerning the matching of logarithms; if this is applied to Barnwell's expansions (67) and (68) it is clear that they may be matched without recourse to an intermediate expansion.

We now discuss the results of Cheng & Hafez. Of the two previous investigations the procedure of Cheng & Hafez has the closest resemblance to ours. Their inner expansion can be shown to be the same as ours and they use a one-term outer expansion similar to that given here. Throughout their paper, Cheng & Hafez use an elaborate parameterization scheme. They also correctly state that their results are valid for $\lambda \equiv b/l = O(1)$; this appears to be inconsistent with the parameterization scheme. Specifically, in equation (2.10) they introduce a parameter

$$\Gamma_* \equiv 8/(\gamma+1)\,\lambda^2|\ln\epsilon|,$$

where ϵ is the ratio of inner and outer length scales analogous to our δ; they further require that Γ_* be non-vanishing as $\epsilon \to 0$. This would seem to imply that λ must vary as $|\ln\epsilon|^{-\frac{1}{2}}$ which violates their $\lambda = O(1)$ assumption. However, this inconsistency in the parameterization does not affect the final results.

In §4.3 the outer equation is introduced and a small $\eta \equiv \epsilon r$ expansion of the outer solution is given. In §4.5 the matching is carried out for the case corresponding to the one discussed here. The boundary condition for the outer problem is given by their equation (4.12); this is seen to disagree with our boundary condition (21). Specifically, the terms

$$\frac{\epsilon'}{2\pi}\,[\bar{D}_1(x)\,(\eta')^{-1}\cos\omega + |\ln\epsilon'|^{-\frac{1}{2}}\,m_{32}(\eta')^{-2}\sin 2\omega]$$

appear in their equation (4.12), but are absent in ours. It may be shown that these terms correspond to the $O(\delta^2/\hat{r}^2)$ term found in the outer expansion of φ_0 and the $O(\delta\hat{r}^{-1}\ln\hat{r}/\delta, \delta/\hat{r})$ term found in the outer expansion of φ_1; these higher-order terms must be truncated in the matching. In a later publication, Cheng (1977) discusses the application of this theory to particular wing configurations; the boundary condition used in this study is equivalent to the one derived here.

With the exception of the errors mentioned above, the results of Barnwell (1975), Cheng & Hafez (1975) and the present study are in agreement. The study presented here approaches the problem from a more fundamental point of view and is therefore believed to be more accessible to the reader.

7. Conclusion

We have presented a theory of thin three-dimensional wings without thickness in transonic flow. The boundary-value problem governing the flow far from the wing has been derived. The calculations presented here are intended to be simpler than those of the previously published studies; they also correct errors found in these earlier studies. Both the previous investigations and the present study show that there are effects which are of second order in the near-field which produce first-order effects in the far-field.

This research was carried out while the author was a Research Associate in the Department of Aerospace and Mechanical Engineering and the Program in Applied Mathematics at the University of Arizona, Tucson, Arizona. It was sponsored by the N.A.S.A. through Grant NSG-2112 and A.F.O.S.R. through Grant 76-2954. The author is indebted to Drs R. C. Ackerberg, R. E. O'Malley, W. R. Sears and A. R. Seebass for valuable comments and criticisms.

Appendix A. Solution for φ_1

Because of the linearity of the Laplacian it is permissible to break φ_1 up into three parts:

$$\varphi_1 = \varphi' + \varphi'' + \tfrac{1}{2}(\gamma+1)\,\varphi''',$$

where φ' satisfies

$$\nabla_2^2\,\varphi' = 0$$

with

$$\varphi'_{\tilde z} = (\varphi_{0\tilde y}Z)_{\tilde y} \quad \text{on} \quad \tilde z = 0\pm, \quad a_1 \leqslant \tilde y \leqslant a_2;$$

φ'' satisfies

$$\nabla_2^2\,\varphi'' = \frac{\partial}{\partial\tilde x}(\varphi_{0\tilde y}^2 + \varphi_{0\tilde z}^2)$$

with

$$\varphi''_{\tilde z} = \varphi_{0\tilde z}Z_{\tilde x} \quad \text{on} \quad \tilde z = 0\pm, \quad a_1 \leqslant \tilde y \leqslant a_2,$$

and φ''' satisfies

$$\nabla_2^2\,\varphi''' = \frac{\partial}{\partial\tilde x}(\varphi_{0\tilde x}^2)$$

with

$$\varphi'''_{\tilde z} = 0 \quad \text{on} \quad \tilde z = 0\pm, \quad a_1 \leqslant \tilde y \leqslant a_2.$$

Equation (14) admits solutions for φ_1 which are symmetric in $\tilde z$, i.e. $\varphi_1(\tilde z) = \varphi_1(-\hat z)$. In the following we will assume that φ_1 as well as φ', φ'', and φ''' are symmetric in $\tilde z$.

The above problem for φ' is homogeneous; thus, we will not only take $[\psi] = 0$, $[\mathscr{H}_H] = 0$ and $f = (\varphi_{0\tilde y}Z)_{\tilde y}$ in (9), but $\Psi = 0$ as well. Thus,

$$\varphi' = \frac{1}{2\pi}\int_{a_1}^{a_2}([\varphi_{0\tilde y}]Z)_{y_1}\ln r_1\,dy_1 + \mathscr{K}_1(\tilde x) + \mathscr{H}',$$

where $\mathscr{H}'$ is the arbitrary harmonic function found in equation (9). An integration by parts yields

$$\varphi' = \frac{1}{2\pi}\{\ln r_1[\varphi_{0\tilde y}]Z\}\Big|_{a_1}^{a_2} - \frac{1}{2\pi}\int_{a_1}^{a_2}[\varphi_{0\tilde y}]Z\frac{y_1-\tilde y}{r_1^2}\,dy_1 + \mathscr{K}_1 + \mathscr{H}'.$$

Here we follow Cheng & Hafez (1975) and require that $[\varphi_{0\tilde y}] \equiv 0$ at the leading edges of the wing and the outer edges of the trailing vortex sheet. Thus,

$$\varphi' = \frac{1}{2\pi}\int_{a_1}^{a_2}[\varphi_{0\tilde y}]Z\frac{\tilde y-y_1}{r_1^2}\,dy_1 + \mathscr{K}_1(\tilde x) + \mathscr{H}'. \tag{A 1}$$

The large $\tilde r$ behaviour of φ' is

$$\varphi' \sim \mathscr{K}_1(\tilde x) + \frac{\cos\omega}{2\pi\tilde r}\int_{a_1}^{a_2}[\varphi_{0\tilde y}]Z\,dy_1 + \mathscr{H}'(\tilde r,\omega;\tilde x) + O\left(\frac{1}{\tilde r^2}\right). \tag{A 2}$$

In the large $\tilde r$ expansions of φ', φ'' and φ''', we will not expand the arbitrary harmonic functions; this behaviour must be obtained from the matching.

We now derive the solution for φ''. The function $\mathscr{F}(\zeta,\bar\zeta;\tilde x)$ in § 3 is seen to be equal to $4(\varphi_{0\zeta}\,\varphi_{0\bar\zeta})_{\tilde x}$; Cheng & Hafez (1973) have shown that when the arbitrary function $\mathscr{H}_p$ in § 3 is taken to be identically zero, the function Ψ, or here Ψ'', is given by

$$\Psi'' = (\tfrac{1}{2}\varphi_0^2)_{\tilde x},$$

and, from the boundary condition for φ_0, we have

$$\Psi''_{\tilde{z}}(\tilde{y}, 0\pm; \tilde{x}) = \varphi_{0\tilde{x}} Z_{\tilde{x}} + \varphi_0 Z_{\tilde{x}\tilde{x}}.$$

Thus, the solution for φ'' which is symmetric in $\tilde{z}$ is

$$\varphi'' = (\tfrac{1}{2}\varphi_0^2)_{\tilde{x}} - \frac{1}{2\pi}\int_{a_1}^{a_2} [\varphi_0]\, Z_{\tilde{x}\tilde{x}} \ln r_1\, dy_1 + \mathscr{K}_2(\tilde{x}) + \mathscr{H}''. \tag{A 3}$$

For large $\tilde{r}$,

$$\varphi'' \sim \frac{1}{2\pi} G(\tilde{x}) \ln \tilde{r} + \mathscr{K}_2(\tilde{x}) + \mathscr{H}'' + O\left(\frac{1}{\tilde{r}}\right), \tag{A 4}$$

where

$$G(\tilde{x}) \equiv -\int_{a_1}^{a_2} [\varphi_0]\, Z_{\tilde{x}\tilde{x}}\, dy_1.$$

Finally, we consider the problem for φ'''. The function $\mathscr{F}(\zeta, \bar{\zeta}; \tilde{x})$ in § 3 is seen to be $\partial(\varphi_{0\tilde{x}}^2(\zeta, \bar{\zeta}; \tilde{x}))/\partial\tilde{x}$, where

$$\varphi_{0\tilde{x}}^2 = -\frac{1}{16\pi^2}\int_{a_1}^{a_2}\int_{a_1}^{a_2} [\varphi_{0\tilde{x}}]_1 [\varphi_{0\tilde{x}}]_2 \left\{\frac{1}{y_1 - \zeta} - \frac{1}{y_1 - \bar{\zeta}}\right\} \left\{\frac{1}{y_2 - \zeta} - \frac{1}{y_2 - \bar{\zeta}}\right\} dy_1\, dy_2,$$

where $[\varphi_{0\tilde{x}}]_i \equiv [\varphi_{0\tilde{x}}]\,(y_i; \tilde{x})$, $i = 1, 2$. Cheng & Hafez (1973) have shown that Ψ, or here Ψ''', can be written

$$\begin{aligned}\Psi''' = &-\frac{1}{64\pi^2}\frac{\partial}{\partial\tilde{x}}\int_{a_1}^{a_2}\int_{a_1}^{a_2} \frac{[\varphi_{0\tilde{x}}]_1 [\varphi_{0\tilde{x}}]_2}{y_1 - y_2} \ln\left(\frac{\zeta - y_1}{\zeta - y_2}\cdot\frac{\bar{\zeta} - y_1}{\bar{\zeta} - y_2}\right) dy_1\, dy_2 \\ &+ \frac{1}{64\pi^2}\frac{\partial}{\partial\tilde{x}}\left\{\int_{a_1}^{a_2} [\varphi_{0\tilde{x}}]_1 \ln(\zeta - y_1)(\bar{\zeta} - y_1)\, dy_1\right\}^2,\end{aligned}$$

provided that we choose $\mathscr{H}_p$ (see § 3) as follows

$$\begin{aligned}\mathscr{H}_p = &\frac{1}{64\pi^2}\frac{\partial}{\partial\tilde{x}}\int_{a_1}^{a_2}\int_{a_1}^{a_2} [\varphi_{0\tilde{x}}]_1 [\varphi_{0\tilde{x}}]_2 \{\ln(\zeta - y_1)(\zeta - y_2) + \ln(\bar{\zeta} - y_1)(\bar{\zeta} - y_2)\}\, dy_1\, dy_2 \\ &- \frac{1}{64\pi^2}\frac{\partial}{\partial\tilde{x}}\int_{a_1}^{a_2}\int_{a_1}^{a_2} \frac{[\varphi_{0\tilde{x}}]_1 [\varphi_{0\tilde{x}}]_2}{y_1 - y_2}\left\{\zeta \ln\left(\frac{\zeta - y_1}{\zeta - y_2}\right) + \bar{\zeta}\ln\left(\frac{\bar{\zeta} - y_1}{\bar{\zeta} - y_2}\right)\right\} dy_1\, dy_2.\end{aligned}$$

At $\tilde{z} = 0\pm$, Cheng & Hafez (1973) have also shown that

$$\Psi'''_{\tilde{z}}(\tilde{y}, 0\pm, \tilde{x}) = \pm\frac{1}{2\pi}\frac{\partial}{\partial\tilde{x}}\left\{[\varphi_{0\tilde{x}}]\,(\tilde{y}; \tilde{x})\ \text{P.V.}\int_{a_2}^{a_2} [\varphi_{0\tilde{x}}]_1 \left(\ln|y_1 - \tilde{y}| + \frac{\tilde{y}}{y_1 - \tilde{y}}\right) dy_1\right\}, \tag{A 5}$$

where the P.V. indicates that the Cauchy Principal Value of the integral is to be taken. Thus, the solution for φ''' which is symmetric in $\tilde{z}$ is

$$\varphi''' = \Psi''' - \frac{1}{2\pi}\int_{a_1}^{a_2} [\Psi'''_z] \ln r_1\, dy_1 + \mathscr{K}_3(\tilde{x}) + \mathscr{H}''', \tag{A 6}$$

where, in terms of the real variables $\tilde{y}$ and $\tilde{z}$, Ψ''' is

$$\Psi''' = -\frac{\tilde{y}}{16\pi^2}\frac{\partial}{\partial\tilde{x}}\left\{\int_{a_1}^{a_2}\int_{a_1}^{a_2} \frac{[\varphi_{0\tilde{x}}]_1 [\varphi_{0\tilde{x}}]_2}{y_1 - y_2} \ln\frac{r_1}{r_2}\, dy_1\, dy_2\right\} + \frac{1}{16\pi^2}\frac{\partial}{\partial\tilde{x}}\left\{\int_{a_1}^{a_2} [\varphi_{0\tilde{x}}]_1 \ln r_1\, dy_1\right\}^2, \tag{A 7}$$

and $\Psi'''_{\tilde{z}}(\tilde{y}, 0\pm; \tilde{x})$ is given by (A 5). For large values of $\tilde{r}$, Ψ''' has the behaviour

$$\Psi''' \sim \frac{1}{16\pi^2}(\ln^2\tilde{r} + \cos^2\omega)\,(F'^2)' + O\left(\frac{\ln\tilde{r}}{\tilde{r}}, \frac{1}{\tilde{r}}\right),$$

where $F' \equiv (d/d\tilde{x})\,F(\tilde{x})$. Thus, as $\tilde{r} \to \infty$

$$\varphi''' \sim \frac{1}{16\pi^2}(\ln^2\tilde{r} + \cos^2\omega)\,(F'^2)' + \frac{1}{2\pi} I(\tilde{x})\ln\tilde{r} + \mathscr{K}_3 + \mathscr{H}''' + O\left(\frac{\ln\tilde{r}}{\tilde{r}}, \frac{1}{\tilde{r}}\right), \tag{A 8}$$

where

$$I(\tilde{x}) \equiv -\int_{a_1}^{a_2} [\Psi'''_{\tilde{z}}]\,dy_1.$$

Thus, φ_1 is given by the sum of the terms φ', φ'' and $\frac{1}{2}(\gamma+1)\,\varphi'''$. The large $\tilde{r}$ behaviour of φ_1 may be obtained by equations (A 2), (A 4) and (A 8); this may be written

$$\varphi_1 \sim \frac{S'(\tilde{x})}{2\pi}\ln\tilde{r} + \mathscr{K}(\tilde{x}) + \frac{\gamma+1}{32\pi^2}(F'^2)'(\ln^2\tilde{r} + \cos^2\omega) + \mathscr{H}_1 + O\left(\frac{\ln\tilde{r}}{\tilde{r}}, \frac{1}{\tilde{r}}\right),$$

where

$$S'(\tilde{x}) \equiv \frac{dS(\tilde{x})}{d\tilde{x}} \equiv G(\tilde{x}) + \frac{\gamma+1}{2} I(\tilde{x}),$$

$$\mathscr{K}(\tilde{x}) \equiv \mathscr{K}_1 + \mathscr{K}_2 + \frac{\gamma+1}{2}\mathscr{K}_3$$

and

$$\mathscr{H}_1(\tilde{r}, \omega; \tilde{x}) \equiv \mathscr{H}' + \mathscr{H}'' + \frac{\gamma+1}{2}\mathscr{H}'''.$$

As we did in the discussion of φ_0, we will now anticipate some of the results of the matching to determine $\mathscr{H}_1$ for all values of $\tilde{x}$, $\tilde{y}$ and $\tilde{z}$. We will require that the boundary condition for the outer problem contains contributions from φ', φ'' and φ'''; the only way that this will be possible is $\mathscr{H}_1 = O(\ln\tilde{r})$ at most, as $\tilde{r} \to \infty$. This condition, combined with the fact that $\mathscr{H}_1$ is symmetric in $\tilde{z}$ and satisfies

$$\nabla_2^2\mathscr{H}_1 = 0 \quad \text{for all} \quad \tilde{x}, \tilde{y}, \tilde{z},$$

and

$$\mathscr{H}_{1\tilde{z}} = 0 \quad \text{on} \quad \tilde{z} = 0^{\pm}, \quad a_1 \leqslant \tilde{y} \leqslant a_2,$$

implies that $\mathscr{H}_1$ is a function of $\tilde{x}$ alone. If we absorb this function of $\tilde{x}$ in $\mathscr{K}(\tilde{x})$ we may now write

$$\begin{aligned}\varphi_1 = \frac{1}{2\pi}\int_{a_1}^{a_2}[\varphi_{0\tilde{y}}]\,Z\frac{\tilde{y}-y_1}{r_1^2}\,dy_1 + \tfrac{1}{2}(\varphi_0^2)_{\tilde{x}} - \frac{1}{2\pi}\int_{a_1}^{a_2}[\varphi_0]\,Z_{\tilde{x}\tilde{x}}\ln r_1\,dy_1 \\ + \frac{\gamma+1}{2}\left\{\Psi''' - \frac{1}{2\pi}\int_{a_1}^{a_2}[\Psi'''_{\tilde{z}}]\ln r_1\,dy_1\right\} + \mathscr{K}(\tilde{x}),\end{aligned} \tag{A 9}$$

and as $\tilde{r} \to \infty$,

$$\varphi_1 \sim \frac{S'(\tilde{x})}{2\pi}\ln\tilde{r} + \mathscr{K}(\tilde{x}) + \frac{\gamma+1}{32\pi^2}(F'^2)'(\ln^2\tilde{r} + \cos^2\omega) + O\left(\frac{\ln\tilde{r}}{\tilde{r}}, \frac{1}{\tilde{r}}\right). \tag{A 10}$$

REFERENCES

ASHLEY, H. & LANDAHL, M. 1965 *Aerodynamics of Wings and Bodies*. Addison Wesley.

BARNWELL, R. W. 1973 *A.I.A.A. J.* **11**, 764.

BARNWELL, R. W. 1975 *N.A.S.A. Tech. Rep.* TR R-440.

CHENG, H. K. 1977 *A.I.A.A. J.* **15**, 366.

CHENG, H. K. & HAFEZ, M. 1972 *A.I.A.A. J.* **10**, 1115.

CHENG, H. K. & HAFEZ, M. 1973 *USC Engng Rep.* no. 124.

Cheng, H. K. & Hafez, M. 1975 *J. Fluid Mech.* **72**, 161.

Cole, J. D. & Messiter, A. F. 1957 *Z. angew Math. Phys.* **8**, 1.

Fraenkel, L. E. 1969 *Proc. Camb. Phil. Soc.* **65**, 209.

Hayes, W. D. 1954 *J. Aero. Sci.* **21**, 721.

Oswatitsch, K. 1952 *Proc. 8th Inst. Cong. Theor. Appl. Mech.* Istanbul.

Spreiter, J. R. & Stahara, S. S. 1971 *A.I.A.A. J.* **9**, 1784.

Van Dyke, M. 1964 *Perturbation Methods in Fluid Mechanics.* Academic.

AIAA 78-1114

New Method for Designing Shock-Free Transonic Configurations

H. Sobieczky, N. J. Yu, K-Y. Fung,
A. R. Seebass

Reprinted from
AIAA Journal Volume 17, Number 7, July 1979, Page 722

E OF AERONAUTICS AND ASTRONAUTICS • 1290 AVENUE OF THE AMERICAS • NEW YORK, NEW YORK, N.Y. 10019

ARTICLE NO. 78-1114

New Method for Designing Shock-Free Transonic Configurations

H. Sobieczky,* N. J. Yu,† K-Y. Fung,‡ and A. R. Seebass§
University of Arizona, Tucson, Ariz.

A new method for the design of shock-free supercritical airfoils, wings, and three-dimensional configurations is described. Results illustrating this procedure in two and three dimensions are given. They include modifications to part of the upper surface of an NACA 64A410 airfoil that will maintain shock-free flow over a range of Mach numbers for a fixed lift coefficient, and the modifications required on part of the upper surface of a swept wing with an NACA 64A410 root section to achieve shock-free flow. While the results are given for inviscid flow, the same procedures can be employed iteratively with a boundary-layer calculation in order to achieve shock-free viscous designs. With a shock-free pressure field, the boundary-layer calculation will be reliable and not complicated by the difficulties of shock wave, boundary-layer interaction.

Introduction

WELL-KNOWN requirements for increased efficiency and, in the case of commercial aircraft, productivity have forced the operating conditions of compressors, turbines, propellers, wing sections, and aircraft into the transonic regime. Unfortunately, once local regions of supersonic flow occur, shock waves are likely with the attendant wave drag and boundary-layer separation losses. In the mid 1950s, Morawetz[1] proved that shock-free, two-dimensional, irrotational, near-sonic flows are mathematically isolated. In other words, any arbitrary¶ changes in the flow or boundary conditions that provide a shock-free flow will lead to the formation of a shock wave. Thus, Morawetz's theorem stated that the shock-free inviscid flow solutions, if and when they existed, were isolated by neighboring solutions that contain shock waves. Recently, this result has been extended to three dimensions by Cook.[2] Fortunately, it was recognized that such flow would have practical significance if, as seemed likely, the shock waves that occurred in neighboring flows were very weak. Wind tunnel research by Whitcomb[3] at the NASA Langley Research Center and Pearcey[4] at the National Physical Laboratory, United Kingdom, led to the development of practical "shock-free" airfoil sections. Subsequent analytical studies by Garabedian and Korn,[5] Nieuwland,[6] Boerstoel,[7] and Sobieczky[8] established theoretical design procedures for two-dimensional inviscid flows. More recently, the development of sophisticated numerical codes for the analysis of transonic flowfields has led to the design of both airfoils and wings by numerical optimization.[9,10] The practical success of the preceding efforts, as documented by the recent NASA Conference on Advanced Technology Research,[11] has been substantial. Further progress, as reported here, seems likely. The senior author recognized that the procedure he was using in the hodograph plane implied an analogous procedure in the physical plane, and furthermore, that this procedure did not seem to be restricted to two-dimensional flows.[12,13] This paper reports the success to date in using this idea to provide shock-free designs in two and three dimensions.

The design procedure invoked here is, in principle, a simple one. While there is no guarantee that a shock-free flow will necessarily result from the procedure, our experience in two dimensions has been that if the hodograph method will work for specified flow and airfoil parameters, then the procedure outlined here will work too. Also, it provides neighboring shock-free airfoil shapes for fixed lift coefficient with varying Mach numbers and varying lift coefficient for fixed Mach numbers, as well as providing a multiplicity of closely related shapes that are shock free at fixed lift coefficient and Mach number. This wealth of shock-free, two-dimensional designs is no great surprise; therefore, it is not surprising that they are found with minimal computational effort. Two-dimensional inviscid flow potential airfoil designs require less than a minute of CYBER 175 CPU time and only a few seconds of CDC 7600 CPU time.

For three-dimensional flows our results are less extensive. Also, while it is clear that the procedure we use rests on a sound mathematical foundation in two dimensions, this is not the case in three dimensions. Indeed, for three-dimensional (that is, nonplanar and nonaxisymmetric) flows we solve an ill-posed boundary value problem.** That this problem can be solved successfully is a result of the practical requirement for specifying chordwise modifications more densely than spanwise ones.

We have demonstrated the ability to modify three-dimensional wings so that, within the context of the numerical algorithm used, shock-free flows are obtained. We have not yet demonstrated an analogous wealth of shock-free flows in the three-dimensional case, but see no reason to believe that this situation is different there. The practical consequences of this wealth should prove to be of interest to the aircraft industry.[14] Its success will depend on the designer being able to choose baseline configurations that will result in good off-design performance and not compromise nonaerodynamic requirements.

Design Procedure

The procedure we use to find shock-free designs assumes that a reliable numerical code is available for computing the flow past a given configuration, such as that sketched in Fig.

Presented as Paper 78-1114 at the AIAA 11th Fluid and Plasmadynamics Conference, Seattle, Wash., July 10-12, 1978; submitted Aug. 18, 1978; revision received Jan. 26, 1979.

Index categories: Transonic Flow; Configuration Design; Computational Methods.

*Adjunct Professor; Research Scientist, DFVLR, Göttingen, Germany. Member AIAA.

†Senior Research Associate; presently, Research Scientist, Boeing Commercial Airplane Company, Seattle, Wash. Member AIAA.

‡Senior Research Associate. Member AIAA.

§Professor, Aerospace and Mechanical Engineering and Mathematics. Associate Fellow AIAA.

¶One of the consequences of our research is that, in two dimensions, for any small change in the flow Mach number, there are an infinity of small changes in the airfoil shape that will insure that the

**The authors are indebted to A. Jameson of the Courant Institute

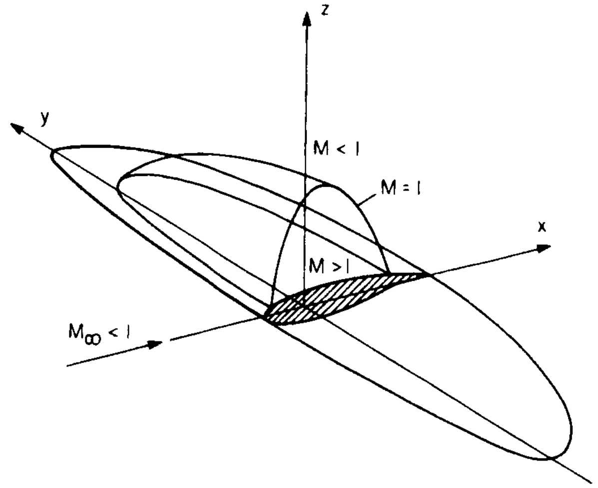

Fig. 1 Sketch of shock-free flow past a lifting wing depicting the sonic surface obtained by introducing fictitious behavior inside this surface that results in elliptic equations.

1. Such codes are available for two- and three-dimensional inviscid flows. When they are coupled with a reliable boundary-layer code, the design procedure outlined here can be used to calculate shock-free viscous flow designs. While this would require some modest iteration, it is certainly possible both in practice and in principle. With the existence of a reliable analysis algorithm presumed we modify this algorithm so that once the flow become hyperbolic we alter the basic equations so that they revert to elliptic behavior. This may be done in a number of ways, but it should be done in a way that it conserves new, but fictitious, "mass" and "momentum" fluxes to a satisfactory degree of accuracy. We may, for example, change the density's dependence from the usual one to one that returns the equations to elliptic form. We might suppose, for the purpose of illustration, that once the equations become parabolic (i.e., sonic) on some surface, then at higher velocities the density will be maintained at its sonic value, giving elliptic equations. We use a numerical algorithm to compute this fictitious flow past a configuration of interest, chosen perhaps on the basis of previous design experience. Because the equations are elliptic, this will result in a discretized, pseudoanalytic description of the velocity, density, and pressure fields on the embedded parabolic surfaces, and this description will be consistent with the correct governing equations. These initial data on the parabolic surfaces are then used to calculate the correct flowfield inside such surfaces. This new flowfield may or may not contain shock waves. This depends on the choice of the fictitious equations, or perhaps better, fictitious gas, used inside the parabolic surfaces. This new flow will define a stream surface that is tangent to, and has the same curvature as, the stream surface at the intersection of the sonic surface and the original body. Inside this surface a new body shape is defined by the stream surface of the new, but now real, flow.

Here, of course, we must also address the question of well-posedness. In two dimensions there is no difficulty because either of the spatial coordinates may be designated as the time-like variable. This is not the case in three dimensions where only the spatial coordinate aligned with the flow is time-like. Because shock-free flows are reversible, the domains of dependence and influence may be interchanged. But neither the normal (nor the binormal) to the stream direction can be considered time-like in the three-dimensional initial-value problem. Thus, data are given on surfaces that are not in the usual domain of dependence and the problem is ill-posed. It is this fact that has made us stress that a reliable analysis algorithm should be the basis for the design computations. An

variations in the spanwise direction that are on scale, that is, small compared to the nominal axial (flow direction) distance, will amplify; thus, the success of the numerical algorithm depends upon not introducing such disturbances. This is not the first time ill-posed problems have been solved to obtain results of engineering interest (see, for example, Ref. 15, pp. 448-472).

Fictitious Gas

As just mentioned, modifications are made to the basic equations to retain their elliptic behavior once the flow has accelerated to sonic speed and a parabolic surface, with the needed initial data, has been generated. The possible modifications are manifold. Our discussion is limited to those used to obtain the results reported here.

For two-dimensional flows we have used Jameson's[16,17] circle-plane algorithm for the full potential equation. Thus, in the analysis mode, we are solving

$$\{\rho\phi_x\}_x + \{\rho\phi_z\}_z = 0 \tag{1a}$$

with

$$\rho/\rho_\infty = \left[1 + \frac{\gamma-1}{2} M_\infty^2 (1 - \phi_x^2 - \phi_z^2)\right]^{1/\gamma-1} \tag{1b}$$

where ϕ is the velocity potential and ρ the density. If we limit our consideration to fictitious gases for which the density is a function of the square of the velocity, viz., $\rho = \rho(q^2)$, where $q^2 = U^2[\phi_x^2 + \phi_z^2]$, then gas laws of the form

$$\rho/\rho_* = (a_*/q)^P \qquad P<1 \qquad \text{for} \quad q>a_* \tag{1c}$$

will insure elliptic behavior; $P=1$ gives parabolic behavior and the fictitious and real gases have the same value of $(\mathrm{d}\rho/\mathrm{d}q)_*$. An alternative choice, and the one used most extensively here, is $P=0$; in this case, Eq. (1a) becomes Laplace's equation. When the flow would normally be hyperbolic, Eq. (1a) is now solved with the density-velocity relationship of Eq. (1c). A fictitious mass flow, which matches the real mass flux at the sonic surface, is thereby conserved and the velocity field remains irrotational.

For three-dimensional flows we have used the Ballhaus-Bailey-Frick algorithm,[18] as implemented by Mason et al.[19] This is a small perturbation calculation, and the classical conservative formulation is adopted here. Thus, in an equivalent form, we solve the system

$$-\tfrac{1}{2}(\gamma+1)\{u^2\}_x + v_y + w_z = 0 \tag{2a}$$

$$v_z - w_y = 0 \tag{2b}$$

$$u_z - w_x = 0 \tag{2c}$$

where the velocity vector is $\boldsymbol{q} = a_*[(1+u)\boldsymbol{i} + v\boldsymbol{j} + w\boldsymbol{k}]$.

A simple modification, Eq. (2), is to replace $\{u^2\}_x$ by $-\mathrm{sgn}(u)\{u^2\}_x$ for all u. This system is elliptic, except on the sonic surface where $u=0$. We may think of the first of Eqs. (2) as being the consequence of the small perturbation expansion for the density, viz.,

$$\frac{\rho}{\rho_*} - 1 = -u - \frac{\gamma-1}{2}u^2 \tag{3}$$

whereas the fictitious equation, with u replaced by $-|u|$ for $u>0$, results from

$$\frac{\rho}{\rho_*} - 1 = -u + \frac{\gamma+3}{2}u^2 \tag{4}$$

This fictitious gas has the same value for $(\mathrm{d}\rho/\mathrm{d}u)_*$ as the real solve Eqs. (2) with $\{u^2\}_x$ replaced by $-\mathrm{sgn}(u)\{u^2\}_x$; this corresponds to using the densities given by Eqs. (3) and (4) for $u<0$ and $u>0$, respectively.

Calculation of the Hyperbolic Flowfield

As previously described, we calculate the flow past a body using the correct equations when the flow is subsonic and a modified, incorrect, set of equations when the flow is supersonic. This calculation serves to define sonic surfaces on which the flowfield calculation is switched from the correct equations to the modified ones. Outside this surface, presuming the trailing edge of the wing is subsonic, the solution satisfies the correct equations, and the potential at infinity has the correct value for the circulation. If infinity in the physical plane is not mapped to a finite part of the computational plane, then there is, in principle, a need to correct the doublet and nonlinear contributions; in practice, these contributions are small and changes in them negligible. Thus, the flow in the elliptic, subsonic domains is fixed and known, as are the initial data we need on the parabolic surface.

For two-dimensional flows, the calculation of the correct hyperbolic behavior is carried out using the method of characteristics. This is done in a hodograph-like working plane in which the characteristics are orthogonal straight lines. If we take $\xi=\theta+\nu$ and $\eta=\theta-\nu$, where θ is the flow deflection angle and ν the Prandtl-Meyer turning angle, then the velocity potential and stream function satisfy

$$\phi_\xi=K\left(\frac{\xi-\eta}{2}\right)\psi_\xi,\quad \phi_\eta=-K\left(\frac{\xi-\eta}{2}\right)\psi_\eta \tag{5}$$

or, equivalently,

$$\left.\frac{\mathrm{d}\psi}{\mathrm{d}\phi}\right|_{\xi,\eta=\mathrm{const}}=\pm K^{-1}$$

where the ± signs refer to $\xi,\eta=\mathrm{const}$, respectively. Here

$$K(\nu)=K[\nu(q)]=\{|M^2(q)-1|\}^{1/2}\rho(0)/\rho(q)$$

Values for the velocity potential on the parabolic line, $z=z^*(x)$, and the shape of this line are used along with the usual relations between the spatial coordinates and ϕ and ψ to find ψ on the sonic line. These initial data are then integrated using Eqs. (5) to determine the locus $\psi(x,z)=0$ which passes through the intersection of the sonic line with the body surface. The values of z for which $\psi(x,z)=0$ determine the new body shape. This shape will have the same slope and, at least theoretically, the same curvature, as the original body at the sonic points. This follows from the observation that flow quantities are not changed at the sonic line; thus, the streamwise momentum and normal pressure gradient are unchanged. Consequently, the local flow curvature must be the same.

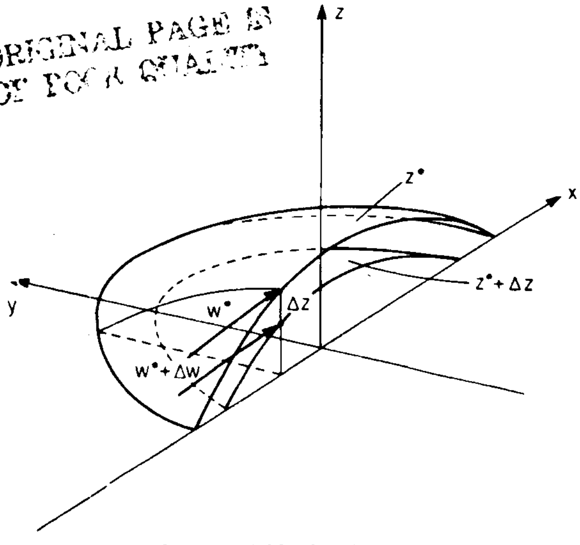

Fig. 2 Sketch of two neighboring isotach surfaces used in the calculation of the supersonic domain for Eqs. (2).

For three-dimensional flows, the calculation of the hyperbolic flowfield is carried out by a procedure that marches inward from the sonic surface by successive surfaces of constant density (isopycnics) for the full potential equation, or constant axial flow speed u for the small perturbation equation. We limit our discussion to the small perturbation equations, as all the results reported here are derived from them. Preliminary results using the full potential equations have been obtained by N. J. Yu.

We may either write Eqs. (2) in the appropriately scaled form or work with them directly as we will do here.

We are given an isotach surface $z^*(x,y)$, as shown in Fig. 2, on which we know $u=u^*=\mathrm{const}$, $w=w^*(x,y)$, and $v=v^*(x,y)$. We use the data on this surface, and the surface shape, to calculate

$$z^*_x,\ z^*_y,\ w^*_x,\ w^*_y,\ v^*_x,\ v^*_y \tag{6}$$

Because these data satisfy Eqs. (2), we can verify that

$$v^*_x=z^*_x w^*_y-z^*_y w^*_x$$

which can be used, if needed, to check the consistency of the initial data. The values given in Eq. (6) can now be used to calculate the z derivatives of u, w, v on $z^*(x,y)$, where $u(x,y,z^*)=\mathrm{const}$, by using

$$u_z=[z^*_y v^*_x-z^*_x v^*_y-w^*_x]/J \tag{7a}$$

$$w_z=[(\gamma+1)u^*z^*_x w^*_x-z^*_y w^*_y+v^*_y]/J \tag{7b}$$

$$v_z=[(\gamma+1)u^*z^*_x v^*_x-w^*_y-z^*_y v^*_y]/J \tag{7c}$$

where J, the Jacobian, $\partial(u,v,w)/\partial(x,y,z)$, is:

$$J=(\gamma+1)u^*z^{*2}_x-z^{*2}_y-1$$

When the Jacobian, which is initially negative, vanishes, we can no longer compute the z derivatives; this corresponds to the subsequent formation of multivalued solutions, i.e., limit surfaces. If $J=0$ occurs before the calculations produce a suitable stream surface defined by $w(x,y,0)$, $v(x,y,0)$, then they must be rejected.

With Eq. (7a) inverted to give $(\mathrm{d}z/\mathrm{d}u)_*$, we take a set increment in u, Δu, to form a new isotach surface $z^*(x,y)+\Delta z^*(x,y)$. This new shape, along with the mean value of u between the two surfaces and the second and third of Eqs. (7), provides the new values, $w^*(x,y)+\Delta w^*(x,y)$, $v^*(x,y)+\Delta v^*(x,y)$, of w^* and v^* on the next isotach. These values and the shape of the subsequent isotach are then converted to continuous functions by one-dimensional cubic splines in the x and y coordinates. This "onion-peel"-like process is then continued until $z=0$, unless a limit surface intervenes. In the latter event, the solution must be rejected. A more detailed discussion of this procedure is given in Ref. 20.

Two-Dimensional Results

We have explored rather extensively some of the modifications that can be made to an existing airfoil, namely, an NACA 64A410 airfoil, to obtain shock-free flow. We will call this the baseline airfoil; the airfoil shapes we generate are identical with this airfoil over that portion wetted by subsonic

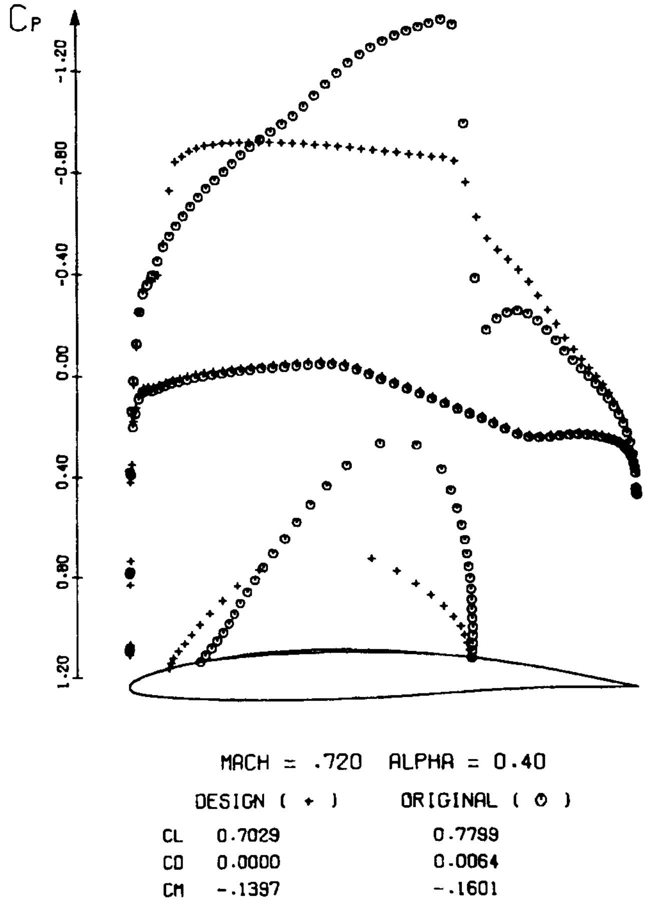

Fig. 3 Comparison of the pressure coefficients and sonic lines for the baseline NACA 64A410 and the shock-free airfoil obtained from it by the direct design procedure.

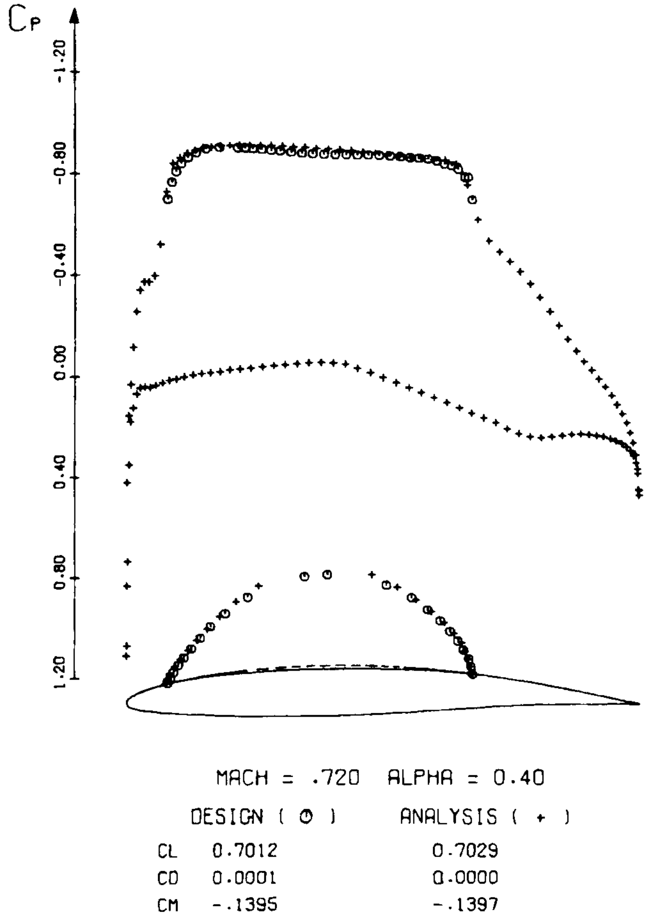

Fig. 5 Comparison of the pressure coefficient and the sonic line obtained by the design calculation that modifies the airfoil shape with those obtained by computing the flow past the modified airfoil.

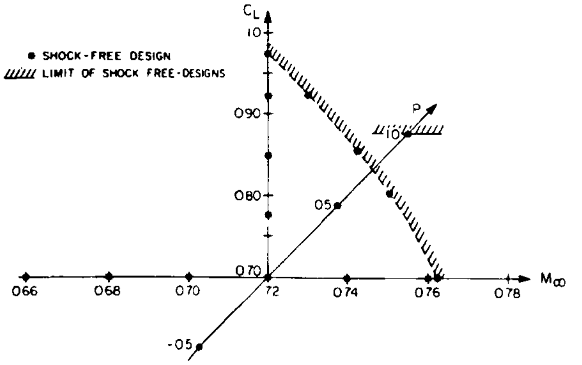

Fig. 4 Parameter space explored for the shock-free airfoils that can be obtained when the baseline configuration is an NACA 64A410 airfoil.

flow; we need only modify the airfoil over a limited portion of its upper surface to obtain shock-free flows. Further, this modification is not unique for fixed flight conditions; rather, if one such shape exists, there usually will be a family of modifications of the baseline airfoil that will produce shock-free flow corresponding to different gas laws. Modifications to NACA 0012 and 64A410 airfoils that resulted in shock-free flows were reported by Eberle in Ref. 21.

With a baseline airfoil selected here mainly for illustrative purposes, we then pick a set of flight conditions for which we wish to find a modification of the airfoil shape that will result in shock-free flow. We choose $M_\infty = 0.72$ and the angle of attack $\alpha = 0.4$ deg. At these conditions inviscid flow calculations for the NACA 64A410 baseline airfoil give a C of 0.78 and a C_D of 0.0064. The design procedure discussed earlier results in an airfoil that is 9.3% thick with a lift coefficient of 0.703. The original and design pressure coefficient, sonic lines and body shapes are compared in Fig. 3a; these results and all other "analysis" results were computed using the numerical algorithm of Ref. 16. Figure 3b compares the pressure coefficients and sonic lines determined by the design procedure with those computed for the design airfoil shape.

With this shock-free design established at $M = 0.72$ and with $C_L = 0.70$, we now wish to determine the families of shapes that provide shock-free flow for a fixed lift coefficient as the Mach number varies, and a fixed Mach number as the lift coefficient varies. This has been done with $P = 0$; that is, with a constant density fictitious gas (at the critical value), requiring an iterative procedure for the case at fixed lift coefficient. Other shapes were then explored that will produce the same lift coefficient, 0.70, at a fixed Mach number by taking P to be -0.5, 0.5, and 1.0. Also, for $P = 0$ we have determined the maximum Mach number for which the design procedure will produce a shock-free airfoil as a function of lift coefficient. This Mach number is nearly a linear function of lift coefficient at larger lift coefficients. The slope of this variation is consistent with that given by Boerstoel.[22] Preliminary studies also indicate that for a fixed lift coefficient of 0.6-0.7, an 0.1% increase in the maximum Mach number requires about an 0.2% reduction in the thickness for shock-free flow when the nominal thickness is about 10%. This result is less optimistic than the envelope of the hodograph designs given by Boerstoel,[22] who found that only an 0.1% reduction was required. In our study the generic

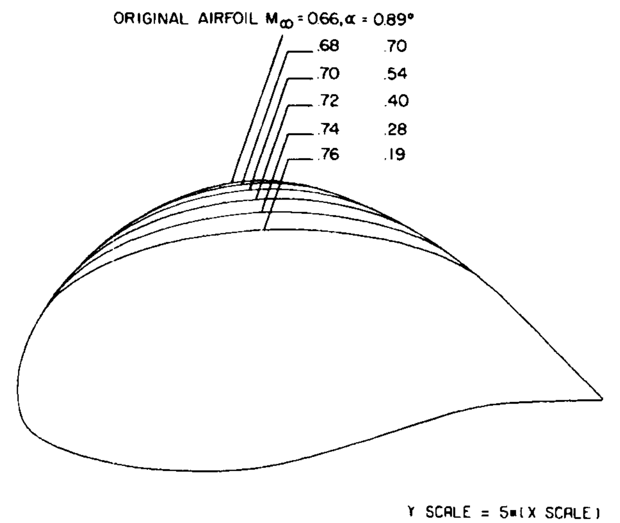

Fig. 6 Shock-free airfoil shapes for fixed lift coefficient $C_L = 0.70$ and varying Mach number. The fictitious gas has a constant density in the supersonic domain ($P = 0$). The baseline airfoil is an NACA 64A410.

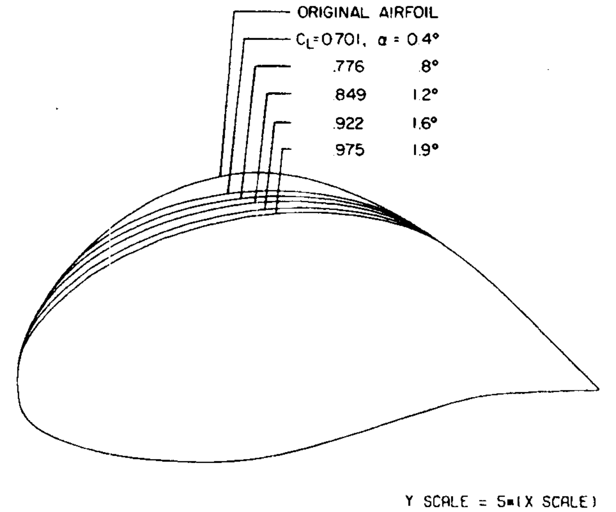

Fig. 7 Shock-free airfoil shapes for fixed Mach number $M_\infty = 0.72$ and varying lift coefficient. The fictitious gas has a constant density in the supersonic domain ($P = 0$). The baseline airfoil is an NACA 64A410.

modifications required when the baseline airfoil is near the envelope of hodograph designs. Positive values of P provide less airfoil thickness reduction, since the fictitious and real-gas densities are more nearly the same. The range of our airfoil studies is depicted in Fig. 4, with shock-free airfoils being determined for the points indicated. Also shown in Fig. 4 is the maximum Mach number for which a design was found as a function of lift coefficient for $P = 0$.

The accuracy of the design procedure was studied at a number of design points by comparing the design's pressure distribution and sonic line shape with those obtained using the unmodified numerical algorithm to analyze the design airfoil shape. Typical results are shown in Fig. 5. The sonic line shape and initial data on the sonic line are determined in the circle-plane; then they are mapped back to the physical plane. The method of characteristics in the hodograph variables is used to compute the design pressure coefficient corresponding to the calculated airfoil surface shape. The agreement, as shown, is excellent. For designs that approach the Mach number at which a limit line first penetrates the surface,

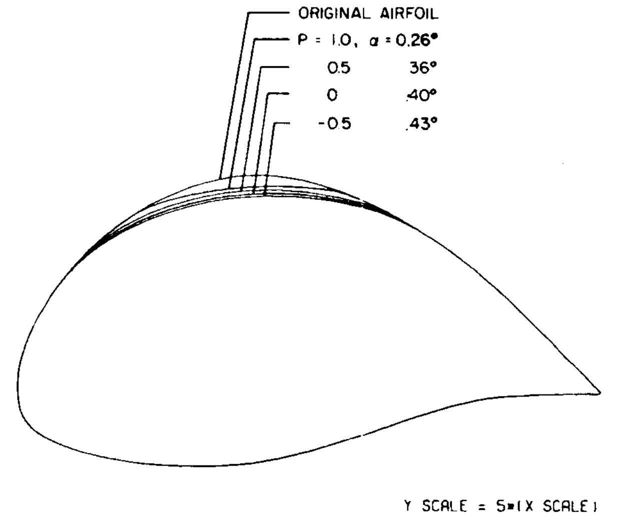

Fig. 8 Shock-free airfoils for fixed Mach number $M_\infty = 0.72$ and lift coefficient $C_L = 0.70$, varying the exponent P of Eq. (1c) and thus changing the density's dependence on flow speed. The baseline airfoil is an NACA 64A410.

obtain a converged solution. These designs have very rapid expansions immediately following the sonic line. Indeed, as Boerstoel[22] has noted, the analysis code used with an optimization scheme will not produce designs of this character.

The shock-free airfoil shapes that are obtained for fixed C_L and P, fixed M_∞ and P, and fixed M_∞ and C_L at various Ps, are shown in Figs. 6-8. One can overlay the results for fixed C_L and find quite similar airfoil shapes that are shock-free over a range of Mach numbers. Because modifications to the baseline airfoil are required only over a limited portion of the upper surface, and a family of specified changes in the airfoil curvature is known for each set of flight conditions, a closely related family of shock-free airfoil shapes can be generated. Thus, the minor modifications to a limited portion of a wing surface needed to produce shock-free flow over a practical range of flight conditions can be easily determined.

Three-Dimensional Results

Our first design results using the method just described were for two-dimensional, small perturbation flow past a parabolic arc airfoil. Consequently, we initiated our three-dimensional studies with a rectangular, unswept wing having an aspect ratio of six and a parabolic arc airfoil. We utilized the small perturbation approximation, Eqs. (2), and a parabolic thickness distribution; the airfoil was taken to be 6% thick at the centerplane. The flow was calculated using the algorithm of Ref. 19, modified to return the equations to elliptic behavior as described earlier. The initial data on the embedded sonic surface were then used to compute the correct flow in the supersonic domain using the "onion-peel" algorithm of Ref. 20. This defines new wing surface slopes. The flow past this shock-free design was then analyzed using the modified numerical algorithm. Figure 9 compares the pressure distributions on the original and design wing at various lateral positions for $M_\infty = 0.87$. Also shown are the cross sections of the sonic surface at the same lateral stations. The only essential differences in the pressure occur in the supersonic domain, which is consistent with the design process. The modifications made to the wing slope, shown in Fig. 10 for several lateral stations, have eliminated the shock wave.

A subsequent, more realistic, calculation was made for the planform sketched in Fig. 11. The wing section chosen was an NACA 64A410 profile at the center section and an elliptic thickness distribution. The leading-edge sweep was taken to

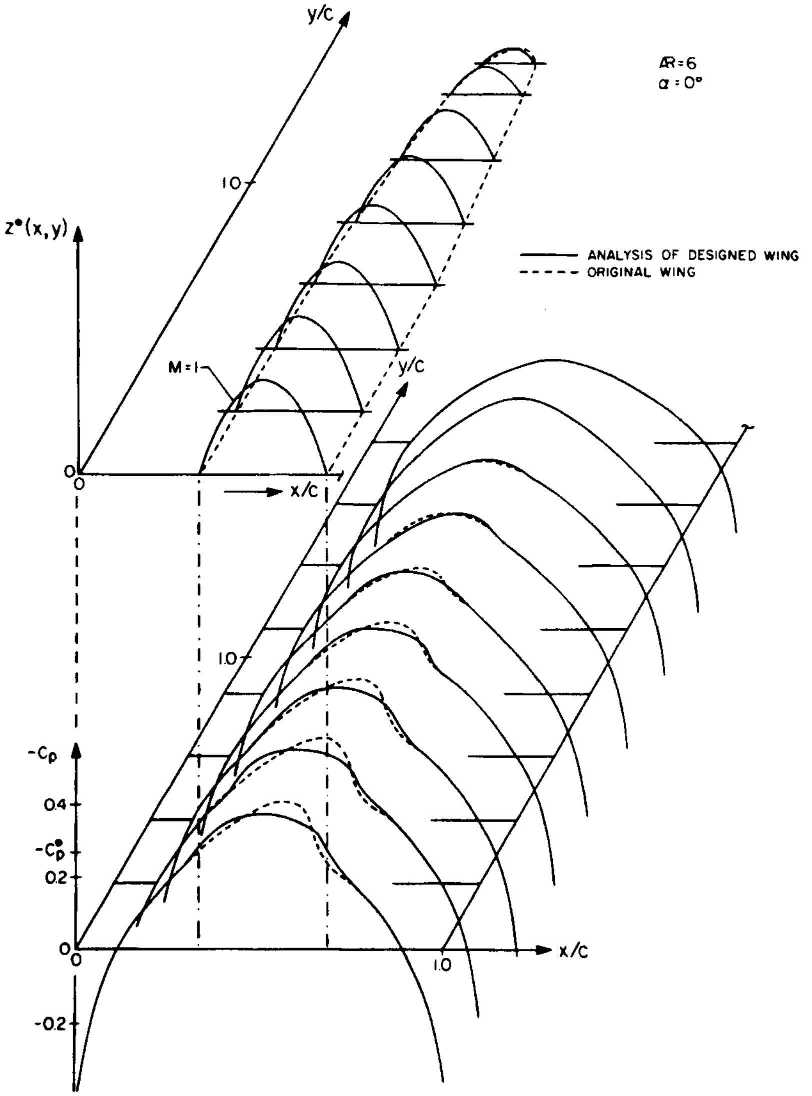

Fig. 9 Sonic surface for the shock-free rectangular wing obtained by modifying a wing with a parabolic arc airfoil section and the pressure coefficients on the original and modified wing, as calculated by the numerical algorithm of Ref. 19. The thickness distribution of the baseline wing is parabolic in *y/c*.

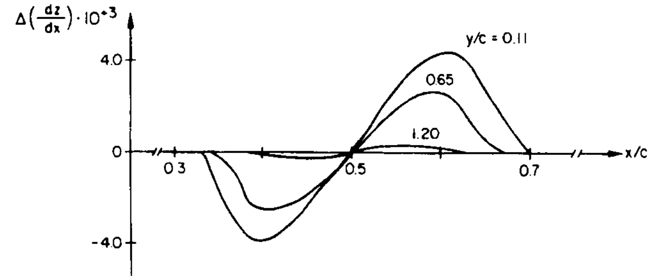

Fig. 10 Changes required in the surface slope at various lateral stations to provide shock-free flow over the rectangular wing of Fig. 9.

ratio was 5. The sonic surface is also depicted in Fig. 11. Figure 12 compares the pressure coefficients on the upper surface of the original wing and the wing designed to be shock free. While the reduction in drag for this wing is small compared to the induced drag, it is clear that the wing modifications have essentially eliminated the shock waves, and, consequently, the wave drag. More importantly, shock wave induced boundary-layer separation is avoided. Impressive results for the ONERA M6 planform have been obtained by Yu[23] using the full potential equation.

At this point we stress that the preceding comparison is obtained by computing the flow past the original wing and the design wing using the same numerical algorithm. The process that leads to the new wing shape also provides the pressure on the wing.

Conclusion

A novel and simple procedure for determining modifications that will make a baseline configuration shock-free for supercritical flight conditions has been delineated. For two-dimensional, inviscid flows, shock-free designs are obtained in seconds on a CYBER 175. Families of airfoils that are shock free at fixed, as well as varying, flight conditions are found. The same procedure has been applied to three-dimensional wings, resulting in wing modifications that make the wings shock-free when the flow is analyzed with the numerical algorithm that was modified to become a design tool. It can also be applied to the design of shock-free cascades. A unique feature of the procedure is that any code that is effective in computing the flowfield may be modified in various ways to be a design algorithm, if it is coupled with a method for calculating the solution in the supersonic domains for given data on the sonic surfaces. A straightforward marching technique for such computations is described for three-dimensional flows; in two dimensions, either the marching procedure or the method of characteristics may be used for the supersonic domain. The algorithm for the supersonic domain serves to define the modifications needed in the configuration to achieve shock-free flow; these modifications will be limited to that portion of the design shape that are wetted by supersonic flow.

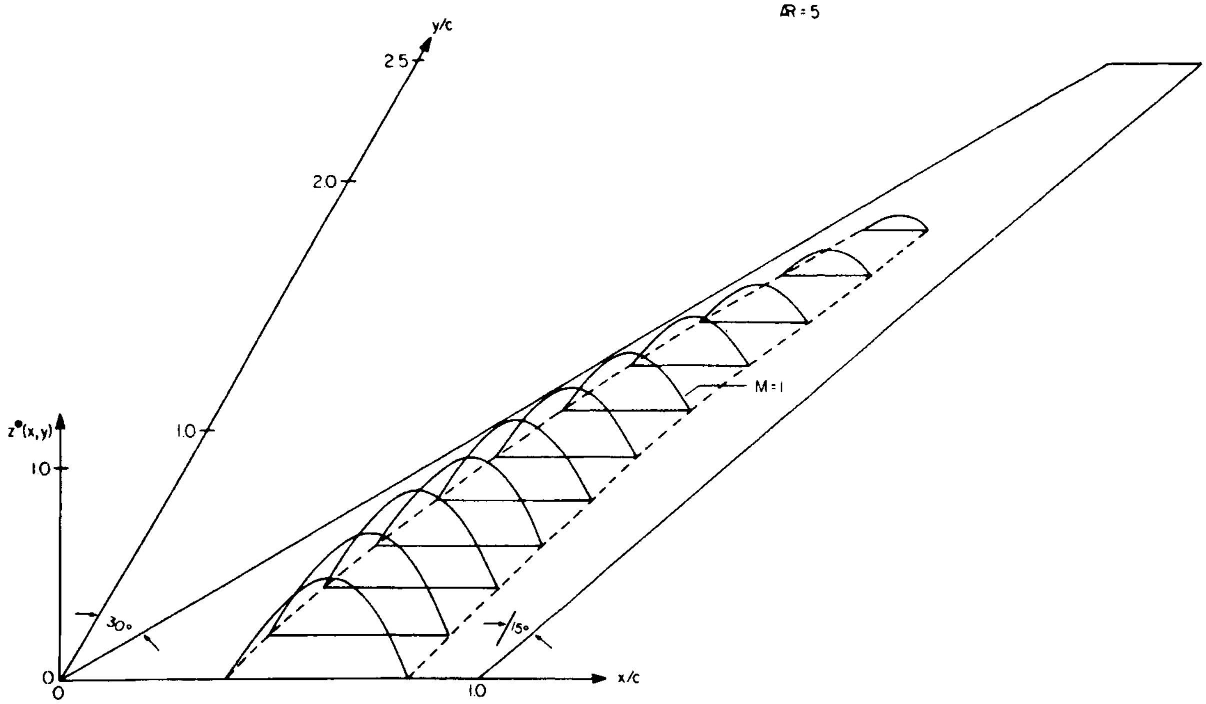

Fig. 11 Sonic surface on the shock-free swept wing designed from a wing with an NACA 64A410 center section profile and an elliptic thickness distribution. The leading edge sweep is 30 deg; the trailing edge sweep 15 deg.

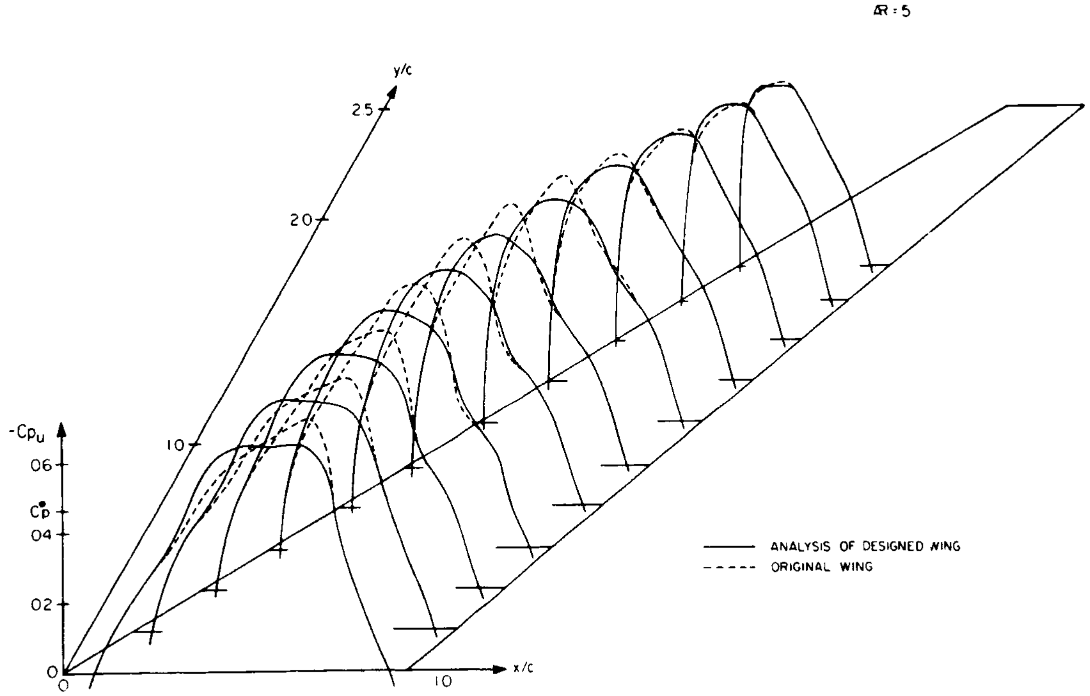

Fig. 12 Comparison of the computed pressure coeffcient on the wing of Fig. 11 with an NACA 64A410 center section profile and an elliptic thickness distribution, with the pressure coefficient obtained by computing the flow past the modified wing using the same numerical algorithm.

Acknowledgment

This research was carried out by the Computational Mechanics Laboratory of the Department of Aerospace and Mechanical Engineering. The work was supported by AFOSR Grant 76-2954E, NASA Grant NSG-2112, and ONR Contract N00014-76-C-0182. The authors are indebted to the technical monitors for constructive comments and encouragement during the course of this investigation. They also wish to thank H. Nebeck for carrying out the calculations for the airfoil studies and P. DeShazo for the development of supporting algorithms.

References

[1] Morawetz, C. S., "On the Non-Existence of Continuous Transonic Flows Past Profiles, I, II, and III," *Communications on Pure and Applied Mathematics*, Vols. 9, 10, and 11, 1956, 1957, and 1958, pp. 45-68, 107-131, and 129-144.

[2] Cook, L. P., "A Uniqueness Proof for a Transonic Flow Problem," *Indiana University Mathematical Journal*, Vol. 27, Jan.-Feb. 1977, pp. 51-72.

[3] Whitcomb, R. T. and Clark, L. R., "An Airfoil Shape for Efficient Flight at Supercritical Mach Numbers," NASA TM X-1109 (confidential report), July 1965.

[4] Pearcey, H. H., "The Aerodynamic Design of Section Shapes for Swept Wings," *Advances in Aeronautical Sciences*, Vol. 3, 1962, pp. 277-322.

[5] Garabedian, P. R. and Korn, D. G., "Numerical Design of Transonic Airfoils," *Numerical Solution to Partial Differential Equations*, Vol. II, Academic Press, New York, 1978, pp. 253-271.

[6] Nieuwland, G. Y., "Transonic Potential Flow Around a Family of Quasi-Elliptical Airfoil Sections," Nationaal Lucht-en Ruimtevaart Laboratorium Rept. TR-T 172, Amsterdam, The Netherlands, 1967.

[7] Boerstoel, J. W., "Design and Analysis of a Hodograph Method for the Calculation of Supercritical Shock-Free Airfoils," Nationaal Lucht-en Ruimtevaart Laboratorium Rept. TR 77046 U, Amsterdam, The Netherlands, 1977; also Boerstoel, J. W, and Huizing, G. H., "Transonic Shock-Free Aerofoil Design by an Analytic Hodograph Method," AIAA Paper 74-539, Palo Alto, Calif., June 1974.

[8] Sobieczky, H., "Entwurf überkritischer Profile mit Hilfe der rheoelektrischen Analogie," Deutsche Forschungs-und Versuchsanstalt für Luft-und Raumfahrt Rept. DLR-FB 75-43, Göttingen, West Germany, 1975.

[9] Hicks, R. M. and Vanderplaats, G. N., "Application of Numerical Optimization to the Design of Supercritical Airfoils Without Drag-Creep," SAE Paper 770440, Business Aircraft Meeting, 1977.

[10] Hicks, R. and Henne, P. A., "Wing Design by Numerical Optimization," AIAA Paper 77-1247, Seattle, Wash., Aug. 1977.

[11] *Advanced Technology Airfoil Research*, Proceedings ATAR Conference, NASA Langley Research Center, March 1978.

[12] Sobieczky, H., "Die Berechnung lokaler Räumlicher Überschallfelder," lecture at Gesellschaft für angewandte Mathematik und Mechanik, Copenhagen, May-June 1977, *ZAMM* 58T, 1978, pp. 215-216.

[13] Sobieczky, H., "Transformation Methods for Three-Dimensional Compressible Flow," Deutsche Forschungs-und Versuchsanstalt für Luft-und Raumfahrt Rept., Göttingen, West Germany, in preparation.

[14] Sobieczky, H. and Seebass, A. R., "Adaptive Airfoils and Wings for Shock-Free Supercritical Flight," Invention Disclosure, University of Arizona, Tucson, Ariz., May 1978.

[15] Hayes, W. D. and Probstein, R. F., *Hypersonic Flow Theory, Vol. I, Inviscid Flows*, Academic Press, New York, 1966.

[16] Jameson, A., "Iterative Solution of Transonic Flows Over Airfoils and Wings," *Communications on Pure and Applied Mathematics*, Vol. 27, 1974, pp. 283-309.

[17] Bauer, F., Garabedian, P., Korn, D., and Jameson, A., "Supercritical Wing Sections," *Lecture Notes in Economics and Mathematical Systems*, M. Beckmann and H. P. Kunzi (Eds.), Vol. 108, Springer-Verlag, Berlin, Heidelberg, New York, 1975.

[18] Ballhaus, W. F., Bailey, F. R., and Frick, J., "Improved Computational Treatement of Transonic Flow about Swept Wings," *Advances in Engineering Sciences*, NASA CP-2001, 1976.

[19] Mason, W. H., Mackenzie, D., Stern, M., Ballhaus, W. F., and Frick, J., "An Automated Procedure for Computing the Three-Dimensional Transonic Flow over Wing-Body Combinations, Including Viscous Effects," Vols. I and II, Air Force Flight Dynamic Laboratory Rept. AFFDL-TR-77, Wright-Patterson AFB, Ohio, Feb. 1978.

[20] Sobieczky, H., "A Computational Algorithm for Embedded Supersonic Flow Domains," University of Arizona Engineering Experiment Station Rept., Tucson, Ariz., July 1978.

[21] Eberle, A., "Profiloptimierung für transsonische Strömung mittels der Methoden der finiten Elemente und Charakteristiken," *MBB Report* UFE 1362 (0), 1977.

[22] Boerstoel, J. W., "Review of the Application of Hodograph Theory to Transonic Airfoil Design and Theoretical and Experimental Analysis of Shock-Free Airfoils," *Symposium Transsonicum II*, K. Oswatitsch and D. Rues (Eds.), Springer-Verlag, Berlin, Heidelberg, New York, 1976, pp. 109-133.

[23] Yu, N. J., "An Efficient Transonic Shock-Free Wing Redesign Procedure Using a Fictitious Gas Method," AIAA Paper 79-0075, New Orleans, La., Jan. 1979.

79-1556

Related Analytical, Analog and Numerical Methods in Transonic Airfoil Design

HELMUT SOBIECZKY
DFVLR GÖTTINGEN, WEST GERMANY

ORIGINAL PAGE IS
OF POOR QUALITY

AIAA 12th FLUID AND PLASMA DYNAMICS CONFERENCE

July 23-25, 1979 / Williamsburg, Virginia

RELATED ANALYTICAL, ANALOG AND NUMERICAL METHODS IN TRANSONIC AIRFOIL DESIGN

Helmut Sobieczky*,
DFVLR Göttingen, West Germany;

Abstract

Design methods for transonic airfoils are presented together with a review of the preceding analytical and analog flow studies both in hodograph and physical space. Transonic analytical results for cusped airfoils in sonic flow provide details of solution structures in hodograph planes to formulate a new transonic boundary value problem. This is used subsequently for extension of the classical rheoelectric analogy for subsonic flow modelling, into the transonic regime. Airfoil design with the resulting hybrid technique is described. Replacement of the analogy by numerical solver routines in the hodograph plane finally leads to an application in physical space and the development of effective computer codes suitable for design of shock-free airfoil families including adaptive wing sections.

1. INTRODUCTION

The development of airfoils in the past has always been an important first step in design aerodynamics. More recently, requirements for increased efficiency have forced the operating conditions of aircraft and turbomachinery into the transonic regime. Broad emphasis is still laid, therefore, on the development of two-dimensional design components like airfoils and cascades in the high speed regime[1]. Various computational algorithms have been developed for analysis of transonic flow past given airfoils, but only few methods are available to the design engineer for airfoil shape definition with specified properties. Research reported here was carried out within the past six years at the DFVLR in Germany and since 1977 at the University of Arizona. It is the purpose of this paper to demonstrate coherence between the first basic analytical models and recent effective computer codes resulting from our research, including a method which belongs actually into pre-computer time but proved to have a high educational value: the Rheoelectric Analogy. This method was used two decades ago for investigation of complicated two- and three-dimensional potential distributions and had useful applications in aerodynamics. However, principal difficulties arised in the high speed subsonic flow regime which prohibited an application for transonic flow research when still no practically useful calculation methods for this field of growing importance were available. These difficulties, however, were overcome by the author in the case of design problems with the aid of the aforementioned analytical findings and an experimental analog procedure was developed to obtain airfoil designs of satisfactory accuracy.

In the meantime, within the past five years, we witnessed the rapid development and widely distributed availability of numerical solver routines for partial differential equations. It was, therefore, necessary to transfer gained experience and techniques from the analog flow experiments to more economical digital computer programming. Application of numerical subroutines and finally the conversion of whole well-established analysis codes into effective design tools are our current practical results resting on previous basic experiments and solutions.

---

*Adjunct Professor, University of Arizona; Member, AIAA

151

2. BELTRAMI DIFFERENTIAL EQUATION IN PLANE POTENTIAL THEORY

2.1 Potential flow in 2D physical space

We consider steady, two-dimensional, isentropic and irrotational flow of a polytropic, inviscid gas. The basic equations of motion are then determined by

$$\operatorname{div}(\varrho \vec{v}) = 0 , \qquad (1\,a)$$

$$\operatorname{curl}(\vec{v}) = 0 , \qquad (1\,b)$$

the continuity equation and irrotationality, respectively, with ϱ the density and $\vec{v}$ the velocity vector in physical space. Isentropic gas properties determine velocity q, sonic velocity a and density ϱ as functions of the Mach number M, for given stagnation conditions, denoted here with subscript 0:

$$\begin{aligned} q &= |\vec{v}| = a M \\ a^2 &= a_0^2 - \frac{\gamma - 1}{2} q^2 \\ \varrho/\varrho_0 &= \left(1 + \frac{\gamma-1}{2} M^2\right)^{-\frac{1}{\gamma-1}} = F(M) \end{aligned} \qquad (2)$$

With (1a, 1b) we may define a velocity potential ϕ and a stream function Ψ, with their gradients in the two directions x, y of 2D physical space equal to the velocity components u, v in these directions:

$$\begin{aligned} \phi_x &= \frac{\varrho_0}{\varrho} \Psi_y = u = q \cos \vartheta , \\ \phi_y &= -\frac{\varrho_0}{\varrho} \Psi_x = v = q \sin \vartheta , \end{aligned} \qquad (3)$$

where ϑ is the flow angle. The system (3) is a generalisation of the Cauchy-Riemann equations, socalled Beltrami equations. Elimination of Ψ or ϕ yields Poisson equations for ϕ or Ψ, respectively:

$$\phi_{xx} + \phi_{yy} = -\frac{\varrho_x}{\varrho} \phi_x - \frac{\varrho_y}{\varrho} \phi_y \qquad (4\,a)$$

$$\Psi_{xx} + \Psi_{yy} = \frac{\varrho_x}{\varrho} \Psi_x + \frac{\varrho_y}{\varrho} \Psi_y \qquad (4\,b)$$

with ϱ a function (2) of M, and therefore

$$\varrho = \varrho(q/a) = \varrho(\phi_x^2 + \phi_y^2) , \qquad (5)$$

the system (3) and the equations (4) are nonlinear. Furthermore, the system is of elliptic type when $M < 1$, and of hyperbolic type when $M > 1$, with a parabolic type dividing line $M = 1$, the sonic line.

2.2 Potential flow in the Hodograph plane

The aforementioned nonlinearity of the basic system (3) may be avoided if a new pair of independent variables is introduced to replace physical coordinates x, y. These variables are suitable functions of the velocity components, they are called hodograph variables. A special pair of such variables is consisting of the flow angle ϑ and a function of the Mach number, known also as the Prandtl-Meyer turning angle

$$\nu = \int_{a^*}^{q} \sqrt{M^2 - 1} \; \frac{dq}{q} \qquad (6)$$

with a^* defining the critical velocity.
The coefficient

$$K = K(M(\nu)) = \frac{\varrho_0}{\varrho} \sqrt{M^2 - 1} \qquad (7)$$

will also be used in the following system.
The new variables ν, ϑ may either be used directly to define a hodograph plane wherein the basic Beltrami system becomes linear:

$$\begin{aligned} \phi_\nu &= \mp K(\nu) \Psi_\vartheta , \qquad (\nu \gtrless 0,\ M \gtrless 1) \\ \phi_\vartheta &= K(\nu) \Psi_\nu , \end{aligned} \qquad (8)$$

or ν and ϑ more generally are functions of a computational working plane obtained from the basic ν, ϑ hodograph by conformal (for $M \leq 1$) or characteristic (for $M \geq 1$) mapping. For subsonic flow including sonic conditions, ($M < 1$, $\nu < 0$), conformal mapping defines a working plane ζ,

$$\zeta_0 = \nu + i \vartheta , \qquad (9\,a)$$

$$\zeta = s + i t = E(\zeta_0) \qquad (9\,b)$$

with the mapping function E. The basic system in ζ becomes then

$$\Phi_s = -K(\nu(s,t))\,\Psi_t$$
$$\Phi_t = K(\nu(s,t))\,\Psi_s \qquad (10)$$

with

$$\nu(s,t) = \mathrm{Re}\,(E^{-1}(\zeta))$$
$$\vartheta(s,t) = \mathrm{Im}\,(E^{-1}(\zeta)). \qquad (11)$$

Equations (10) form, as (8), a linear Beltrami system, while (3) is nonlinear. Elimination of Ψ or Φ yields linear Poisson equations for Φ or Ψ, respectively:

$$\Phi_{ss} + \Phi_{tt} = \frac{K_s}{K}\,\Phi_s + \frac{K_t}{K}\,\Phi_t \qquad (12a)$$

$$\Psi_{ss} + \Psi_{tt} = -\frac{K_s}{K}\,\Psi_s - \frac{K_t}{K}\,\Psi_t \qquad (12b)$$

As we will see later, boundary value problems for practically interesting solutions of the basic system (8) may be significantly simpler to solve in a working plane ζ with (10) rather than in the original ζ_0 where (8) is valid.

The same is true, in principle, for the supersonic part of the flow. Here we introduce characteristic variables with a suitable mapping function H,

$$\xi = H(\vartheta + \nu),$$
$$\eta = H(\vartheta - \nu), \qquad (13)$$

yielding the system valid in the ξ, η plane

$$\Phi_\xi = K(\nu(\xi,\eta))\,\Psi_\xi$$
$$\Phi_\eta = -K(\nu(\xi,\eta))\,\Psi_\eta \qquad (14)$$

or equivalently,

$$\left.\frac{d\Psi}{d\Phi}\right|_{\xi,\,\eta\,=\,\mathrm{const}} = \pm K^{-1} \qquad (15)$$

which is the basic relation for the method of characteristics to integrate the flow equations (8) for $M > 1$.

2. 3 Near sonic flow in the hodograph plane

A given solution of (8) allows the integration of physical coordinates x, y with the formula

$$dz = dx + i\,dy = e^{i\vartheta}\left(d\Phi - i\frac{\rho_0}{\rho}\,d\Psi\right)/q \qquad (16)$$

For flows with only small perturbations to a sonic parallel flow,

$$(M-1) \ll 1,$$
$$\vartheta \ll \pi/2 \qquad (17)$$

we may eliminate Φ and Ψ so that a basic system for the physical plane coordinates x, y is obtained. Furthermore, introduction of a similarity parameter σ allows the use of reduced variables for place (x, y) and state (q, ϑ) which contain the well-known Transonic similarity laws[2]

$$S = \pm 2\cdot 3^{-1}\sigma^{-1}(\gamma+1)^{1/2}\left|1-\frac{q}{a^*}\right|^{3/2}$$
$$T = \sigma^{-1}\cdot\vartheta$$
$$X = \Phi/a^* \qquad (18)$$
$$Y = \sigma^{1/3}\cdot 3^{1/3}\left[2^{-1}(\gamma+1)\right]^{\frac{1}{\gamma-1}+\frac{1}{3}}\cdot\Psi/a^*$$

with positive S for $q \geqq a^*$ and negative S for $q \leqq a^*$, thus $S = 0$ equivalent to sonic flow conditions.

The basic system (8) then yields a corresponding Beltrami system for the reduced physical plane Variables X, Y in the reduced variables of state working plane S, T:

$$X_S = \pm\,|S^{1/3}|\,Y_T, \quad (S \gtrless 0,\ M \gtrless 1)$$
$$X_T = \quad |S^{1/3}|\,Y_S \qquad (19)$$

Linearity again, and the simple structure of the coefficient gave rise to extensive studies of this system and the structure of its solutions. It is equivalent to the well known Tricomi equation for near sonic flow[3]. Also, it is a special case of Generalized Axisymmetric Potential Theory[4]. Numerous particular solutions were described[5] and used for better understanding of experimentally observed transonic flow phenomena at a time, when computers and numerical methods were still not available. An analytical example for transonic airfoil flow will illustrate the possibilities of this approach

2.4 Electric Potential in a Plane Conductor

Let us consider the distribution of electric current in a three-dimensional conductor. Let E be the electrical potential and $\lambda\ (x,\ y,\ z)$ be the conductivity. The intensity of current, di, which crosses a surface element, dS is given by Ohm's law:

$$di = -\lambda \frac{dE}{dn}\ dS \tag{20}$$

where n is the surface normal to dS. In the case of a two-dimensional (x, y) conductor, variable conductivity can be simulated by constant conductivity but variable thickness distribution, h (x, y), of the conductor. The current intensity, di, crossing the surface element, dS, described by the perpendiculars along the arc, ds, in the x, y plane, is

$$di = -\lambda \cdot h\ (x,\ y) \frac{dE}{dn}\ ds \tag{21}$$

With the assumption of conservation within the conductor,

$$\mathrm{div}\ (h\ \mathrm{grad}\ E) = 0, \tag{22}$$

a partial differential equation is obtained then for E:

$$E_{xx} + E_{yy} = -\frac{h_x}{h} E_x - \frac{h_y}{h} E_y \tag{23}$$

There exists, moreover, a current function, W, which is associated to the electrical potential by the Beltrami system

$$\begin{aligned} E_x &= \frac{1}{\lambda h}\ W_y\ , \\ E_y &= -\frac{1}{\lambda h}\ W_x\ . \end{aligned} \tag{24}$$

Having described flows by different forms of Beltrami equations earlier, we note here the analogy between subsonic gas flow and electric current variables: there are obviously two types of analogy[6,7], called Rheoelectric Analogies A and B:

Analogy A

$$\begin{aligned} \Phi &\mathrel{\hat{=}} E \\ \Psi &\mathrel{\hat{=}} W \\ \lambda h &\mathrel{\hat{=}} \begin{cases} \varrho/\varrho_o & \text{(Equ. (3))} \\ K^{-1} & \text{(Equ. (8), (10))} \end{cases} \end{aligned} \tag{25}$$

Analogy B

$$\begin{aligned} \Phi &\mathrel{\hat{=}} W \\ \Psi &\mathrel{\hat{=}} E \\ \lambda h &\mathrel{\hat{=}} \begin{cases} (\varrho/\varrho_o)^{-1} & \text{Equ. (3)} \\ K & \text{Equ. (8), (10).} \end{cases} \end{aligned} \tag{26}$$

As we stated earlier, the existence of these analogies led to many applications, mainly to solve system (3) for complicated flow boundary conditions and most effectively for the incompressible limit $\varrho = \varrho_o$ at a time when computers where not operational or available. From an experimental standpoint, the simpler operation is the measurement of the electrical potential, E. Analogy A thus gives with measured electrical potential a distribution of Φ in the analog working plane (x, y), (ν, ϑ) or (s, t) in (3), (8) or (10), respectively, while analogy B provides a solution of the Ψ-distribution, for a given and analogously solved boundary value problem in the physical or hodograph plane.

It is the purpose of this paper to illustrate some applications of the outlined analogies to transonic flow problems, in particular airfoil design. At a time when the analogy already was used for numerous problems[8], transonic applications seemed impossible due to difficulties near the sonic flow conditions, as will be illustrated later.

The following chapter will outline a new idea, which led to fruitful use of the analogy in transonic airfoil design. At the same time, however, digital computers became widely used and at first the use of analog computation of purely elliptic (subsonic flow) problems was more or less terminated. But transonic computational aerodynamics remained a problem so that at least few researchers considered it worth to investigate the use of analog computation. Results shown in this paper stem from such research.

Finally, however, rapid progress in numerical methods - also in transonic aerodynamics- invited to introduce some of the ideas developed with the analogy into digital computation and thus obtain solutions now much more economically. Results of these methods are presented here, too, and it is the purpose of this paper to present a recent effective numerical approach to transonic airfoil design as a logical step to be taken after some very educational experiments with rheoelectric analogy.

3. A TWO-STEP DESIGN PROCEDURE FOR TRANSONIC FLOW

3.1 Elliptic Continuation Principle and local supersonic flow fields

Let us recall the basic equations (8) in the working plane ζ_0, (9). Since the name "Hodograph plane" is usually associated with the plane defined by the velocity components u, v (3), we will use here the more general description "Rheograph" for planes like ζ_0 or ζ. With this name it is intended to relate to the applicability of the rheoelectric analogy for description of two-dimensional gas flow.

Equations (8) are elliptic in the subsonic half plane ($\nu < 0$, ϑ) and hyperbolic in the supersonic half plane ($\nu > 0$, ϑ). A transonic flow example with occurrence of mixed subsonic - supersonic flow, say, a local supersonic region embedded in subsonic flow, with smooth transition of the flow properties across the sonic line will, therefore, map into contacting regions E and H in Rheograph ζ_0, see Fig. 1 a, b. We wish to describe quantitatively a solution of system (8) representing such a flow and ask for a method. For a subsonic flow example a boundary value problem might be formulated in the physical plane z as well as in the Rheograph ζ_0 by prescribing Neumann- or Dirichlet-conditions along a given boundary. For our transonic problem this would require the solution of a nonlinear equation (3) or (4) of mixed type in z, or solution of the mixed type linear system (8) in ζ_0. For the latter the boundary value problem in ζ_0 is not well posed[9]. Tricomi's boundary value problem[10] is the proper formulation in ζ_0, it is different from prescribing an arc ψ = const in the supersonic part of the Rheograph ζ_0.

We propose a different way to formulate the problem in ζ_0. This is possible if we restrict ourself to obtain some solution with a resulting closed arc ψ = const and not with a prescribed one.

First, we omit the change of sign in the first of equations (8). We take the negative sign for both half-planes $\nu \gtrless 0$, thus having an elliptic system for the subsonic and the supersonic Rheograph ζ_0. We now define a boundary value problem for this linear, elliptic system, as sketched in Fig 2a. It is well posed and we assume to have a method to obtain a solution. This solution will, locally, be one of the correct mixed type system (8) in region E_1 where $\nu < 0$, but it is a fictitious one in E_2 for $\nu > 0$, because real compressible flow requires solution of the hyperbolic part of (8) with the positive sign for $\nu > 0$. The solution in E_2 has here the purpose to provide a reasonable solution in E_1 with sonic line data

$$\begin{aligned} \phi^* (\vartheta) &= \phi\,(\nu = 0,\ \vartheta_A \geq \vartheta \geq \vartheta_B) \\ \psi^* (\vartheta) &= \psi\,(\nu = 0,\ \vartheta_A \geq \vartheta \geq \vartheta_B) \end{aligned} \qquad (27)$$

This can be achieved also with some modification of the fictitious elliptic system in E_2:
The coefficient $K(\nu)$ can be changed in some prescribed way, as long as it stays real and positive in E_2. One possibility is taking simply

$$K\,(\nu > 0) = K_E = \text{const.} \qquad (28)$$

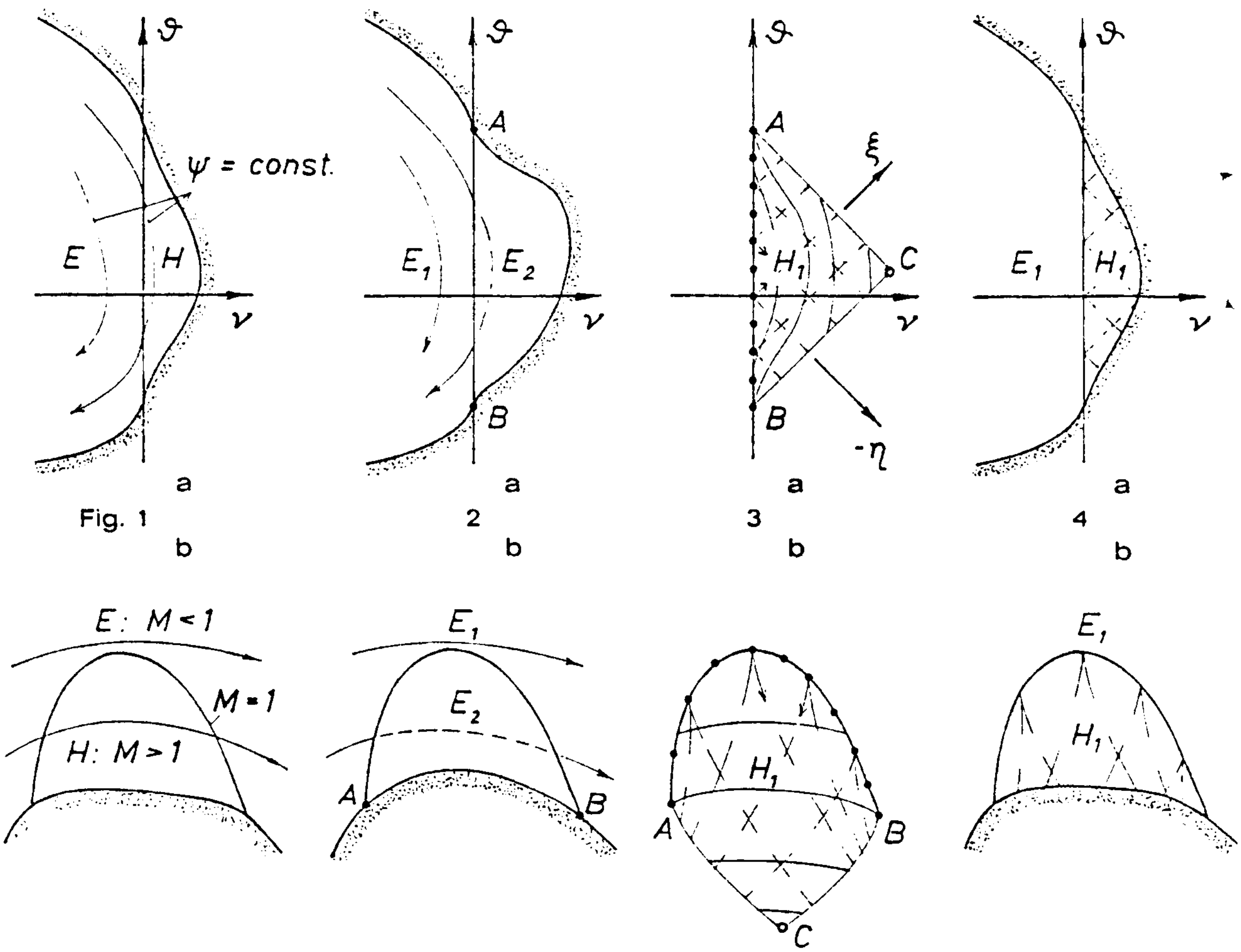

Figure 1 - 4. Elliptic Continuation Principle

which would result in a Cauchy-Riemann system in E_2. In this case, the part in E_2 of the elliptic solution can then easily be described analytically if the resulting data φ^*, $\psi^*(\vartheta)$ at $\nu = 0$ are expanded in terms of a harmonic analysis .

There is also a physical interpretation for this artificial solution in the flow plane x, y if ν in E_2 is reinterpreted

$$\nu(E_2) = \nu_E = \ln \frac{q_E}{a^*} \qquad (29)$$

and K_E takes the value ϱ_0/ϱ^*:
The solution of the elliptic system in E_2 represents an example of "supersonic incompressible flow" with critical constant density ϱ^*, embedded into the subsonic compressible solution obtained in E_1, see Fig. 2b. Streamlines, and most important, the streamline $\psi = \psi^*_A = \psi^*_B = \text{const.}$ defining our flow boundary for this fictitious flow, are integrated by use of (16) with the velocity variables q_E, ϑ, and $\varrho = \varrho^*$. The whole solution in $E_1 + E_2$ results in a flow with density obeying isentropic flow relations (2) only up to sonic velocity, beyond it density is frozen to the critical value. This interpretation led to a design method[11] which is not restricted to two-dimensional flow, results will be presented later.

We return now to our problem in the plane ζ_0. We still have to solve the equations for the real supersonic part of the flow, represented by the hyperbolic system (8) with positive sign and valid in the half plane ζ_0 ($\nu > 0$). We choose the characteristic form of this system as outlined in (13) - (15). With the given data ϕ^*, ψ^* along the ϑ-axis in the given interval A B we can solve this initial value problem at the sonic line with the method of characteristics. Although well known and used for many practical problems we would like to stress the fact, that we solve the system in the characteristic triangle A B C (Fig. 3 a) by calculating downstream along characteristics ξ = const, and upstream along characteristics η = const, with ξ, η defined in (13). Starting at A B we proceed toward C, the method therefore being a marching procedure normal to the flow direction, from the sonic line to a surface streamline yet to be determined. This concept is, in principle, also used in a procedure to calculate three-dimensional flow fields[12,13]. A line $\Psi = \Psi_A^* = \Psi_B$ = const is found in triangle A B C (it is different from the prescribed boundary in E_2!) and if it does not intersect one of the characteristics ξ = const and η = const. more than once, then its integration (16) in the physical plane, see Fig. 3 b, will give a new streamline arc A B and, along it, a velocity and pressure distribution. We use only the part between this streamline and the sonic line for our flow example and call this flow field H_1.

We go back now to our all-elliptic solution $E_1 + E_2$, Fig. 2 b, and replace the part E_2 and also the surface streamline arc A B by the solution H_1 and its new arc A B of Fig. 3 b. This gives us a mixed subsonic - supersonic flow field which is a solution of the linear mixed system (8) in the hodograph plane, Fig. 4 a, but also one of the nonlinear mixed system (3), or equations (4), in the physical plane, Fig. 4 b. It can be shown, that the new arc A B of H_1 fits smoothly into the E_1 subsonic flow boundary, streamline curvature across any point on the sonic line is continuous.

We have outlined a method to obtain solutions for transonic flow, to be applied mainly to subsonic flows with embedded local supersonic regions. Applications to flows with predominantly supersonic flow and embedded subsonic regions involve the treatment of bow and tail shock waves, results have been obtained for airfoil flow with sonic or slightly supersonic freestream conditions only in special cases where analytical solutions of the near sonic equations (19) were applicable. An example will be illustrated later, to show transition from the problem of supercritical airfoil flow with subsonic freestream conditions, to sonic and slightly supersonic freestream conditions. However, supercritical flow is our main concern here, and more precisely, the use of the idea outlined for design of such flows which are shock-free.

3. 2 The Rheograph structure of supercritical airfoil flow

The structure of supercritical airfoil flow is well known and needs no explanation here. However, some details are treated here shortly because they are of consequence for the practical indirect design method which will be outlined later.

We know from incompressible flow past lifting airfoils, that the isotachs in the flow field near the pressure (lower) surface exhibit a saddlepoint. This is the result of locally contracting streamlines due to the far field-effective circulation and the near field-effective body thickness. For compressible flow including supercritical conditions with or without a recompression shock, this is equally true, lines of constant local Mach number form a saddlepoint N below the lifting airfoil, see Fig. 5 a. This point is of interest for the mapping of a, say, given result of airfoil flow into our Rheograph plane ζ_0:

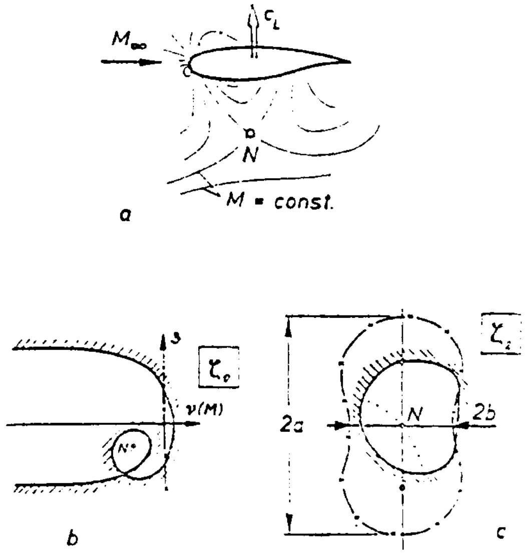

Figure 5. Saddlepoint, lift coefficient and Rheographs ζ_0, ζ_2

because we want to know the principal structure of the boundary conditions for such flows in order to design new examples. The airfoil image in ζ_0 for shock-free flow shows two complications in view of formulating a closed elliptic boundary value problem according to the first step of our design procedure:

First, the stagnation point of the airfoil is mapped into $\nu\ (M = 0) = -\infty$. Second, a part of the flow-field obviously covers the plane ζ_0 twice, as indicated by the loop in the airfoil image. The structure of the field image has to be completed now with the mapping of the aforementioned saddlepoint N, defined by $\nu\ (M_N)$, ϑ_N. A second Riemann sheet provides the second deck of ζ_0, it is connected with the basic deck along a cut from the airfoil mapping intersection to the point N, forming a branchpoint in the Rheograph ζ_0. A detailed description of the mathematical structure of these flow properties has been given in[14]. In order to arrive at a single-sheeted boundary value problem of closed, finite structure we perform now two mappings (9): first the stagnation point S is moved into a finite domain with the mapping

$$\zeta_1 = e^{\zeta_0}. \qquad (30)$$

Another mapping unwraps the loop of the airfoil image and we obtain a single sheeted domain by

$$\zeta_2 = c\ (\zeta_1 - \zeta_{1N})^{1/2}, \qquad \zeta_{1N} = e^{\nu(M_N) + i\,\vartheta_N} \qquad (31)$$

with c an arbitrary scaling constant. The airfoil image maps in ζ_2 into a closed curve including the stagnation point S as illustrated in Fig. 5c. The aforementioned saddlepoint maps into the origin, the sonic line into a Cassini curve or outer lemniscate with half axes a, b. The ratio b/a is a function of the local Mach number M_N in the saddlepoint:

$$b/a = \sqrt{\frac{1 - e^{\nu(M_N)}}{1 + e^{\nu(M_N)}}} \qquad (32)$$

The value M_N is related to the Mach number at infinity M_∞ in a similar way as the velocities in the saddlepoint and at infinity for an incompressible flow example past a Joukowsky airfoil or a circular cylinder with circulation. These latter examples are known analytically and from these we arrive at the ratio M_N/M_∞ as a function of the lift coefficient c_L:

$$M_N/M_\infty \sim 1 - A\,c_L^2 \qquad (33)$$

with a constant A. The circular cylinder example gives at least an idea about the magnitude of A:

$$A \sim 1/(2\,\pi^2). \qquad (34)$$

These relations invite to be checked on airfoil flow examples. We have a possibility to do this with existing results for hodograph supercritical airfoil design examples by Nieuwland[15], Boerstoel[14], or by Garabedian and Korn[16]. Some of these authors' designs are evaluated in Fig. 6, we see that the given relations (33), (34) are fulfilled satisfactory for not too large c_L. We conclude that for given (b/a) in (32) and for given M_∞ obsiously a certain band of c_L is possible. We stress this fact because we will later use an electric analog flow tool which will work with devices designed for fixed b/a where the given relations and the diagram Fig. 6 provides possible lift coefficients c_L (M_∞, b/a).

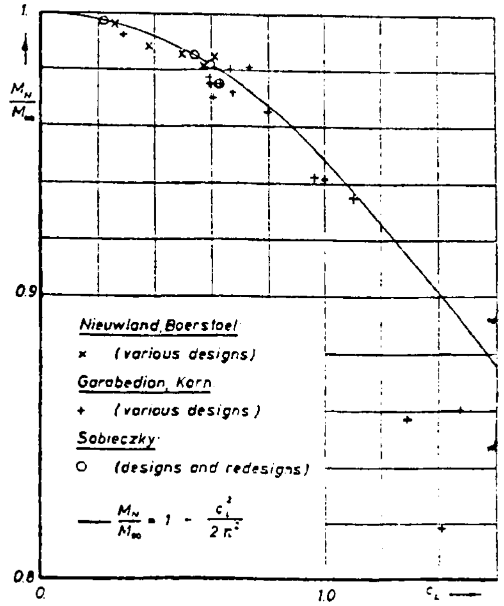

Figure 6. Mach number ratio vs. lift coefficient

2.3 Free stream singularities in the Rheograph plane

We further investigate the structure of supercritical flow in our working plane ζ_2. With the mapping of the airfoil into a closed curve as sketched in Fig. 5 c, the domain enclosed is the mapping of the whole flow. Infinity in the physical plane with $M = M_\infty$, $\vartheta = 0$ maps into a point I, where the solution of system (10) has a singularity. It has the structure

$$\Phi_I - i K_I \Psi_I = A\,(\zeta_2 - \zeta_{2I})^{-1} + B\ln(\zeta_2 - \zeta_{2I}). \tag{35}$$

The first term is a dipole, with the axis defined by the complex coefficient A. The second term is representing circulation, with B an imaginary coefficient. For nonlifting flow B vanishes and, in the case of a symmetrical airfoil, I and N coincide, $M_N = M_\infty$, the airfoil mapping is symmetrical to the vertical axis of ζ_2. For lifting airfoil flow the free stream singularity I is situated between saddlepoint N and the sonic line $M = 1$, see Fig. 7 a. For higher subsonic Mach numbers M_∞, I moves toward the sonic line and, with c_L fixed, M_N therefore has to be higher too. This results in a smaller "waist" b/a (32), as sketched Fig. 7 b. Finally, arriving at sonic freestream conditions, the waist reduces to zero, Fig. 7 c. This limiting case of airfoil flow with $M_\infty = 1$ is already beyond the relations (32) - (35) for supercritical conditions. Nevertheless, it is an interesting topic to study the change of hodograph structures if $M_\infty \to 1$, arriving from $M_\infty < 1$.

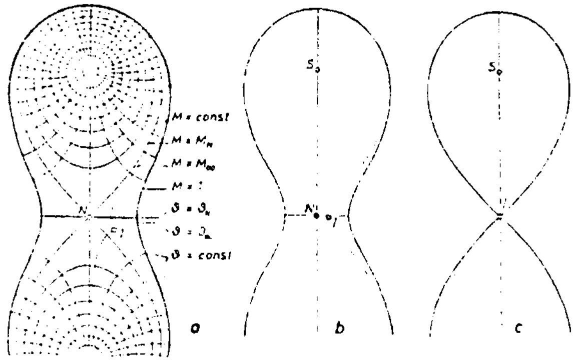

Figure 7. Rheograph ζ_2 for freestream conditions $M_\infty \to 1$

Airfoils with round leading edge have a stagnation point, which results in the fact, that the airfoil image in ζ_2 includes the mapped stagnation point S_o, see Fig. 5 c, or for sonic free stream conditions, Fig. 8 a. There are analytical results of the near sonic equations (19) for cusped airfoils[3,5,17] in sonic flow, with a sharp leading edge in smooth entry conditions therefore having no stagnation point. The airfoil contour wetted by subsonic flow maps into a region around the free stream singularity in I^*, see Fig. 8 b. This singularity is different from the subsonic far field solution (35), the transition from one to the other involves far field influence of the tail shock wave, similar to the transition from $M_\infty > 1$ to sonic free stream involving the far field of a detached bow wave. The latter problem is solved analytically[18] with use of the transonic shock polar mapped into the near sonic Rheograph Fig. 8 c.

We give some detailed illustrations for the aforementioned analytical results of cusped airfoil flow in Figures 9 - 11 although their value for practical flows is limited. On the other hand, these results represent educational examples for transonic flow phenomena, where the problem is solved for the subsonic part first, with the supersonic part either given analytically together with the subsonic results, or being calculated starting at suitable initial conditions provided by the subsonic solution.

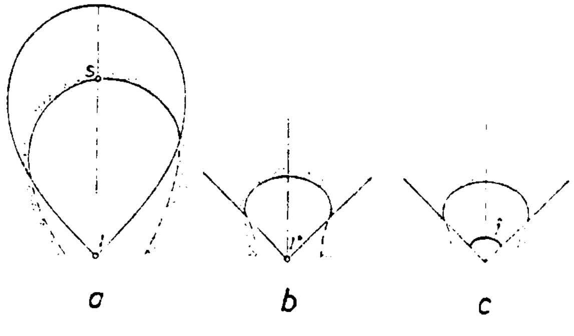

Figure 8. Rheograph ζ_2 for freestream conditions $M_\infty \geqq 1$

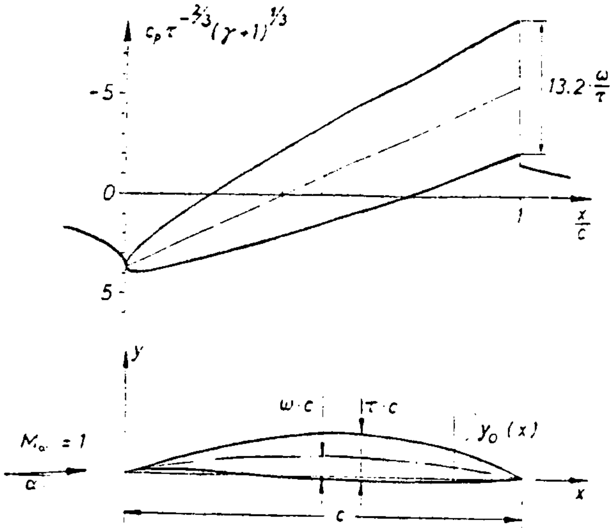

$$y_c = \tau \cdot x \cdot (1 - \frac{x}{c}) \left[2^2 \frac{\omega}{\tau} \pm 2^{-2} 3^{-3/2} 5^{5/2} (\frac{x}{c})^{1/2} \right]$$

Figure 9. Cusped lifting airfoil in sonic freestream

In Fig. 9 the cusped airfoil and its geometry formula is drawn. The sonic free-stream $M_\infty = 1$ has a certain angle of attack, α, which leads to smooth entry conditions, with α but also the local pressure on the airfoil, lift and drag functions of the camber/thickness ratio ω/τ, see Fig. 10 a, b. This analytical result is a generalisation of Guderley's cusp, where $\omega/\tau = 0$, a detailed description is given in [17].

There are results also for supersonic Mach numbers. Fig. 11 a shows a configuration of a bow wave and the local subsonic far field in a similarity flow plane, which illustrates the extent of a local subsonic region for $M_\infty \to 1$.

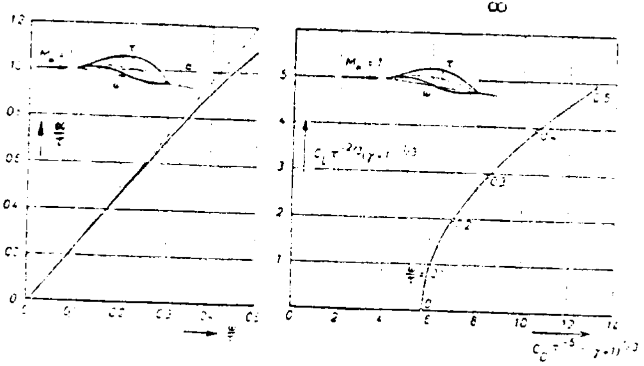

Figure 10. Cusped lifting airfoil: Smooth entry conditions, lift, drag

In terms of airfoil geometry, this extent is illustrated in Fig. 11 b for a Guderley cusp. Stand - off distance of a detached bow wave is obtained, e. g. for a 10% thick airfoil the bow wave attaches at $M_\infty = 1.17$. The extent of the local subsonic field normal to the flow direction is large, as the far field solution Fig. 11 a indicates. This is important for wind tunnel tests with detached bow waves, where the tunnel wall should not be reached by the subsonic field. A 10% thick Guderley - airfoil placed in a wind tunnel, at $M_\infty = 1.15$ for instance, requires a distance from airfoil to wall of about four times the chord length, while the bow wave stand off distance from the cusp is then only a fifth of the chord length.

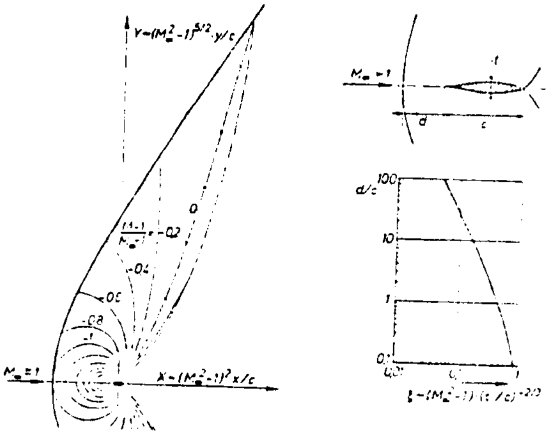

Figure 11. Detached bow wave:

a) Similarity solution for $M_\infty \to 1$
b) Cusped airfoil stand-off distance

4. RHEOELECTRIC ANALOGY

4. 1. Rheoelectric tank for transonic flow analogy

The structure of the particular solutions used for the illustrated examples gives information also about the details of the mapping near the sonic line, $\nu = 0$. It is easy to verify, that a solution for Φ, Ψ of system (8), describing an element of curved flow in transition from subsonic to supersonic flow, or reverse, is described by the locally valid expansion in ζ_0,

$$\varphi(\nu,\vartheta) = \varphi^*(\vartheta) - c' \cdot \nu^{4/3} \cdot \dot{\psi}^*(\vartheta) - O(\nu^2,\vartheta) \quad (36a)$$

$$\psi(\nu,\vartheta) = \psi^*(\vartheta) + c'' \cdot \nu^{2/3} \cdot \dot{\varphi}^*(\vartheta) + O(\nu^2,\vartheta) \quad (36b)$$

This is a very weakly singular behavior into the ν - direction, it is a consequence of generalized axisymmetric potential theory mentioned earlier and knowledge of this structure enables us to avoid certain difficulties occurring when a solution (8) or (10) in ζ has to be evaluated. The following description of transonic rheoelectric analogy mainly concentrates on outlining a technical solution for problems stemming from this singularity.

From definitions (25), (26) for the two types of analogy we see that local thickness h of a plane conductor, multiplied by its conductivity λ, is analogous to the coefficient K in analogy B, or to the reciproke K^{-1} in analogy A. As we see directly from the near sonic equations (19), the coefficient has a cubic root zero at the sonic line

$$K(\nu \rightarrow 0) = K^* \sim |\nu|^{1/3} \quad (37)$$

which leads to the above mentioned exponents 4/3 and 2/3 occurring in expansion (36). The necessary requirement of a slowly variing thickness h of a plane conductor for validity of the plane Beltrami system (24) for the electrical variables is therefore not fulfilled near the sonic line: conductor thickness would have to go to infinity or to zero with steep gradient.

Almost classical applications of the analogy to simulate aerodynamic problems some decades ago include the compressible flow hodograph for subsonic flow[8,19], but less actuality of transonic flow at this time in general and the above mentioned limitations stemming from the zero in the coefficient (37) prohibited an efficient extension of the analogy into the Mach number unity regime.

The first author's research on the aforementioned analytical structure of transonic flow in the modified hodograph plane, especially relation (37) led to a practical design of a new electrolytic tank - with water used as conductor - which allows an electric continuation of the analog flow beyond the sonic line in a Rheograph ζ. The basic idea is the use of an inclined wall boundary for the tank simulation of the sonic line, as shown in Fig. 12. The idea is the use of a locally three-dimensional electric potential to be evaluated on the surface. For Analogy A, Fig. 12a, sonic line electrodes are inclined forming a 67.5 degree wedge of the water body in the (ν, ϑ, μ) - space. On the surface μ = 0, where electric potential is evaluated, exponent 4/3 for representation of (36a) is observed and understood easily as a result of the local potential distribution in the (ν, μ) -plane.

In Fig. 12b the idea is illustrated for Analogy B: here we have an undercut sonic line with a 135° water body to represent the exponent 2/3 in (36b).

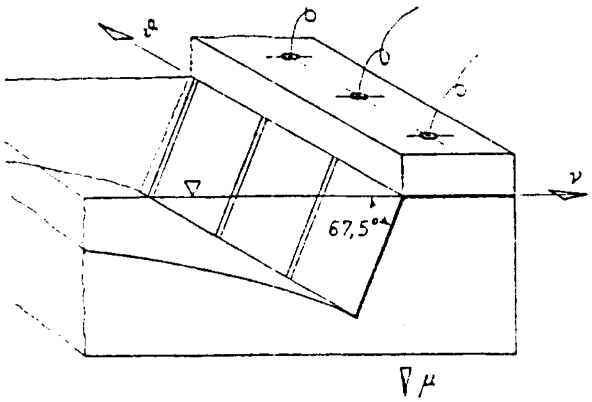

a) Analogy for velocity potential

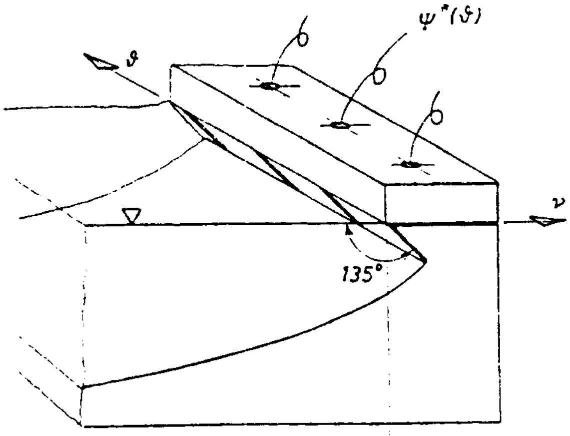

b) Analogy for stream function $\nabla \mu$

Figure 12. Electrolytic tank for transonic flow analogies

The idea is, like some of the analytical properties of transonic flow in our Rheograph plane, a generalization of axisymmetric potential distribution: the "Inclined Electrolytic Tank" or a hyperbolic shape bottom with a 45 degree wedge water body is familiar to researchers having used the analogy to represent incompressible axisymmetric flows[8,20].

4.2. Application of the analogy for design of Supercritical airfoils

The outlined idea of the inclined tank walls avoids the technical difficulties with infinite or zero depth of the electrolytic tank, but also allows the electric continuation of the potential distribution beyond the sonic line in order to establish a certain distribution on it, see Fig. 12. While the tank with water as conductor is a very accurate way to model the analogy, there are other possibilities avoiding this "wet" technique and still of acceptable accuracy. One is the use of conducting graphite paper. It is, of course, of constant thickness and has therefore to be inhomogenized in order to simulate variable tank depth. Perforation of the graphite paper was used in some experiments[21] with transonic flow analog representation. It is the first step into the discretisation of an electric network. This is an expensive tool if the grid is fine enough, it requires automated evaluation, being part therefore of a hybrid computational system including a digital computer. A network for solution of transonic hodograph problems was used in France[22], where the analogy has a long tradition.

The present author used the less expensive possibilities given by the graphite conducting paper. At 1970 digital computational codes for transonic potential flow analysis were just beginning to appear, design methods were not available. A project at the DFVLR in Germany was, therefore, the development of computational methods for transonic flow with the aid of the analogy[23]. This led to experiments with simple set-ups and data evaluation on the digital computer. A simple simulation of the rheoelectric tank with variable depth was achieved with acceptable accuracy through the use of compressed sheets of graphite paper, the sheets shaped parallel to isotachs in the analogy plane ζ in order to simulate $H(\nu)$. Fig. 13 shows a cut view through a rectangular "dry tank" outfitted with a grid of probes. Between top and bottom plate, and an elastic cushion layer, the graphite paper sheets are placed. The basic sheet extends into the regime $\nu > 0$ of the Rheograph plane, where the flow may be influenced by source distributions. The basic sheet also is provided with electrodes for singularity representation, in the case of a subsonic lifting airfoil with a quadrupole in order to represent a dipole with arbitrary orientation.

A set-up for Analogy B has been established and for airfoil design application, Rheograph ζ_2 is the working plane with the useful relations (31) - (34) for lifting airfoils. In Fig. 14a the grid of probes is drawn, with external flow and singularity feeding electrodes. The latter are placed into a nearly parallel electric flow and create a line of constant E ($\equiv \Psi$) with saddlepoints and

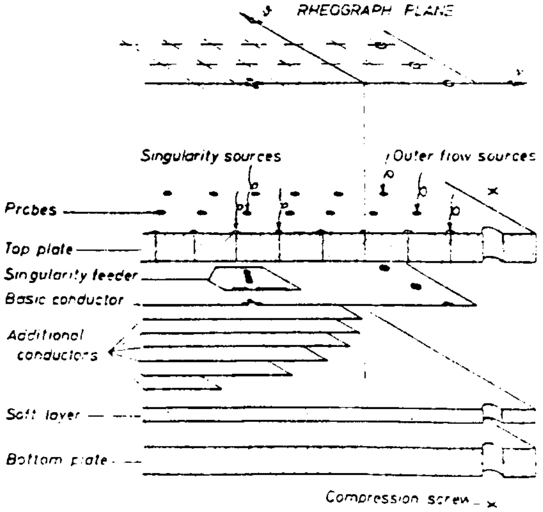

Figure 13. Analog flow table using compressed graphite paper

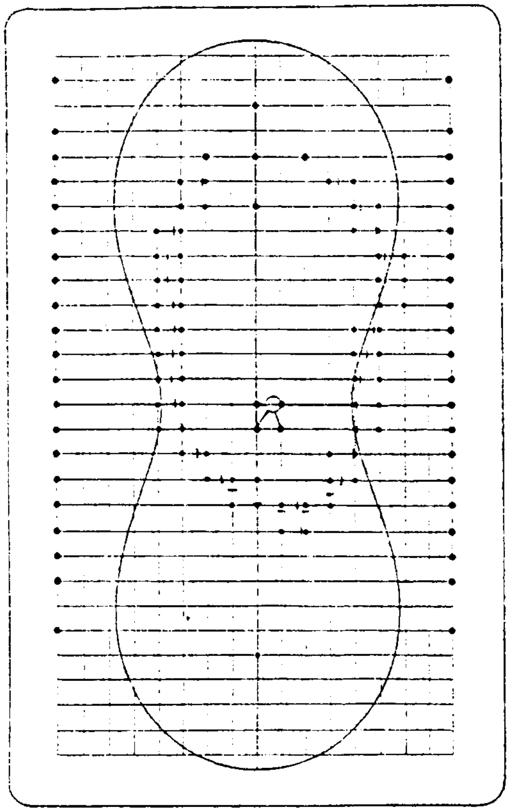

Figure 14a. Analog flow table for Rheograph ζ_2. Evaluation grid, equipotential line interpolation

forming a closed domain, Fig. 14b. One of the saddlepoints is shifted into the mapping of the stagnation point, S, by varing the potentimeters R_A, R_B. The subsonic flow domain is shown by drawing of the sonic line lemniscate. If the enclosed domain extends outside of it, then the domain may be evaluated as an elliptic continuation analog airfoil flow representation. The line ψ = const. is located in a limited number of intervals between probe grid points, Fig. 14a, and the potential values are transferred to the digital computer, along with the (manually) selected position of these probes. Interpolation, potential gradient evaluation and data spline fitting along $\psi = 0$ and along the sonic line, as well as integration of the supersonic field, boundary layer computation and viscous displacement subtraction, is carried out in the digital computer. The analog part of this hybrid technique is shown in Fig. 15.

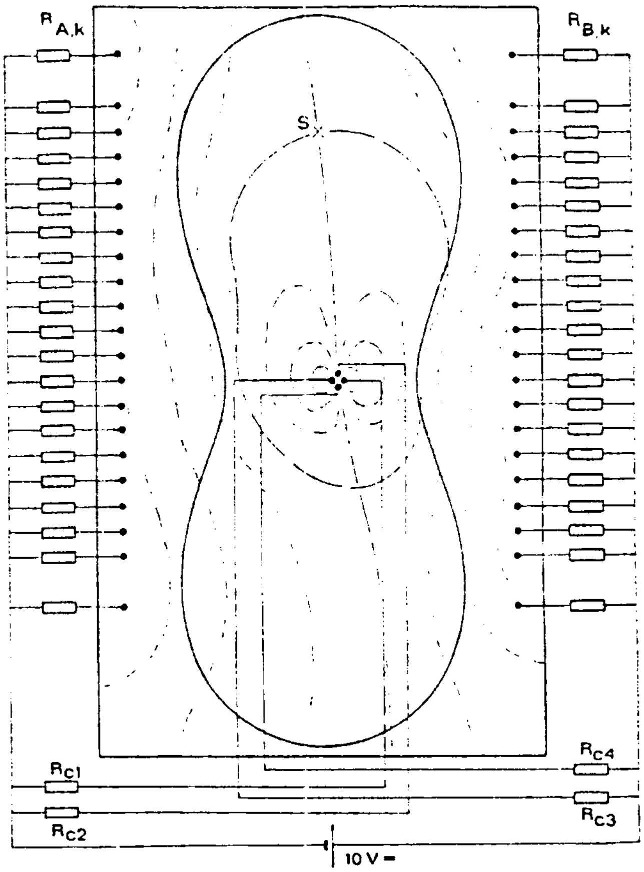

Figure 14b. Analog flow in ζ_2. Exterior flow and singularity

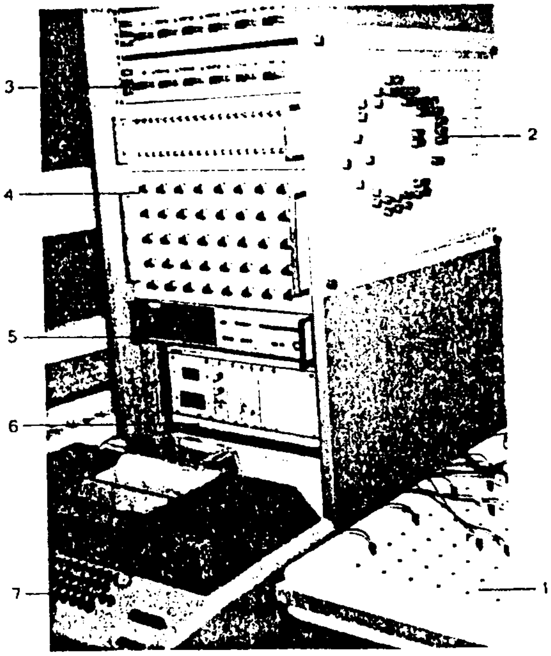

Figure 15. Analog flow evaluation with Analog flow table (1), Solution orientation (2), Bridge circuit (3), Flow adjustment Potentiometers (4), Digital Voltmeter (5), Data transfer unit and Scanner (6), Terminal and tape punch (7)

163

The method outlined was intended to give information about possible simplifications of hodograph techniques in the transonic regime. Availability of numerical analysis codes at a time when the first design results were obtained, accelerated the improvements and some airfoil designs were obtained for further use in supercritical wing design[24]. A result is shown in Fig 16, the airfoil was tested in the DFVLR Göttingen Transonic Wind Tunnel[25].

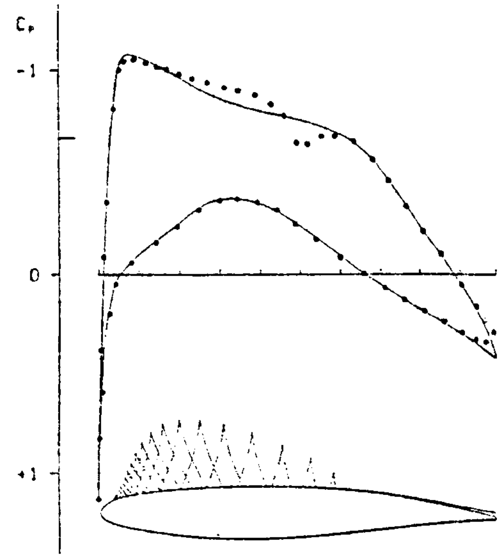

Figure 16. DFVLR 48080 Airfoil
- Theory: M_∞ = 0.73, Re = 10^7, C_L = 0.53
• Experiment: M_∞ = 0.755, Re = $2.4 \cdot 10^6$, C_L = 0.53

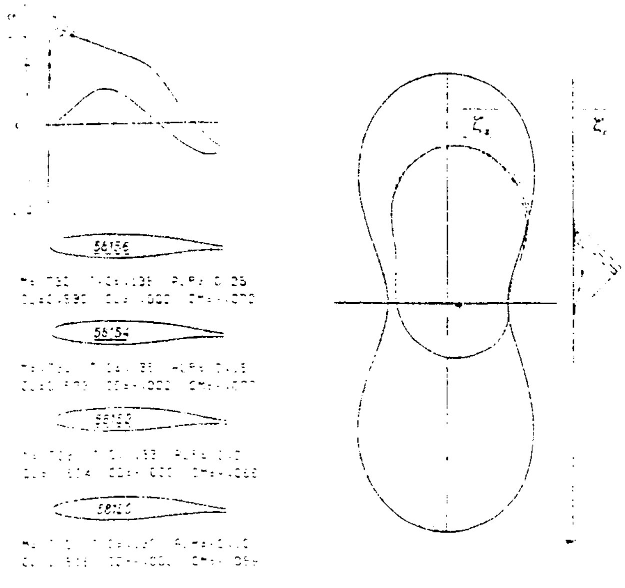

Figure 17. Variation of pressure peak

The tested airfoil is part of a series of designs differing only in the pressure peak region, Fig. 17. This was achieved by a local deformation of the analog flow airfoil mapping in the appropriate area of ζ_0. The characteristic triangles for supersonic flow field integration in ζ_0 are also drawn.

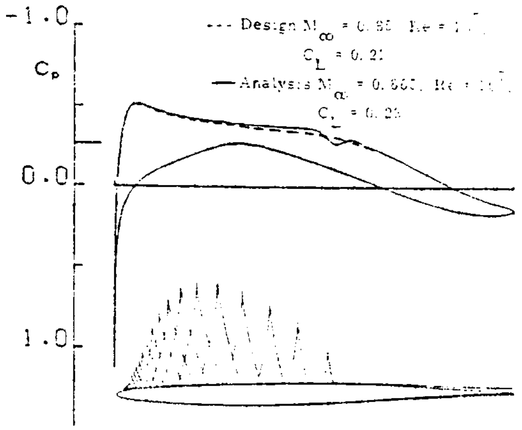

Figure 18. DFVLR 49201 Airfoil

For airfoils designs with a Mach number $M_\infty >$ 0.82 difficulties in the evaluation occur as a result of the slender "waist" of the sonic line lemniscate. The configuration Fig. 7 b results from a projected c_L of 0.2 and M_∞ = 0.85. The resulting airfoil is 5.4% thick, it is drawn in Fig. 18 with the designed supersonic region. Analysis calculations were carried out for slightly different Mach numbers and angles of attack, with the result that useful designs obviously can be obtained but design Mach number and angle of attack differ somewhat from the values defining singularity location in the analog flow. The airfoil was tested in the Braunschweig Transonic Wind Tunnel[26], some of the experimental polars are shown in Fig. 19.

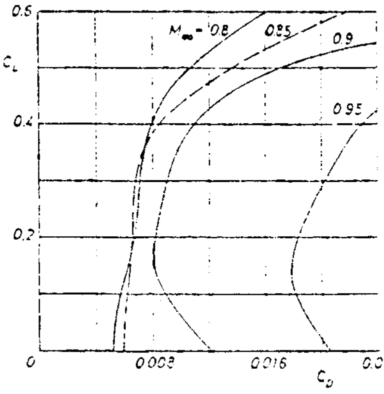

Figure 19. DFVLR 49201 Airfoil Polars
Experiment Re = $4 \cdot 10^6$

5. NUMERICAL HODOGRAPH METHODS

5.1 Panel Methods

The preceding description of airfoil design resulting from Rheoelectric analogy experiments was intended to give a background of educational value for further, more economical treatment of transonic design aerodynamics with numerical methods.

The hodograph methods developed by Nieuwland and Boerstoel, or by Garabedian and Korn belong into this chapter, but they are well-documented elsewhere[14,16] and, also we want to restrict this review on methods making use of the outlined Elliptic Continuation Principle, Fig. 1 - 4.

Analog electric flow was replaced by a numerical method first by Eberle[27]. A panel method, initially developed for incompressible flow past airfoils, was modified to solve the Poisson equation (12a) for the velocity potential ϕ, in a working plane where the appropriate boundary value problem is similar to the one for a given body in parallel flow. The Rheograph

$$\zeta_3 = (\zeta_2 - \zeta_{2I})^{-1} \qquad (38)$$

is suitable for this formulation. In Fig. 20 the computational grid for a chosen arbitrary boundary is drawn.

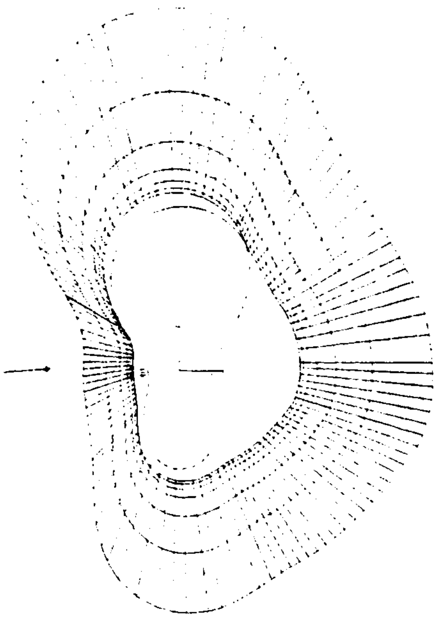

Figure 20. Rheograph ζ_3 with panel grid

A similar method was developed for the design of turbomachinery cascades[28]. It makes use of another working plane, where the stagnation point is mapped into infinity and the blade contour into the real part axis. This has the advantage of a limited area of compressibility influence and application of an incompressible flow solution for the far field.

5.2 Use of a Fast Poisson Solver

The panel method is a useful but relatively time-consuming and therefore expensive computer code. Another, more economical way to solve elliptic problems is the Fast Poisson Solver routine, which is used here for an airfoil/cascade design code. Application of this method requires formulation of a boundary value problem on a rectangle. We have to leave, therefore, the simple mappings $\zeta = \zeta(\zeta_0)$, as given by the formulas (30), (31), (38) and prescribe ζ_0 along the unit circle in a new plane ζ_c, which subsequently can be mapped into a rectangle.

The function

$$\bar{\zeta}_0 = \nu - i\vartheta = \ln(\zeta_c + 1) + \sum_n C_n \zeta_c^n \qquad (39)$$

with the coefficients C_n obtained from harmonic analysis of prescribed data ν_0 along the unit circle in ζ_c, (Fig. 21), defines the variables of state within the circle. We choose, for airfoil design, a ν_0-distribution as sketched in Fig. 21. This will result in a saddle-like surface of $\nu(\zeta_c)$. The saddlepoint on it plays the same role as the point N in ζ_2 outlined in a previous chapter. Choice of free stream conditions $\nu(M_\infty)$, ϑ_∞ defines the mapping ζ_{cI} of infinity into ζ_c. As we will see from the following, the Elliptic Continuation region E_2 (Fig. 2) is reduced here to vanishing size, the sonic line is now part of the boundary, sonic line data are obtained differently.

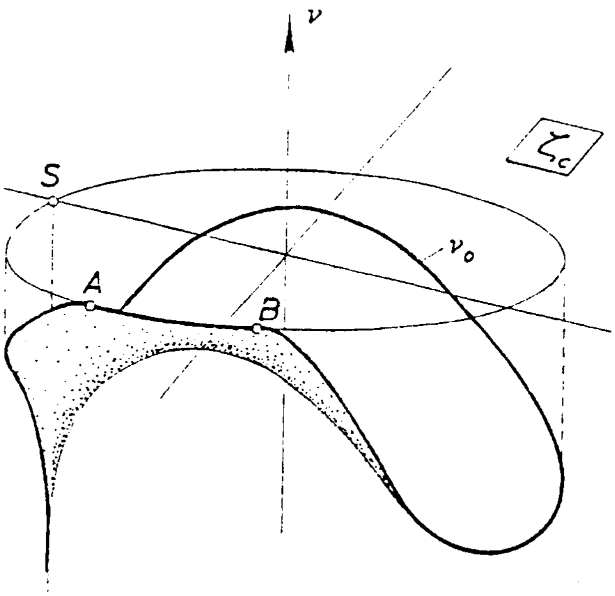

Figure 21. Circle Rheograph plane

To solve our potential flow basic equations we use Poisson equation (12 b) for the stream function Ψ. Application of the Fast Poisson Solver requires a mapping of our circle plane ζ_c to a rectangle. This is, with knowledge of ζ_{cI}, performed with the function

$$\zeta_P = i \ln[(1 - \zeta_{cI})(\zeta_c - \bar{\zeta}_{cI})] - i \ln[(1 - \bar{\zeta}_{cI}) \cdot (\zeta_c - \zeta_{cI})] \tag{40}$$

It maps the unit circle of ζ_c into the real axis of ζ_P and infinity I into $\mathrm{Im}(\zeta_P) \to +\infty$. The interior of the circle is therefore mapped periodically into stripes of the upper half plane in ζ_P, Fig. 22.

Flexibility in the formulation of boundary conditions for the chosen numerical solver routine[29] allows a more direct creation of sonic line data: the s-axis (Fig. 22) is both subsonic airfoil contour $\Psi = 0$ and - within the interval AB - sonic line, where an arc $\Psi^*(s)$ may be prescribed. The far field singularity (35) is represented by

$$\Psi_I(s) = c_I + \sin(s - s_I) \tag{41}$$

along a line $t = t_I$ = const. The constants c_I, s_I are used to obtain closed airfoil sections while the function $\Psi^*(s)$ defines size and shape of the local supersonic flow field.

These boundary data form Dirichlet conditions along two sides of the rectangle and we ask for a solution $\Psi(s, t)$ with periodical connection on the remaining sides. The solver routine can handle this boundary value problem, but an iterative procedure in two loops is required: First, the right hand side of the basic equation (12 b) requires the partial derivatives Ψ_s, Ψ_t. They are obtained from the previous computation, with a starting solution obtained by taking Laplace's equation for (12 b). The process usually converges very fast, 5 - 7 iterations are found sufficient. The second iteration loop is necessary to obtain (a) the correct stagnation point solution which is mapped into S on the s-axis, and (b) a physically meaningful closed airfoil. A variation of the constants c_I, s_I in the far field boundary conditions effectively provides this in 3 iterations. Sonic line data $\Psi^*(s)$, ϑ (s) are available, but $\Phi^*(\vartheta)$ has to be obtained by use of the expansion (36 a). With Φ^*, $\Psi^*(\vartheta)$ given, the local supersonic region is computed with the method of characteristics as in the previously outlined techniques.

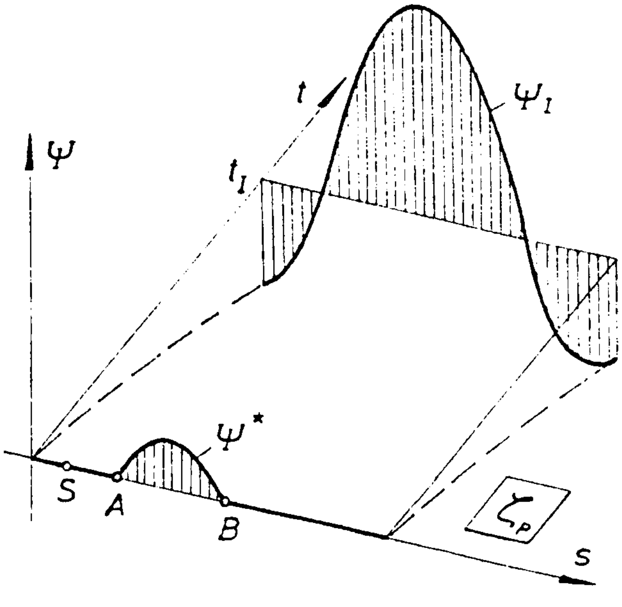

Figure 22. Poisson solver Rheograph with periodic boundaries for stream function

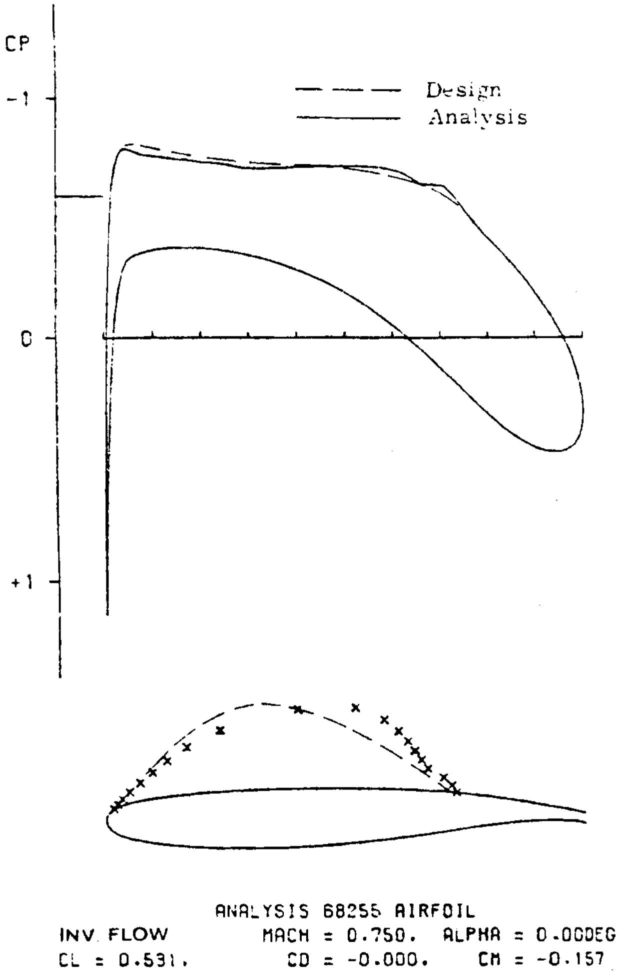

Figure 23. Poisson solver design example, and analysis verification

An example of airfoil design and its analysis verification is shown in Fig. 23. The results agree very satisfactory. The method can be switched to cascade design, but the boundary value problem for Ψ is more complicated

The method outlined is closely related to Garabedian's recent version of a numerical design method for airfoils and cascades, which is a complex characteristics method. This is a basically hyperbolic approach to the transonic problem, while our methods are primarily elliptic, with an appended hyperbolic technique. Garabedian's recent design code[30] allows a prescription of the pressure distribution along the (unknown) airfoil surface, this is a remarkable improvement of earlier versions, which should be applicable also to the code outlined here.

6 A DIRECT NUMERICAL DESIGN METHOD

6.1 Extension of an analysis code into a design tool

A replacement of the analogy to solve the elliptic part of our basic equations by numerical methods for elliptic problems was made possible by application of digital solver routines for elliptic flow. Like all hodograph or indirect design methods, the advantage of linear equations is in contrast to difficulties with nonlinear boundary conditions. The latter requires much of the designer's experience and iteration loops in the computer programs to arrive at reasonable designs, as briefly outlined above. Therefore a new idea, concerning application of the design techniques in physical space, seemed to be the necessary and logical step to be taken next. The result obviously brings up some very effective computer codes with applications on plane as well as on three-dimensional flow[11,31].

One of these methods is the extension of Jameson's[32] finite difference analysis program for compressible flow with shocks, into a design code for shock-free airfoils. The idea is the introduction of a fictitious gas locally if the flow becomes supersonic. This gas has a modified compressibility law

$$\varrho \sim 1/q^P \qquad (42)$$

in the supersonic region replacing the correct isentropic relations (2). For an exponent $P < 1$ this gas will result in elliptic basic equations for the fictitious supersonic flow, corresponding to the Elliptic Continuation region E_2 in Fig. 2b. The sonic line in the flow field is found by interpolation and the supersonic region is recalculated with the method of characteristics as performed in the indirect methods.

The first instructive results of the direct method are the optimization of conventional NACA airfoils into transonic shock-free configurations. Only minor changes of a NACA airfoil upper surface are required to arrive at a shock-free airfoil.

These first results were inviscid flow designs. the method is now operational including a boundary layer program and serves as a computational test-bed for various theoretical approaches to remaining problems in transonic flow including viscous interaction at the trailing edge.

An important question was asked frequently since the method become operational: is there a way to verify a given shock-free airfoil - e. g. a result from the indirect methods - with this computer code? The answer is positive and will be outlined now briefly.

We observe from the calculated examples that the conventional input configuration is usually thicker than the resulting shock-free airfoil. The reason is, as sketched in Fig. 2b and Fig. 4b, that the fictitious elliptic flow in E_2 requires less space according to higher flow density $\varrho \cdot q$ than the real supersonic flow H_1. This results in a flatter surface of the resulting boundary streamline in H_1 in order to allow the passing of supersonic flow at fixed sonic line. Just this flattened region in characteristic for shock-free airfoil design. Some still unknown thicker contour within the known sonic line arc of a shock-free design therefore would be the initial configuration to obtain this design. In the case of the use of a fictitious incompressible flow - with $P = 0$ in (42) - the initial contour for a design can be found theoretically by using the reinterpretation formula (29) for a local incompressible flow solution within the sonic line. A flow boundary results and it usually thickens the configuration. But there are cases of shock-free airfoils leading to initial contours with surface discontinuities, representing singularities stemming from Riemann cuts like the hyperbolic limit lines. This means, that not every type of shock-free airfoil can be obtained with the model of incompressible fictitious gas. However, our recent findings indicate, that for different compressibility laws $P \neq 0$ obviously any type of shock-free pressure distribution and the generating airfoil may be verified. We illustrate this for the case of the well-known Korn - 1 - airfoil.

The airfoil was made thicker in the interval between 5 and 70 percent of the upper side surface using a simple analytical bump function. A compressibility exponent of

$$P = 0.9 \tag{43}$$

was found most useful. Only a few program runs were necessary to find this and the amount of added thickness in order to obtain a shock-free airfoil resembling KORN - 1 - airfoil very closely. The result is drawn in Fig. 24. The initial airfoil is approximately one half percent thicker than the resulting KORN-1 redesign.

The found initial airfoil contour can be used now to design a whole series of neighboring shock-free airfoils for variing operating conditions M_∞, ϑ_∞. For industrial practice, this seems to be useful, if an existing wing section design needs to be modified for e. g. a slightly different operating Mach number.

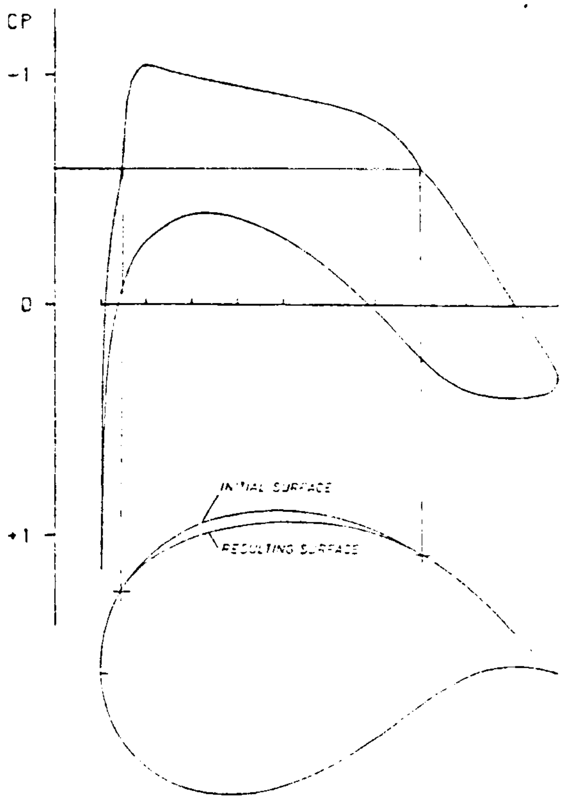

REDESIGN KORN 1 AIRFOIL
INVISCID FLOW. MACH = 0.750. ALPHA = 0.00DEG
CL = 0.626. CD = 0.000. CM = -0.146

Figure 24. Redesign of KORN 1 Airfoil

6.2 Design of Adaptive Wing Sections

The example of Fig. 24 is an inviscid design, the airfoil has a cusped trailing edge. In real flow viscous interaction has to be taken into account, in the case of airfoil design it means that boundary layer displacement has to be added to the airfoil thickness. Special care is required in the trailing edge region, where separation of the boundary layer may occur. A favorable trailing edge design avoids steep pressure gradients on the upper surface and expands the flow from a rear loading of the lower surface. Generalisations of the analytical results of flow past cusped leading edges in smooth flow, Fig. 9, lead to shapes with such favorable pressure distributions[33] and also provide outer flow models for computational treatment of wake-boundary layer interaction[34]. This problem is important for design methods since it influences circulation remarkably. Another application of the direct design method is illustrated in the following, the example takes into account viscous flow effects.

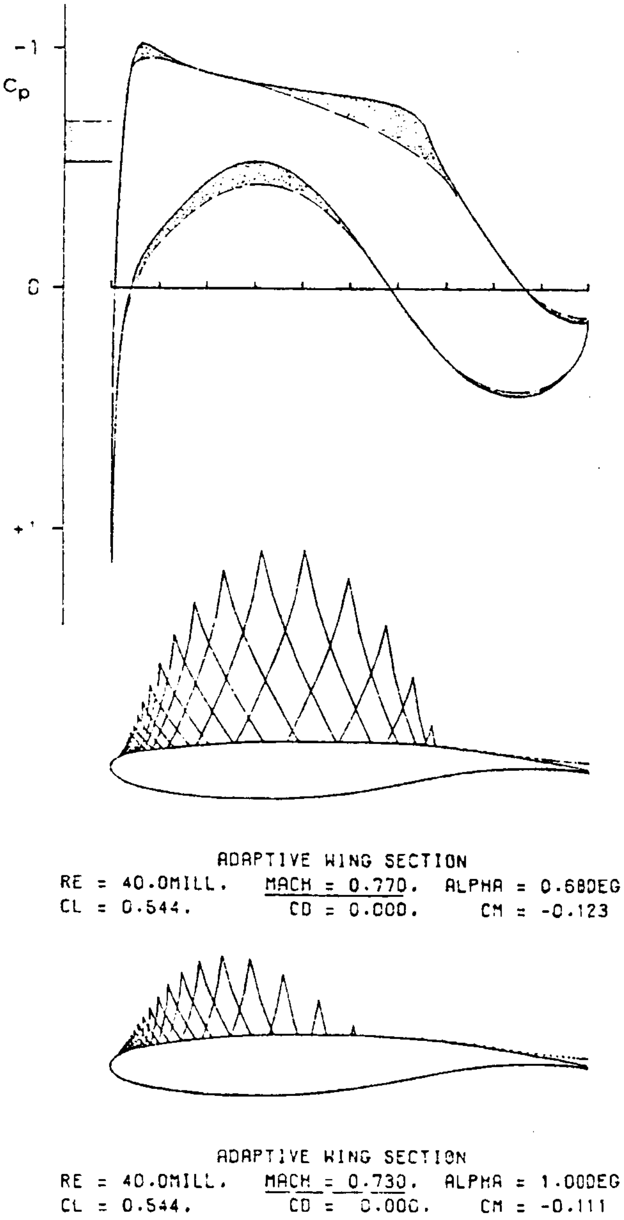

Figure 25. Adaptive Wing Section: pressure distribution

The aforementioned use of the initial configuration to obtain a family of shock-free airfoils led to the idea of Adaptive Configurations[35]. Since only a part of the upper surface has to be modified for shock-free flow in different operating conditions, such modifications might be technically carried out on a wing surface by elastic or pneumatic devices, or by suction and blowing. In Fig. 25 an airfoil with adaptive shape for shock-free flow in the range of $0.73 \le M_\infty \le 0.77$ is shown, with a fixed lift coefficient. The basic airfoil is an industrial design[36] representing the configuration at $M_\infty = 0.73$. Gradual shape change from 2 to 70 percent chord illustrated in Fig. 26 extend the range of shock-free operation up to $M_\infty = 0.77$. There was not one single initial

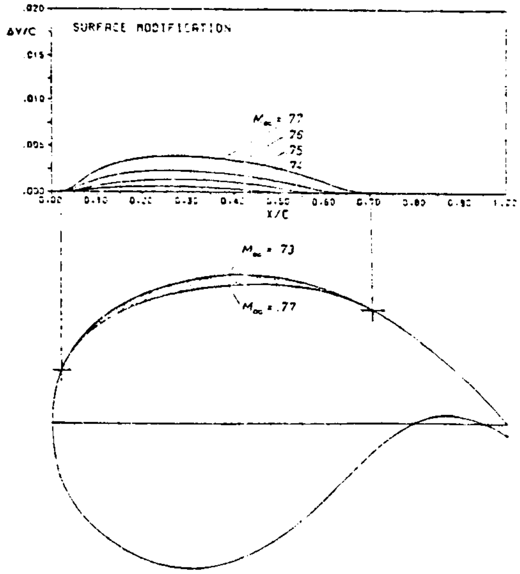

Figure 26. Adaptive Wing Section: Shape changes

configuration for the design of these surface alterations: Bumps of variable size and height were added to the basic airfoil for the different Mach numbers, the code subsequently subtracted more than the bump, resulting in the illustrated surface modifications. The choice of different initial surfaces at the various Mach numbers is desirable in order to obtain similar supercritical pressure distributions. A fixed initial surface results in sharp pressure peaks which set lower limits in the Mach number range of shock-free flow.

7 CONCLUDING REMARKS

We have presented different techniques for transonic airfoil design having in common the use of a new boundary value problem for mixed flow, the Elliptic Continuation Principle. Design methods resulting from this approach were shown growing in an evolutionary process finally leading to effective computer programs. Presentation of the first steps like the analytical results and the experiments with Rheoelectric Analogy was intended to provide initial understanding for the more economical numerical methods. This seems to be important in a time when the design engineer familiar to and dependent on large computing facilities, looses contact to educational flow models obtained with more classical techniques.

Besides this reviewing character of the paper, we arrived at a new design method opening several interesting possibilities. The concept of Adaptive Wings is the theoretical base for experiments with new fuel efficient transonic configurations. Extension into three-dimensional flow problems proved possible and the first shock-free wings and wing body combinations have been obtained[11,13,37].

Acknowledgement

Research reported in this paper was carried out at the DFVLR, Göttingen, West Germany and at the University of Arizona, Tucson, USA. The work was funded by DFVLR basic funds, AFOSR Grant 76 - 2954 E and ONR Contract N 00014 - 76 - C - 0182. The author wishes to thank Mr. Lutz Leopold for his assistance with programming and carriing out calculations.

8. REFERENCES

1. Advanced Technology Airfoil Research Conference, NASA Conference publication 2045, March 1978.

2. Oswatitsch, K., Spezialgebiete der Gasdynamik, Springer Verlag, Wien - New York (1977).

3. Guderley, K. G., Theorie Schallnaher Strömungen, Springer Verlag, Berlin, Göttingen/Heidelberg 1957.

4. Weinstein, A., Generalized axially symmetric potential theory, Bull. Amer. Math. Soc. 59 (1953), p. 20 - 38.

5. Sobieczky, H., Exakte Lösungen der ebenen gasdynamischen Gleichungen in Schallnähe, Zeitschrift f. Flugwiss. 19, Heft 5 (1971).

6. Taylor, G. I., and C. F. Sharman, A mechanical method for solving problems of flow in compressible fluids. ARC R and M 1195. (1928).

7. Taylor, G. I., and C. F. Sharman, Problems of flow in compressible fluids. Proc Roy. Soc of London, Serie A, v. 121 (1928).

8. Malavard, L. C., The use of rheoelectrical analogies in aerodynamics, AGARDograph 18 (1956)

9. Morawetz, C. S., Nonexistence of transonic flow past a profile, Comm. Pure and Appl. Math., vol. 17, (1964) p. 357 - 367.

10. Ferrari, C., and F. G. Tricomi, Transonic Aerodynamics, Academic Press, New York/London (1968).

11. Sobieczky, H., K.-Y. Fung, A. R. Seebass, N. J. Yu, A New Method for Designing Shock-free Transonic Configurations, AIAA paper 78-1114 (1978).

12. Sobieczky, H., A Computational Algorithm for Embedded Supersonic Flow Domains, The University of Arizona, Tucson, AZ, Engineering Experiment Station, Report TFD 78-03 (1978).

13. Fung, K.-Y., H. Sobieczky, A. R. Seebass, Numerical aspects of the design of shock-free wings and wing-body combinations, AIAA paper 79-1557 (1979).

14. Boerstoel, J. W., Design and analysis of a hodograph method for the calculation of supercritical shock-free airofoils, NLR TR 77046 U (1977).

15. Nieuwland, G. Y., Transonic potential flow around a family of quasi-elliptical aerofoil sections, NLR-TR 172 (1967).

16. Bauer, F., P. Garabedian, D. Korn, (A. Jameson), Supercritical wing sections I, II, III Lecture Notes in Economics and Mathematical Systems Nrs. 66 (1972), 108 (1975), 150 (1977) Springer Verlag Berlin, Heidelberg, New York.

17. Sobieczky, H., Tragende Schnabelprofile in stoßfreier Schallanströmung, Zeitschrift f. angew. Math. Physik, Vol. 26 (1975).

18. Sobieczky, H., Die abgelöste transsonische Kopfwelle, Zeitschrift f. Flugwiss. 22, Heft 3 (1974).

19. Vandrey, F., Untersuchungen über die Behandlung ebener Unterschallströmungen mit Hilfe einer elektrischen Analogie, AVA Göttingen, Bericht 44-A-10 (1944).

20. Babister, A. W., et. al., The use of a potential flow tank for testing axi-symmetric contraction shapes suitable for wind tunnels. The College of Aeronautics Cranfield, Report no. 46, (1951)

21. Sobieczky, H., Rheoelektrische Analogie zur Darstellung transsonischer Strömungen. Deutsche Luft- und Raumfahrt DLR-FB 71-26 (1971).

22. Rigaut, F., Determination analogique de profils d'aile en regime transsonique, Transonic Aerodynamics. AGARD Conference Proceedings No. 35 (1968).

23. Sobieczky, H., Entwurf überkritischer Profile mit Hilfe der rheoelektrischen Analogie, Deutsche Luft- und Raumfahrt DLR-FB 75-43 (1975).

24. Redeker, G., N. Schmidt, Design and experimental investigations of a wing for a transonic transport aircraft, DGLR/GARTEur 6 Symposium on Transonic Configurations. DGLR paper 78-085 (1978).

25. Stanewsky, E., Windkanalerprobung des überkritischen Profils AVA-1 (DFVLR 48080) im Rahmen des ZKP-Programms (LFK 7511) Ergebnisbericht No. 13 (1978).

26. Puffert, W., Vorläufige Ergebnisse der Messungen an den Profilen DFVLR 49201, Whitcomb 05, NACA 64 A (1.33) 05 im Transsonischen Windkanal Braunschweig, DFVLR IB 151-79 B 1 (1979).

27. Eberle, A., An exact hodograph method for the design of supercritical wing sections. Symposium Transsonicum (ed. K. Oswatitsch and D. Rues), p. 314-321 Springer Verlag Berlin, Heidelberg, New York (1976).

28. Sobieczky, H., Entwurf eines transsonischen Kompressorengitters, DFVLR-AVA IB 251-77 A 22 (1977).

29. Sweet, R. A., A generalized cyclic reduction algorithm, SIAM J. Numerical Analysis Vol. 11 No. 3 (1974).

30. Garabedian, P., Korn, D., A systematic method for computer design of supercritical airfoils in cascade. Comm. Pure Appl. Math. Vol. 24, (1976).

31. Eberle, A., H. Sobieczky, Erweiterung des transsonischen 2D-Panalverfahrens auf die Berechnung gepfeilter Tragflügel. Messerschmitt-Bölkow-Blohm GmbH, Ottobrunn/München, Report UF 1451 (1978).

32. Jameson, A., Iterative solution of transonic flows over airfoils and wings, including flows at Mach 1. Comm. Pure Appl. Math. 27 (1974).

33. Garabedian, P., On the design of airfoils having no boundary layer separation, Advances in Mathematics 15, (1975).

34. Melnik, R. W., R. Chow, H. R. Mead, Theory of viscous transonic flow over airfoils at high Reynolds numbers, AIAA paper No. 77-680 (1977).

35. Sobieczky, H., A. R. Seebass, Adaptive Airfoils and Wings for Shock-free Supercritical Flight, Invention Disclosure, The University of Arizona, Tucson, AZ, Engineering Experiment Station, Report TFD 78-02 (1978).

36. Boehe, R. D., Transonic measurements with VFW-F-airfoil Va 2 at the DFVLR Göttingen, ZKP-Flügelsektion (LFK 7511) Ergebnisbericht No. 8 (1976).

37. Yu, N. J., An Efficient Transonic Shock-free Wing Redesign Procedure using a fictitions gas method, AIAA paper 79-0075 (1979).

AGARD

ADVISORY GROUP FOR AEROSPACE RESEARCH & DEVELOPMENT

7 RUE ANCELLE 92200 NEUILLY SUR SEINE FRANCE

Paper Reprinted from
Conference Proceedings No. 227
Unsteady Aerodynamics

NORTH ATLANTIC TREATY ORGANIZATION

UNSTEADY TRANSONIC FLOW COMPUTATIONS

by

A. R. Seebass, N. J. Yu, and K-Y. Fung
Department of Aerospace and Mechanical Engineering
University of Arizona
Tucson, Arizona 85721

SUMMARY

We investigate the effects of unsteady modes of motion on two-dimensional transonic flows; we do so in the context of the inviscid small perturbation approximation. The study is a numerical one and draws upon the alternating-direction implicit procedure developed for such calculations by Ballhaus and his co-workers at the NASA Ames Research Center. Our numerical algorithm treats shock waves as moving discontinuities. Results of nonlinear and time-linearized calculations of the transonic flow past an NACA 64A006 airfoil experiencing harmonic motions in several of its modes are presented and discussed.

1. INTRODUCTION

In unsteady transonic flows, relatively small periodic changes in the boundary conditions can lead to substantial changes in the loads and moments with marked phase lags. These are of major concern in the aerodynamic design of aircraft that operate in the transonic regime. A short, but timely, review of various aspects of unsteady transonic flow may be found in Reference 1. Of particular concern are aeroelastic behavior, and flutter and buffet boundaries. Here the unsteady perturbations may sometimes be small enough that linearization about a nonlinear steady flow, as suggested by Landahl (2) long ago, is possible.

In such flows the behavior of the boundary layer, especially as it is affected by the pressure rise caused by any shock waves in the flow, is clearly of major importance. Additionally, in the neighborhood of the leading edge the flow perturbations are large; consequently, highly accurate inviscid results require the use of the full potential equation. It seems likely that eventually the computational algorithms used in routine studies of unsteady transonic flows will use the Reynolds averaged Navier-Stokes equations now used in research studies. However, such algorithms (3) currently require substantial computer time and are too inefficient for exploratory studies such as this one. The ability of these algorithms to model complex unsteady transonic flow phenomena, such as buffet, has recently been demonstrated (4).

An important consideration in constructing an algorithm for unsteady transonic flows is the treatment of moving shock waves. The experimental observations of Tijdeman (5-7) indicate that even for simple airfoil motions shock wave motions can be complicated, and that they can strongly affect aerodynamic force and moment variations. Time-linearized methods, i.e., methods that assume the unsteady perturbations are small compared to the basic steady disturbance have not usually considered shock motions (8, 9), although they can be modified to do so for small shock excursions (10). Time-integration methods (11-18) treat shock waves by "capturing" them, a procedure that can present a number of difficulties.

Unsteady experiments (5-7), analysis (10) and numerical studies (10) all indicate that the amplitude of the shock wave motions increases inversely with reduced frequency. Thus some of the most important effects occur with low-frequency motions. This is not surprising; nonlinear behavior is suppressed at higher frequencies, with the small perturbation equation becoming linear for frequencies higher than the two-thirds power of the airfoil's thickness-to-chord ratio. Explicit finite-difference schemes are not efficient when applied to low-frequency cases because the stability restriction on the time step is substantially more severe than that required for accuracy. As a result, efficient semi-implicit methods (13) and even more efficient fully implicit methods (11, 12, 17, 18) have been developed. Caradonna and Isom (17) use an iterative implicit procedure, i.e., the nonlinear implicit finite-difference equations must be solved iteratively at a given time level. In an earlier, unpublished, study we also used such a procedure. Ballhaus and Steger (11) and Beam and Warming (18) constructed more efficient algorithms that solve the nonlinear equations directly by the solution of simple matrix equations generated by an alternating-direction implicit (ADI) procedure. This method has proven to be so efficient that it is now used as an alternative to successive line over-relaxation (SLOR) for steady flow calculations (Reference 19 and Yu and Seebass, unpublished).

As mentioned above, these implicit schemes "capture" shock waves, i.e., shock waves evolve automatically as part of the numerical solution. Shock capturing produces shock profiles that are distorted in a manner that depends on the truncation errors in the finite-difference scheme. The use of mixed-difference schemes (11, 18) can improve the situation for cases in which the flow changes from supersonic to subsonic across the shock. However, when this condition is not satisfied the differencing cannot be switched across the shock and shock resolution is poor. In any case, shock capturing requires spatial grid spacings, in regions where shock waves are anticipated, that are sufficiently small to resolve the shock waves. The grid spacing required to do this is usually much smaller than that required to resolve flow variable gradients in most of the rest of the flow field. Shock fitting removes the large gradients from the finite difference solution and permits equivalent flow field resolution with fewer grid points, both in space and time (20, 21). If shock waves are not treated as discontinuities, but are to be captured correctly, the difference equations must be solved in conservation form. This imposes an additional constraint on the construction of finite-difference schemes that can be difficult to satisfy.

A need for shock fitting also arises in computing time-linearized solutions for very small unsteady perturbations. Time-linearized solutions for indicial motions can be used to determine force and moment coefficient variations at various reduced frequencies, obviating the need for a numerical solution at each reduced frequency (see, e.g., Reference 22).

Traci, et al., (8, 23, 24) have developed relaxation methods for solving the resulting time-linearized equations of motion for harmonic disturbances. Less complete, but comparable, studies have been made by Weatherill et al. (25); these derive from an earlier study by Ehlers (26). In both of these studies shock motions, which contribute substantially to the time-varying loads and moments, are neglected. Difficulties also arise in the convergence of the iterative numerical scheme. Unsteady small amplitude motions have shock wave excursions that are the order of the amplitude of the motion divided by the reduced frequency of the motion. Consequently, these shock motions dominate other low frequency contributions to the lift and moment coefficients. Such time-linearized shock motions can be computed in a rational way, but the accuracy of the results depends critically on an accurate resolution of the steady flow field in the vicinity of the shock wave (10); this is best accomplished by shock fitting.

This paper briefly reviews the numerical procedures we have developed for computing nonlinear and time-linearized small perturbation unsteady transonic flows. We use an ADI scheme and treat shock waves as discontinuities in the flow. Calculations of the transonic flow past an NACA 64A006 airfoil experiencing harmonic or indicial pitching and flap oscillations are discussed.

2. FORMULATION

We write the unsteady small disturbance equation for low frequency transonic flows in the commonly used form

$$-2KM_\infty^2\phi_{xt} + \{1 - M_\infty^2 - (\gamma + 1)M_\infty^2\phi_x\}\phi_{xx} + \phi_{yy} = 0. \tag{1}$$

The spatial coordinates, the time, and the velocity potential in (1) have been non-dimensionalized by the chord, the reciprocal of the angular frequency, and the free stream velocity times the chord, respectively. Other, perhaps more useful and suitable, forms are given in References 21 and 27. This equation results from a systematic expansion of the velocity potential in the thickness ratio τ and applies for reduced frequencies $K = O(\tau^{2/3})$ where $K = \omega c/U$, i.e., the angular frequency multiplied by the time it takes the flow to traverse the airfoil chord. Lin, Reisner and Tsien (28) showed that, with restriction to small perturbations throughout the flow, this is the only nonlinear equation that arises. For moderate frequencies the equation

$$-K^2\phi_{tt} - 2K\phi_{xt} + \{1 - M_\infty^2 - (\gamma + 1)M_\infty^2[\phi_x + \frac{\gamma - 1}{\gamma + 1}K\phi_t]\}\phi_{xx} + \phi_{yy} = 0$$

is frequently used, with or without the ϕ_t term, and may provide results that apply at higher frequencies than those obtained from (1).

The boundary condition on the body takes the simple form

$$\phi_y(x,0,t) = \tau[Y_x^\circ + \frac{\delta}{\tau}(Y_x^u + KY_t^u)], \quad -\frac{1}{2} \le x \le \frac{1}{2}, \tag{2}$$

where $Y(x,t)$, the instantaneous body shape, has been decomposed into a steady part, Y°, and an unsteady part, Y^u. Here δ is the amplitude of the unsteady oscillation. Because $K = O(\tau^{2/3})$, the last term in (2) is dropped unless $Y_x^u \equiv 0$ or is small. For this reason, the time-linearized perturbation velocity potential for plunging motions $(Y_x^u = 0)$ is just K times that for the analogous pitching motion, where $Y^u(x,t) = (x - x_o)\sin t$.

Numerical studies conducted by Magnus (15) show that erroneous boundary data on a finite domain can lead to significant errors. The low frequency approximation implies that any changes in the circulation are communicated instantly downstream to infinity. Consequently, the simplest boundary conditions are $\phi_x = 0$ on the downstream boundary and $\phi = 0$ on the other boundaries. Ballhaus and Goorjian (12) used these boundary conditions in their study and obtained satisfactory results. The validity of such far-field boundary conditions can only be justified by numerical experiments; i.e., near the boundary the disturbance quantities ϕ_x, and ϕ_y, must be much smaller than the values at the airfoil surfaces. For the lifting case, ϕ depends on the instantaneous circulation, Γ. This dependence can be derived theoretically by assuming that in the far field all the perturbations are small compared to the basic steady state (see, e.g., Reference 27). Here we use a stretched coordinate system that maps the doubly infinite domain into $|\xi| \le 1$, $|\eta| \le 1$, and set $\phi_x = 0$ on the downstream boundary $\xi = 1$ and $\phi = 0$ elsewhere on the boundary of this domain. As a numerical test for this procedure we have computed the steady state circulation about an NACA 64A006 airfoil for various flap deflection angles, using the ADI method with appropriate far-field values of ϕ, corrected for the usual steady state circulation contribution. These results have been compared with the results obtained by the ADI calculations with the boundary conditions employed here for an unsteady flap deflection to the correct angle. These results are identical within the accuracy with which we have computed the solutions.

Any shock wave that exists in the flow field must satisfy the jump relation derived from the conservative form of the governing equation (1), namely

$$-2KM_\infty^2[\![\phi_x]\!]^2\left(\frac{dx}{dt}\right)_s - \{1 - M_\infty^2 - (\gamma + 1)M_\infty^2\tilde{\phi}_x\}[\![\phi_x]\!]^2 + [\![\phi_y]\!]^2 = 0 \tag{3}$$

together with the condition derived from the assumption of irrotationality,

$$\left(\frac{dy}{dx}\right)_s = -[\![\phi_x]\!]/[\![\phi_y]\!]. \tag{4}$$

Here $\tilde{\phi}_x$ refers to the mean value of ϕ_x evaluated on each side of the discontinuity, and $[\![\phi_x]\!]$ indicates the jump in ϕ_x across the discontinuity; the subscript "s" denotes the quantity evaluated at the shock surface.

The pressure coefficient, defined so that it vanishes at sonic conditions, takes the form

$$C_p = -2 \left\{ \frac{M_\infty^2 - 1}{(\gamma + 1)M_\infty^2} + \phi_x \right\} . \tag{5}$$

In the small disturbance approximation, the Kutta condition is imposed by requiring that C_p be continuous at $y = 0$ for $x > 1/2$.

2.1 Time-Linearized Equations

We now assume that the unsteady disturbances, characterized by δ, are small enough that we may write

$$\phi(x,y,t) = \phi^\circ(x,y) + \delta\psi(x,y,t) + o(\delta) \tag{6}$$

and neglect higher-order terms in δ. The restriction imposed on δ for this to be true will depend on the other parameters of the problem, viz., $\kappa \equiv (1 - M_\infty^2)/[(\gamma + 1)M_\infty^2\tau]^{2/3}$ and K. This gives

$$\{1 - M_\infty^2 - (\gamma + 1)M_\infty^2\phi_x^\circ\}\phi_{xx}^\circ + \phi_{yy}^\circ = 0, \quad \phi_y^\circ(x,0) = \tau Y^{\circ\prime}(x), \quad -\frac{1}{2} \leq x \leq \frac{1}{2} ; \tag{7}$$

$$-2KM_\infty^2\psi_{xt} + \{[1 - M_\infty^2 - (\gamma + 1)M_\infty^2\phi_x^\circ]\psi_x\}_x + \psi_{yy} = 0, \quad \psi_y(x,0,t) = Y_x^u + KY_t^u, \quad -\frac{1}{2} \leq x \leq \frac{1}{2} . \tag{8}$$

The solution to (7) must satisfy the steady version of the shock relations (4) and (5). The shock relations for (8) are discussed in Section 2.2.

We avoid writing

$$\psi(x,y,t) = \mathrm{Re}\{\bar{\psi}(x,y)e^{i\omega t}\} \tag{9}$$

as this restricts the study to harmonic motions. Because indicial motions can be superimposed to obtain the results for any frequency, they seem more important. Equation (9) results in an equation for a complex-valued $\bar{\psi}$ which may be solved by line relaxation. Our experience with unsteady ADI techniques has been that they are at least as effective as line relaxation for problems of this type, and hence there is no advantage to the decomposition (9).

The numerical algorithm developed in Reference 21 and described briefly in Section 3 can be used to solve the basic equation (1) subject to the boundary conditions (2), the shock conditions, (3) and (4), the far-field boundary conditions and the Kutta condition. Steady state solutions, $\phi^\circ(x,y)$, may be obtained rapidly by subjecting a basic steady state, such as undisturbed flow, to rapidly changing boundary data until a new steady configuration is prescribed. This, then, determines the steady state result for (7) needed to solve (8).

2.2 Shock Fitting

The basic algorithm for shock fitting in mixed flows was developed in a previous study of steady transonic flows (20). A different approach to shock fitting has also been used by Hafez and Cheng (29) in their study of steady transonic flow problems. Their procedure essentially replaced the shock-point operator of Murman (30) by an analogous difference statement derived from the shock jump conditions. Subsequently, the velocity potential on each side of the shock wave is extrapolated to locate the shock wave.

To understand the shock-fitting procedure for unsteady transonic flow calculations it is necessary to recall how shock waves form in an unsteady field. Shock waves are generated when the local flow becomes supersonic and compressive. While the initial shock formation may not be predicted exactly by the numerical solution when shock fitting is used in the early stages of shock wave formation, it eliminates spurious oscillations in the numerical solution and does provide the correct development of the shock wave in later stages of the calculations (31). The criteria that we set for the initial shock formation is that the local flow become sonic (relative to the airfoil) and compressive. In the body-fixed coordinate system, a shock wave can exist both in the usual supersonic-supersonic and supersonic-subsonic transitions, but also in a purely subsonic flow field, sometimes referred to as a "subsonic-subsonic" shock. In any case, the flow ahead of the shock relative to a coordinate system fixed on the shock must be always supersonic. Consequently, the correct judgment for the existence of a shock wave in the unsteady field is to evaluate the local flow velocity ahead of a prospective shock with respect to the coordinate system fixed on it; i.e., if the local flow is supersonic a shock may exist, if the local flow becomes sonic the shock strength diminishes, and if it is subsonic a shock cannot exist.

Any shock wave that exists in the flow field must satisfy the jump relations (3) and (4). In two-dimensional small perturbation transonic flows the shock waves that usually occur are nearly normal to the flow direction. While it is not necessary to do so, in the numerical calculations reported here we have assumed that if the basic steady flow has a shock wave, then this shock may be approximated by a shock wave normal to the free stream flow. To be consistent with this approximation we must also assume that the motion of any shock wave that arises from unsteady changes in the flow, as well as the motion of existing shock waves, is also calculated by this normal shock approximation. For this simplified model, (3) and (4) reduce to

$$\llbracket\phi\rrbracket = 0 \quad \text{on} \quad \dot{x}_s \equiv \left(\frac{dx}{dt}\right)_s = \frac{\gamma + 1}{2K}\left\{\frac{M_\infty^2 - 1}{(\gamma + 1)M_\infty^2} + \tilde{\phi}_x\right\}, \tag{10}$$

which gives the speed of the normal shock in the flow field. For steady flows $\tilde{\phi}_x$ is a function of x alone; this, of course, still permits $\llbracket\phi_x\rrbracket$ to vary with y. For unsteady flows, while $\dot{x}_s$ is a function of t alone, the strength of the shock will still vary with y.

For time-linearized flows the steady state result for ϕ_x° with normal shock fitting will give a steady state shock position x_s°, $0 \leq |y| \leq y_\pm^*$. We now determine the shock wave's motion by writing the perturbed shock position as $x_s = x_s^\circ + \delta\chi(\bar{t})$ and using the time-linearized version of (10); we note that an expression of the form $x_s^\circ + \delta\chi(t)/K$ would probably be more appropriate. From (10), we conclude that the shock motion is governed by

$$\frac{d\chi}{dt} = \frac{\gamma + 1}{2K}\tilde{\psi}_x(x,0,t) \quad \text{with} \quad \llbracket\phi\rrbracket = \llbracket\phi^\circ\rrbracket + \delta\llbracket\psi\rrbracket = 0 \tag{11}$$

on the shock. Linearizing the expression in (11) for the velocity potential about the steady shock position we find

$$\phi(x_s,y,t) = \phi(x_s^\circ,y,t) + \phi_x(x_s^\circ,y,t)\delta d\chi$$

$$= \phi^\circ(x_s^\circ,y) + \phi_x^\circ(x_s^\circ,y)\delta d\chi + \delta\psi(x_s^\circ,y,t) + O(\delta^2).$$

Because we have treated the shock as a normal one, y appears here simply as a parameter. Now $\llbracket\phi(x_s,y,t)\rrbracket$ and $\llbracket\phi^\circ(x_s^\circ,y)\rrbracket$ are both zero; consequently we have

$$\llbracket\psi(x_s^\circ,y,t)\rrbracket = -\frac{(\gamma + 1)}{2K}\llbracket\phi_x^\circ(x_s^\circ,y)\rrbracket\int_0^t \tilde{\psi}_x(x_s^\circ,0,\hat{t})d\hat{t} \tag{12}$$

which must be integrated in time in conjunction with the solution to (8).

3. NUMERICAL PROCEDURES

In a preliminary study of the unsteady transonic flows a normal shock-fitting procedure was implemented in an implicit-iterative scheme. Satisfactory results were obtained, but the procedure was time-consuming because of the iterative process required at each time step. The recent studies of Ballhaus and Steger (11) and Ballhaus and Goorjian (22) show that an ADI scheme is more efficient that the implicit-iterative scheme in treating the low frequency transonic flows. The shock-fitting algorithm was modified and implemented with an ADI scheme. In this section the ADI procedure and the method used for unsteady shock fitting are briefly reviewed.

3.1 Coordinate Stretching

To minimize the far-field boundary effects on the numerical results a relatively large computational region is usually required. For some of the cases studied in this paper the shock excursions are large and the unsteady disturbances carried several chord lengths away from the airfoil; thus, the use of a relatively large computational domain seems desirable. A simple and straightforward way of computing the solution in a large computational domain is to use nonuniform mesh distributions with most of the mesh points concentrated in the region of interest. An alternative is to introduce analytical coordinate stretchings. In the present study, we use the following coordinate stretchings:

$$\xi = \pm\{1 - \exp(\mp a_1 x)\} \quad \text{for} \quad x \gtrless 0 \quad \text{and} \quad \eta = \pm\{1 - \exp(\mp a_2 y)\} \quad \text{for} \quad y \gtrless 0,$$

where a_1 and a_2 are constants that control the mesh distributions. The infinite physical domain is transformed into the finite computational domain bounded by $|\xi| \leq 1$, and $|\eta| \leq 1$. The transformation provides a concentrated mesh distribution near the airfoil which is suitable for the present study. While this scaling is not consistent with the known algebraic decay of the perturbations, calculations made with an algebraic scaling, viz., $\xi = x/(|x| + a_1)$ etc., gave essentially identical results. The exponential variation used here seems more desirable near the airfoil.

The governing equation (1), written in the stretched coordinate system, is

$$\left\{\frac{-2KM_\infty^2}{a_2^2(1 - |\eta|)}\phi_\xi\right\}_t - \left\{\frac{(\gamma + 1)M_\infty^2}{2a_2^2(1 - |\eta|)}\left[\frac{M_\infty^2 - 1}{(\gamma + 1)M_\infty^2} + a_1(1 - |\xi|)\phi_\xi\right]^2\right\}_\xi + \left\{\frac{1 - |\eta|}{a_1(1 - |\xi|)}\phi_\eta\right\}_\eta = 0. \tag{13}$$

Because (13) is in divergence-free form, a conservative difference approximation can be constructed if the shock wave is to be "captured" rather than "fitted."

The normal shock jump relation follows directly from (13); this relation and the boundary condition on the airfoil surface are now

$$\left(\frac{d\xi}{dt}\right)_s = \frac{a_1(1-|\xi|)(\gamma+1)}{2K}\left\{\frac{M_\infty^2-1}{(\gamma+1)M_\infty^2} + a_1(1-|\xi|)\bar{\phi}_\xi\right\} \tag{14}$$

and

$$\phi_\eta(0,\xi) = \frac{a_1}{a_2}(1-|\xi|)\frac{\partial Y(\xi,t)}{\partial \xi} + \frac{K}{a_2}\frac{\partial Y(\xi,t)}{\partial t}, \quad -1+\exp(a_1/2) \leq \xi \leq 1-\exp(-a_1/2).$$

Equations analogous to (13) and (14) for the time-linearized results are given in Reference 10.

3.2 Alternating-Direction Implicit (ADI) Method

The low frequency equation in the stretched coordinate system is solved by the alternating-direction implicit scheme developed by Ballhaus and Steger (11). To simplify this discussion, equation (13) is rewritten in the form

$$\Psi_{\xi t} + F_\xi + G_\eta = 0, \tag{15}$$

where the function Ψ, F and G may be determined by comparing equations (13) and (15). The solution is advanced from time level "n" to level "n+1" by the following two-step procedure:

$$\frac{1}{\Delta t}(\Psi_\xi^+ - \Psi_\xi^n) + D_\xi F^+ + \delta_\eta G^n = 0; \quad \frac{1}{\Delta t}(\Psi_\xi^{n+1} - \Psi_\xi^+) + \frac{1}{2}\delta_\eta(G^{n+1} - G^n) = 0. \tag{16}$$

Here "+" refers to an intermediate value of Ψ, D_ξ is the type-dependent difference operator for ξ-derivatives and δ_η the central-difference approximation for η-derivative. The backward difference approximation for Ψ_ξ^n can be either a first-order or a second-order difference approximation, with the latter giving improved results. The nonlinear term F is evaluated, using a linearization somewhat different from the two-time level averaging procedure of Ballhaus and Steger. The difference approximations described above provide first- or second-order accuracy for $\Psi_{\xi t}$, second-order accuracy for F_ξ and G_η in subsonic regions, and first-order accuracy for F_ξ in supersonic regions. A local analysis shows that the procedure is unconditionally stable.

In the first step a quadradiagonal system is generated and can be easily solved by direct elimination. For lifting calculations two grid lines are used to represent the lower and upper surfaces of the airfoil. The circulation, Γ, is calculated by $\Gamma = \phi_{ITE}^U - \phi_{ITE}^L$ through each sweep. Here "ITE" denotes the upper and lower values at the first grid point behind the trailing edge. This circulation is incorporated into the construction of the η-derivatives behind the airfoil for $\eta = 0$.

In the second step a tridiagonal system is generated by the body. Ahead of the leading edge and behind the trailing edge the double grid notation for $\eta = 0$ destroys the tridiagonal system. However, ahead of the leading edge, $\phi^U = \phi^L$, and behind the trailing edge, $\phi^U = \phi^L + \Gamma$; thus the difference equations can be reordered to give a tridiagonal system. On the airfoil surface, the matrix equations above and below the airfoil are decoupled; they can either be solved separately or simultaneously by packing the matrix equations together.

Again, analogous but somewhat simpler equations and procedures are used for the time-linearized calculations. In these calculations the type dependent operator, D_ξ, changes at the steady state sonic line and shock wave. The coefficient, $f(\xi,\eta)$, that appears in (8) in the form $\{f(\xi,\eta)\psi_\xi\}_\xi$ depends on the steady state results $\phi^\circ(\xi,\eta)$ and must be stored. On the other hand, the matrices used do not depend on the solution ψ and, consequently, need only be inverted once. In its present form our algorithm does not take advantage of this feature.

3.3 Shock Fitting

We start the unsteady nonlinear flow calculations by using an ADI scheme. When the local flow becomes sonic and compressive, we introduce the shock-fitting algorithm described in detail in Reference 21. Sonic, compressive points are treated as shock points where differentiation in t and ξ across discontinuities is avoided. Initially, the shock has zero strength and is stationary. The flow properties ahead of and behind the shock can be easily extrapolated from neighboring points. The shock wave can either increase or decrease in strength during the unsteady process. This results in three possibilities for shock motion that have to be considered separately in the fitting procedure: The shock moves upstream and crosses grid points; the shock remains stationary or moves within a grid spacing; the shock moves downstream and crosses grid points. At each new time level the shock position is determined by applying (10). The formulations of the difference approximations for each case are quite similar.

For time-linearized calculations the solution is advanced in time using the time-linearized analogues of (16) coupled with (12) in the form

$$[\![\psi]\!]^+ = -C(\eta)\Delta t\bar{\psi}_\xi^n + [\![\psi]\!]^n; \quad [\![\psi]\!]^{n+1} = -C(\eta)\Delta t\bar{\psi}_\xi^{n+1} + [\![\psi]\!]^+.$$

Here

$C(\eta) = \frac{\gamma+1}{4K}a_1^2(1-|\xi_s^\circ|)^2[\![\phi_\xi^\circ(\xi_s^\circ,\eta)]\!]$, and ξ_s° denotes the steady state position of the shock wave.

This procedure corrects the ψ values for shock motions as the solution progresses. The shock motion is easily determined simultaneously by using (11) and (12) in the form

$$X^{n+1}(0,t) = -[\psi(x_s^*,0,t)]^{n+1}/[\phi_x(x_s^*,0)].$$

Further details are given in Reference 10.

4. RESULTS AND DISCUSSION

Both the nonlinear and time-linearized algorithms have been used to compute the flow past an NACA 64A006 airfoil subjected to indicial, i.e., step, changes and harmonic motions in pitch and flap oscillation. The latter calculations have included a range of Mach numbers, amplitudes for the nonlinear algorithm, and reduced frequencies for the harmonic changes. The nonlinear algorithm has also been used to compute the flow past a pulsating parabolic arc airfoil. In this latter flow, at $M_\infty = 0.85$, as the airfoil thickens a shock wave forms and moves downstream until shortly after mid-cycle. As the airfoil thins, the shock wave moves upstream with increasing speed, eventually leaving the airfoil. A comparison of the results, with and without shock fitting (21), indicates that shock fitting predicts the formation of the shock wave more accurately. It also properly defines the shock wave when it becomes "subsonic-subsonic" in the fixed grid system. The shock wave decays slowly as it propagates into the free stream after passing the location of the leading edge when the airfoil's thickness has just become zero.

4.1 NACA 64A006 Airfoil, Nonlinear Calculations

Steady state solutions were computed as discussed in Section 2.1 for an NACA 64A006 airfoil for various values of the freestream Mach number by using the ADI scheme with shock fitting outlined in Section 3. The free stream Mach number was varied between 0.8 and 0.9. The mesh system had 101 by 82 grid points in the x- and y-directions respectively. About 250 to 450 time steps were required for the solution to converge $|\Delta\phi|_{max} \leq 10^{-4}$. These steady state solutions are used as initial data for the nonlinear and time-linearized unsteady flow calculations

Results were computed for the airfoil with quarter-chord flap for various values of the reduced frequency, the free stream Mach number, and the oscillation amplitude, in order to simulate the shock motions observed by Tijdeman (5, 6). These motions were classified by him as: type A - small shock oscillation; type B - the shock becomes very weak or disappears during part of a cycle; type C - the shock leaves the airfoil. Results for type A motions are not given, as they are easy to treat computationally. For all cases studied it took three to six cycles for the flow field to become periodic. Stability seems to require that the time step be small enough that Δt(in degrees)/$K < 10$.

Figure 1 illustrates the pressure coefficients on the airfoil surface at various times for $M_\infty = 0.854$, $K = 0.358$ and $\delta = 1°$. For these conditions Ballhaus and Goorjian (12) were able to simulate type B motion where the shock disappears during some part of the cycle. Here the shock does not disappear during the cycle; rather, it becomes quite weak during a small portion of the cycle. This difference is probably due in part to the assumption of a normal shock, which results in a stronger shock than would normally occur, and to the use of shock fitting, which is able to resolve very weak shock waves.

Figure 2 depicts the pressure coefficient on the airfoil surfaces for $M_\infty = 0.822$, $K = 0.496$ and $\delta = 2°$, simulating type C shock motion. Because we have used less spatial resolution and have not scaled the equation and boundary conditions with various powers of the Mach number, a slightly larger deflection angle seems to be needed in order to generate the type C shock motion; that is, we need a 2° deflection angle rather than the 1.5° of Reference 12 to obtain analogous behavior. In this case the flow field is subcritical during most of the cycle, where the shock wave is barely "captured" in the non-shock-fitting procedure. During the unsteady process the shock moves toward the leading edge. However, the strong singular behavior in pressure at the leading edge prevents the shock from propagating off the airfoil. The perturbation velocity becomes large and is negative; thus, the flow used to calculate the relative velocity ahead of the shock can no longer support a shock wave. Normal shock-fitting calculations determine the shock speed from the pressure jump across the shock at the airfoil surface. This eliminates the possibility that a portion of the shock may propagate off the leading edge in the computations. But this does not imply it cannot occur; rather this is a limitation of the normal shock fitting.

Magnus and Yoshihara (15) have solved the Euler equations using an explicit procedure for the conditions of Figure 1. Their results are compared with our calculation in Figure 3 for two angular times chosen to represent the least and the largest discrepancies. These discrepancies are thought to be mainly due to the inaccuracy of the small perturbation solution near the leading edge. Small errors there change the size and shape of the sonic line and influence the shock's position. For the conditions considered, the shock is nearly normal and the normal shock approximation should be a good one. Rather good agreement is obtained.

Additional nonlinear calculations have been carried out for $M_\infty = 0.880$ and $K = 0.48$. Both pitching and flap motions have been calculated for indicial and harmonic changes. For these conditions very small unsteady changes lead to very small shock motions and the shock wave remains between grid points. Because of the extrapolation procedure used in the shock-fitting, the ξ mesh distribution used here can introduce errors, albeit small ones, in the shock's position when a grid line is crossed. We wished to eliminate these errors in order to use the nonlinear calculations to judge the accuracy of time-linearized calculations. These results indicate that for pitching about mid-chord, nonlinear, amplitude dependent, behavior occurs for $\delta/\tau \geq 0.1$ for $K = 0.48$. Because the amplitude of the shock motions increases with decreasing K, nonlinear effects occur at smaller values of δ/τ at lower reduced frequencies.

Indicial motions require about eight hundred time steps of varying size to resolve the response. For harmonic motions, initiated from rest, three to ten cycles are required for the solution to become harmonic, with large values of K and M_∞ requiring more cycles. The pitching mode requires more cycles than the flap mode. The amplitude of the positive and negative phases of the motion could be varied from cycle to cycle to reduce the number of cycles required. Each cycle requires 60 to 180 time steps to compute, with more steps required for smaller values of K. Each time step takes about 5 seconds of CPU time on a CDC 6400, or about 0.25 seconds of CPU time on a CDC 7600.

4.2 NACA 64A006 Airfoil, Time-Linearized Calculations

Time-linearized results have been computed for an NACA 64A006 airfoil experiencing harmonic and indicial pitching and flap motions. As noted earlier, in the low frequency approximation made here pitching and plunging motions lead to the same result except that the time-linearized perturbations are proportional to the maximum pitch angle for the former, and K times the maximum amplitude for the latter. Harmonic motions initiated from a steady state become nearly periodic in three to ten cycles, with the changes induced by flap oscillations becoming periodic more rapidly than those resulting from pitching oscillations. More cycles were required for larger reduced frequencies and, to a lesser degree, higher Mach numbers.

In order to confirm the validity of the time-linearized calculations, both the time-linearized and nonlinear algorithms were used to compute the response to a step change in angle of attack and the harmonic response to pitching motions. Figure 4 compares the nonlinear and time-linearized results for the normalized circulation and shock position for harmonic pitching motions at $M_\infty = 0.88$ and $K = 0.48$. Results are given for the fifth cycle; note that the nonlinear results are not yet periodic. Figure 5 compares the nonlinear and time-linearized pressure deviation from steady state at six angular times for the same conditions. Good agreement between the results is obtained for δ/τ less than 0.1.

Time-linearized pressure distributions at six angular positions for an oscillating quarter-chord flap with $K = 0.06$ and $M_\infty = 0.875$ are shown in Figure 6. The flap deflection is downward during the first half of the cycle. The results for the second half of the period, for the symmetrical problem shown here, are just the results shown with the lower and upper surface pressures interchanged. Thus the results for 0° are not given as they are just those for 180° with the lower and upper surface pressures reversed. Because the flap hinge occurs very close to the steady state shock location, the pressure singularity due to the change in flow direction at the hinge is missed. The circulation and shock excursion obey the following relations:

$$\Gamma(t)/\delta = 9.26 \sin (t - 59°),$$

$$\chi(t) = 12 \sin (t - 51°).$$

Note the substantial phase lag in the circulation and the shock's position.

Time-linearized pressure distributions at six angular positions for an oscillating airfoil with $K = 0.12$ and $M_\infty = 0.875$ are depicted in Figure 7. If these results are multiplied by K, then they represent the pressure perturbations for a plunging airfoil. As in the previous case of an oscillating flap, changes in forces and moments of $O(\delta/K)$ occur due to shock wave motion. In this case

$$\Gamma(t)/\delta = 5.48 \sin (t - 70°),$$

$$\chi(t) = 5.62 \sin (t - 87°).$$

Analogous computations have been carried out for [illegible] = 0.12, 0.24, 0.36, and 0.48. Figure 8 depicts the shock wave's excursion and maximum circulation as a function of K^{-1}. The nearly linear variation of the shock excursion substantiates an observation made in a one-dimensional model where the shock wave excursion is directly proportional to $1/K$ (see Reference 10).

In these calculations the circulation gives an immediate evaluation of the lift coefficient as a function of time; the moment coefficient must be evaluated by integrating the moment of the pressure coefficient. This is done by integrating the moment of pressure perturbations with the shock wave in its steady-state position and then correcting these results for the moment due to the shock wave motion, assuming that the shock's strength is defined by the steady-state pressure field. This makes an error in the shock strength of $O(\delta)$, but the effect on the moment is $O(\delta^2/K)$; because we have neglected other higher-order terms it is consistent to neglect this change in the strength of the shock wave.

Figure 9 depicts the absolute value and phase angle of the normalized lift and moment coefficients, as a function of the inverse reduced frequency K^{-1}, for harmonic flap and pitching motions at $M_\infty = 0.875$.

The time-linearized algorithm used here is a derivative of that used for the nonlinear calculations. Consequently, computational times are not greatly reduced from those required for the nonlinear calculations. The linearity of these computations may make it possible to greatly reduce the computational effort required. A local stability analysis shows that the computations should be unconditionally stable, but numerical experience has shown some difficulties for Δt(in degrees)$/K \geq 50$. Each time step requires about two seconds of CPU time on a CDC 6400, or about 0.1 seconds on a CDC 7600. The number of time steps required for a given computation is somewhat less than those required for the nonlinear computations at small values of K, and comparable at larger values of K.

5. CONCLUSION

Efficient and accurate methods for computing low frequency, unsteady behavior in transonic flows have been developed. They utilize the ADI procedure developed at NASA Ames for the small perturbation equation, but treat shock waves as discontinuities. The time-linearized calculations allow shock wave motions, which are shown to be $O(\delta/K)$ and often dominate changes in the force and moment coefficients. Comparison of the time-linearized results with fully nonlinear calculations delineates their range of applicability. The unsteady behavior due to harmonic pitching and flap oscillations of an NACA 64A006 airfoil is discussed.

ACKNOWLEDGMENT

This research was sponsored by the AFOSR through Grant 76-2954B, the NASA through Grant 2112, and the ONR through Contract N0014-76-C-0182.

REFERENCES

1. Ballhaus, W. F.: Some Recent Progress in Transonic Flow Computations. VKI Lecture Series on Computational Fluid Dynamics, von Karman Institute for Fluid Dynamics, Rhode-St-Genese, Belgium, 1976.
2. Landahl, M. T.: Unsteady Transonic Flow. Pergamon Press, New York, 1961, 111-113.
3. MacCormack, R. W.: An Efficient Numerical Method for Solving the Time-Dependent Navier-Stokes Equations at High Reynolds Number. NASA TM X-73129, 1976.
4. Levy, L. L., Jr.: An Experimental and Computational Investigation of the Steady and Unsteady Transonic Flow Field About an Airfoil in a Solid-Wall Test Channel. AIAA Paper No. 77-678, 1977.
5. Tijdeman, H.: On the Motion of Shock Waves on an Airfoil with Oscillation Flap in Two-Dimensional Transonic Flow. NLR TR 75038U, 1975.
6. Tijdeman, H.: On the Motion of Shock Waves on an Airfoil with Oscillating Flap. Ed. K. Oswatitsch and D. Rues, IUTAM Symposium Transsonicum II, Göttingen, 1975, 49-56.
7. Tijdeman, H., Schippers, P., and Persoon, A. J.: Unsteady Air Loads on an Oscillating Supercritical Airfoil. NLR MP 77008 U, 1977.
8. Traci, R. M., Albano, E., and Farr, J. L.: Perturbation Method for Transonic Flows about Oscillating Airfoils. AIAA J., Vol. 14, No. 9, 1976, 1258-1265.
9. Weatherill, W. H., Ehlers, R. E., and Sebastian, J. D.: Computation of the Transonic Perturbation Flow Fields Around Two- and Three-Dimensional Oscillating Wings. NASA CR-2599, 1975.
10. Fung, K-Y., Yu, N. J., and Seebass, A. R.: Small Unsteady Perturbations in Transonic Flows. Informal report, submitted for publication 1977.
11. Ballhaus, W. F. and Steger, J. L.: Implicit Approximate-Factorization Schemes for the Low-Frequency Transonic Equation. NASA TM X-73082, 1975.
12. Ballhaus, W. F. and Goorjian, P. M.: Implicit Finite Difference Computations of Unsteady Transonic Flows about Airfoils, Including the Treatment of Irregular Shock Wave Motions. AIAA Paper 77-20, 1977.
13. Ballhaus, W. F. and Lomax, H.: The Numerical Simulation of Low Frequency Unsteady Transonic Flow Fields. Lecture Notes in Physics, Springer-Verlag, Vol. 35, 1975, 57-63.
14. Magnus, R. and Yoshihara, H.: Unsteady Transonic Flows Over an Airfoil. AIAA J., Vol. 13, No. 12, 1975, 1622-1628.
15. Magnus, R. and Yoshihara, H.: The Transonic Oscillating Flap. AIAA Paper No. 76-327, 1976.
16. Magnus, R. J.: Computational Research on Inviscid, Unsteady, Transonic Flow over Airfoils. ONR Report CASD/LVP 77-010, 1977.
17. Caradonna, F. X. and Isom, M. P.: Numerical Calculation of Unsteady Transonic Potential Flow Over Helicopter Rotor Blades. AIAA J., Vol. 14, No. 4, 1976, 482-488.
18. Beam, R. M. and Warming, R. F.: An Implicit Finite-Difference Algorithm for Hyperbolic Systems in Conservation-Law Form. Journal of Computational Physics, Vol. 22, No. 1, 1976, 87-110.
19. Ballhaus, W. F., Jameson, A., and Albert, J.: Implicit Approximate Factorization Schemes for the Efficient Solution of Steady Transonic Flow Problems. AIAA 3rd Computational Fluid Dynamics Conference, June, 1977, 27-34.
20. Yu, N. J. and Seebass, A. R.: Inviscid Transonic Flow Computations with Shock Fitting. Ed. K. Oswatitsch and D. Rues, IUTAM Symposium Transsonicum II, Göttingen, 1975, 449-456.
21. Yu, N. J., Seebass, A. R., and Ballhaus, W. F.: An Implicit Shock-Fitting Scheme for Unsteady Transonic Flow Computations. AIAA 3rd Computational Fluid Dynamics Conference, June, 1977, 13-26.
22. Ballhaus, W. F. and Goorjian, P. M.: Computation of Unsteady Transonic Flows by the Indicial Method. AIAA Paper No. 77-477, 1977.
23. Traci, R. M., Albano, E. D., and Farr, J. L., Jr.: Perturbation Method for Transonic Flow about Oscillating Airfoils. AIAA Paper No. 75-877, 1975.

24. Traci, R. M., Albano, E. D., Farr, J. L., Jr., and Cheng, H. K.: Small Disturbance Transonic Flows about Oscillating-Airfoils. Air Force Flight Dynamics Laboratory, Wright-Patterson Air Force Base, Ohio, AFFDL-TR-75-100, 1974.

25. Weatherill, W. A., Ehlers, F. E., and Sebastian, J. D.: Computation of the Transonic Perturbation Flow Field Around Two- and Three-Dimensional Oscillating Wings. NASA CR-2599, 1975.

26. Ehlers, F. E.: A Finite Difference Method for the Solution of the Transonic Flow About Harmonically Oscillating Wings. NASA CR-2257, 1974.

27. Krupp, J. A. and Cole, J. D.: Studies in Transonic Flow IV, Unsteady Transonic Flow. UCLA Engineering Report 76104, 1976.

28. Lin, C. C., Reissner, E., and Tsien, H. S.: On Two-Dimensional Non-Steady Motion of a Slender Body in a Compressible Fluid. J. Math. and Physics, 27, 1948, 220-231.

29. Hafez, M. M. and Cheng, H. K.: Shock-Fitting Applied to Relaxation Solutions of Transonic Small-Disturbance Equations. AIAA J. Vol. 15, No. 6, 1977, 786-793.

30. Murman, E. M.: Analysis of Embedded Shock Waves Calculated by Relaxation Methods. AIAA J., Vol. 12, No. 5, 1973, 626-633.

31. Moretti, G.: Thoughts and Afterthoughts about Shock Computations. PIBAL Report No. 72-37, 1972.

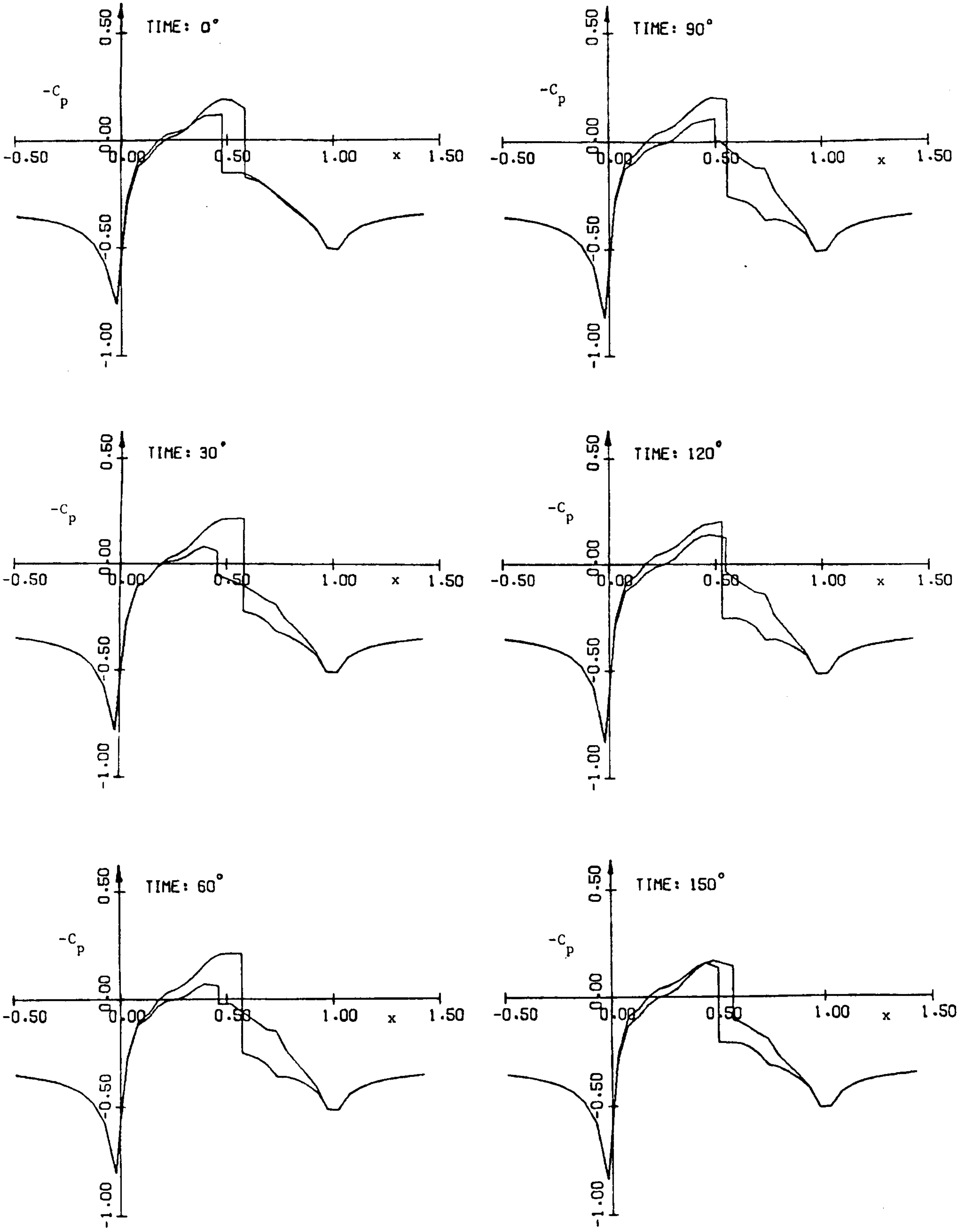

FIGURE 1. C_p ON AN NACA 64A006 AIRFOIL AT $M_\infty = 0.854$, $K = 0.358$ WITH $\delta = 1°$ sin t (NONLINEAR CALCULATIONS).

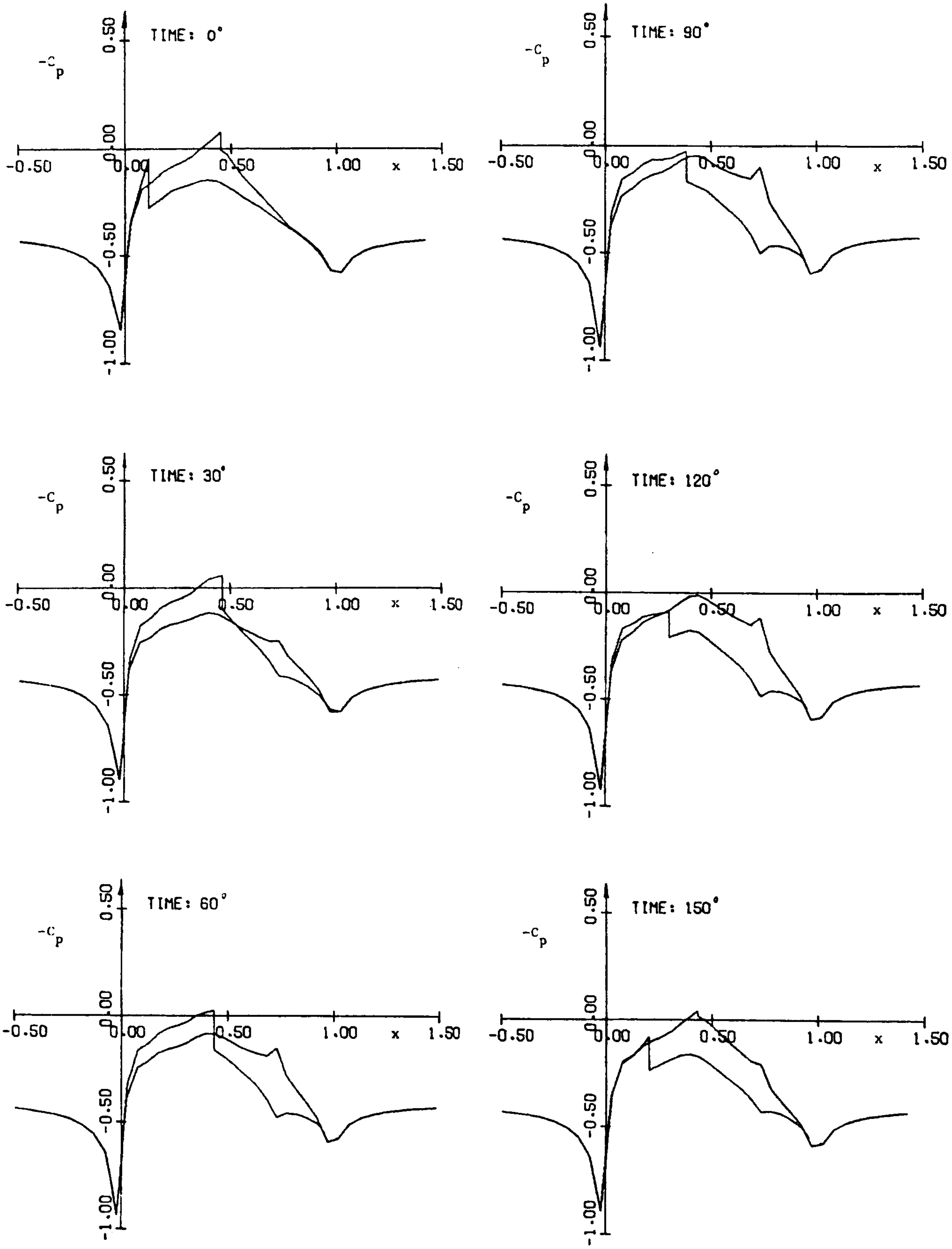

FIGURE 2. C_p ALONG AN NACA 64A006 AIRFOIL AT $M_\infty = 0.822$,
$K = 0.496$ WITH $\delta = 2° \sin t$ (NONLINEAR CALCULATIONS).

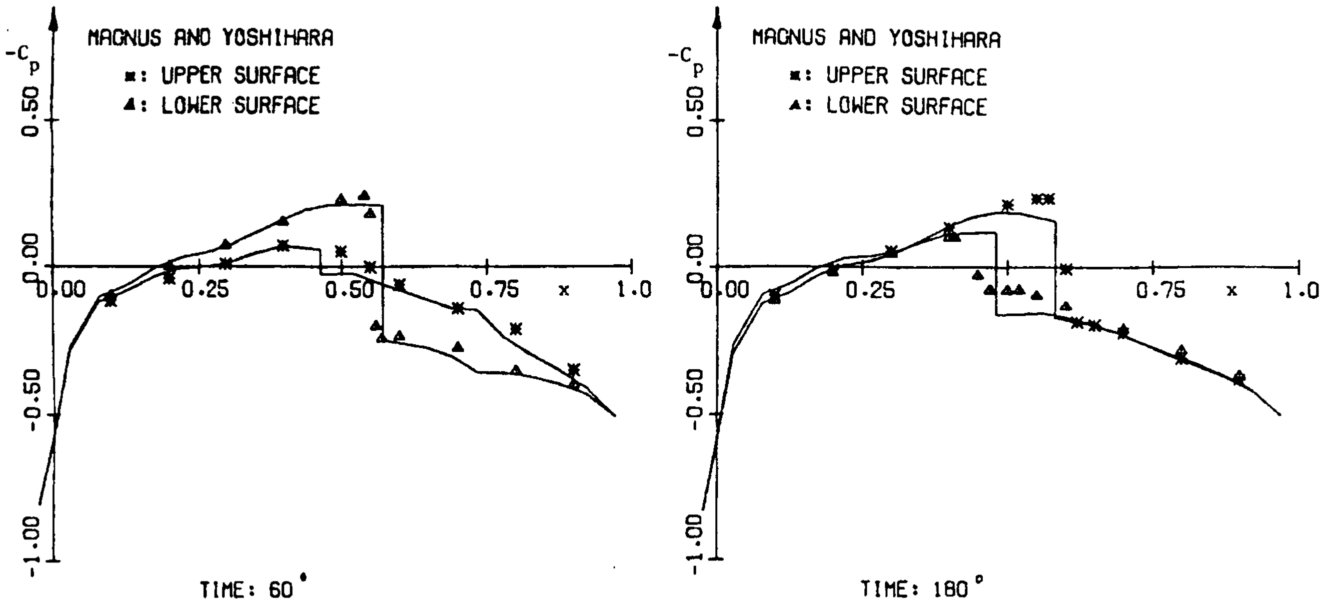

FIGURE 3. COMPARISONS OF THE RESULTS FOR C_p ON AN NACA 64A006 AIRFOIL, AT $M_\infty = 0.854$, $K = 0.358$ WITH $\delta = 1° \sin t$, WITH THOSE OF MAGNUS AND YOSHIHARA (NONLINEAR CALCULATIONS).

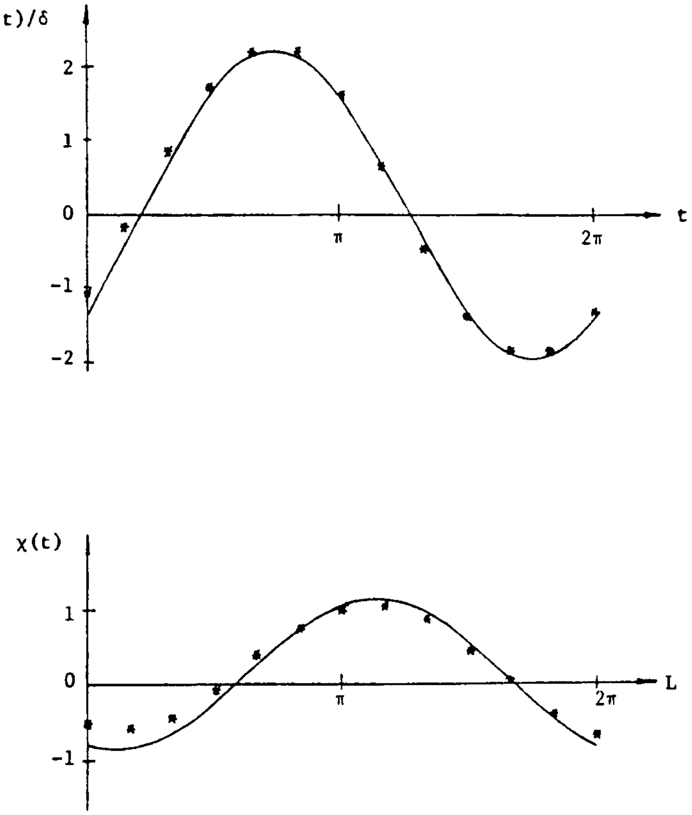

FIGURE 4. NONLINEAR (***) AND TIME-LINEARIZED(———) CIRCULATION AND SHOCK POSITION FOR THE PITCHING MOTION OF AN NACA 64A006 AIRFOIL. RESULTS SHOWN ARE FOR THE FIFTH CYCLE. THE NONLINEAR RESULTS ARE FOR $\delta = 0.1°$ AND ARE NOT YET PERIODIC. $M_\infty = 0.880$, $K = 0.48$.

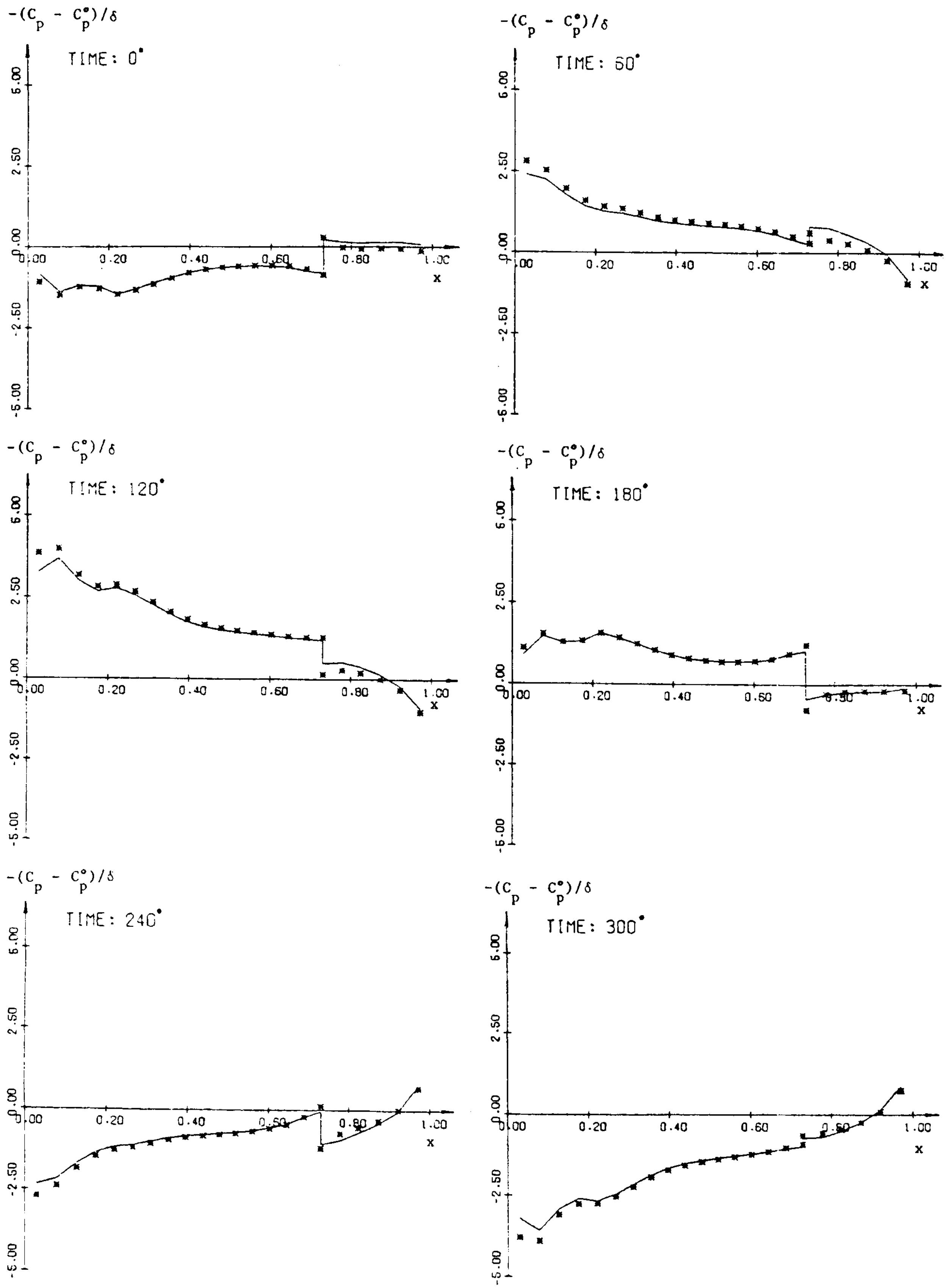

FIGURE 5. NORMALIZED NONLINEAR (****) AND TIME-LINEARIZED (——) PRESSURE PERTURBATIONS ON THE UPPER SURFACE OF AN NACA 64A006 AT SIX TIMES. PITCHING MOTION WITH $M_\infty = 0.880$, $K = 0.48$. FOR THE NONLINEAR CALCULATIONS $\delta = 0.1°$.

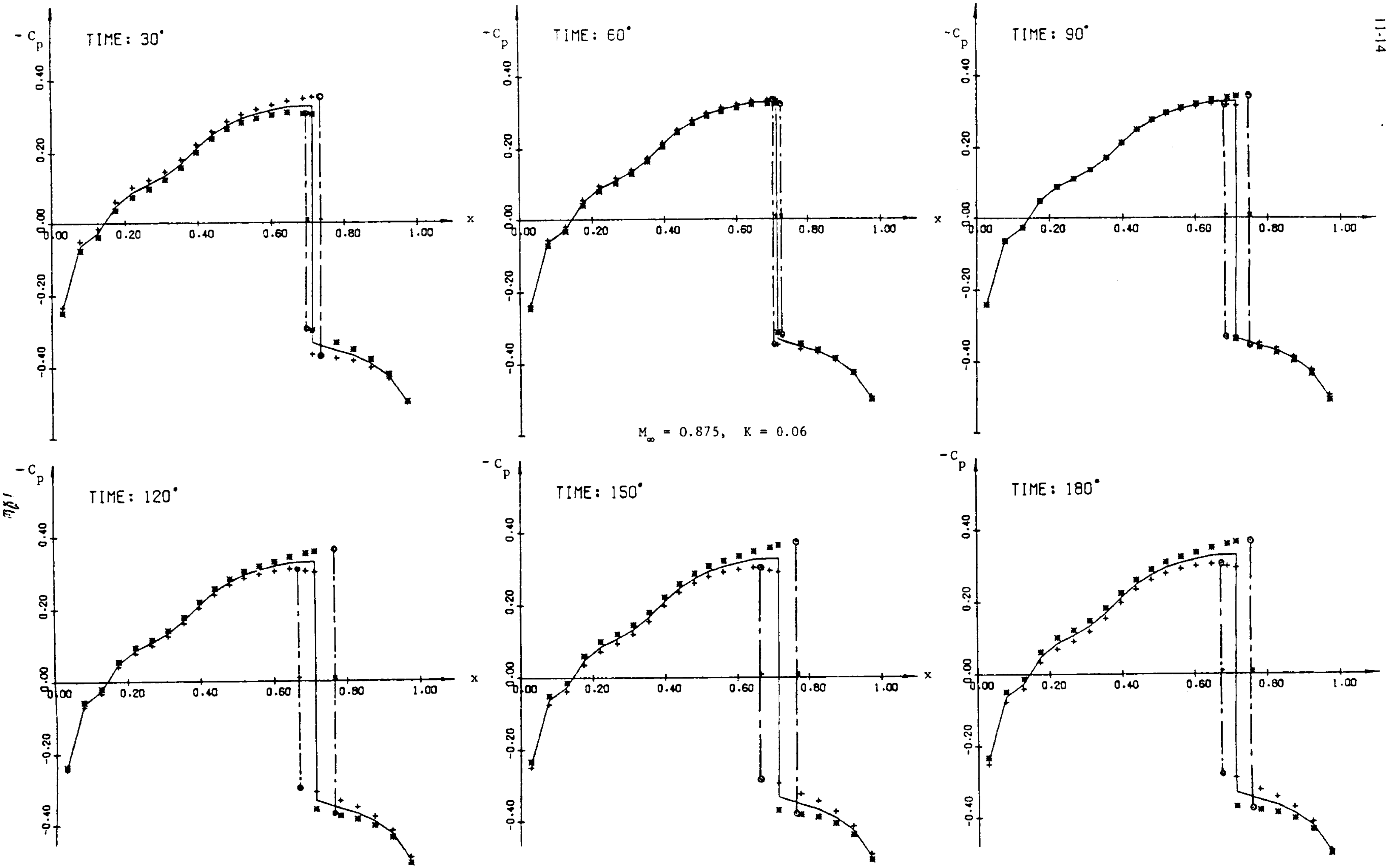

FIGURE 6. TIME-LINEARIZED PRESSURE COEFFICIENTS ON THE UPPER (+) AND LOWER (*) SURFACES OF AN NACA 64A006 AIRFOIL WITH OSCILLATING QUARTER-CHORD FLAP

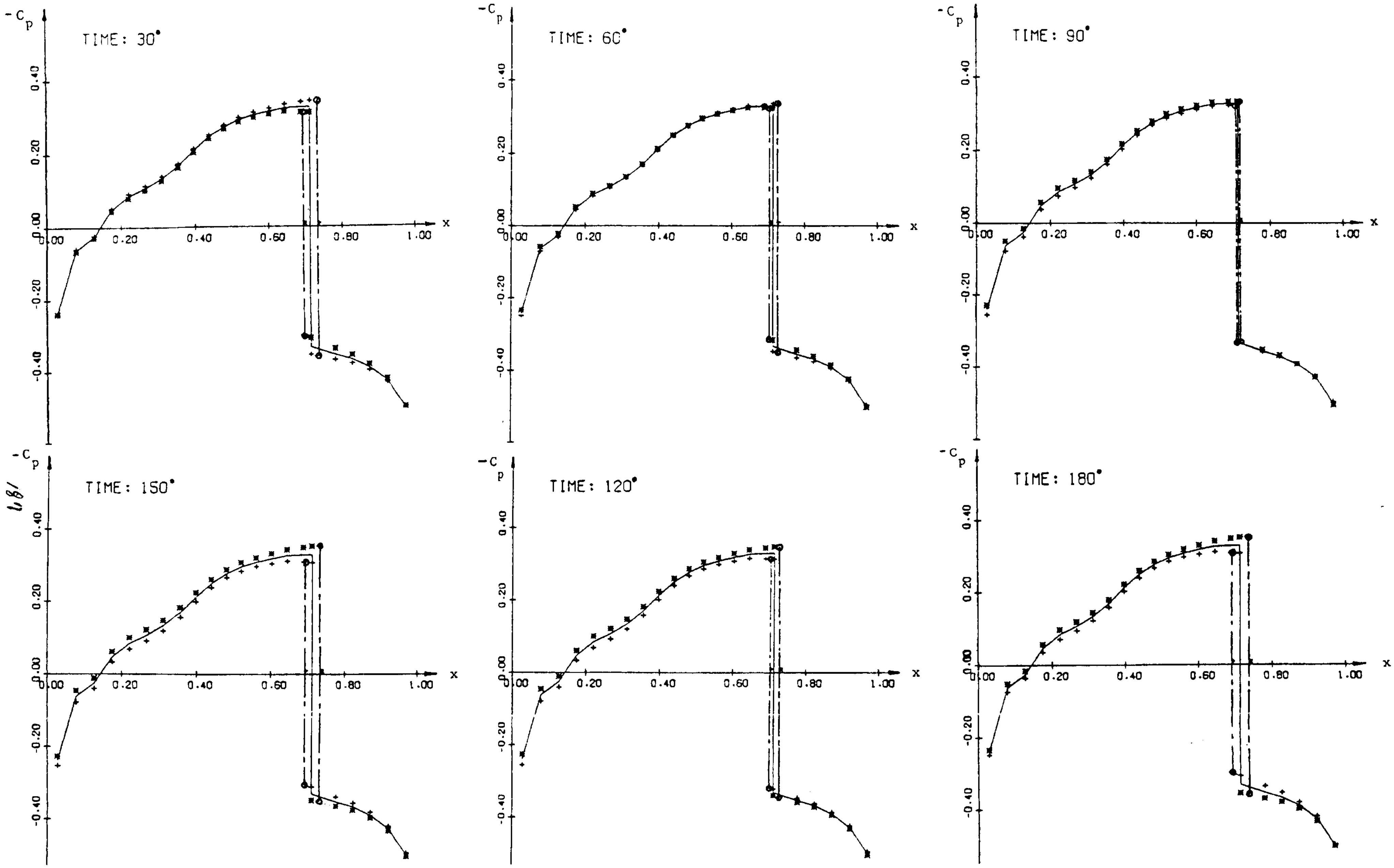

FIGURE 7. TIME-LINEARIZED PRESSURE COEFFICIENTS ON THE UPPER (+) AND LOWER SURFACES OF AN NACA 64A006 AIRFOIL OSCILLATING IN PITCH (δ = 1/4°). M_∞ = 0.875, K = 0.12.

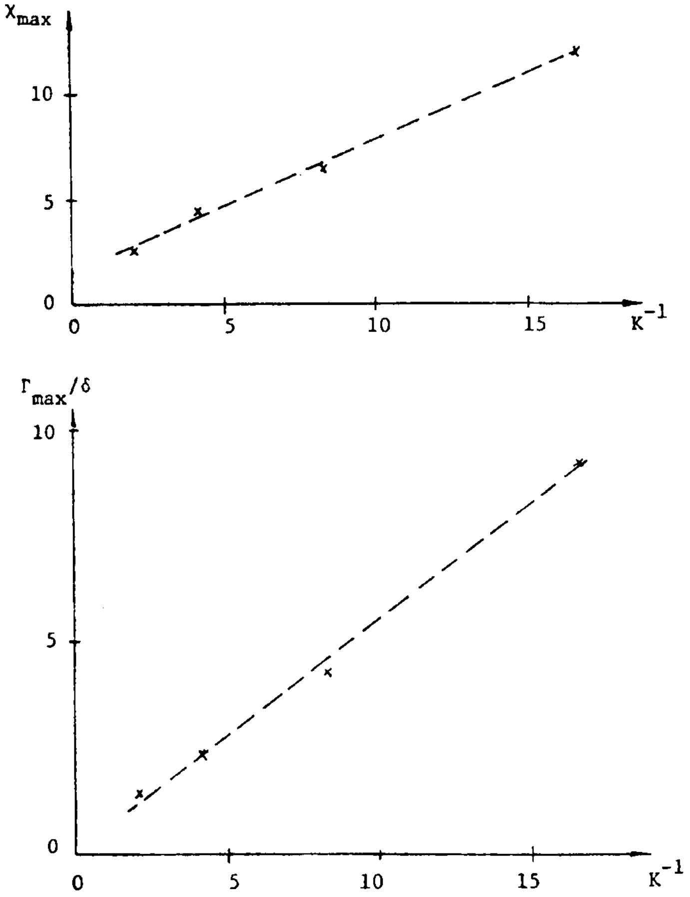

FIGURE 8. NORMALIZED MAXIMUM SHOCK EXCURSION AND CIRCULATION AS A FUNCTION OF INVERSE REDUCED FREQUENCY FOR AN NACA 64A006 AIRFOIL WITH OSCILLATING QUARTER-CHORD FLAP. $M_\infty = 0.875$.

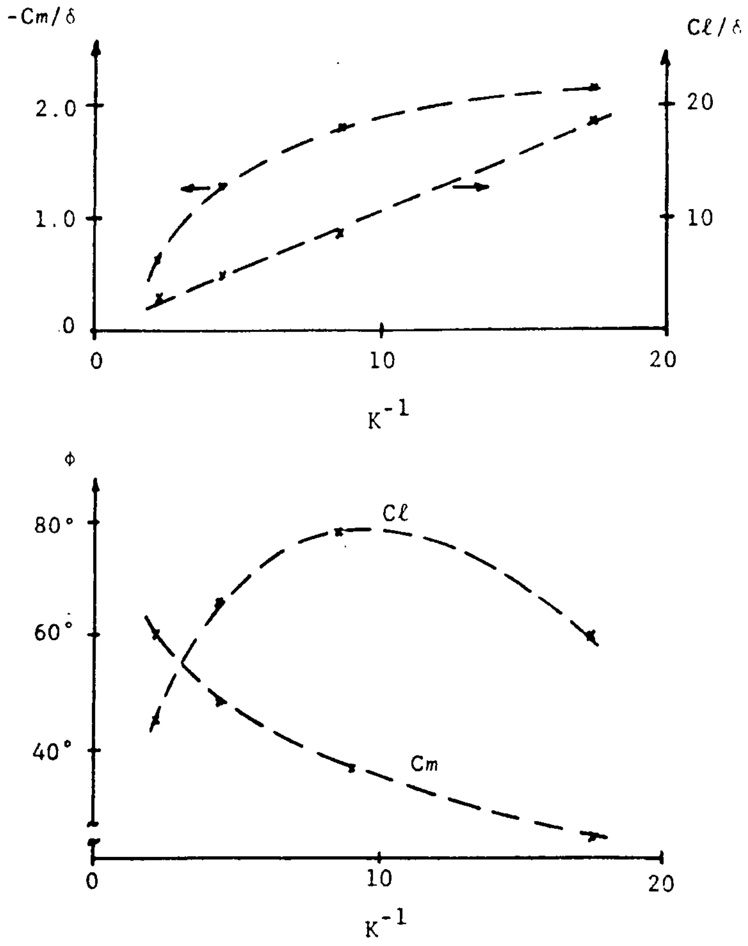

NORMALIZED LIFT AND MID-CHORD MOMENT COEFFICIENT AMPLITUDES AND PHASE LAGS FOR AN NACA 64A006 AIRFOIL WITH HARMONIC FLAP OSCILLATIONS AT $M_\infty = 0.875$.

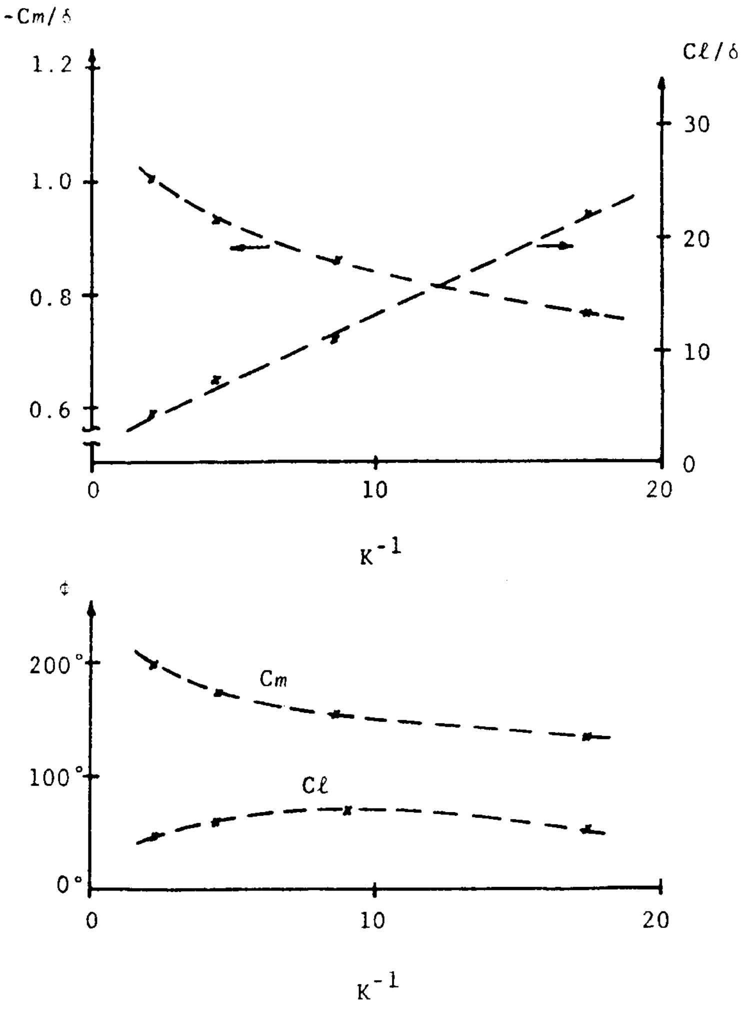

NORMALIZED LIFT AND MID-CHORD MOMENT COEFFICIENT AMPLITUDES AND PHASE LAGS FOR HARMONIC PITCHING MOTIONS OF AN NACA 64A006 AIRFOIL AT $M_\infty = 0.875$.

FIGURE 9.

Reprinted from AIAA JOURNAL, Vol. 16, No. 8, August 1978, pp. 815-822

Small Unsteady Perturbations in Transonic Flows

K-Y. Fung,* N. J. Yu,* and R. Seebass†
University of Arizona, Tucson, Ariz.

The effects of very small, low-frequency perturbations on steady transonic flows, in the context of two-dimensional flows described by the small perturbation equation, are investigated. Previous time-linearized studies failed to account for the shock wave motions that are known to occur. A method is provided that allows one to correctly account for shock wave motions due to arbitrary but small unsteady changes in the boundary conditions. Consequently, both harmonic and indicial responses may be determined. Time-linearized results for the transonic flow past an NACA 64A006 airfoil experiencing harmonic motions in one of several modes are presented. Selected results are compared with those obtained from nonlinear calculations using a shock-fitting algorithm.

Introduction

IN unsteady transonic flow, relatively small periodic changes in the boundary conditions can lead to substantial changes in the magnitude and phase lag of loads and moments. These are of major concern in the aerodynamic design of aircraft that operate in the transonic regime. Reference 1 contains a short but timely review of various aspects of unsteady transonic flow. Of particular concern are aeroelastic behavior and flutter boundaries. Here the unsteady perturbations may be considered small, and linearization about a nonlinear steady flow, as suggested by Landahl[2] long ago, would seem to be appropriate. Indeed, it has been suggested[3] more recently that the steady flow be determined experimentally. Difficulties arise, however, which detract from this procedure. Although the equation is linear, its coefficients are variable and must be determined by numerical solution of a nonlinear problem that, in the cases of prime interest, has a discontinuous solution; that is, there are embedded shock waves. Also, although a change of variables in the linear equation provides a scaling of parameters which is indicative of the tradeoffs between, e.g., Mach number and reduced frequency, the only similitude is the one basic to the nonlinear formulation.

Traci et al.[4] have developed relaxation methods for solving the resulting time-linearized equations of motion. Less complete but comparable studies have been made by Weatherill et al.[5]; these derive from an earlier study by Ehlers.[6] In both of these studies shock motions, which contribute substantially to the time-varying loads and moments,[7,8] are neglected. Also, difficulties arise in the convergence of the iterative numerical scheme.

Here we pursue a different numerical course. Yu et al.[9] have developed a numerical procedure for computing solutions to the unsteady small perturbation equation for transonic flows which treats embedded shock waves as discontinuities. This procedure can be used to calculate the basic steady flow that we wish to subject to small unsteady perturbations. A simplified version of this algorithm then can be used to calculate the linearized unsteady perturbations to the flow. These calculations can be carried out in conjunction with an algorithm that determines the shock wave motion. The procedure that we have used to calculate the shock wave motion is a rather obvious one; it is not surprising, then, that it, too, was given in the monograph by Landahl[2] (Sec. 10.2). An alternative procedure, related in some ways to that used here, is implied by Nixon's[10] study of perturbations to steady discontinuous transonic flows.

Formulation

We write the unsteady small-disturbance equation for low-frequency transonic flows in the commonly used form

$$-2KM_\infty^2\phi_{xt} + \{1 - M_\infty^2 - (\gamma+1)M_\infty^2\phi_x\}\phi_{xx} + \phi_{yy} = 0 \tag{1}$$

The spatial coordinates, the time, and the velocity potential in Eq. (1) have been nondimensionalized by the chord, the reciprocal of the angular frequency, and the freestream velocity times the chord, respectively. Other, perhaps more suitable, forms are given in Ref. 9. This equation results from a systematic expansion of the velocity potential in the thickness ratio τ and applies for reduced frequencies $K = O(\tau^{2/3})$, where $K = \omega c/U$, i.e., the angular frequency multiplied by the time it takes the flow to traverse the airfoil chord. Lin et al.[11] showed that, with restriction to small perturbations throughout the flow, Eq. (1) is the only nonlinear equation that arises. For moderate frequencies, the equation

$$-K^2M_\infty^2\phi_{tt} - 2KM_\infty^2\phi_{xt} + \left\{1 - M_\infty^2 - (\gamma+1)M_\infty^2 \times \left[\phi_x + \frac{\gamma-1}{\gamma+1}K\phi_t\right]\right\}\phi_{xx} + \phi_{yy} = 0$$

frequently is used, with or without the ϕ_t term, and may provide results that apply at higher frequencies than those obtained from Eq. (1) or the linear form of the preceding equation.

Because $K = O(\tau^{2/3})$, the boundary condition on the body takes the simple form

$$\begin{aligned}\phi_y(x,0,t) &= \tau[\partial Y(x,t)/\partial x + K\partial Y(x,t)/\partial t] \\ &= \tau[Y_x^o + (\delta/\tau)(Y_x^u + KY_t^u)], \quad -\tfrac{1}{2} \le x \le \tfrac{1}{2}\end{aligned} \tag{2}$$

where $Y(x,t)$, the instantaneous body shape, has been decomposed into a steady part Y^o and an unsteady part Y^u. The last term, KY_t^u, is dropped except when Y_x^u is small or zero because $K = O(\tau^{2/3})$. Here δ is the amplitude of the unsteady oscillation. Far from the body we require that the derivatives of ϕ vanish. In this approximation the pressure

---

Presented as Paper 77-675 at the AIAA 10th Fluid and Plasmadynamics Conference, Albuquerque, N. Mex., June 27-29, 1977; submitted Nov. 14, 1977; revision received March 15, 1978. Copyright © American Institute of Aeronautics and Astronautics, Inc., 1977. All rights reserved.

Index categories: Transonic Flow; Nonsteady Aerodynamics; Computational Methods.

*Senior Research Associate. Member AIAA.

†Professor. Associate Fellow AIAA.

coefficient, defined so that it vanishes at sonic conditions, takes the form

$$C_p = -2\left\{\frac{M_\infty^2 - 1}{(\gamma+1)M_\infty^2} + \phi_x\right\} \tag{3}$$

In the small-disturbance approximation, the Kutta condition is imposed by requiring that C_p be continuous at $y=0$ for $x>½$.

Any shock wave that exists in the flowfield must satisfy the jump relation derived from the conservative form of the governing equation, Eq. (1), namely,

$$-2KM_\infty^2 [\![\phi_x]\!]^2 \left(\frac{\mathrm{d}x}{\mathrm{d}t}\right)_s - \{1 - M_\infty^2 - (\gamma+1)M_\infty^2\tilde{\phi}_x\} [\![\phi_x]\!]^2 + [\![\phi_y]\!]^2 = 0 \tag{4}$$

together with the condition derived from the assumption of irrotationality,

$$\left(\frac{\mathrm{d}y}{\mathrm{d}x}\right)_s = \frac{-[\![\phi_x]\!]}{[\![\phi_y]\!]} \tag{5}$$

Here $\tilde{\phi}_x$ refers to the mean value of ϕ_x evaluated on each side of the discontinuity, and $[\![\phi_x]\!]$ indicates the jump in ϕ_x across the discontinuity; the subscript s denotes the quantity evaluated at the shock surface.

Time-Linearized Equations

We now assume that the unsteady disturbances, characterized by δ, are small enough so that we may write

$$\phi(x,y,t) = \phi^\circ(x,y) + \delta\psi(x,y,t) + o(\delta) \tag{6}$$

and neglect higher-order terms in δ. The restriction imposed on δ for this to be true will depend on the other parameters of the problem, viz., $\kappa \equiv (1 - M_\infty^2)/[(\gamma+1)M_\infty^2\tau]^{2/3}$ and K. This gives

$$\{1 - M_\infty^2 - (\gamma+1)M_\infty^2\phi_x^\circ\}\phi_{xx}^\circ + \phi_{yy}^\circ = 0 \tag{7a}$$

$$\phi_y^\circ(x,0) = \tau Y^{\circ\prime}(x), \quad -½ \le x \le ½ \tag{7b}$$

and

$$-2KM_\infty^2\psi_{xt} + \{[1 - M_\infty^2 - (\gamma+1)M_\infty^2\phi_x^\circ]\psi_x\}_x + \psi_{yy} = 0 \tag{8a}$$

$$\psi_y(x,0,t) = Y_x^u(x,t), \quad -½ \le x \le ½ \tag{8b}$$

The solution to Eqs. (7) must satisfy the steady version of the shock relations, Eqs. (4) and (5). The shock relations for Eqs. (8) are discussed later.

As mentioned previously, a shock-fitting scheme that approximates the shock waves as discontinuities normal to the freestream has been developed[9] with an alternating-direction implicit scheme (i.e., ADI) to compute the solution to Eq. (7). Comparison of these results with the results obtained[12] using an exact shock-fitting algorithm and line relaxation indicates that they should suffice for most studies. At the very least, they should prove adequate for the time-linearized studies of interest here, as only small shock excursions can be allowed.

We assume, then, that we have the numerical values for ϕ_x° required in Eqs. (8). These data will be discontinuous across some vertical line, the shock wave, $x = x^*$, $0 \le |y| \le y^*$. We then ask, under what conditions are Eqs. (8) valid? And how do we account for shock wave motions in the linearized analysis? The answers to these questions are inferred from a simple one-dimensional model discussed in the next section.

Anticipating that we will wish to solve Eqs. (8) with the same technique that proved successful for Eq. (1), we avoid writing

$$\psi(x,y,t) = Re\{\tilde{\psi}(x,y)e^{i\omega t}\} \tag{9}$$

Assumption (9) restricts the study to harmonic linear motions. Because indicial motions can be superimposed to obtain the results for any frequency, they too are important. Assumption (9) suppresses the time dimension of the calculation, but it results in two coupled equations, or one equation for a complex-valued $\tilde{\psi}$, which may be solved by line relaxation. Our experience with unsteady ADI techniques has been that they are at least as effective as line relaxation for problems of this type, and hence there is no numerical advantage to the decomposition, Eq. (9). This conclusion also was arrived at by Ballhaus et al.[13] in a related study.

An appropriate scaling of the dependent and independent variables in Eqs. (7) and (8) allows either the thickness or the frequency to be normalized to the value 1, as expected. This scaling, in terms of the transonic similarity parameter κ, the amplitude of the unsteady motion δ, its frequency ω, and the body's basic thickness τ, leads to

$$\psi(\bar{x},\bar{y};\kappa;\delta;\omega;1) = \omega\tilde{\psi}\left(\bar{x}, \frac{\bar{y}}{\omega^{1/2}}; \frac{\kappa}{\omega^{1/2}}; 1; \frac{1}{\omega^{1/2}}\right)$$

where $\bar{x}$ and $\bar{y}$ are suitably scaled replacements for the x and y coordinates. This result can be used to check trends noted in the numerical results.

One-Dimensional Model

To answer the questions just raised, we study a simple unsteady one-dimensional analog of Eq. (2). We consider a one-dimensional unsteady equation that models the important features of Eq. (2), and ascertain how a simple steady solution is modified by small unsteady perturbations. We consider, then,

$$2\phi_{xt} + (1-\phi_x)\phi_{xx} = 2\phi_{xt} - ½\{(1-\phi_x)^2\}_x = 0 \tag{10}$$

subject to $\phi(0,t) = f_1(t)$, $\phi_x(0,t) = f_2(t)$, and either $\phi(1,t)$ or $\phi_x(1,t) = f(t)$. There are restrictions on f which, for brevity, we do not list. Our study could be generalized by replacing $1-\phi_x$ in Eq. (10) by $[A(x) - \phi_x]$, where $A(x)$ is a continuous function of x, but little added insight is gained.

To simplify matters further, consider the especially simple subcase $f_1 = 0$, $f_2 = -1$, $f = 3 + \delta p(t)$. When $\delta \equiv 0$, we have the steady solution

$$\phi^\circ = \begin{cases} -x, & 0 \le x \le ¾ \\ -3(1-x), & ¾ \le x \le 1 \end{cases}$$

This satisfies Eq. (10) and the jump condition that one derives from it, viz.,

$$[\![\phi]\!] = 0 \text{ on } 2\frac{\mathrm{d}x_s}{\mathrm{d}t} = 1 - \bar{\phi}_x \tag{11}$$

Now a general solution of Eq. (10), in terms of ϕ_x, is

$$\phi_x = \text{arbitrary function of } \left(t + \frac{2(1-x)}{1-\phi_x}\right)$$

This can be verified by substitution. With, say $\upsilon_x(1,t) = 3 + \delta p(t)$, we have, for $x > x_s$,

$$\phi(x,t) = 3(x - x_s) + \delta\int_{x_s}^{x} p\left(t + \frac{2(1-\hat{x})}{1-\phi_x(\hat{x},t)}\right)\mathrm{d}\hat{x} - h(t) \tag{12}$$

where the choice $h(t) = x_s(t)$ insures that $[\![\phi]\!] = 0$ at $x = x_s$ because $\phi = \phi^\circ$ for $x < x_s$.

The shock motion must be determined by the direct integration of Eq. (11):

$$2\frac{dx_s}{dt} = 1 - \tilde{\phi}_x = -\frac{\delta}{2}p[x_s(t),t] \tag{13}$$

Now, for comparison, we determine the results that are obtained by time linearization; i.e., we write

$$\phi(x,t;\delta) = \phi^\circ(x) + \delta\psi(x,t) + o(\delta) \tag{14}$$

and solve the linear equation for ψ which results by dropping higher-order terms in δ. That is, we solve

$$2\psi_{xt} + (1 - \phi_x^\circ)\psi_{xx} - \phi_{xx}^\circ\psi_x = 0 \tag{15}$$

subject to $\psi_x(1,t) = p(t)$.

We now linearize the first of Eqs. (11) as follows:

$$[\![\phi(x,t)]\!] = 0 = [\![\phi(x_s^\circ,t) + \phi_x(x_s^\circ,t)[x_s(t) - x_s^\circ] + \ldots]\!]$$
$$= [\![\phi^\circ(x_s^\circ) + \delta\psi(x_s^\circ,t) + \phi_x^\circ[x_s(t) - x_s^\circ]]\!]$$

Thus we conclude that

$$\delta[\![\psi(x_s^\circ,t)]\!] = -[\![\phi_x^\circ(x_s^\circ)]\!](x_s - x_s^\circ) \tag{16}$$

From the second of Eqs. (11), with $x_s(t) = x_s^\circ + \delta\chi(t)$, we find

$$\frac{d\chi}{dt} = -\frac{1}{2}\tilde{\psi}_x = -\frac{1}{4}\psi_{x_b}$$

where $(\ )_b$ refers to the value behind the shock. Thus we may replace Eq. (11) by

$$[\![\psi(x_s^\circ,t)]\!] = -[\![\phi_x^\circ(x_s^\circ)]\!]\chi$$

or

$$\psi_b(x_s^\circ,t) = -4\chi(t) \tag{17a}$$

and

$$\frac{d\chi}{dt} = -\frac{1}{4}\psi_{x_b} \tag{17b}$$

Example

Consider now, for example, $p(t) = \sin\omega t$; it is easy to show that a general solution to Eq. (15) is

$$\psi(x,t) = -(1/\omega)[\cos\omega(1 - x - t) - h(t)]$$

The function $h(t)$ follows from Eqs. (17a) and (17b) and assuming, e.g., that $\psi(\tfrac{3}{4},0) = 0$. Thus,

$$\psi(x,t) = -(1/\omega)[\cos\omega(1 - x - t) - \cos(\omega/4)] \tag{18}$$

and

$$\chi(t) = (1/4\omega)[\cos\omega(\tfrac{1}{4} - t) - \cos(\omega/4)] \tag{19}$$

Had we solved Eq. (15) with $\psi \equiv 0$ for $x < x_s(t)$ and determined the exact shock motion from Eq. (11) with $1 - \phi_x = -2 + O(\delta)$ used in Eq. (12), we would find that behind the shock

$$\phi(x,t) = \phi^\circ + 3 - 4x_s - (\delta/\omega)[\cos\omega(1 - x - t)$$
$$- \cos\omega(1 - x_s - t)] \tag{20}$$

where the shock motion is given explicitly by

$$x_s = \frac{2}{\omega}\tan^{-1}\left\{\frac{\tan\frac{\omega}{2}(t+c) - \left[\tan\frac{\omega}{2}(t-1) - \frac{\delta}{4}\right]}{1 + \tan\frac{\omega}{2}(t-1)\left[\tan\frac{\omega}{2}(c+t) + \frac{\delta}{4}\right]}\right\} \tag{21}$$

with $c = -2(\tan^{-1}[\tan(\omega/8) + \delta/4])/\omega$. For $\omega \gg \delta$, which is required for small shock motions, Eq. (21) simplifies to

$$x_s = \tfrac{3}{4} + (\delta/4\omega)[\cos\omega(\tfrac{1}{4} - t) - \cos(\omega/4)]$$

Thus these results are in agreement with Eqs. (18) and (19) to lowest order in δ.

The time-linearized results, Eqs. (18) and (19), now are compared with the exact results. The nonlinear result for $x > x_s$, given by Eqs. (12) and (13), is

$$\phi = \phi^\circ + 3 - 4x_s(t) + \delta\int_{x_s}^{x}\sin\omega\left(t + \frac{2(1-\hat{x})}{1 - \phi_x(\hat{x},t)}\right)d\hat{x} \tag{22}$$

where

$$\frac{dx_s}{dt} \equiv \dot{x}_s = -\frac{\delta}{4}\sin\omega\left(t + \frac{1 - x_s}{1 - 2\dot{x}_s}\right) \tag{23}$$

The results, Eqs. (22) and (23), are consistent with the time-linearized results, Eqs. (18) and (19), to $O(\delta)$, except for a slow secular drift in the shock position of $O(\delta^2 t)$ that occurs in Eq. (23) but not in Eq. (19). This is an artifact of our one-dimensional model; even if it were not, it would not invalidate the use of the linear results for flutter studies where δ is small and structural damping determines the time scale of interest.

The main conclusions that we derive from this study are that it is essential to consider shock motion in computing time-linearized solutions if we are to determine the effects of small unsteady perturbations correctly to lowest order, and that shock excursions increase as the frequency is decreased. Additionally, this motion can be computed in a straightforward manner.

Two-Dimensional Time-Linearized Analysis

The results from our simple model show that the time-linearized results must be corrected for shock motion if they are to be consistently correct to lowest order. This can be accomplished by calculating the shock motion in conjunction with the time-linearized solution. Here we follow an analogous procedure and calculate the change with time of the values of the perturbed potential behind the shock required by the linearized shock jump relations. Thus, we wish to solve Eq. (8a) with Eq. (8b) subject to the far-field boundary and Kutta conditions. As we noted, the steady result for ϕ_x° can be calculated adequately for most small-disturbance flows using normal shock fitting, as described in Ref. 9. Under the assumption that the shock wave is normal, the shock jump conditions, Eqs. (4) and (5), can be replaced by requiring

$$[\![\phi]\!] = 0 \text{ on } \frac{dx_s}{dt} = \frac{\gamma+1}{2K}\left\{\frac{M_\infty^2 - 1}{(\gamma+1)M_\infty^2} + \tilde{\phi}_x\right\} \tag{24}$$

For steady flow, $\dot{x}_s = 0$ and in Eq. (24) $\{\cdots\} = 0$. We express the shock positon as

$$x_s = x_s^\circ + \delta\chi(t)$$

and conclude that the shock motion is governed by

$$\frac{d\chi}{dt} = \frac{\gamma+1}{2K}\tilde{\psi}_x$$

192

As discussed in Ref. 9, $\tilde{\psi}_x$ is evaluated at $y=0$. On the shock

$$[\![\phi]\!] = [\![\phi^\circ]\!] + \delta [\![\psi]\!] \tag{25}$$

Linearizing Eq. (25) for the velocity potential about the steady shock position, we find

$$\phi(x_s,y,t) = \phi(x_s^\circ,y,t) + \phi_x(x_s^\circ,y,t)\delta\chi$$

$$= \phi^\circ(x_s^\circ,y) + \phi_x^\circ(x_s^\circ,y)\delta\chi + \delta\psi(x_s^\circ,y,t) + O(\delta^2)$$

Because we have treated the shock as a normal one, y appears here simply as a parameter. Now $[\![\phi(x_s,y,t)]\!]$ and $[\![\phi^\circ(x_s^\circ,y)]\!]$ are both zero; consequently, we have

$$[\![\psi(x_s^\circ,y,t)]\!] = -\frac{(\gamma+1)}{2K} [\![\phi_x^\circ(x_s^\circ,y)]\!] \int_0^t \tilde{\psi}_x(x_s^\circ,0,\hat{t})\,\mathrm{d}\hat{t} \tag{26}$$

which must be integrated in time in conjunction with the solution to Eq. (8).

Equation (8) now is solved numerically in time and space in conjunction with Eq. (26), which is used to update the values of ψ behind the shock. We start with a steady solution and initiate a body motion, such as the harmonic oscillation of a flap. The calculations proceed in time until they are judged to be periodic. Note that indicial as well as harmonic motions may be considered because we have not utilized the usual harmonic decomposition, Eq. (9).

Numerical Procedure

The numerical procedure used here derives from that developed for the nonlinear equation, Eq. (1). The main simplification occurs in the shock jump conditions. In order to minimize the far-field boundary effects on the results which, as Magnus[14] has noted, can be significant, we again use coordinate stretching[9] in the form

$$\xi = \pm[1-\exp(-a_1|x|)] \quad \text{for } x \gtrless 0$$

$$\eta = \pm[1-\exp(-a_2|y|)] \quad \text{for } y \gtrless 0$$

where a_1 and a_2 are constants that determine the mesh distribution. This stretching transforms the infinite physical domain into a computational domain bounded by $|\xi| \le 1$ and $|\eta| \le 1$. The mesh distribution is concentrated on the airfoil. In these coordinates, Eq. (8) becomes

$$A_1\{\psi_\xi\}_t + A_2\{f(\xi,\eta)(1-|\xi|)\psi_\xi\}_\xi + A_3\{(1-|\eta|)\psi_\eta\}_\eta = 0 \tag{27}$$

where

$$A_1 = \frac{-2KM_\infty^2 a_1}{a_2(1-|\eta|)}, \quad A_2 = \frac{a_1^2}{a_2(1-|\eta|)}, \quad A_3 = \frac{a_2}{1-|\xi|}$$

and

$$f(\xi,\eta) = 1 - M_\infty^2 - a_1(\gamma+1)M_\infty^2(1-|\xi|)\phi_\xi^\circ$$

is known in discrete form from the steady numerical solution. This function is discontinuous at $\xi = \xi_s^\circ$ for $0 \le |\eta| \le \eta^*$. First-order backward time and spatial differences are used for the first term. Centered or first-order backward differences are used for the second term if f is less than or greater than zero, respectively; $f(\xi,\eta)$ is known in advance, with the derivative ϕ_ξ° automatically evaluated correctly. Centered differences are used for the third term and denoted by δ_η.

The solution is computed using an alternating-direction implicit procedure first applied to transonic flow problems by Ballhaus and Steger[15] and by Beam and Warming,[16] and subsequently refined further by Ballhaus and Goorjian.[17] The solution is advanced in time from its initial steady state to subsequent time levels with the following two-step procedure.

New values of ψ, denoted by ψ^+, are calculated along $\eta = $ const lines using

$$A_1\frac{\psi_\xi^+ - \psi_\xi^n}{\Delta t} + A_2\{f(\xi,\eta)(1-|\xi|)\psi_\xi^+\}_\xi$$

$$+ A_3\delta_\eta\{(1-|\eta|)\psi_\eta^n\} = 0$$

This is coupled with the computation of new values of ψ^+ behind the shock obtained by using Eq. (26). With the shock located at ξ_s° such that $\xi_s < \xi_s^\circ < \xi_{s+1}$, we can express the values of ψ ahead of and behind the shock in a Taylor series, finally arriving at the result

$$[\![\psi]\!]^+ = -C(\eta)\Delta t\tilde{\psi}_\xi^n + [\![\psi]\!]^n \tag{28}$$

where

$$C(\eta) = [(\gamma+1)/4K]a_1^2(1-|\xi_s^\circ|)^2 [\![\phi_\xi^\circ(\xi_s^\circ,\eta)]\!]$$

and $\tilde{\psi}_\xi^n$ is evaluated, following Eq. (26), at $\eta = 0$. One-half the change in ψ across the shock is accounted for in this step, effectively using the trapezoidal rule in the time integration, Eq. (26); hence C is half the value implied by Eq. (26).

With the values of ψ^+ determined, the new values of ψ at the subsequent time level, ψ^{n+1}, are calculated using

$$A_1\frac{\psi_\xi^{n+1} - \psi_\xi^+}{\Delta t} + \frac{A_3}{2}\delta_\eta\{(1-|\eta|)(\psi_\eta^{n+1} - \psi_\eta^n)\} = 0$$

in conjunction with the completion of the time integration, Eq. (26):

$$[\![\psi]\!]^{n+1} = -C(\eta)\Delta t\tilde{\psi}_\xi^{n+1} + [\![\psi]\!]^+ \tag{29}$$

Again, $\tilde{\psi}_\xi^{n+1}$ is evaluated at $\eta = 0$.‡

The full procedure is, effectively,

$$A_1[(\psi_\xi^{n+1} - \psi_\xi^n)/\Delta t] + A_2\{f(\xi,\eta)(1-|\xi|)\psi_\xi^+\}_\xi$$

$$+ \tfrac{1}{2}A_3\delta_\eta\{(1-|\eta|)(\psi_\eta^{n+1} + \psi_\eta^n)\} = 0$$

with Eq. (26) implemented in the form of Eqs. (28) and (29). The procedure outlined here effectively corrects the ψ values for shock motions as the solution progresses. The shock motion is easily determined simultaneously by using Eq. (26) and the expression for $\mathrm{d}\chi/\mathrm{d}t$ to find

$$\chi^{n+1}(0,t) = -[\![\psi(x_s^\circ,0,t)]\!]^{n+1}/[\![\phi_x(x_s^\circ,0)]\!] \tag{30}$$

The computations then provide results for ϕ_x like those sketched in Fig. 1. This figure depicts the steady-state result and the unsteady changes, as well as the shock positions at two different time levels where the shock is behind the steady-state position. When the shocks have been inserted in their known positions, we see that we need to continue data analytically ahead of and behind the shock in order to complete the solution. For shock excursions that are $o(1)$, we simply can extrapolate the steady-state data, both ahead of and behind the shock, to determine the pressure distribution on the body correctly to lowest order. Larger shock motions are, of course, not admissable in this theory.

---

‡The results given by the authors in Ref. 18 were in error because $\tilde{\psi}_\xi$ was allowed to vary with η; this is not consistent with the normal shock approximation that gives Eq. (24).

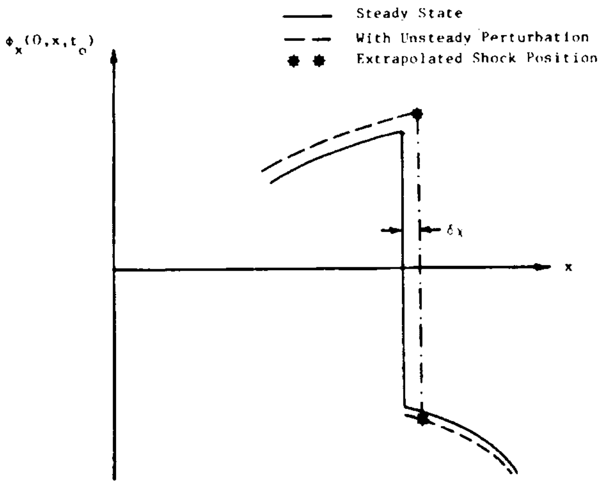

Fig. 1 Sketch of steady state ϕ_x, effect of perturbation $\delta\psi_x$, and resulting shock excursion.

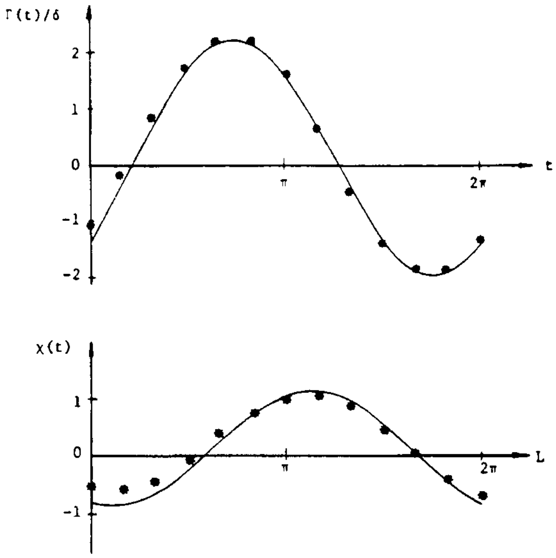

Fig. 2 Nonlinear (***) and time-linearized (———) circulation and shock position for the pitching motion of an NACA 64A006 airfoil. Results shown are for the fifth cycle. The nonlinear results are for $\delta = 0.1$ deg and are not yet periodic ($M_\infty = 0.880$, $K = 0.48$).

Results and Discussion

Time-linearized results have been computed for an NACA 64A006 airfoil experiencing harmonic pitching and flap motions. As noted earlier, in the low-frequency approximation made here, pitching and plunging motions lead to the same result except that the time-linearized perturbations are proportional to the maximum pitch angle for the former, and K times the maximum amplitude for the latter. Harmonic motions initiated from a steady state become nearly periodic in three to ten cycles, with the changes induced by flap oscillations becoming periodic more rapidly than those resulting from pitching oscillations. More cycles were required for larger frequencies and, to a lesser degree, higher Mach numbers.

In order to confirm the validity of the time-linearized calculations, both the time-linearized and nonlinear algorithms were used to compute the response to a step change in angle of attack and the harmonic response to pitching motions. Figure 2 compares the nonlinear and time-linearized results for the normalized circulation and shock position for harmonic pitching motions at $M_\infty = 0.88$ and $K = 0.48$. For these conditions, very small unsteady changes lead to very small shock motions, and in both calculations the shock wave remains between grid points. Because of the extrapolation procedure used in the nonlinear shock-fitting, the finite mesh size used can introduce errors, albeit small ones, in the shock's position when a grid line is crossed. We wished to eliminate these errors in order to use the nonlinear

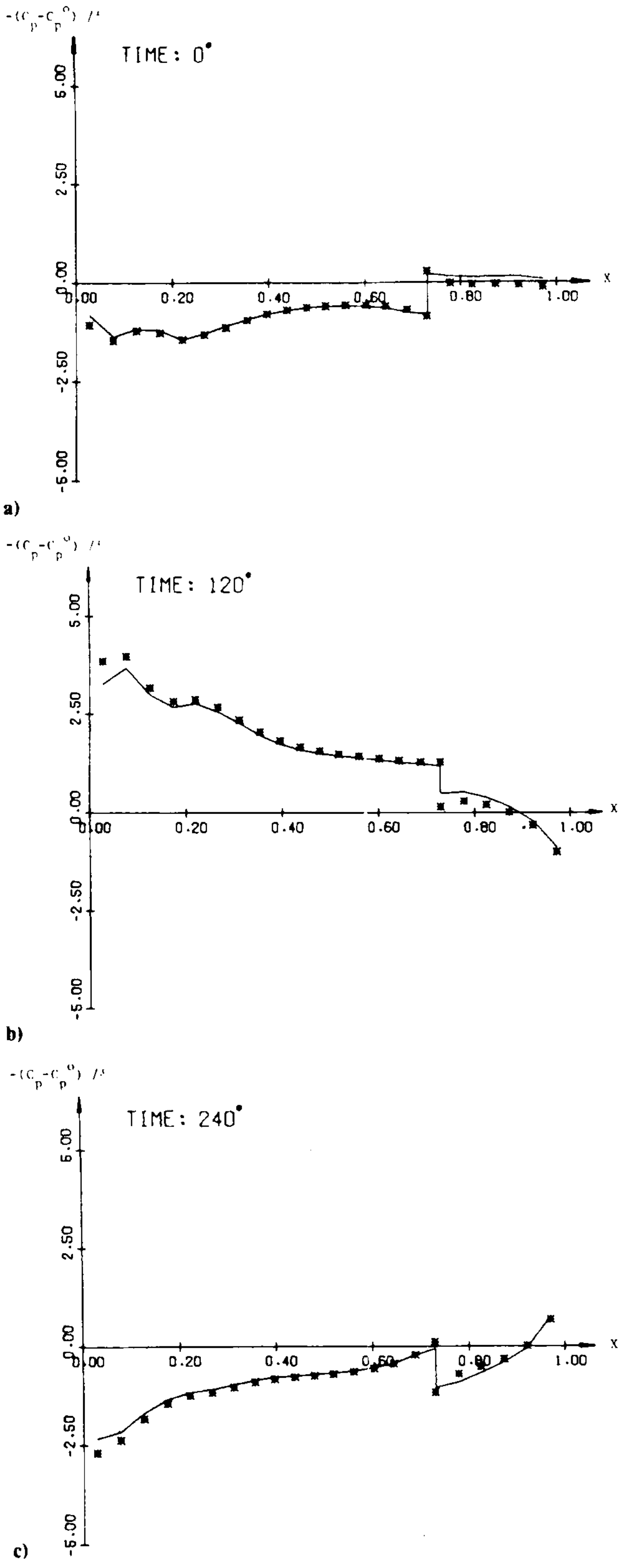

Fig. 3 Normalized nonlinear (***) and time-linearized (———) pressure perturbations on the upper surface of an NACA 64A006 at three times. Pitching motion with $M_\infty = 0.880$, $K = 0.48$. For the nonlinear calculations, $\delta = 0.1$ deg.

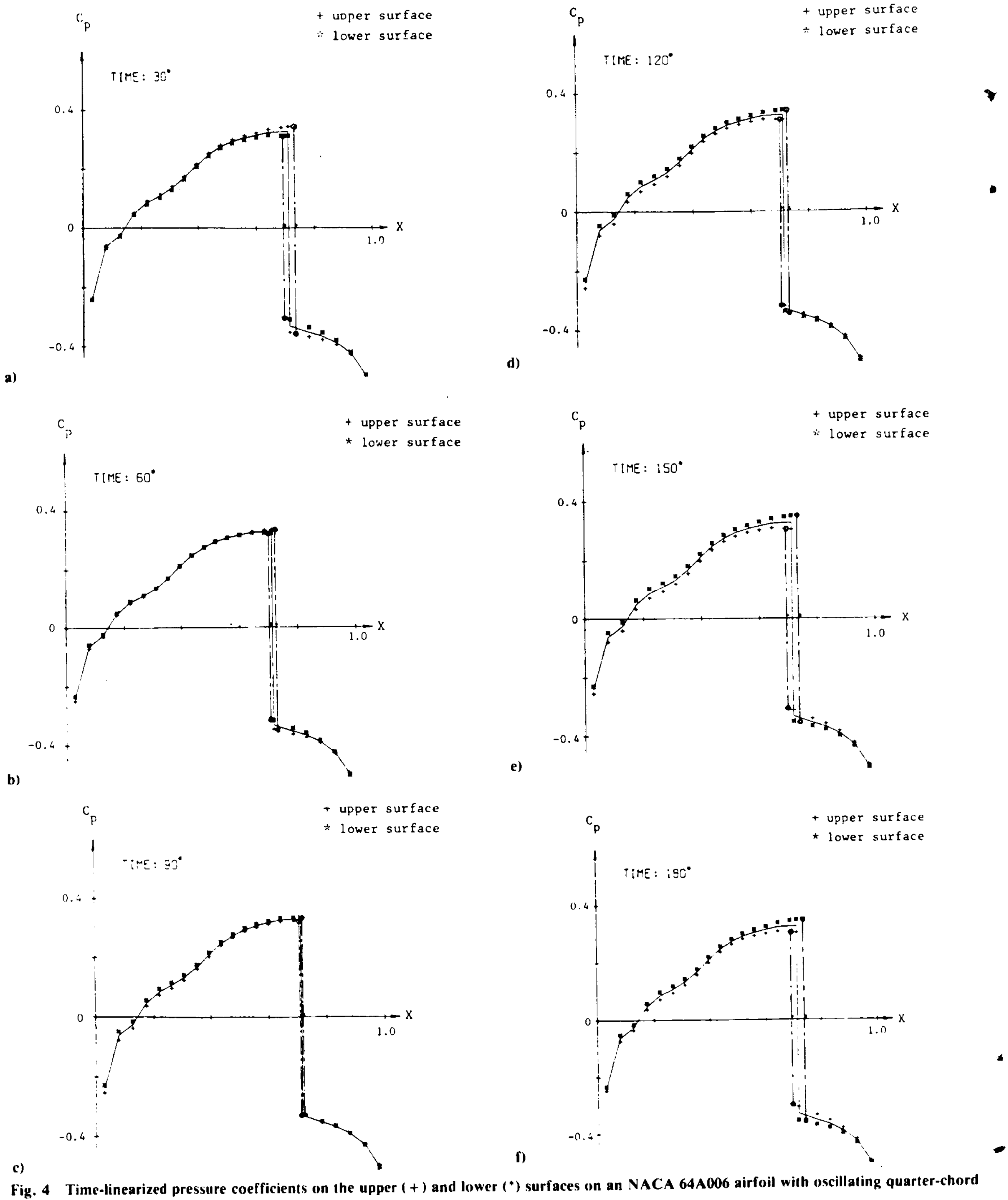

Fig. 4 Time-linearized pressure coefficients on the upper (+) and lower (*) surfaces on an NACA 64A006 airfoil with oscillating quarter-chord flap ($M_\infty = 0.875$, $K = 0.06$, $\delta = 0.25$ deg).

calculations to judge the accuracy of time-linearized calculations. These results indicate that for pitching about midchord, nonlinear, amplitude-dependent behavior occurs for $\delta/\tau \geq 0.1$ for $K = 0.48$. Because the amplitude of the shock motion increases with decreasing K, nonlinear effects occur at smaller values of δ/τ at lower reduced frequencies. Results are given for the fifth cycle; note that the nonlinear results are not yet periodic. Figure 3 compares the nonlinear and time-linearized pressure deviation from steady state at three angular times for the same conditions. Good agreement between the results is obtained for δ/τ less than 0.1.

Time-linearized pressure distributions at six angular positions for an oscillating quarter-chord flap with $K = 0.06$ and $M_\infty = 0.875$ are shown in Fig. 4. The flap deflection is

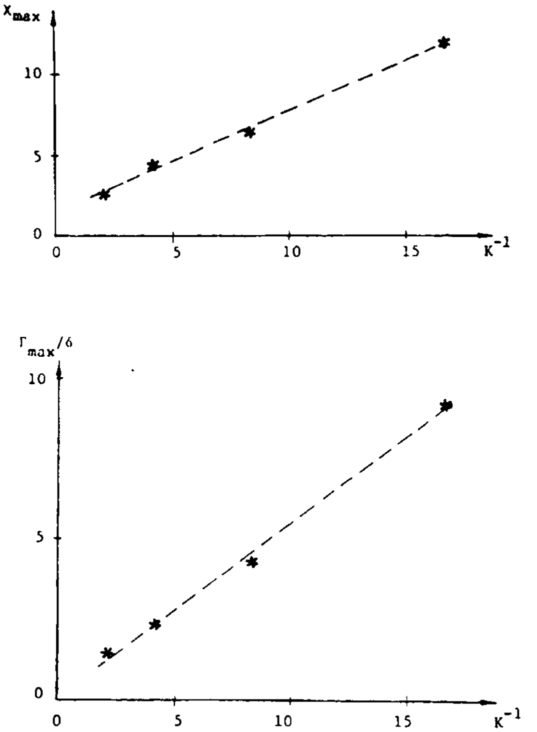

Fig. 5 Normalized maximum shock excursion and circulations as a function of inverse reduced frequency for an NACA 64A006 airfoil with oscillating quarter-chord flap ($M_\infty = 0.875$).

downward during the first half of the cycle. The results for the second half of the period, for the symmetrical problem shown here, are just the results shown with the lower and upper surface pressures interchanged. Thus the results for 0 deg are not given, as they are just those for 180 deg with the lower and upper surface pressures reversed. Because the flap hinge occurs very close to the steady-state shock location, the pressure singularity due to the change in flow direction at the hinge is missed. The circulation and shock excursion obey the following relations:

$$\Gamma(t)/\delta = 9.26 \sin(t - 59\,\text{deg})$$

$$\chi(t) = 12 \sin(t - 51\,\text{deg})$$

Note the substantial phase lag in the circulation and the shock's position.

Time-linearized pressure distributions for an oscillating airfoil with $K = 0.12$ and $M_\infty = 0.875$ also were computed. The results, if multiplied by K, represent the pressure perturbations for a plunging airfoil. As in the previous case of an oscillating flap, changes in forces and moments of $O(\delta/K)$ occur due to shock wave motion. In this case,

$$\Gamma(t)/\delta = 5.48 \sin(t - 70\,\text{deg})$$

$$\chi(t) = 5.62 \sin(t - 87\,\text{deg})$$

Analogous computations have been carried out for $K = 0.06$, 0.12, 0.24, and 0.48. Figure 5 depicts the shock wave's excursion and maximum circulation as a function of K^{-1}. The nearly linear variation of the shock excursion substantiates an observation made in a one-dimensional model where the shock wave excursion is directly proportional to $1/K$.

In these calculations the circulation gives an immediate evaluation of the lift coefficient as a function of time; the moment coefficient must be evaluated by integrating the moment of the pressure coefficient. This is done by integrating the moment of pressure perturbations with the shock wave in its steady-state position and then correcting these results for the moment due to the shock wave motion, assuming that the shock's strength is defined by the steady-state pressure field. This makes an error in the shock strength of $O(\delta)$, but the effect on the moment is $O(\delta^2/K)$; because we have neglected other higher-order terms, it is consistent to neglect this change in the strength of the shock wave.

For the time-linearized results to be valid, we must really require $\delta/\tau K \ll 1$. Our numerical results indicate that, for $\delta/\tau K \leq 0.2$, the unsteady perturbations are essentially linear.

The time-linearized algorithm used here is a derivative of that used for the nonlinear calculations. Consequently, computational times are not greatly reduced from those required for the nonlinear calculations. The linearity of these computations may make it possible to greatly reduce the computational effort required. Numerical experience has shown some difficulties for Δt (deg)/$K \geq 50$. This is in agreement with the consistency requirement for thg ADI algorithm used here. Both the domain-of-dependence condition and a local linearized stability analysis show the procedure to be unconditionally stable. Each time step requires about 2 s of CPU time on a CDC 6400, or about 0.1 s on a CDC 7600. The number of time steps required for a given computation is somewhat less than that required for the nonlinear computations at small values of K, and comparable at larger values of K.

Conclusion

An accurate and efficient procedure for computing time-linearized, small-perturbation, low-frequency transonic flows, including shock wave motions, has been developed. Shock motions must be included, as their amplitude is proportional to that of the motion divided by the reduced frequency. Both indicial and harmonic responses for various modes of motion may be computed in seconds on a CDC 7600.

Acknowledgement

This research was sponsored by the Air Force Office of Scientific Research through Grant 76-2954E and the Office of Naval Research through Grant N0014-76-C-0182.

References

[1] Ballhaus, W. F., "Some Recent Progress in Transonic Flow Computations," *VKI Lecture Series on Computational Fluid Dynamics*, von Kármán Institute for Fluid Dynamics, Rhode-St-Genese, Belgium, March 15-19, 1976.

[2] Landahl, M. T., *Unsteady Transonic Flow*, Pergamon Press, New York, 1961.

[3] Tijdeman, H., "Remarks on the Transonic Flow Around Oscillating Airfoils," *AGARD Fluid Dynamics Panel Symposium on Unsteady Aerodynamics*, Paper 227-10, Ottawa, Canada, 1977.

[4] Traci, R. M., Albano, E. D., and Farr, J. L., Jr., "Perturbation Method for Transonic Flow about Oscillating Airfoils," AIAA Paper 75-877, 1975.

[5] Weatherill, W. A., Ehlers, F. E., and Sebastian, J. D., "Computation of the Transonic Perturbation Flow Field Around Two- and Three-Dimensional Oscillating Wings," NASA CR-2599, 1975.

[6] Ehlers, F. E., "A Finite Difference Method for the Solution of the Transonic Flow About Harmonically Oscillating Wings," NASA CR-2257, 1974.

[7] Tijdeman, H., "On the Motion of Shock Waves on an Airfoil with Oscillation Flap in Two-Dimensional Transonic Flow," NLR TR 75038U, 1975.

[8] Tijdeman, H., "On the Motion of Shock Waves on an Airfoil with Oscillating Flap," *IUTAM Symposium Transsonicum II*, edited by K. Oswatitsch and D. Rues, Göttingen, 1975, pp. 49-56.

[9] Yu, N. J., Seebass, A. R., and Ballhaus, W. F., "An Implicit Shock-Fitting Scheme for Unsteady Transonic Flows Computations," AIAA Paper 77-633, 1977; also *AIAA Journal*, Vol. 16, July 1978, pp. 673-678.

[10] Nixon, D., "Perturbation of Discontinuous Transonic Flow," *AIAA Journal*, Vol. 16, Jan. 1978, pp. 47-53.

[11] Lin, C. C., Reissner, E., and Tsien, H. S., "On Two-Dimensional Non-Steady Motion of a Slender Body in a Compressible Fluid," *Journal of Mathematics and Physics*, Vol. 27, No. 3, 1948, pp. 220-231.

[12] Yu, N.J. and Seebass, R., "Accuracy of Transonic Flow Computations" (unpublished), 1977.

[13] Ballhaus, W. F., Jameson, A., and Albert J., "Implicit Approximate-Factorization of Steady Transonic Flow Problems," NASA TM X-73202, 1977.

[14] Magnus, R. J., "Computational Research on Inviscid, Unsteady, Transonic Flow over Airfoils," Office of Naval Research, Rept. CASD/LVP 77-010, 1977.

[15] Ballhaus, W. F. and Steger, J. L., "Implicit Approximate-Factorization Schemes for the Low-Frequency Transonic Equation," NASA TM X-73082, 1975.

[16] Beam, R. M. and Warming, R. F., "An Implicit Finite-Difference Algorithm for Hyperbolic Systems in Conservation-Law Form," *Journal of Computational Physics*, Vol. 22, Jan. 1976, pp. 87-110.

[17] Ballhaus, W. F. and Goorjian, P. M., "Implicit Finite Difference Computations of Unsteady Transonic Flows about Airfoils, Including the Treatment of Irregular Shock Wave Motions," *AIAA Journal*, Vol. 15, Dec. 1977, pp. 1728-1735.

[18] Fung, K.-Y., Yu, N. J., and Seebass, R., "Small Unsteady Perturbations in Transonic Flows," AIAA Paper 77-675, Albuquerque, N. Mex., June 1977.

Focusing of weak shock waves at an arête

By M. S. CRAMER AND A. R. SEEBASS

J. Fluid Mech. (1978), *vol.* 88, *part* 2, *pp.* 209–222
Printed in Great Britain

Focusing of weak shock waves at an arête

By M. S. CRAMER
Sibley School of Mechanical and Aerospace Engineering,
Cornell University, Ithaca, New York 14853†

AND A. R. SEEBASS
Department of Aerospace and Mechanical Engineering,
University of Arizona, Tucson, Arizona 85721

(Received 28 June 1976 and in revised form 13 February 1978)

The focusing of very weak and slightly concave symmetrical shock waves is examined. The equation that describes this focusing is derived and the resulting similitude discussed. The initial conditions come from a formal matching of this nonlinear description with the linear solution. The maximum value of the pressure coefficient is shown to be proportional to the two-thirds power of both the initial strength of the wave front and a parameter characterizing its rate of convergence.

1. Introduction

There are many sources of weak shock waves; they arise naturally and through the activities of man. Examples include the commonly experienced phenomena of thunder and the sonic bang generated by supersonic aircraft. In this paper we use the terms shock wave and wave front interchangeably to refer to a surface of discontinuity in the pressure and velocity fields in the fluid. It frequently happens that such wave fronts become curved. This curvature may be the result of inhomogeneities in the medium, reflexion from curved surfaces or unsteady boundary conditions. Wave fronts which are concave in the direction of propagation exhibit different kinds of behaviour depending upon the strength of the wave front and the rate of focusing. When the focusing is weak relative to the magnitude of the pressure rise across the wave front, the wave front will straighten and no focusing will occur. When the strength of the wave front is sufficiently small, the wave front will focus along a caustic surface and at a cusp in this surface, called an arête, if it occurs. A perfect focus occurs when a finite portion of the wave front converges to a single point.

The focusing process is characterized by large pressure amplification and a nonlinear interaction between the shock and the flow behind it. Despite considerable analytical, numerical and experimental work, many important questions remain unanswered. Analytical studies are hampered by the fact that available theories, such as the shock dynamic theory of Whitham (1957) and the theory of geometrical acoustics, are inapplicable at a focus. The first fails because it does not account for the interaction between the shock and the flow behind it; the second fails because it is a linear theory and predicts infinite pressures at focal points. Important theoretical studies of the

---

† Present address: Department of Aerospace and Mechanical Engineering, University of Arizona, Tucson, Arizona 85721.

199

behaviour of weak shock waves at a caustic include those of Guiraud (1965) and Hayes (1968). For the case of a smooth caustic they gave the similitude that relates the amplification of the wave front to its initial strength and geometry. An important contribution to our understanding of the behaviour of focusing wave fronts comes from the experimental investigations of Sturtevant & Kulkarny (1974, 1976). Using shadowgraph techniques and pressure measurements they studied the focusing of curved shocks for a wide range of geometries and strengths and delineated the complicated wave patterns and pressure histories which occur.

Because the caustics associated with smooth wave fronts are generally cusped, the arête is one of the more frequently observed foci. In this paper the focusing of very weak shocks at an arête is examined. We consider nearly straight symmetrical wave fronts and use the method of matched asymptotic expansions to determine the initial-value problem and related similitude that govern the flow in the vicinity of the arête. The dependence of the maximum pressure coefficient on the initial strength and shape of the wave front is discussed; the main result is that the pressure levels at the arête are proportional to the two-thirds power of both the initial strength of the wave front and a parameter characterizing the rate at which the wave-front converges.

2. Physical problem

In this section we give a qualitative account of the physical effects that govern the propagation of curved wave fronts. One effect is that a wave front always propagates normal to itself and therefore has a tendency to converge. Another is that the speed of propagation of the wave front increases monotonically with its strength. The latter effect will tend to straighten converging shocks. The behaviour that results depends on which effect dominates.

The behaviour of shock waves which are relatively strong was discussed by Whitham (1957, 1959, 1974) using his theory of shock dynamics. To understand the behaviour of such shock waves, consider the propagation of a concave symmetrical shock into a homogeneous medium as sketched in figure 1 (*a*). The shock's strength is taken to be a maximum in the plane of symmetry and, because the amplification is greatest in this plane, the maximum strength will remain there. However, the shock speed will also have its maximum in the plane of symmetry and the resultant variation in propagation speed will straighten the shock. This behaviour is expected even for shocks with pressure coefficients much less than one, provided that the focusing is sufficiently slow.

When the strength of the shock is sufficiently small its speed of propagation is approximately the sound speed of the undisturbed medium. In many respects the flow will resemble that predicted by geometrical acoustics, and we first discuss the behaviour of such weak shocks from this viewpoint. In this approximation the propagation speed is taken to be the sound speed of the undisturbed medium and, if we take this to be homogeneous, the trajectories of points on the shock, called rays, will be straight. Adjacent rays originating on concave portions of the wave front will intersect, and the locus of these intersections will form a surface in space, called a caustic. When the wave front has a minimum radius of curvature the caustic will be cusped and the wave front will emerge from the cusp in a crossed configuration, as sketched in figure 1(*b*). Experimental evidence of weak shocks which focus and cross is found in the sonic-bang measurements made by Wanner *et al.* (1972) and in the laboratory

2ct

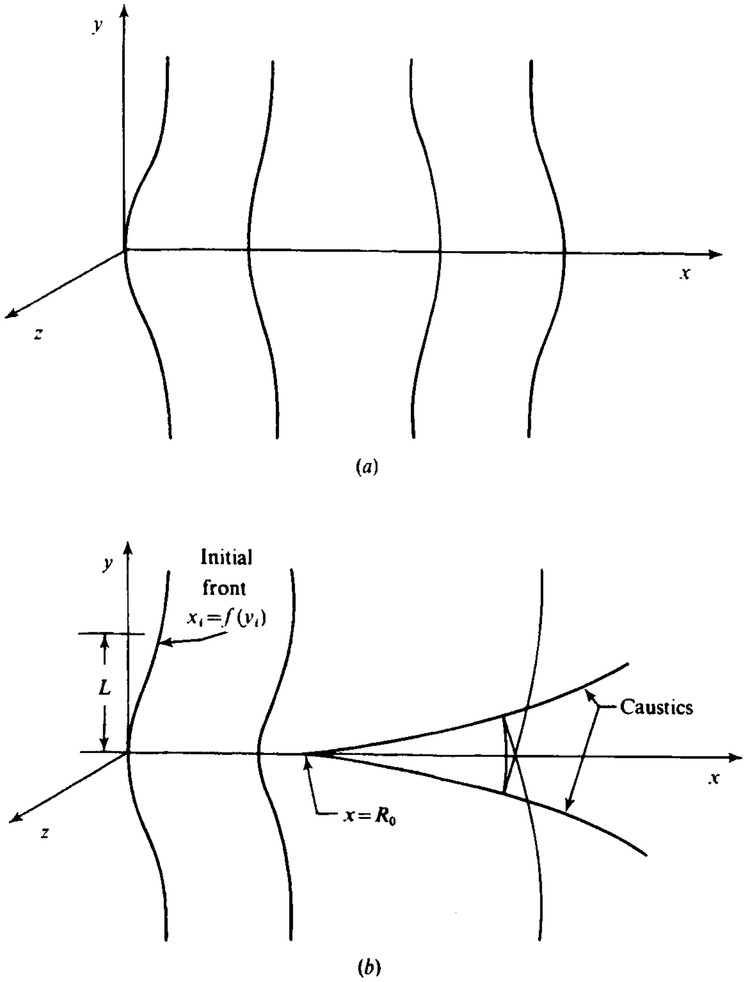

FIGURE 1. Focusing of (*a*) a moderate strength shock and (*b*) an acoustic discontinuity; $f''(L) \equiv 0$, $R_0 = 1/f''(0)$.

investigations by Beasley, Brooks & Barger (1969), Cornet (1972) and Sturtevant & Kulkarny (1974, 1976).

Geometrical acoustics predicts that when the wave front reaches the caustic surface its pressure jump becomes infinite. At the cusp in the caustic this singularity is even stronger because portions from either side of the plane of symmetry focus there simultaneously. Of course, these singularities are never observed, and they merely indicate a local failure of the geometrical-acoustics approximation. Sturtevant & Kulkarny have discussed the nonlinear effects which limit the shock strength to finite values in the focal region. They showed that as the shock approaches a cusp in the caustic it is immediately followed by a sharp expansion. This is due to the amplification of the shock relative to the rest of the flow. When the pressure gradient behind the shock becomes sufficiently great the weakening effect of the expansion as it overtakes the shock becomes noticeable, even if the shock is still weak. Because of the shock's interaction with the expansion wave, the strength of the shock is limited to finite values.

3. Mathematical formulation

We consider the wave front shown in figure 1 (*b*) and take the co-ordinate system to have its origin at the point of minimum radius of curvature of the initial wave front. The $+x$ axis is in the direction of propagation and the y axis is tangential to the initial wave front at $y = 0$. The equation of the initial wave front is taken to be $x_i = f(y_i)$, where x_i and y_i are the co-ordinates of the initial shock and f is symmetrical about $y = 0$. We are considering the propagation of very weak shocks in an inviscid perfect gas with no heat conduction. In the case considered here the shock strength is always small. The results of Hayes (1957) may be used to argue that for the spatial and temporal gradients expected here the flow may be assumed irrotational. If we assume that a velocity potential ϕ exists, the inviscid equations of motion reduce to

$$\phi_{tt} + 2\phi_x\phi_{xt} + 2\phi_y\phi_{yt} + 2\phi_x\phi_y\phi_{xy} = (a^2 - \phi_x^2)\,\phi_{xx} + (a^2 - \phi_y^2)\,\phi_{yy}, \tag{1}$$

where a is the local speed of sound, which for a perfect gas it is given by the isentropic Bernoulli integral for unsteady flow:

$$a^2 = a_0^2 - (\gamma - 1)\,[\phi_t + \tfrac{1}{2}(\phi_x^2 + \phi_y^2)], \tag{2}$$

where a_0 is the constant speed of sound in the undisturbed medium and γ is the ratio of specific heats. The velocity potential must satisfy the initial conditions

$$\phi(x, y, 0) = \phi_0(x, y), \quad \phi_t(x, y, 0) = \phi_1(x, y), \tag{3}$$

where the functions ϕ_0 and ϕ_1 are taken to be zero ahead of the wave front, i.e. for $x > f(y)$; immediately following the shock, their values must be consistent with the appropriate shock jump relations.

As mentioned in previous sections, we consider the shocks to be not only initially weak but also nearly straight. We take the maximum strength of the wave front to be at $y = 0$ and the pressure coefficient, $C_p(x, y, t) = -2\phi_t/a_0^2$ to lowest order, to be small for all x and y at $t = 0$. We define

$$\epsilon \equiv C_p(0^-, 0, 0) \ll 1$$

as the small parameter associated with the shock strength. For the shock to be practically straight we require that f be such that the maximum slope f' is small. If we define L to be the point of maximum slope, i.e. $f''(L) \equiv 0$, then the requirement $\delta \equiv L/R_0 \ll 1$, where R_0 is the minimum radius of curvature of the shock, ensures that the slope is small everywhere. Another restriction we shall need to place on the shape of the wave front concerns the rate of change of the radius of curvature of the wave front at $t = 0$. Denoting the radius of curvature by $R(y_i)$, we have

$$R(y_i) = [1 + f'(y_i)^2]^{\frac{3}{2}}/f''(y_i). \tag{4}$$

In §4 we shall need to require that $R_0'' R_0 \delta^2 \equiv (3 - f^{\text{iv}}(0)\,R_0^3)\,\delta^2$ be of order one in the limit of vanishing δ. Here R_0'' denotes the second derivative of $R(y_i)$ at $y_i = 0$ and $f^{\text{iv}}(0)$ is the fourth derivative of f at $y_i = 0$. Examples of possible wave-front shapes are

$$f_1(y;\, A, l) = A[1 - \exp(-y^2/l^2)], \quad f_2(y;\, c_1, c_2) = \tfrac{1}{2}c_1 y^2 - \tfrac{1}{30}c_2 y^6.$$

Both shapes are smooth and possess inflexion points. The parameter δ is found to be $2^{\frac{1}{2}}A/l$ in the first case and $c_1^{\frac{5}{4}}c_2^{-\frac{1}{4}}$ in the second, and it is clear that the limit $\delta \to 0$ may always be taken. The above formulae may be used to calculate $R_0'' R_0 \delta^2$. In the first case this equals $3(1+\delta^2)$ exactly and the requirement that $R_0'' R_0 \delta^2 = O(1)$ as $\delta \to 0$ is satisfied; thus the results derived in this paper may be applied to the first example. The second case is given because it is a wave-front shape which does not satisfy this condition; essentially, this is because $f_2^{\text{iv}}(0) \equiv 0$ and, consequently, $R_0'' R_0 \delta^2 \to 0$ as $\delta \to 0$. In the following sections we shall always assume

$$\kappa \equiv -f^{\text{iv}}(0) R_0^3 \delta^2 \approx R_0'' R_0 \delta^2 = O(1).$$

Our main objective is the determination of solutions to (1) and (3) which are valid for small ϵ and δ and, for consistency, whose pressure and velocity perturbations are always small. In particular we wish to study the case where wave-front crossing occurs. In this paper we give approximations to (1) in two distinct regions. The first is just the linear wave equation and is valid for times of order L/a_0. The solution, subject to the initial conditions (3), is easily found; this is the outer solution. An approximation to (1) which is valid as the wave front approaches the arête, i.e. the cusp in the caustic, is derived in § 5. The initial condition for this equation is obtained by the method of matched asymptotic expansions, thus establishing the initial-value problem governing the flow in the vicinity of the arête.

In the next section the outer solution and the expression for the caustic shape near the cusp are derived. In § 5 the inner region in which the nonlinear effects predominate is discussed and the inner equation deduced. In § 6 the appropriate initial condition for this equation is obtained through the method of matched asymptotic expansions. These results provide a similitude which shows that the solution to the inner problem involves only a single parameter.

4. Outer region

To determine the outer equation it is convenient to work in a co-ordinate system that moves with the wave front. Accordingly, we write the full potential equation (1) in terms of the co-ordinates $X \equiv x - a_0 t$, y and t:

$$\begin{aligned}\phi_{tt} - 2a_0 \phi_{Xt} + 2\phi_X \phi_{Xt} + (\gamma-1)\phi_t \phi_{XX} - (\gamma+1) a_0 \phi_X \phi_{XX} \\ = a_0^2 \phi_{yy} - [2\phi_y \phi_{ty} + (\gamma-1)\phi_t \phi_{yy}] + a_0[2\phi_y \phi_{Xy} + (\gamma-1)\phi_X \phi_{yy}] + \ldots, \quad (5)\end{aligned}$$

where (2) has been used and the terms omitted are cubic in ϕ.

In the outer region it is natural to take

$$a_0 t = O(L), \quad y = O(L), \quad X = O(\Lambda^*), \quad \phi = O(a_0 k^*),$$

where the length scales Λ^* and k^* are yet to be determined. According to the theory of geometrical acoustics the square of the pressure coefficient immediately following the shock varies inversely with the ray-tube area. For our problem all the rays are straight lines and, consequently, the pressure coefficient behind the shock obeys (see, for example, Friedlander 1958, pp. 51–56)

$$C_{ps}(t; y_i) = C_{ps}(0; y_i)\left(\frac{R(y_i)}{R(y_i) - a_0 t}\right)^{\frac{1}{2}}.$$

Here $R(y_i)$ is the radius of curvature of the initial wave front at the point $y = y_i$; y_i effectively labels the ray of interest. Thus, for times of order L/a_0, we see that the time rate of change of the shock's strength is of order $a_0/R(y_i)$. This suggests that the appropriate outer scaling for the derivative $(\partial/\partial t)_X$ is a_0/R_0. Accordingly, we adopt the following outer scaling for the derivatives in (5):

$$\frac{\partial}{\partial t} = \frac{a_0}{R_0}\frac{\partial}{\partial \tilde{t}}, \quad \frac{\partial}{\partial y} = \frac{1}{L}\frac{\partial}{\partial \tilde{y}}, \quad \frac{\partial}{\partial X} = \frac{1}{\Lambda^*}\frac{\partial}{\partial \tilde{X}}$$

and $\phi = a_0 k^* \phi$. For $t = O(L/a_0)$, there is no amplification to lowest order in δ; we therefore assume that k^*/Λ^* and k^*/L are small. When the above expressions are substituted in (5) we find that it may be written in the following form:

$$\tilde{\phi}_{\tilde{t}\tilde{t}} - 2\frac{R_0}{\Lambda^*}\tilde{\phi}_{\tilde{X}\tilde{t}} + \frac{k^*}{\Lambda^*}\frac{R_0}{\Lambda^*}[2\tilde{\phi}_{\tilde{X}}\tilde{\phi}_{\tilde{X}\tilde{t}} + (\gamma-1)\tilde{\phi}_{\tilde{t}}\tilde{\phi}_{\tilde{X}\tilde{X}}] - (\gamma+1)\frac{k^*}{\Lambda^*}\frac{R_0^2}{\Lambda^{*2}}\tilde{\phi}_{\tilde{X}}\tilde{\phi}_{\tilde{X}\tilde{X}}$$

$$= \frac{1}{\delta^2}\tilde{\phi}_{\tilde{y}\tilde{y}} + \frac{k^*}{\Lambda^*}\frac{1}{\delta^2}[2\tilde{\phi}_{\tilde{y}}\tilde{\phi}_{\tilde{X}\tilde{y}} + (\gamma-1)\tilde{\phi}_{\tilde{X}}\tilde{\phi}_{\tilde{y}\tilde{y}}] - \frac{k^*}{\Lambda^*}\frac{1}{\delta^2}\frac{\Lambda^*}{R_0}[2\tilde{\phi}_{\tilde{y}}\tilde{\phi}_{\tilde{y}\tilde{t}} + (\gamma-1)\tilde{\phi}_{\tilde{t}}\tilde{\phi}_{\tilde{y}\tilde{y}}] + \dots .$$

We now assume that k^*/Λ^* and k^*/L are small; it may be shown that this implies that the omitted cubic terms are negligible compared with the largest of the first- and second-order terms. Furthermore, when k^*/Λ^* is small, the third term on the left-hand side and the second term on the right-hand side are seen to be negligible compared with the $\tilde{\phi}_{\tilde{X}\tilde{t}}$ term and the $\tilde{\phi}_{\tilde{y}\tilde{y}}$ term, respectively. When these terms are dropped, the terms remaining are

$$\tilde{\phi}_{\tilde{t}\tilde{t}} - 2\frac{R_0}{\Lambda^*}\tilde{\phi}_{\tilde{X}\tilde{t}} - (\gamma+1)\frac{k^*}{\Lambda^*}\frac{R_0^2}{\Lambda^{*2}}\tilde{\phi}_{\tilde{X}}\tilde{\phi}_{\tilde{X}\tilde{X}} = \frac{1}{\delta^2}\tilde{\phi}_{\tilde{y}\tilde{y}} - \frac{k^*}{\Lambda^*}\frac{1}{\delta^2}\frac{\Lambda^*}{R_0}[2\tilde{\phi}_{\tilde{y}}\tilde{\phi}_{\tilde{y}\tilde{t}} + (\gamma-1)\tilde{\phi}_t\tilde{\phi}_{\tilde{y}\tilde{y}}].$$

This expression is reduced further by assuming that δ is small. An immediate consequence of this assumption is that the $\tilde{\phi}_{\tilde{t}\tilde{t}}$ term is negligible compared with the $\tilde{\phi}_{\tilde{y}\tilde{y}}$ term. Inspection of the remaining terms shows that the only choice of Λ^* which yields a non-trivial balance of terms, i.e. one which contains derivatives with respect to $\tilde{X}$, $\tilde{y}$ and $\tilde{t}$, is $\Lambda^*/R_0 = \delta^2$, or $\Lambda^* = L\delta$. Here, for convenience, we have dropped the order symbols. The resulting balance of terms may be written as

$$2\tilde{\phi}_{\tilde{X}\tilde{t}} + (\gamma+1)\frac{\epsilon}{\delta^2}\tilde{\phi}_{\tilde{X}}\tilde{\phi}_{\tilde{X}\tilde{X}} + \tilde{\phi}_{\tilde{y}\tilde{y}} = 0.$$

The coefficient of the nonlinear term is obtained by noting that $\Lambda^* = \delta L$ implies that $(\partial/\partial t)_x \approx -a_0(\partial/\partial X)_t$ in the outer region and therefore that

$$C_p = O(\epsilon) = -\frac{1}{a_0^2}\phi_t \approx \frac{1}{a_0}\phi_X = O\left(\frac{k^*}{\Lambda^*}\right),$$

or simply $k^* = \Lambda^*\epsilon$. Thus, provided that $\epsilon/\delta^2 = o(1)$, nonlinear effects are negligible. We now assume that this is the case, so that the outer equation becomes

$$2\tilde{\phi}_{\tilde{X}\tilde{t}} + \tilde{\phi}_{\tilde{y}\tilde{y}} = 0.$$

Transforming back to the physical variables and back to the x, y, t co-ordinates, we see that our outer equation is just the wave equation

$$\phi_{tt} = a_0^2(\phi_{xx} + \phi_{yy}), \tag{6}$$

where we have used the fact that $(\partial/\partial t)_x \approx -a_0(\partial/\partial X)_t$ in the outer region.

The explicit form of the outer solution is obtained by solving the linear wave equation (6) with the initial conditions (3). The solution to (6) which satisfies (3) is given by the well-known Poisson integral formula

$$4\pi\phi = \frac{1}{a_0^2 t} I_1 + \frac{\partial}{\partial t}\left[\frac{1}{a_0^2 t} I_0\right].$$

The quantities I_0 and I_1 are the integrals of ϕ_0 and ϕ_1 over a sphere of radius $a_0 t$ centred at the point $(x, y, 0)$. This sphere has the equation

$$(x_s - x)^2 + (y_s - y)^2 + z_s^2 = a_0^2 t^2, \tag{7}$$

where the subscript s refers to points on the sphere of integration.

We now consider the distance s measured along a ray from the initial wave front to any point $(x, y, 0)$; then

$$s = [1 + f'(y_i)^2]^{\frac{1}{2}}\,[x - f(y_i)] = -\frac{[1 + f'(y_i)^2]^{\frac{1}{2}}}{f'(y_i)}\,(y - y_i). \tag{8}$$

Here we have defined s to be positive ahead of the initial wave front and negative behind it. In the following sections it will be useful to have the functions ϕ_0 and ϕ_1 in terms of s instead of x and y. Using the fact that f/L and f' are small, we may replace (8) by

$$y_s = y_i + o(s_s), \quad s_s = x_s - f(y_s) + o(s_s). \tag{9}$$

Using (9) to replace x_s in the integrands of I_0 and I_1, we may write these integrals to lowest order as

$$I_0 = \iint \phi_0(s_s, y_s)\,dA, \quad I_1 = \iint \phi_1(s_s, y_s)\,dA;$$

the area element dA of the sphere (7) may be written as

$$dA = \frac{a_0 t\,dz_s\,dy_s}{[a_0^2 t^2 - (y_s - y)^2 - z_s^2]^{\frac{1}{2}}}.$$

Using (7) and (9), we now write s_s explicitly in terms of y_s and z_s:

$$s_s = X + a_0 t \pm [a_0^2 t^2 - (y_s - y)^2 - z_s^2]^{\frac{1}{2}} - f(y_s) + o(s_s),$$

where the ± sign refers to points on the sphere of integration with $x_s \gtrless x$, respectively.

The above results have been derived in terms of the physical variables X, y, t, etc. We formally define the outer variables

$$\tilde{t} \equiv \frac{a_0 t}{L}, \quad \tilde{y} \equiv \frac{y}{L}, \quad \tilde{z} \equiv \frac{z}{\delta^{\frac{1}{2}} L}, \quad \tilde{X} \equiv \frac{X}{\Lambda^*} = \frac{X}{\delta L}, \quad \tilde{\phi} \equiv \frac{\phi}{k^* a_0} = \frac{\phi}{\epsilon \delta L a_0}.$$

The outer solution may now be written as

$$4\pi\tilde{\phi} = \frac{1}{\tilde{t}}\tilde{I}_1 - \frac{1}{\tilde{t}}\frac{\partial}{\partial \tilde{X}}\tilde{I}_0, \tag{10}$$

where $$\tilde{I}_0 \equiv \iint \tilde{\phi}_0(\tilde{s}_s, \tilde{y}_s)\,d\tilde{A}, \quad \tilde{I}_1 \equiv \iint \tilde{\phi}_1(\tilde{s}_s, \tilde{y}_s)\,d\tilde{A},$$

in which $$\tilde{\phi}_0(\tilde{s}_s, \tilde{y}_s) \equiv \phi_0(s_s, y_s)/\epsilon a_0 \delta L, \quad \tilde{\phi}_1(\tilde{s}_s, \tilde{y}_s) \equiv \phi_1(s_s, y_s)/a_0^2 \epsilon$$

and $$\tilde{s}_s(\tilde{y}_s, \tilde{z}_s; \tilde{X}, \tilde{y}, \tilde{t}) \equiv \frac{s_s}{\delta L} = \tilde{X} + \frac{1}{\delta}\tilde{t} \pm \frac{1}{\delta}[\tilde{t}^2 - (\tilde{y}_s - \tilde{y})^2 - \delta \tilde{z}_s^2]^{\frac{1}{2}} - \tilde{f}(\tilde{y}_s), \tag{11}$$

$$d\tilde{A} \equiv dA/\delta L^2.$$

In determining the scaling for s_s, we have used the fact that the functions ϕ_0 and ϕ_1 are identically zero for $s_s > 0$; therefore it is necessary to consider only non-positive values of s_s in the above integrations. As a result of this, s_s is of order δL in the outer region and, although $\tilde{y}_s$ and $\tilde{y}$ are each of order one in the outer region, their difference $y_s - y$ will always be of order $\delta^{\frac{1}{2}}L$ there. Because z_s is also found to be of order $\delta^{\frac{1}{2}}L$, the last two terms under the square root are of the same order. In the outer region $\bar{l}$ can vanish; (11) is therefore the lowest-order expression for $\tilde{s}_s$ which is uniformly valid in the outer region.

Strictly speaking, the outer solution is valid only for times of order L/a_0. The result (10), of course, predicts infinite pressures when the wave front reaches the caustic surface. This surface is defined by the intersection of adjacent rays, i.e. of adjacent normals to the initial wave front. These considerations imply that the distance, measured along a ray, from a point on the initial wave front to the caustic is just $R(y_i)$, the local radius of curvature of the wave front. In terms of the Cartesian co-ordinates x and y the equation of the caustic surfaces is found by substituting $s = R(y_i)$ in (8). Doing so and expanding for small δ, we find that the caustic is cusped and that near this cusp it has the shape

$$\frac{x_c - R_0}{R_0} = \tfrac{1}{2}R_0'' R_0 \delta^2 \left(\frac{y_i}{L}\right)^2, \quad \frac{y_c}{L} = -\tfrac{1}{3}R_0'' R_0 \delta^2 \left(\frac{y_i}{L}\right)^3$$

to lowest order. Or, if we eliminate y_i,

$$\left(\frac{x_c - R_0}{R_0}\right)^3 = \tfrac{9}{8}R_0'' R_0 \delta^2 \left(\frac{y_c}{L}\right)^2,$$

where the subscript c refers to the caustic. As discussed in §3, we require that $\kappa \approx R_0'' R_0 \delta^2$ be of order one. Initial shock shapes which have $\kappa = o(1)$, such as the second example discussed in §3, require the inclusion of higher-order terms in the above expansions. This will change the relative sizes of the x and y in the inner scaling, thereby increasing the strength of the singularity at the focal point. For wave fronts with $\kappa = o(1)$ but such that a δ may be found and made small, the procedure of this paper may be used to obtain analogous results.

The singular behaviour of the solution at the caustic suggests that nonlinear effects are important there. In the next section we assume that the initial strength of the wave front is so small that these nonlinear effects are important only in the vicinity of the caustic. We then find the appropriate nonlinear equation governing the flow near the cusp in the caustic.

5. Inner region

We now seek an inner expansion valid in the vicinity of the arête. We introduce the inner variables $\hat{x}, \hat{t}, \hat{y}, \chi$ and $\hat{\phi}$ and corresponding inner scales Δ, λ, Λ and k, viz.

$$\hat{x} \equiv \frac{x - R_0}{\Delta R_0}, \quad \hat{t} \equiv \frac{a_0 t - R_0}{\Delta R_0}, \quad \hat{y} \equiv \frac{y}{\lambda}, \quad \chi \equiv \frac{X}{\Lambda}, \quad \hat{\phi} \equiv \frac{\phi}{a_0 k}. \tag{12}$$

We assume that the nonlinear effects are important in only a small neighbourhood of the cusp, and we shall therefore take $\Delta = o(1)$ and $\lambda/L = o(1)$. The amplification is greatest in the region immediately following the shock and we expect nonlinear effects to be most important there; consequently, we use the same scaling for x and t. Furthermore, we assume that, although the strength of the shock is considerably amplified in the focal region, it remains small. Thus we shall take $\phi_\chi/a_0 = O(k/\Lambda) = o(1)$ and $\phi_y/a_0 = O(k/\lambda) = o(1)$. When the scaling (12) is substituted into (5) the full potential equation may be written as

$$\begin{aligned}\hat{\phi}_{\hat{t}\hat{t}} - 2\frac{\Delta R_0}{\Lambda}\hat{\phi}_{\chi\hat{t}} + \frac{k}{\Lambda}\frac{\Delta R_0}{\Lambda}[2\hat{\phi}_\chi\hat{\phi}_{\chi\hat{t}} + (\gamma-1)\,\hat{\phi}_{\hat{t}}\hat{\phi}_{\chi\chi}] - (\gamma+1)\frac{k}{\Lambda}\frac{\Delta^2R_0^2}{\Lambda^2}\hat{\phi}_\chi\hat{\phi}_{\chi\chi} \\ = \frac{\Delta^2R_0^2}{\lambda^2}\hat{\phi}_{\hat{y}\hat{y}} + \frac{k}{\Lambda}\frac{\Delta^2R_0^2}{\lambda^2}[2\hat{\phi}_{\hat{y}}\hat{\phi}_{\chi\hat{y}} + (\gamma-1)\hat{\phi}_\chi\hat{\phi}_{\hat{y}\hat{y}}] \\ - \frac{k}{\Lambda}\frac{\Delta^2R_0^2}{\lambda^2}\frac{\Lambda}{\Delta R_0}[2\hat{\phi}_{\hat{y}}\hat{\phi}_{\hat{y}\hat{t}} + (\gamma-1)\,\hat{\phi}_{\hat{t}}\hat{\phi}_{\hat{y}\hat{y}}] + \dots.\end{aligned}$$

As in our analysis of the outer region, the assumptions that k/Λ and k/λ are $o(1)$ imply that we may drop not only the cubic terms, but also the third term on the left-hand side and the second term on the right-hand side. The resulting equation reads

$$\begin{aligned}\hat{\phi}_{\hat{t}\hat{t}} - 2\frac{\Delta R_0}{\Lambda}\hat{\phi}_{\chi\hat{t}} - (\gamma+1)\frac{k}{\Lambda}\frac{\Delta^2R_0^2}{\Lambda^2}\hat{\phi}_\chi\hat{\phi}_{\chi\chi} \\ = \frac{\Delta^2R_0^2}{\lambda^2}\hat{\phi}_{\hat{y}\hat{y}} - \frac{k}{\Lambda}\frac{\Delta^2R_0^2}{\lambda^2}\frac{\Lambda}{\Delta R_0}[2\hat{\phi}_{\hat{y}}\hat{\phi}_{\hat{y}\hat{t}} + (\gamma-1)\,\hat{\phi}_{\hat{t}}\hat{\phi}_{\hat{y}\hat{y}}].\end{aligned}$$

On physical grounds it is clear that we must require that the inner equation contains χ, $\hat{y}$ and $\hat{t}$ derivatives and at least one nonlinear term; the only choice of Λ which results in such an equation satisfies $\Lambda/\Delta R_0 = o(1)$. For small $\Lambda/\Delta R_0$, the nonlinear term on the right-hand side and the $\hat{\phi}_{\hat{t}\hat{t}}$ term may be dropped. In order to balance the remaining terms we need

$$\frac{\Delta R_0}{\Lambda} = \frac{\Delta^2R_0^2}{\lambda^2} = \frac{k}{\Lambda}\frac{\Delta^2R_0^2}{\Lambda^2} \gg 1. \tag{13}$$

Thus, to lowest order, the inner equation is

$$2\hat{\phi}_{\chi\hat{t}} + (\gamma+1)\,\hat{\phi}_\chi\hat{\phi}_{\chi\chi} + \hat{\phi}_{\hat{y}\hat{y}} = 0. \tag{14}$$

We remark here that (14) also describes low frequency, unsteady, transonic flows, as one might have anticipated.

We now assume that in the inner region the relative size of the x and y length scales is given by the caustic surface calculated in §4. This requires that we take $\Delta^3 = O(\lambda^2/L^2)$. Dropping the order symbol and simply substituting $\lambda^2 = \Delta^3L^2$ in (13), we may express λ, Λ and k in terms of Δ and δ:

$$\lambda/L = \Delta^{\frac{3}{2}}, \quad \Lambda/L = \Delta^2\delta, \quad k/\Lambda = \Delta\delta^2. \tag{15}$$

Thus Λ, λ and k are known in terms of the physical parameters ϵ and δ once Δ has been determined.

The flow in the focal region is found by solving the inner equation (14) subject to an appropriate initial condition. In the next section we determine this initial condition through matching with the outer solution.

6. The matching and the similitude

In this section the initial data for the inner problem are obtained through the method of matched asymptotic expansions. It is further shown that, apart from a simple scaling of the independent and dependent variables, the solution to the resultant initial-value problem depends on only a single combination of the physical parameters: the similarity parameter.

We first consider the outer expansion, which we shall write in the inner variables (12) and then expand for small Δ and δ with the inner variables fixed. We begin by expressing (11) in terms of the inner variables (12) and expanding for small Δ and δ. As a result of this expansion we find that the inner scaling for the integration variables y_s and z_s is given by

$$\hat{y}_s = \Delta^{-\frac{1}{2}}\tilde{y}_s = \Delta^{-\frac{1}{2}}L^{-1}y_s,$$

$$\hat{z}_s = \delta^{\frac{1}{2}}\Delta^{-1}\tilde{z}_s = \Delta^{-1}L^{-1}z_s$$

and that, to lowest order, the inner expansion of $\tilde{s}_s$ is

$$\tilde{s}_s(\Delta^{\frac{1}{2}}\hat{y}_s,\ \Delta\delta^{-\frac{1}{2}}\hat{z}_s;\ \Delta^2\chi, \Delta^{\frac{3}{2}}\hat{y}_s, (1+\Delta\hat{t})/\delta) = \Delta^2[\tfrac{1}{2}\hat{z}_s^2 - \beta(\hat{y}_s)], \tag{16}$$

where $\beta(\hat{y}_s)$ is defined by

$$\beta(\hat{y}_s) = \beta(\hat{y}_s;\ \chi, \hat{y}, \hat{t}) \equiv -\tfrac{1}{24}\kappa\hat{y}_s^4 + \tfrac{1}{2}\hat{t}\hat{y}_s^2 + \hat{y}_s\hat{y} - \chi.$$

In the derivation of (16) we have chosen the lower sign in (11). Any other choice corresponds to portions of the integration sphere with $x_s > f(y_s)$ and contributes nothing to the integrals $\tilde{I}_0$ and $\tilde{I}_1$.

The integrals $\tilde{I}_0$ and $\tilde{I}_1$ are to be evaluated over the surface of a sphere. However, when the inner expansion of the outer area element $d\tilde{A}$ is taken, we see that it may be replaced by $\Delta^{\frac{3}{2}}\delta^{-1}d\hat{z}_s d\hat{y}_s$. Thus, in the inner expansions of $\tilde{I}_0$ and $\tilde{I}_1$, we may transfer the integration from the sphere to the $\hat{z}_s$, $\hat{y}_s$ plane.

We need the expansion of $\tilde{\phi}$ near the cusp only for times less than R_0/a_0, i.e. $\hat{t} < 0$. The area of integration will therefore be bounded by the single closed curve $\tilde{s}_s = 0$, or $\hat{z}_s = \pm[2\beta(\hat{y}_s)]^{\frac{1}{2}}$, as sketched in figure 2. The $\hat{z}_s = 0$ intercepts $\hat{y}_u$ and $\hat{y}_l$ are just the two real roots of $\beta = 0$.

When the inner expansions of the integrals $\tilde{I}_0$ and $\tilde{I}_1$ are taken it will be useful to have the Taylor series expansions of $\tilde{\phi}_0$ and $\tilde{\phi}_1$ for small $\tilde{s}_s$ and $\tilde{y}_s$:

$$\tilde{\phi}_0 = \tfrac{1}{2}\tilde{s}_s[1 + O(\tilde{s}_s, \tilde{y}_s^2)], \quad \tilde{\phi}_1 = -\tfrac{1}{2}[1 + O(\tilde{s}_s, \tilde{y}_s^2)].$$

These are, of course, consistent with the weak-shock jump conditions.

The above results may now be used to show that the inner expansions of $\tilde{I}_0$ and $\tilde{I}_1$ are

$$\tilde{I}_0 = \tfrac{1}{2}\Delta^{\frac{7}{2}}\delta^{-1}\int_{\hat{y}_l}^{\hat{y}_u}\int_0^{(2\beta)^{\frac{1}{2}}}[\hat{z}_s^2 - 2\beta(\hat{y}_s)]\,d\hat{z}_s d\hat{y}_s$$

and

$$\tilde{I}_1 = -\Delta^{\frac{3}{2}}\delta^{-1}\int_{\hat{y}_l}^{\hat{y}_u}\int_0^{(2\beta)^{\frac{1}{2}}} d\hat{z}_s d\hat{y}_s = -\Delta^{-2}\frac{\partial\tilde{I}_0}{\partial\chi}$$

to lowest order. When the $\hat{z}_s$ integration is performed and the result substituted in (10), we find

$$\tilde{\phi}\left(\Delta^2\chi, \Delta^{\frac{3}{2}}\hat{y}, \frac{1+\Delta\hat{t}}{\delta}\right) = -\frac{1}{\pi \times 2^{\frac{1}{2}}}\Delta^{\frac{3}{2}}\int_{\hat{y}_l}^{\hat{y}_u}\beta^{\frac{3}{2}}(\hat{y}_s)\,d\hat{y}_s.$$

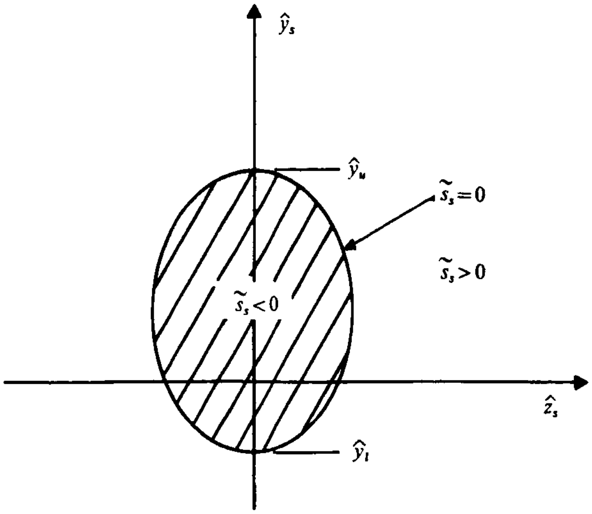

FIGURE 2. Area of integration for I_0 and I_1.

Thus, when written in inner variables, the inner expansion of the outer solution is given by

$$\tilde{\phi} \equiv \frac{k^*}{k}\tilde{\phi}\left(\Delta^2\chi, \Delta^{\frac{3}{2}}\hat{y}, \frac{1+\Delta\hat{t}}{\delta}\right) = -\frac{1}{\pi\times 2^{\frac{1}{2}}}\frac{\epsilon}{\Delta^{\frac{3}{2}}\delta^2}\int_{\hat{y}_l}^{\hat{y}_u}\beta^{\frac{1}{2}}\,d\hat{y}_s. \tag{17}$$

This result is essentially the expansion of the linear solution (10) as the wave front approaches the cusp in the caustic. As mentioned in previous sections, the pressure distribution associated with this pressure field can be singular. The pressure coefficient based on (17) is

$$C_p = \frac{1}{\pi\times 2^{\frac{1}{2}}}\frac{\epsilon}{\Delta^{\frac{1}{2}}}\int_{\hat{y}_l}^{\hat{y}_u}\beta^{-\frac{1}{2}}\,d\hat{y}_s.$$

At $t = R_0/a_0$ or, in terms of the inner variables, $\hat{t} = 0$, the pressure coefficient is proportional to $(R_0-x)^{-\frac{1}{4}}$ along the x axis and to $|y|^{-\frac{1}{3}}$ along the y axis. This is more singular than the analogous result for a smooth caustic, where the pressure behaves as the $-\frac{1}{6}$ power of the distance along the caustic and the $-\frac{1}{4}$ power of the distance normal to it (see, for example, Friedlander 1958, pp. 67–70; or Hayes 1968).

Another interesting feature of (17), which turns out to be essential for the matching, is that it is self-similar in time, i.e. it may be written as

$$\hat{\tilde{\phi}} = (-\hat{t})^{\frac{3}{2}}F(\chi/\hat{t}^2, \hat{y}/(-\hat{t})^{\frac{3}{2}}).$$

To show this, we define similarity variables σ and Γ by

$$\sigma \equiv -\tfrac{2}{3}\xi/\tau^2, \quad \Gamma \equiv 24\eta/(-6\tau)^{\frac{3}{2}},$$

where $\xi \equiv \chi/\kappa$, $\eta \equiv \hat{y}/\kappa$ and $\tau \equiv \hat{t}/\kappa$. Using these definitions and replacing the integration variable $\hat{y}_s$ in (17) by $(-6\tau)^{\frac{1}{2}}q$, we find that (17) may be rewritten as

$$\hat{\tilde{\phi}} = -\tfrac{1}{2}(\tfrac{1}{2}\kappa)^{\frac{1}{2}}\frac{\epsilon}{\Delta^{\frac{3}{2}}\delta^2}(-\tau)^{\frac{3}{2}}G(\sigma,\Gamma), \tag{18}$$

where G is defined by

$$G(\sigma,\Gamma) \equiv \frac{6}{\pi}\int_{q_l}^{q_u}\bar{\beta}^{\frac{1}{2}}(q)\,dq,$$

in which $\bar{\beta} \equiv -q^4-2q^2+\Gamma q+\sigma$ and q_u and q_l are the two real roots of $\bar{\beta} = 0$.

209

We now consider the inner solution. Although, in general, solutions of the form (18) do not satisfy (14), the inner solution must have such a form as $\hat{t} \rightarrow -\infty$. Thus it is most convenient to do the matching in the co-ordinates σ, Γ and τ. Accordingly, we write the solution $\hat{\phi}(\chi, \hat{y}, \hat{t})$ to (14) in terms of σ, Γ and τ and then rewrite $\hat{\phi}$ in outer variables:

$$\hat{\phi} = \hat{\phi}(\sigma, \Gamma, \tau) = \hat{\phi}(\tilde{\sigma}, \tilde{\Gamma}, (\delta\tilde{t} - 1)/\Delta\kappa),$$

where $\tilde{\sigma} \equiv -\frac{2}{3}\tilde{X}/(\delta\tilde{t} - 1)^2$ and $\tilde{\Gamma} \equiv 4\tilde{y}/6^{\frac{1}{2}}(1 - \delta\tilde{t})^{\frac{3}{2}}$. The usual matching principle states that, in the limit $\epsilon \rightarrow 0$, $\Delta \rightarrow 0$, $\delta \rightarrow 0$ with $\tilde{X}$, $\tilde{y}$ and $\tilde{t}$ fixed, $\hat{\phi}(\tilde{\sigma}, \tilde{\Gamma}, (\delta\tilde{t} - 1)/\Delta\kappa)$ must approach (18) asymptotically. Thus the function $\hat{\phi}(\sigma, \Gamma, \tau)$ must satisfy

$$\hat{\phi}(\sigma, \Gamma, \tau) \sim -\tfrac{1}{2}(\tfrac{1}{2}\kappa)^{\frac{1}{2}}(-\tau)^{\frac{3}{2}}G(\sigma, \Gamma)$$

as $\tau \rightarrow -\infty$ for all values of σ and Γ. In order that the initial condition be non-zero and finite, we must take

$$\Delta^{\frac{3}{2}} \equiv \epsilon/\delta^2 = o(1).$$

This last result determines the scaling (15) completely in terms of the physical parameters ϵ and δ, viz.

$$\frac{\lambda}{L} = \Delta^{\frac{3}{2}} = \frac{\epsilon}{\delta^2}, \quad \frac{\Lambda}{L} = \frac{\epsilon^{\frac{1}{3}}}{\delta^{\frac{5}{3}}}, \quad \frac{k}{\Lambda} = \epsilon^{\frac{2}{3}}\delta^{\frac{2}{3}}.$$

When written in terms of the variables ξ, η and τ the initial-value problem for the inner region is

$$2\hat{\phi}_{\xi\tau} + (\gamma + 1)\kappa^{-1}\hat{\phi}_{\xi}\hat{\phi}_{\xi\xi} + \hat{\phi}_{\eta\eta} = 0,$$

where as $\tau \rightarrow -\infty$

$$\hat{\phi}(\xi, \eta, \tau) \sim -\tfrac{1}{2}(\tfrac{1}{2}\kappa)^{\frac{1}{2}}(-\tau)^{\frac{3}{2}}G(\xi, \eta, \tau)$$

for all values of ξ and η. Here $G(\xi, \eta, \tau)$ is just the integral $G(\sigma, \Gamma)$ rewritten in terms of the variables ξ, η and τ.

We have now established the initial-value problem governing the flow in the focal region. The solution to this problem is seen to possess a similitude, i.e. it depends on only a single combination of the remaining physical parameters γ and κ. This is readily seen when the above initial-value problem is recast in terms of the scaled velocity potential

$$\Phi \equiv \tfrac{1}{2}(\tfrac{1}{2}\kappa)^{\frac{1}{2}}\hat{\phi}.$$

The problem then becomes

$$2\Phi_{\xi\tau} + Q\Phi_{\xi}\Phi_{\xi\xi} + \Phi_{\eta\eta} = 0,$$

where as $\tau \rightarrow -\infty$

$$\Phi \sim -(-\tau)^{\frac{3}{2}}G(\xi, \eta, \tau).$$

The similarity parameter Q is defined by

$$Q \equiv \tfrac{1}{2}(\gamma + 1)/(2\kappa)^{\frac{1}{2}}.$$

Except for a scaling of the dependent and independent variables, any two flows with the same value of Q will be identical. The flow quantity of especial interest here is the pressure coefficient, which is given by

$$C_p = \frac{\epsilon}{(2\kappa\Delta)^{\frac{1}{2}}}\Phi_{\xi}(\xi, \eta, \tau; Q) = \frac{\epsilon^{\frac{2}{3}}\delta^{\frac{2}{3}}}{(2\kappa)^{\frac{1}{2}}}\Phi_{\xi}(\xi, \eta, \tau; Q).$$

From this we see that the pressure levels at an arête are of order $\epsilon^{\frac{2}{3}}\delta^{\frac{2}{3}}$ and the amplification is of order $\epsilon^{-\frac{1}{3}}\delta^{\frac{2}{3}}$. The result that the pressure is proportional to the two-thirds power of the initial strength of the shock was also deduced by Pierce (1971).

We conclude this section with some remarks regarding the requirement that $\epsilon = o(\delta^2)$. An important result, but one which is outside the scope of the present theory, is the prediction of the transition shock strength; that is, for a given initial shock shape, the prediction of the initial shock strength above which the straightening of the shock associated with shock dynamic theory occurs. In § 4 we have seen that when

$$\epsilon = O(\delta^2) = o(1)$$

nonlinear effects are important even for times of order L/a_0. Because the distance to the caustic is large compared with L, we expect that the shock straightens without focusing. On the basis of this, we conjecture that the order of magnitude of the transition shock strength is given by $\epsilon = O(\delta^2)$. Of course, a more precise estimate must be given either by laboratory or numerical experiments or by a more comprehensive analysis.

7. Conclusion

The focusing of a very weak and almost straight shock at an arête has been examined. The method of matched asymptotic expansions has been used to establish the initial-value problem and similitude governing the flow in the focal region. The fundamental parameters in this problem are seen to be ϵ, a measure of the initial strength of the shock, and δ, which measures the rate at which the wave front converges. The maximum pressures at the arête have been shown to be proportional to $(\epsilon\delta)^{\frac{2}{3}}$. The results of this paper are valid for wave fronts with $\epsilon = o(\delta^2)$ and $\delta = o(1)$.

This research was supported by the office of Naval Research through contract N0014-76-C-0182 and the Air Force Office of Scientific Research through grant 76-2954B.

REFERENCES

BEASLEY, W. D., BROOKS, J. D. & BARGER, R. L. 1969 A laboratory investigation of N-wave focusing. *N.A.S.A. Tech. Note* D-5306.

CORNET, E. P. 1972 Focusing of an N-wave by a spherical mirror. *Appl. Res. Lab., Univ. Texas, Austin, Rep.* ARL-TR-72-40.

FRIEDLANDER, F. G. 1958 *Sound Pulses.* Cambridge University Press.

GUIRAUD, J. P. 1965 Acoustique géometrique, bruit ballistique des avions supersoniques et focalisation. *J. Méc.* 4, 215–267.

HAYES, W. D. 1957 The vorticity jump across a gasdynamic discontinuity. *J. Fluid Mech.* 2, 595–600.

HAYES, W. D. 1968 Similarity rules for nonlinear acoustic propagation through a caustic. *2nd Conf. Sonic Boom Res.* (ed. I. R. Schwartz). *N.A.S.A. Special Publ.* no. 180, pp. 165–171.

PIERCE, A. D. 1971. Maximum overpressures of sonic booms near the cusps of caustics. In *Noise and Vibration Control Engineering* (ed. M. J. Crocker), pp. 478–487. Purdue University Press.

STURTEVANT, B. & KULKARNY, V. A. 1974 Dynamics of weak shock waves at a focus. *Proc. 2nd Inter-Agency Symp. Univ. Res. Transportation Noise, North Carolina State Univ., Raleigh*, pp. 402–415.

STURTEVANT, B. & KULKARNY, V. A. 1976 The focusing of weak shock waves. *J. Fluid Mech.* **73**, 651–671.

WANNER, J. C., VALLEE, J., VIVIER, C. & THERY, C. 1972 Theoretical and experimental studies of the focus of sonic booms. *J. Acoust. Soc. Am.* **52**, 13–32.

WHITHAM, G. B. 1957 A new approach to the problems of shock dynamics. Part 1. Two-dimensional problems. *J. Fluid Mech.* **2**, 146–171.

WHITHAM, G. B. 1959 A new approach to the problems of shock dynamics. Part 2. Three-dimensional problems. *J. Fluid Mech.* **5**, 369–386.

WHITHAM, G. B. 1974 *Linear and Nonlinear Waves.* Interscience.

2/2

Reprinted from AIAA JOURNAL, Vol. 16, No. 7, July 1978, pp. 673–678

Implicit Shock-Fitting Scheme for Unsteady Transonic Flow Computations

N. J. Yu,* A. R. Seebass,† and W. F. Ballhaus‡
University of Arizona, Tucson, Ariz.

The alternating-direction implicit scheme developed by NASA Ames for unsteady transonic flows has been modified to include a shock-fitting algorithm, as well as an analytically stretched coordinate system. The shock-fitting procedure treats shock waves as discontinuities normal to the freestream. Improvements in shock position and the unsteady pressure distributions are obtained by this modification. The various types of shock motion observed experimentally by Tijdeman are well simulated in calculations using the modified computational scheme. The method for detecting shock-wave formation and the procedure for fitting a moving shock wave are illustrated. Results for an NACA 64A006 airfoil with oscillating quarter-chord flap are presented and discussed.

Introduction

THERE is a need for the numerical simulation of unsteady transonic flows about airfoils in order to predict unsteady aerodynamic loads and to provide an understanding of the behavior of unsteady transonic flowfields. A number of methods[1-11] have been proposed for computing such flows, and there is continuing improvement in the results obtained. This paper describes a shock-fitting procedure,[12] coupled with an implicit finite-difference algorithm,[1,2] which can accurately and efficiently simulate most unsteady transonic flows about thin airfoils.

A major consideration in constructing an algorithm for unsteady transonic flows is the treatment of moving shock waves. Experimental observations of Tijdeman[13,14] indicate that even for simple airfoil motions shock-wave motions can be complicated, and they can affect aerodynamic force and moment variations strongly. Time-linearized methods,[9,10] i.e., methods that assume that the unsteady perturbation is small compared to the basic steady disturbance, presently do not consider shock motions although they can be modified to do so for small shock excursions.[15,16] Time-integration methods[1-8] treat shock waves by "capturing" them, a procedure that can present a number of problems that will be discussed subsequently.

Tijdeman's experiments also indicate that shock motion amplitudes increase with decreasing frequency. This is supported by a simplified analysis of the time-linearized equations.[16] Thus, some of the most interesting transonic flowfields result from low-frequency motion. Explicit finite-difference schemes are not efficient when applied to low-frequency cases because the stability restriction on the time step is substantially more severe than that required for accuracy. As a result, efficient semi-implicit methods[3] and even more efficient fully implicit methods[1,2,7,8] have been developed. Caradonna and Isom[7] use an iterative implicit procedure; i.e., the nonlinear implicit finite-difference equations must be solved at a given time iteratively. In an earlier unpublished study we also used such a procedure. Ballhaus and Steger[1] and Beam and Warming[8] constructed more efficient algorithms that solve the nonlinear equations directly by the solution of simple matrix equations generated by an alternating-direction implicit (ADI) procedure. This method has proven to be so efficient, especially for the calculations with nonuniform mesh distributions, that we now often use it as an alternative to successive line overrelaxation (SLOR) for steady flow calculations.[17,18]

All of these implicit schemes "capture" shock waves; i.e., shock waves evolve automatically as part of the numerical solution. This procedure has several deficiencies associated with it. They can be eliminated, at the expense of coding complexity, by "fitting" shock waves as discontinuities in the flow. Shock capturing produces shock profiles that are distorted in a manner that depends on the truncation errors in the finite-difference scheme. The use of mixed-difference schemes[1,8] can improve the situation for cases in which the flow changes from supersonic to subsonic across the shock. However, when this condition is not satisfied, as in the later stages of pulsating motion of a parabolic-arc airfoil, the differencing cannot be switched across the shock and shock resolution is poor. In any case, shock capturing requires spatial grid spacings, in regions where shock waves are anticipated, which are sufficiently small to resolve the shock waves in a reasonable distance. The grid spacing required to do this is frequently much smaller than that required to resolve flow variable gradients in most of the rest of the flowfield. This also results in an unnecessarily severe time-step restriction because time steps for implicit schemes are chosen such that shocks move less than one spatial grid point per time step.[1,8] This is necessary to preserve both accuracy and stability. Shock fitting removes the large gradients from the finite-difference solution and generally permits equivalent flowfield resolution with fewer grid points, both in space and time. Finally, if shock waves are not treated as discontinuities but are to be captured correctly, the difference equations must be solved in conservation form. This imposes an additional constraint on the construction of finite-difference schemes which can be difficult to satisfy. For example, no fully conservative difference scheme for the full potential equations have been developed yet that can match the convergence reliability and computational efficiency of Jameson's non-conservative "rotated" difference procedure.[19]

In principle, the shock-fitting procedure discussed in this paper could be applied to the full potential equation. For steady flows it may substantially reduce the time required to obtain a converged solution. Here, as a first step, it is applied to a simpler formulation that contains the essential nonlinear unsteady behavior associated with low-frequency transonic flows. Furthermore, the algorithm is simplified by treating

---

Presented as Paper 77-633 at the AIAA 3rd Computational Fluid Dynamics Conference, Albuquerque, N. Mex., June 27-29, 1977; submitted July 26, 1977; revision received April 17, 1978. Copyright © American Institute of Aeronautics and Astronautics, Inc., 1977. All rights reserved.

Index categories: Transonic Flow; Nonsteady Aerodynamics; Computational Methods.

*Senior Research Associate. Member AIAA.

†Professor. Associate Fellow AIAA.

‡Research Scientist, NASA Ames Research Center and Aeromechanics Laboratory, U.S. Army AVRADCOM.

the shocks as discontinuities normal to the freestream. The procedures could be generalized to a curved shock with additional programming complexity. Methods of detecting shock formation and of judging the existence of a shock wave in the unsteady flowfield are described.

A production code, LTRAN2, has been developed for the efficient solution of low-frequency transonic flows about airfoils in motion.[2] LTRAN2 is based on the ADI method of Ballhaus and Steger,[1] and is being released on request to industry and government agencies. The modification of the ADI procedure to include shock fitting, which is the main subject of this paper, will improve LTRAN2 significantly. Substantially fewer grid points will be required to achieve equivalent flowfield resolution, and the time-step restriction due to shock motion can be relaxed considerably.

Numerical simulations of various types of shock motions for an NACA 64A006 airfoil with oscillating quarter-chord flap are described. Significant improvements in shock resolution and, consequently, in unsteady pressure distributions are obtained using the shock-fitting procedure. The results show the marked effect of shock-wave motion.

Formulation of Governing Equations

Low-Frequency Approximation

The unsteady, small-disturbance, transonic equation for low frequency commonly is written as

$$-2KM_\infty^2\phi_{xt}+\{1-M_\infty^2-(\gamma+1)M_\infty^2\phi_x\}\phi_{xx}+\phi_{yy}=0 \tag{1}$$

which may be derived[20] from a systematic expansion of the velocity potential with respect to the thickness ratio τ and the reduced frequency K, where $K=\omega c/U$, i.e., the angular frequency multiplied by the time that it takes the flow to traverse the airfoil chord. The spatial coordinates, the time, and the velocity potential in Eq. (1) have been nondimensionalized by the chord c, the inverse of the angular frequency ω^{-1}, and Uc, respectively.

The tangency condition and the unsteady pressure coefficient that are consistent with the low-frequency approximation are

$$\phi_y=\frac{\tau\partial Y(x,t)}{\partial x}=\tau\left[Y_{s_x}+\frac{\delta}{\tau}(Y_{u_x}+Y_{u_t})\right] \tag{2}$$

and

$$C_p=-2\left\{\frac{M_\infty^2-1}{(\gamma+1)M_\infty^2}+\phi_x\right\}$$

where $Y(x,t)$, the instantaneous body shape, has been decomposed into a steady part Y_s and an unsteady part Y_u.§ Here δ is the amplitude of the unsteady oscillation. Note that C_p is defined such that, at sonic conditions, $C_p=C_p^*=0$.

Any shock wave that exists in the flowfield must satisfy the jump relation derived from the conservative form of the governing equation (1), viz.,

$$-2KM_\infty^2[\![\phi_x]\!]^2\left(\frac{dx}{dt}\right)_s-\{1-M_\infty^2-(\gamma+1)M_\infty^2\bar{\phi}_x\}[\![\phi_x]\!]^2+[\![\phi_y]\!]^2=0 \tag{3}$$

together with the condition derived from the assumption of irrotationality,

$$\left(\frac{dy}{dx}\right)_s=-\frac{[\![\phi_x]\!]}{[\![\phi_y]\!]} \tag{4}$$

Here $\bar{\phi}_x$ refers to the mean value of ϕ_x evaluated on each side of the discontinuity, $[\![\phi_x]\!]$ indicates the jump in ϕ_x across the discontinuity, and the subscript s denotes the quantity evaluated at the shock surface.

In two-dimensional small-perturbation transonic flows, the shock waves that usually occur are nearly normal to the flow direction. We assume here that if the basic steady flow has a shock wave then this shock may be approximated by a shock wave normal to the freestream flow. Furthermore, we assume that the motion of any shock wave that arises from unsteady changes in the flow, as well as the motion of existing shock waves, also may be calculated by this normal shock approximation. For this simplified model, Eqs. (3) and (4) reduce to the single equation

$$\left(\frac{dx}{dt}\right)_s=\frac{\gamma+1}{2K}\left\{\frac{M_\infty^2-1}{(\gamma+1)M_\infty^2}+\bar{\phi}_x\right\} \tag{5}$$

which gives the speed of the normal shock in the flowfield. For steady flows, $\bar{\phi}_x$ is a function of x alone; this, of course, still permits $[\![\phi_x]\!]$ to vary with y. For unsteady flows, although $\dot{x}_s$ is a function of t alone, the strength of the shock will still vary with y.

Coordinate Stretching

To minimize the far-field boundary effects on the numerical results, a relatively large computational region is usually required. For the cases studied in this paper, the shock excursion may be large and the unsteady disturbances carried several chord lengths away from the airfoil; thus, the use of a relatively large computational domain seems inevitable. A simple and straightforward way of computing the solution in a large computational domain is to use nonuniform mesh distributions, with most of the mesh points concentrated in the region of interest.[2] An alternative is to introduce analytical coordinate stretchings. In the present study, we use the following coordinate stretchings:

$$\xi=\pm\{1-\exp(\mp a_1x)\}\quad\text{for } x\gtrless 0 \tag{6a}$$

$$\eta=\pm\{1-\exp(\mp a_2y)\}\quad\text{for } y\gtrless 0 \tag{6b}$$

where a_1 and a_2 are constants that control the mesh distributions.¶ Equations (6) transform the infinite physical domain to the finite computational domain bounded by $|\xi|\leq 1$ and $|\eta|\leq 1$. The transformation provides a concentrated mesh distribution near the airfoil which is suitable for the present study. The governing Eq. (1), written in the stretched coordinate system, is

$$\left\{\frac{-2KM_\infty^2}{a_2^2(1-|\eta|)}\phi_\xi\right\}_t-\left\{\frac{(\gamma+1)M_\infty^2}{2a_2^2(1-|\eta|)}\left[\frac{M_\infty^2-1}{(\gamma+1)M_\infty^2}+a_1(1-|\xi|)\phi_\xi\right]^2\right\}_\xi+\left\{\frac{1-|\eta|}{a_1(1-|\xi|)}\phi_\eta\right\}_\eta=0 \tag{7}$$

Because Eq. (7) is in divergence-free form, a conservative difference approximation to Eq. (7) can be constructed if the shock wave is to be "captured" rather than "fitted."

The normal shock jump relation follows directly from Eq. (7); this relation and the boundary condition on the airfoil surface are now

$$\left(\frac{d\xi}{dt}\right)_s=\frac{a_1(1-|\xi|)(\gamma+1)}{2K}\left\{\frac{M_\infty^2-1}{(\gamma+1)M_\infty^2}+a_1(1-|\xi|)\bar{\phi}_\xi\right\} \tag{8}$$

---

§In the cases studied numerically, $Y_{u_x}=O(Y_{u_t})$; consequently, the last term in Eq. (2) is of higher order and was neglected.

¶Calculations made with an algebraic scaling, viz., $\xi=x/(|x|+a_1)$, etc., gave essentially identical results.

and

$$\phi_\eta = \frac{a_1}{a_2}(1-|\xi|)\frac{\partial Y(\xi,t)}{\partial \xi} \quad \text{at } \eta=0 \tag{9}$$

Scaling of the Perturbation Equation

In his study of steady, small-disturbance transonic flow, Krupp[21] introduced a scaling of the governing equation and the body shape to provide better agreement between the results of the perturbation calculations and those from the Euler equations. The reasoning that leads to various scalings is discussed in the review by Ballhaus.[22] One also may use such a scaling in the low-frequency approximation by rewriting the governing equation and the boundary condition as

$$-2KM_\infty^p \phi_{xt} + \{1-M_\infty^2-(\gamma+1)M_\infty^m\phi_x\}\phi_{xx}+\phi_{yy}=0 \tag{10}$$

and

$$\phi_y = M_\infty^n \tau\left\{Y_{s_x}+\frac{\delta}{M_\infty^n\tau}Y_{u_x}\right\} \tag{11}$$

where p, m, and n are scaling constants to be chosen to enhance agreement with more sophisticated calculations. If one introduces the nondimensional quantities

$$\bar{\phi} = \frac{(\gamma+1)^{1/3}}{M_\infty^{1/3(2n-m)}\tau^{2/3}}\phi \tag{12a}$$

$$\bar{y} = \{(\gamma+1)M_\infty^{m+n}\tau\}^{1/3}y \tag{12b}$$

$$\bar{t} = \{(\gamma+1)^2 M_\infty^{2m+2n-3p}\tau^2\}^{1/3}t/2K \tag{12c}$$

$$\alpha = \frac{1-M_\infty^2}{\{(\gamma+1)M_\infty^{n+m}\tau\}^{2/3}} \tag{12d}$$

$$\beta = \delta/M_\infty^n\tau \tag{12e}$$

then Eqs. (10) and (11) reduce to the canonical form

$$-\bar{\phi}_{x\bar{t}}+(\alpha-\bar{\phi}_x)\bar{\phi}_{xx}+\bar{\phi}_{\bar{y}\bar{y}}=0 \tag{13}$$

and

$$\bar{\phi}_{\bar{y}} = Y_{s_x}+\beta Y_{u_x} \tag{14}$$

Because there is a one-to-one correspondence between Eqs. (1) and (2) and Eqs. (13) and (14), results obtained without scaling are equivalent to scaled calculations for a slightly different flow. Thus, although we restrict our calculations to the unscaled equation, the Mach number and the body shape can be modified to obtain results equivalent to those for the scaled equation by noting the equivalencies [Eqs. (12)].

Boundary Conditions

The boundary condition on the airfoil is the usual tangency condition evaluated at $y=0$. For an NACA 64A006 airfoil with an oscillating quarter-chord flap, the boundary conditions are

$$\phi_y = \begin{cases} \tau Y_{s_x} & \text{for } 0\le x\le 0.75 \\ \tau\left(Y_{s_x}+\dfrac{\delta}{\tau}\sin t\right) & \text{for } 0.75< x\le 1 \end{cases}$$

With the proper combinations of the reduced frequency K, the free Mach number M_∞, and the oscillating amplitude δ, we can simulate the three types of shock motions observed experimentally by Tijdeman[13,14]: the shock oscillates on the airfoil (type A); the shock disappears during part of the period (type B); and the shock propagates upstream and leaves the airfoil (type C). The thickness distribution for an NACA 64A006 airfoil may be obtained from Ref. 23 and the desired airfoil slope at the grid locations approximated by fitting a polynomial to the data.

The far-field boundary condition for the nonlifting case is simply $\phi=0$ on $|\xi|=1$ and $|\eta|=1$. For the lifting case, ϕ depends on the instantaneous circulation Γ. This dependence can be derived theoretically by assuming that in the far field all of the perturbations are small compared to the basic steady state.[24] An advantage of our stretched coordinate system is that the last grid lines are at infinity. Numerical studies conducted by Magnus[6] show that erroneous boundary data on a finite domain can lead to significant errors. The low-frequency approximation implies that any changes in the circulation are communicated instantly downstream to infinity ($\xi=1$). Consequently, the simplest boundary conditions are $\phi_x=0$ on the downstream boundary and $\phi=0$ on the other boundaries. Ballhaus and Goorjian[2] used similar boundary conditions in their study and obtained satisfactory results. The validity of such far-field boundary conditions can be justified only by numerical experiments; i.e., near the boundary the disturbance quantities ϕ_x and ϕ_y must be much smaller than the values at the airfoil surfaces. In all of the results reported here, this requirement is met. As a numerical test of this procedure, we have computed the steady-state circulation about an NACA 64A006 airfoil for various flap deflection angles, using the ADI method with appropriate far-field values of ϕ corrected for the usual steady-state circulation contribution. These results have been compared with the results obtained by the ADI calculations with the boundary conditions employed here for an unsteady flap deflection to the correct angle. These results agree to one part in 10^{-4}, verifying that the far-field conditions used here are more than satisfactory.

Finite-Difference Approximations

In a preliminary study of the unsteady transonic flows, we implemented a normal shock-fitting procedure in the implicit-iterative scheme of Caradonna and Isom.[7] Satisfactory results were obtained, except that the procedure was time-consuming because of the iterative process required at each time step. The recent studies of Ballhaus and Steger[1] and Ballhaus and Goorjian[2] show that an ADI scheme is more efficient than the implicit-iterative scheme in treating the low-frequency transonic flow equation. The shock-fitting algorithm was modified and implemented with an ADI scheme. In this section, the ADI procedure is reviewed briefly and the method for unsteady shock fitting detailed.

Alternating-Direction Implicit (ADI) Method

The low-frequency equation in the stretched coordinate system, i.e., Eq. (7), is solved by the alternating-direction implicit scheme developed by Ballhaus and Steger.[1] To simplify this discussion, Eq. (7) is rewritten in the form

$$\psi_{\xi t}+F_\xi+G_\eta=0 \tag{15}$$

where the functions ψ, F, and G may be determined by comparing Eqs. (7) and (15). The solution is advanced from time level n to level $n+1$ by the following two-step procedure:

ξ Sweep

$$(1/\Delta t)(\psi_\xi^+-\psi_\xi^n)+D_\xi F^+ + \delta_\eta G^n=0 \tag{16a}$$

η Sweep

$$(1/\Delta t)(\psi_\xi^{n+1}-\psi_\xi^+)+\tfrac{1}{2}\delta_\eta(G^{n+1}-G^n)=0 \tag{16b}$$

Here a plus sign refers to an intermediate value of ψ, D_ξ is the type-dependent difference operator for ξ derivatives, and δ_η is the central-difference approximation for the η derivative. The backward difference approximation for ψ_ξ can be either the first-order difference approximation

$$\psi_\xi = (1/\Delta\xi)(\psi_i - \psi_{i-1}) \tag{17}$$

or the second-order difference approximation

$$\psi_\xi = (1/2\Delta\xi)(3\psi_i - 4\psi_{i-1} + \psi_{i-2})$$

For simplicity the first-order scheme, Eq. (17), has been used for all of the results reported here. The nonlinear term F is evaluated, using a two-time-level averaging procedure analogous to that of Ballhaus and Steger[1] but modified by the coordinate stretching used here. The difference approximations described previously provide first-order accuracy for $\psi_{\xi t}$, second-order accuracy for F_ξ and G_η in subsonic regions, and first-order accuracy for F_ξ in supersonic regions.

On the ξ sweep, Eq. (16a), a quadradiagonal system is generated and can be solved easily by direct elimination. For lifting calculations, two grid lines are used to represent the lower and upper surfaces of the airfoil. The circulation Γ is calculated by $\Gamma = \phi^U_{ITE} - \phi^L_{ITE}$ through each sweep. Here ITE denotes the upper and lower values at the first grid point behind the trailing edge. This circulation is incorporated into the construction of the η derivatives behind the airfoil for $\eta = 0$.

On the η sweep, Eq. (16b), a tridiagonal system is generated on the body. Ahead of the leading edge and behind the trailing edge, the double grid notation for $\eta = 0$ destroys the tridiagonal system. However, ahead of the leading edge, $\phi^U = \phi^L$, and behind the trailing edge, $\phi^U = \phi^L + \Gamma$; thus the difference equations can be reordered to give a tridiagonal system. On the airfoil surface the matrix equations above and below the airfoil are decoupled; they can be solved either separately or simultaneously by packing the matrix equations together.

Shock-Fitting Procedure

The basic algorithm for shock fitting was developed in a previous study of steady transonic flows.[12] A different approach to shock fitting also has been developed by Hafez and Cheng[25] in their study of steady transonic flow problems. Their procedure essentially replaces the shock-point operator by an analogous difference statement derived from the shock jump conditions. Subsequently, the velocity potential on each side of the shock wave is extrapolated to locate the shock wave.

To understand the shock-fitting procedure for unsteady transonic flow calculations it is necessary to recall how shock waves form in an unsteady field. Shock waves are generated when the local flow becomes supersonic and compressive. Although the initial shock formation may not be predicted accurately by the numerical solution when shock fitting is used in the early stages of shock-wave formation, it eliminates spurious oscillations in the numerical solution and does provide the correct development of the shock wave in later stages of the calculations.[26] The criterion that we set for the initial shock formation is that the local flow become sonic (relative to the airfoil) and compressive. In the body-fixed coordinate system, a shock wave can exist both in the usual supersonic-supersonic and supersonic-subsonic transition and also in a purely subsonic flowfield, sometimes referred to as a "subsonic-subsonic" shock. In any case, the flow ahead of the shock relative to a coordinate system fixed on the shock must be always supersonic. Consequently, the correct judgment for the existence of a shock wave in the unsteady field is to evaluate the local flow velocity ahead of a prospective shock with respect to the coordinate system fixed on it, i.e., we evaluate V_r, where

$$V_r \approx \frac{M_\infty - 1}{M_\infty} + \left\{1 + \frac{(\gamma - 1)M_\infty}{2}\right\} a_1 (1 - |\xi|)\phi_\xi - \frac{K}{a_1(1 - |\xi|)}\left(\frac{d\xi}{dt}\right)_s$$

If $V_r > 0$, the local flow is supersonic and a shock may exist; if $V_r \to 0^+$, the local flow becomes sonic and the shock strength diminishes. For $V_r \leq 0$, a shock cannot exist.

We start the unsteady flow calculations by using an ADI scheme. When the local flow becomes sonic and compressive, we introduce the shock-fitting algorithm. Sonic, compressive points are treated as shock points where cross differentiations in t and ξ derivatives are avoided. Initially, the shock has zero strength and is stationary. The flow properties ahead of and behind the shock can be extrapolated easily from neighboring points. The shock wave can either increase or decrease in strength during the unsteady process. This results in three possibilities for shock motion that have to be considered separately in the fitting procedure: the shock moves upstream and crosses grid points; the shock remains stationary or moves within a grid spacing; and the shock moves downstream and crosses grid points. At each new time level the shock position is determined by applying Eq. (8). The formulations of the difference approximations for each case are quite similar; the specific formulas used may be found in Ref. 27.

Results and Discussion

To illustrate the advantages of shock fitting over shock capturing, we compare the flow past a pulsating parabolic arc whose time history is shown in Fig. 1, as computed by the two methods. Major differences occur when the shock wave propagates ahead of the airfoil as its thickness returns to zero. Figure 2 compares the pressure coefficient for these later stages when $t \geq 25$ (chord/U) in units of $\Delta t = 2$ computed by the ADI method, with and without shock fitting. The full time history of this motion, as computed by the two methods, is compared in Ref. 27. Later studies have shown, as suggested by a reviewer, that the compression preceding the fitted shock wave is a result of the first-order approximation made here. In subsequent calculations with a second-order procedure, which is possible with shock fitting, this behavior does not occur.

Results were computed for an NACA 64A006 airfoil with quarter-chord oscillating flap for various values of the reduced frequency K, the freestream Mach number M_∞, and the oscillation amplitude δ, in order to simulate the shock motions observed by Tijdeman.[13,14] The steady-state solutions at the mean flap deflection angle for each M_∞ are computed first, using the ADI method of shock fitting. We have found that the ADI scheme is more efficient than successive over-relaxation in computing steady flows. The results of the ADI calculations are identical with those obtained by line relaxation and converge more rapidly when performed with the stretched coordinates. For the problems studied here, i.e., the NACA 64A006 airfoil, the freestream Mach number was varied between 0.8 and 0.9. The mesh system had 101 by 82 grid points in the x and y directions, respectively. About 250 to 450 time steps were required for the solution to converge, $|\Delta\phi|_{max} \leq 10^{4}$. These steady-state solutions are used as initial data for the unsteady flow calculations. For all cases

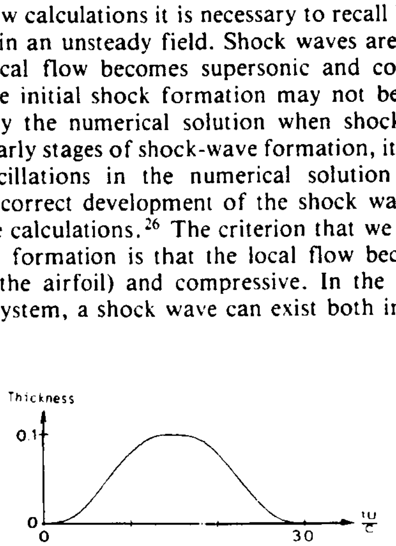

Fig. 1 Maximum thickness vs time for pulsating parabolic arc in units of percent thickness vs time in units of chord/speed

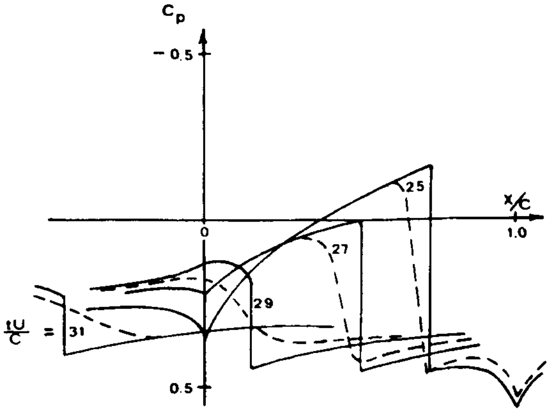

Fig. 2 Pressure coefficient in the later stages of the motion of Fig. 1 computed with (——) and without (---) shock-fitting.

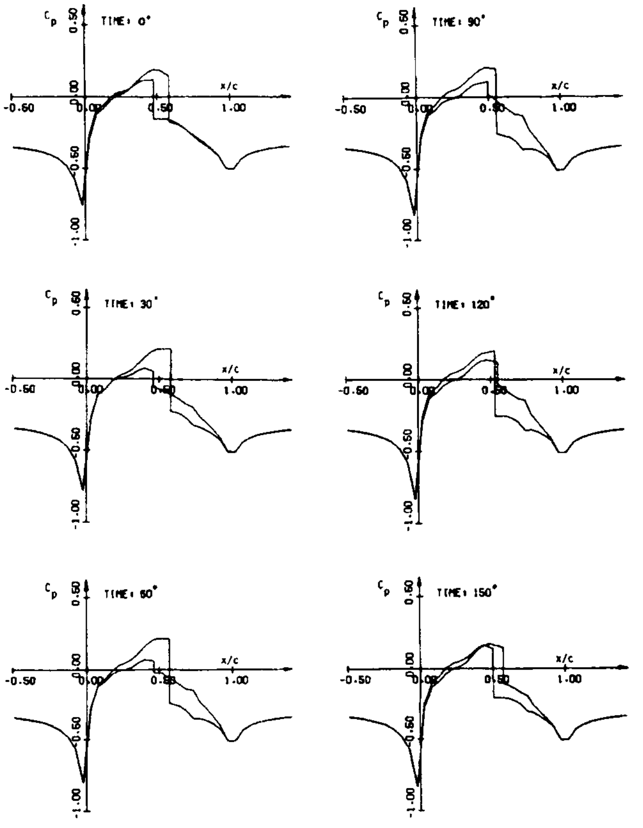

Fig. 3 C_p on an NACA 64A006 airfoil at $M_\infty = 0.854$, $K = 0.358$, with $\delta = 1$-deg sin$t$.

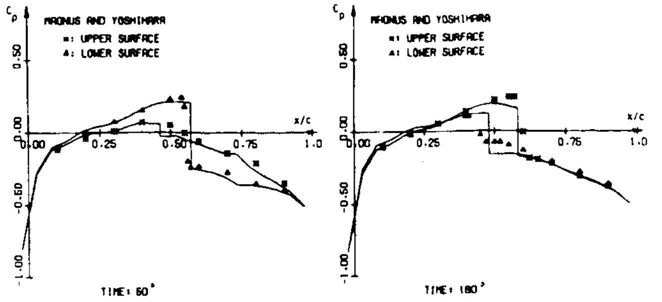

Fig. 4 Comparisons of the results for C_p on an NACA 64A006 airfoil at $M_\infty = 0.854$, $K = 0.358$, with $\delta = 1$-deg sin$t$, with those of Magnus and Yoshihara.[4,5]

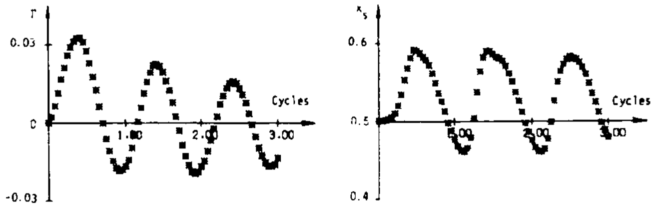

Fig. 5 History of the circulation and shock position for the first three cycles for the flow conditions of Fig. 3.

studied it took three to six cycles for the flowfield to become periodic. Stability seems to require that the time step Δt be small enough that Δt (deg)/$K < 10$. Figure 3 illustrates the pressure coefficients on the airfoil surface for $M_\infty = 0.854$, $K = 0.358$, and $\delta Y_{u_x} = 1$-deg sin$t$. For these conditions, Ballhaus and Goorjian[2] were able to simulate type B motion where the shock disappears during some part of the cycle. Here the shock does not disappear during the cycle; instead, it becomes quite weak during a small portion of the cycle. This difference is due to the assumption of a normal shock, which results in a stronger shock than would normally occur, and to the use of shock fitting. Magnus and Yoshihara's explicit results for the full Euler equations are compared with these results for two time levels in Fig. 4. The discrepancy between the two results is due mainly to the small-disturbance approximation and the lack of resolution at the leading edge of the present study. Figure 5 shows the time history during the first three cycles, of the circulation and the shock position. After three cycles of oscillation, the pressure field is essentially periodic; the circulation requires four cycles to become periodic. The circulation reaches its maximum value, and the shock wave its most downstream location, 57 and 83 deg after full flap deflection. Results for type C motion are given in Ref. 27 and hence not repeated here.

The results for $M_\infty = 0.822$, $K = 0.496$, and $\delta Y_{u_x} = 2$ deg sin$t$ simulate type C shock motion. Because we have used less spatial resolution and the unscaled equation, a deflection angle slightly larger than that of Ref. 2 is needed in order to generate the type C shock motion; that is, we need a 2-deg deflection angle rather than the 1.5 deg used in Ref. 2 to get analogous behavior. The results are given in Ref. 27. In this case, the flowfield is subcritical during most of the cycle, and the shock wave is barely "captured" in the non-shock-fitting procedure. During the unsteady process, the shock wave moves toward the leading edge. The strong singular behavior in pressure at the leading edge prevents the shock from propagating off the airfoil. The perturbation velocity becomes large and is negative; thus, the flow used to calculate the relative velocity ahead of the shock can no longer support a shock wave. Normal shock-fitting calculations determine the shock speed from the pressure jump across the shock at the airfoil surface. This eliminates the possibility that a portion of the shock may propagate off the leading edge in the computations. But this does not imply that it cannot occur; instead this limitation is a consequence of the normal shock fitting.

The addition of the shock-fitting algorithm to the basic ADI scheme increased the computational time, for fixed grid spacing, by less than 7% for all cases studied here. It is difficult to compare the time required by the two schemes to achieve the same accuracy. Without shock fitting, when the shock is not of the supersonic-subsonic type, a very fine grid is required for a reasonable resolution at the shock. The need for such a grid is obviated by shock fitting, and improved accuracy in the shock region can be obtained simultaneously with reduced computational time. Because it is difficult to determine when the two procedures give comparable accuracy, a definitive evaluation of the computing time saved by shock fitting has not been attempted.

Typical computation times for the NACA 64A006 airfoil calculations reported here are about 5 to 10 min/cycle on a

CDC 6400 computer. A mesh of 101 by 82 grid lines in x and y directions, respectively, was used in these calculations, and the number of time steps per cycle ranged from 90 to 180. No effort was made to optimize the program. The additional central memory required for the shock-fitting algorithm is about 10 to 20% of that for the basic ADI scheme.

Conclusion

The unsteady behavior of a large number of inviscid low-frequency transonic flows can be studied accurately and efficiently using the present shock-fitting procedure coupled with the alternating-direction implicit method. The ADI method relaxes the stability restriction on the time step, greatly improving the computational efficiency; the shock-fitting procedure treats shock waves as discontinuities, which resolves the computational difficulties that can arise in the usual shock "capturing" procedure. Computed results using the present procedure compare favorably with the explicit time integrations carried out by Magnus and Yoshihara. They should be sufficiently accurate for engineering studies of airfoil motions for which the normal shock approximation made here is a reasonable one. They also reproduce well the types of shock motions observed experimentally by Tijdeman,[13,14] as well as the propagation of the shock wave ahead of the pulsating parabolic arc.

Acknowledgment

This research was sponsored by NASA through Grant NSG-2112 and the Air Force Office of Scientific Research through Grant 76-2954.

References

[1] Ballhaus, W. F. and Steger, J. L., "Implicit Approximate-Factorization Schemes for the Low-Frequency Transonic Equation," NASA TM X-73082, 1975.

[2] Ballhaus, W. F. and Goorjian, P. M., "Implicit Finite Difference Computations of Unsteady Transonic Flows about Airfoils," *AIAA Journal*, Vol. 15, Dec. 1977, pp. 1728-1735.

[3] Ballhaus, W. F. and Lomax, H., "The Numerical Simulation of Low Frequency Unsteady Transonic Flow Fields," *Lecture Notes in Physics*, Vol. 35, Springer-Verlag, Berlin, 1975, pp. 57-63.

[4] Magnus, R. and Yoshihara, H., "Unsteady Transonic Flows Over an Airfoil," *AIAA Journal*, Vol. 13, Dec. 1975, pp. 1622-1628.

[5] Magnus, R. and Yoshihara, H., "The Transonic Oscillating Flap," AIAA Paper 76-327, 1976.

[6] Magnus, R. J., "Computational Research on Inviscid, Unsteady, Transonic Flow over Airfoils," Office of Naval Research, Rept. CASD/LVP 77-010, 1977.

[7] Caradonna, F. X. and Isom, M. P., "Numerical Calculation of Unsteady Transonic Potential Flow Over Helicopter Rotor Blades," *AIAA Journal*, Vol. 14, April 1976, pp. 482-488.

[8] Beam, R. M. and Warming, R. F., "An Implicit Finite-Difference Algorithm for Hyperbolic Systems in Conservation-Law Form," *Journal of Computational Physics*, Vol. 22, Jan. 1976, pp. 87-110.

[9] Traci, R. M., Albano, E., and Farr, J. L., "Perturbation Method for Transonic Flows about Oscillating Airfoils," *AIAA Journal*, Vol. 14, Sept. 1976, pp. 1258-1265.

[10] Weatherill, W. H., Ehlers, F. E., and Sebastian, J. D., "Computation of the Transonic Perturbation Flow Fields Around Two- and Three-Dimensional Oscillating Wings," NASA CR-2599, 1975.

[11] Ballhaus, W. F. and Goorjian, P. M., "Computation of Unsteady Transonic Flows by the Indicial Method," *AIAA Journal*, Vol. 16, Feb. 1978, pp. 117-124.

[12] Yu, N. J. and Seebass, A. R., "Inviscid Transonic Flow Computations with Shock Fitting," *IUTAM Symposium Transsonicum II*, edited by K. Oswatitsch and D. Rues, Göttingen, Germany, 1975, pp. 449-456.

[13] Tijdeman, H., "On the Motion of Shock Waves on an Airfoil with Oscillation Flap in Two-Dimensional Transonic Flow," NLR TR 75038U, 1975.

[14] Tijdeman, H., "On the Motion of Shock Waves on an Airfoil with Oscillating Flap," *IUTAM Symposium Transsonicum II*, edited by K. Oswatitsch and D. Rues, Göttingen, Germany, 1975, pp. 49-56.

[15] Hafez, M. M., Rizk, M. H., and Murman, E. M., "Numerical Solution of the Unsteady Transonic Small-Disturbance Equations," *AGARD Meeting*, Lisbon, Portugal, April 1977.

[16] Fung, K-Y., Yu, N. J., and Seebass, A. R., "Small Unsteady Perturbations in Transonic Flows," to be published in *AIAA Journal*.

[17] Ballhaus, W. F., Jameson, A., and Albert, J., "Implicit Approximate-Factorization Schemes for Steady Transonic Flow Problems," AIAA Paper 77-634, 1977; also *AIAA Journal* (to be published).

[18] Yu, N. J. and Seebass, A. R., unpublished results, 1976.

[19] Jameson, A., "Iterative Solution of Transonic Flows Over Airfoils and Wings, Including Flows at Mach 1," *Communications in Pure and Applied Mathematics*, Vol. 27, 1974, pp. 283-309.

[20] Lin, C. C., Reissner, E., and Tsien, H. S., "On Two-Dimensional Non-Steady Motion of a Slender Body in a Compressible Fluid," *Journal of Mathematics and Physics*, Vol. 27, March 1948, pp. 220-231.

[21] Krupp, J. A., "The Numerical Calculations of Plane Steady Transonic Flows past Thin Lifting Airfoils," Boeing Scientific Research Lab., Rept. 0180-12958-1, 1971.

[22] Ballhaus, W. F., "Some Recent Progress in Transonic Flow Computations," *VKI Lecture Series on Computational Fluid Dynamics*, 1976.

[23] Abbott, I. H. and von Doenhoff, A. E., *Theory of Wing Sections*, McGraw-Hill, New York, 1949, Appendix I, p. 354.

[24] Krupp, J. A. and Cole, J. D., "Studies in Transonic Flow IV, Unsteady Transonic Flow," Univ. of California at Los Angeles, Engineering Rept. 76104, 1976.

[25] Hafez, M. M. and Cheng, H. K., "Convergence Acceleration and Shock Fitting for Transonic Aerodynamics Computations," AIAA Paper 75-51, 1975.

[26] Moretti, G., "Thoughts and Afterthoughts about Shock Computations," Polytechnic Inst. of Brooklyn, PIBAL Rept. 72-37, 1972.

[27] Yu, N. J., Seebass, A. R., and Ballhaus, W. F., "An Implicit Shock-Fitting Scheme for Unsteady Transonic Flow Computations," AIAA Paper 77-633, 1977, pp. 13-26.